ADVANCED COMPOSITES CENTRE FOR INNOVATION & SCIENCE

Fatigue of Composite Truss Structures

Paul Harper

Department of Aerospace Engineering

April 2009

A thesis submitted to the University of Bristol in accordance with the requirements of the degree of Doctor of Philosophy in the Faculty of Engineering

38,775 words

University of BRISTOL

Abstract

Truss assemblies offer a high stiffness, light-weight option for the construction of aerospace and civil structures. Their more widespread use is currently limited by significant design challenges associated with the nodal joints between struts, particularly in relation to fatigue. The initial focus of this research degree was the multi-partner, DTI funded 'Nodal Optimisation of Truss Structures (NOTS)' project, which explored the potential of replacing a conventional metallic panel aircraft rib with a composite truss structure. The role of the author's work within NOTS was to aid the design of the adhesively bonded nodal joint through the implementation of a fatigue test programme.

The NOTS project highlighted the need for improved analysis techniques in relation to both bond-line failure and delamination. To address this requirement, a numerical fatigue crack propagation law was developed within the explicit finite element code 'LS-Dyna.' The law can be used to evaluate whether the crack tip strain energy release rate is sufficient for crack growth to occur and if so, to simulate the rate and direction of growth. The novelty of this work lies in the detailed analysis of the numerical cohesive zone which forms ahead of the crack tip and is critical to the accurate implementation of the fatigue degradation law. The extraction of strain energy release rate from the cohesive zone enables a direct link with the Paris Law for crack growth and experimental parameters obtained from standard fracture toughness specimens.

The analysis technique has been validated using models of standard mode I, mode II and mixed mode specimens. It has then been applied to analyse fatigue crack propagation in both an adhesively bonded single-lap joint and the nodal joint developed within the NOTS project. Recommendations have been provided to guide further development of the analysis technique and to enable its integration within the design process.

Acknowledgements

Special thanks to Dr Stephen Hallett for his invaluable advice, guidance and feedback throughout this research project. I could not have hoped for a better supervisor. I am also very grateful to the following colleagues at the University of Bristol who have aided this research:

- Dr Kevin Potter, Dr Bijoysri Khan and Dr Mostefa Bourchak for their help and guidance concerning the experimental work conducted.
- Xiangqian Li and Michael May for their support with the numerical aspects of the research.

I would like to thank the Engineering and Physical Sciences Research Council (EPSRC) and Airbus UK for funding this research through a CASE studentship. Thanks also to the NOTS partners and in particular, Jago Pridie (Airbus), Dr Natalia Becerra and Dr James Broughton (Oxford Brookes University) for their help in conducting the NOTS fatigue test programme.

Finally, I would like to thank my family for their love, support and friendship throughout. I would be lost without them.

Author's Declaration

"I declare that the work in this dissertation was carried out in accordance with the requirements of the University's Regulations and Code of Practice for Research Degree Programmes and that it has not been submitted for any other academic award. Except where indicated by specific reference in the text, the work is the candidate's own work. Work done in collaboration with, or with the assistance of, others, is indicated as such. Any views expressed in the dissertation are those of the author.

SIGNED: ...P. Harper..... DATE:.....22/5/09"

Table of Contents

List of Figures

List of Tables

List of Abbreviations

2D	Two Dimensional
3D	Three Dimensional
3ENF	3 Point End Notched Flexure
4ENF	4 Point End Notched Flexure
ACG	Advanced Composites Group
ARP	Aeronautics Research Programme
ASTM	American Standard Test Method
BSI	British Standards Institution
CFRP	Carbon-Fibre Reinforced Plastic
CTG	Crompton Technology Group
DCB	Double Cantilever Beam
DLS	Double Lap Shear
DTI	Department of Trade and Industry
FRMM	Fixed-Ratio Mixed Mode
FRP	Fibre Reinforced Plastic
MMB	Mixed-Mode Bending
NCF	Non-Crimp Fabric
NDT	Non-Destructive Test
NOTS	Nodal Optimisation of Truss Structures
NPL	National Physical Laboratory
RTM	Resin Transfer Moulding
S2	Stage 2
UTS	Ultimate Tensile Strength
VCCT	Virtual Crack Closure Technique

List of Symbols

Interface Element Properties:

G_C	Critical Strain Energy Release Rate
K	Interface Element Stiffness prior to damage initiation
σ	Interface Element Stress
σ_{max}	Interfacial Strength
δ	Interface Element Relative Displacement
δ_e	Interface Element Relative Displacement at damage initiation
δ_f	Interface Element Relative Displacement at final failure

Subscripts *I*, *II* and *m* are used to denote properties under mode I, mode II and mixed mode loading respectively

Geometric Properties:

A	Area
a	Crack Length
a_0	Initial Crack Length prior to crack propagation
B	Laminate Width
h	Laminate Half Thickness
I	Second Moment of Area
X	Specimen Length

Material Properties:

E_{11}, E_{22}, E_{33}	Young's Moduli
G_{12}, G_{13}, G_{23}	Shear Moduli
$\nu_{12}, \nu_{13}, \nu_{23}$	Poisson's Ratios

where subscripts 1, 2 and 3 denote the principal material axes

Miscellaneous:

D_{tot}	Damage parameter, consisting of both quasi-static and fatigue damage, used to degrade interfacial strength in fatigue law
d_s	Quasi-static damage parameter
d_{fat}	Fatigue damage parameter
$E^{'}$	Equivalent Elastic Modulus used in the characteristic length equation for orthotropic materials
G	Strain Energy Release Rate
L_{CZ}	Numerical Cohesive Zone Length
$L_{CZ,f}$	Fully Developed Numerical Cohesive Zone Length
L_D	Damaged length of element
L_{el}	Element Length
L_{fat}	Fatigue Damage Length
L_{qs}	Quasi-static Damage Length
l_{ch}	Characteristic Cohesive Zone Length in an infinite body
$l_{ch,slender}$	Characteristic Cohesive Zone Length in a slender body
N	Number of fatigue cycles
N_{el}	Number of elements within the numerical cohesive zone
P	Load
S	Stress
t	Time
Δ	Cantilever Tip Displacement

1. Introduction

Composite truss structures can enable significantly reduced mass in a range of applications where light-weight design is important, such as aerospace structures, bridges and support masts. However, more widespread use is currently limited by significant design challenges associated with the nodal joints between struts, particularly in relation to fatigue and durability. The current chapter provides an overview of the fundamental challenges associated with the design and fatigue life analysis of composite truss structures. It also provides an introduction to the multi-partner Nodal Optimisation of Truss Structures (NOTS) project, which provided the initial focus of work conducted during the author's studentship. This background links the experimental and numerical work subsequently detailed and provides justification for the research objectives defined at the end of the chapter.

1.1 Background

1.1.1 Composite Truss Structures: Benefits, Applications and Challenges

A truss can be defined as a framework of beams forming a rigid structure. Although metallic truss structures are already widely used due to their high strength-weight ratio, fibre reinforced plastic (FRP) composites provide scope for further improvements in structural efficiency. This arises from the ability to optimise mechanical properties by aligning fibres in specific directions, for example, along the length of each beam to provide maximum tensile/compressive strength. Potential applications for composite truss structures include:

i) Primary aerospace structures where reduced structural weight is key to achieving minimum operational costs through reduced fuel burn.

ii) Civil engineering structures such as bridges and masts where material weight has a large influence on both the structural volume and complexity required to achieve the given strength requirements.

iii) Off-shore structures such as platforms and pipelines, where long service lifetimes and harsh marine environments demand highly durable, corrosion resistant materials.

The initial focus of work conducted during the author's studentship was the multi-partner Nodal Optimisation of Truss Structures (NOTS) project, funded by the Department of Trade and Industry (DTI), which ran between 2003 and 2006. This explored the potential of replacing a conventional metallic panel aircraft rib with a composite truss structure, as shown in Figure 1.1.

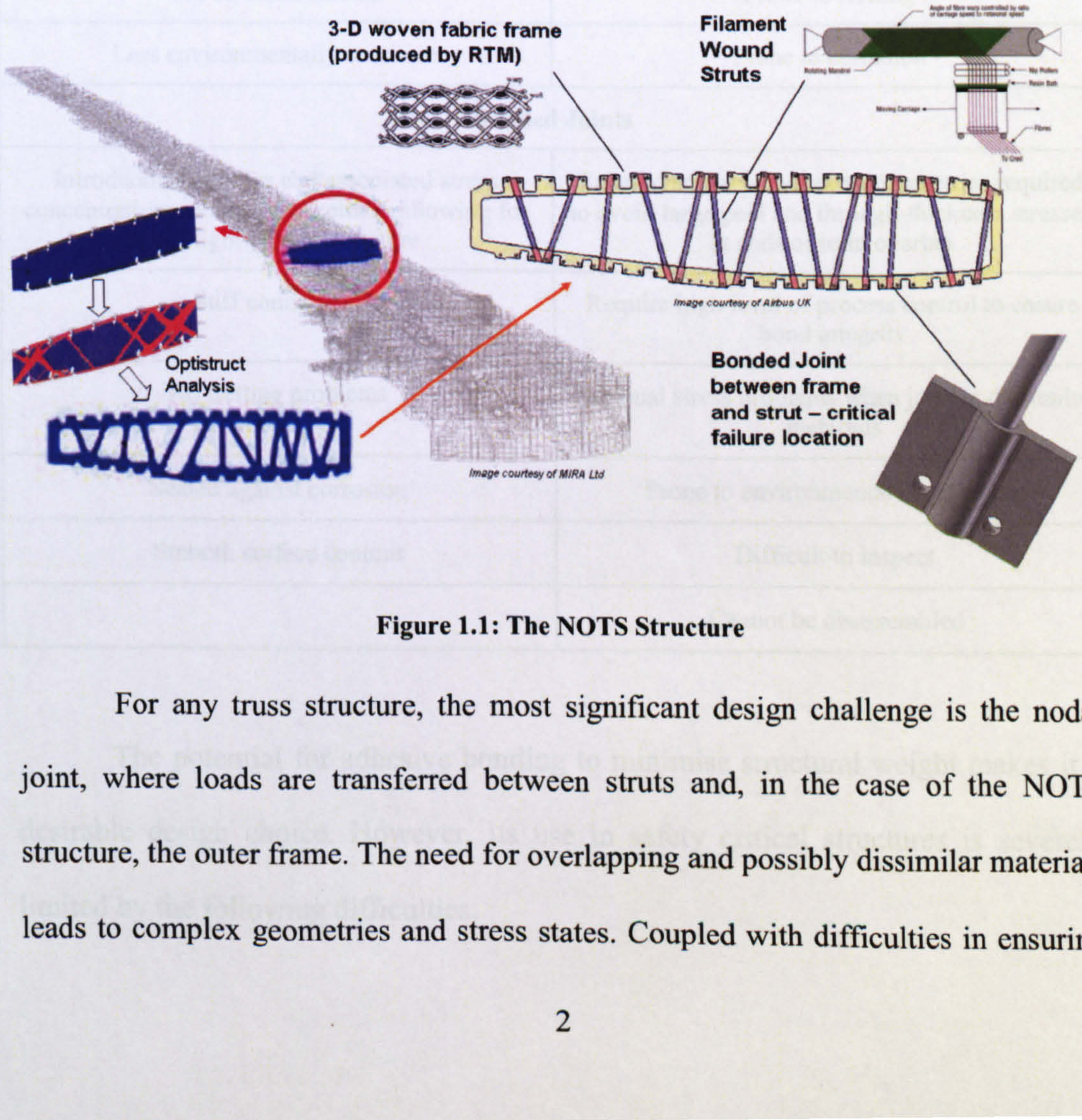

Figure 1.1: The NOTS Structure

For any truss structure, the most significant design challenge is the nodal joint, where loads are transferred between struts and, in the case of the NOTS structure, the outer frame. The need for overlapping and possibly dissimilar materials leads to complex geometries and stress states. Coupled with difficulties in ensuring

defect-free joint manufacture, effective node design is vital in minimising structural weight whilst preventing failure. Potential nodal joining methods can be split into two main categories; mechanical connections (e.g. bolts, rivets) and adhesive bonding. Table 1.1 summarises the various advantages and disadvantages of these two approaches.

Table 1.1: Advantages/disadvantages of adhesive bonding relative to mechanical fasteners

Advantages	Disadvantages
Mechanical Fasteners	
No thickness limitations on adherends	Large stress concentrations around holes
Pins provide through-thickness reinforcement (i.e. joint is less sensitive to peel stress)	Relatively compliant connection
No residual stress problems	Hole formation may damage composite
Can be disassembled	Prone to fretting
Less environmentally sensitive	Prone to corrosion
Bonded Joints	
Introduction of holes and associated stress concentrations avoided, potentially allowing for more light-weight structure	Tapered adherend/adhesive geometries required to avoid large peel and through-thickness stresses at ends of joint overlap
Stiff connection	Require high level of process control to ensure bond integrity
No fretting problems	Residual stress problems when joining dissimilar materials
Sealed against corrosion	Prone to environmental degradation
Smooth surface contour	Difficult to inspect
	Cannot be disassembled

The potential for adhesive bonding to minimise structural weight makes it a desirable design choice. However, its use in safety critical structures is severely limited by the following difficulties:

i) Creating a high quality bond with uniform geometric details such as bond-line thickness and fillet geometry, which have a significant influence on joint stress distribution and the resulting failure mechanisms.

ii) Validating bond integrity and the nature of any defects present using non-destructive test (NDT) techniques.

iii) Predicting damage initiation and growth under repeated cyclic loading, a process known as fatigue.

A primary objective of the NOTS Project was to address these issues and identify further research and development work required for improved design and more widespread use of adhesively bonded nodal joints. Although the current thesis focuses on developing an improved predictive capability for fatigue failure, there is significant reference to adhesive joint design and manufacturing issues. This is due to their fundamental importance in determining both the type and rate of progression of fatigue failure mechanisms.

1.1.2 The Fatigue Process

Fatigue refers to the damage and failure of materials under cyclic loads, where the maximum load in each cycle is below the static failure load of the material. The progression of damage from an initially undamaged to a failed state can be divided into two main stages:

i) An initiation stage, during which microscopic cracks form and coalesce to form a dominant macrocrack.

ii) A propagation stage, during which the macrocrack grows in either a stable or unstable manner until complete fracture occurs.

There is no clearly defined boundary between these two stages and the definition of a dominant macrocrack is generally determined by the minimum flaw size that can be detected using NDT equipment. When considering the initiation and growth of a single crack, similarities can be drawn between the fatigue process in ductile and brittle materials. Ritchie[1] describes damage initiation and propagation in each case as the result of competition between two classes of mechanism:

i) Crack growth is promoted ahead of the crack tip by intrinsic microstructural damage mechanisms. These are an inherent property of the material and are active irrespective of the crack length or geometry of the test specimen.

ii) Crack growth is impeded by extrinsic mechanisms acting primarily behind the crack tip. These are critically dependent on crack size and to a lesser extent, geometry. Extrinsic mechanisms can have no effect on crack initiation since there is no crack wake at this stage.

As can be seen from Figure 1.2, there are many varieties of both extrinsic and intrinsic mechanisms. These are often unique to either ductile, isotropic materials such as metals or brittle, anisotropic materials such as carbon-fibre composites.

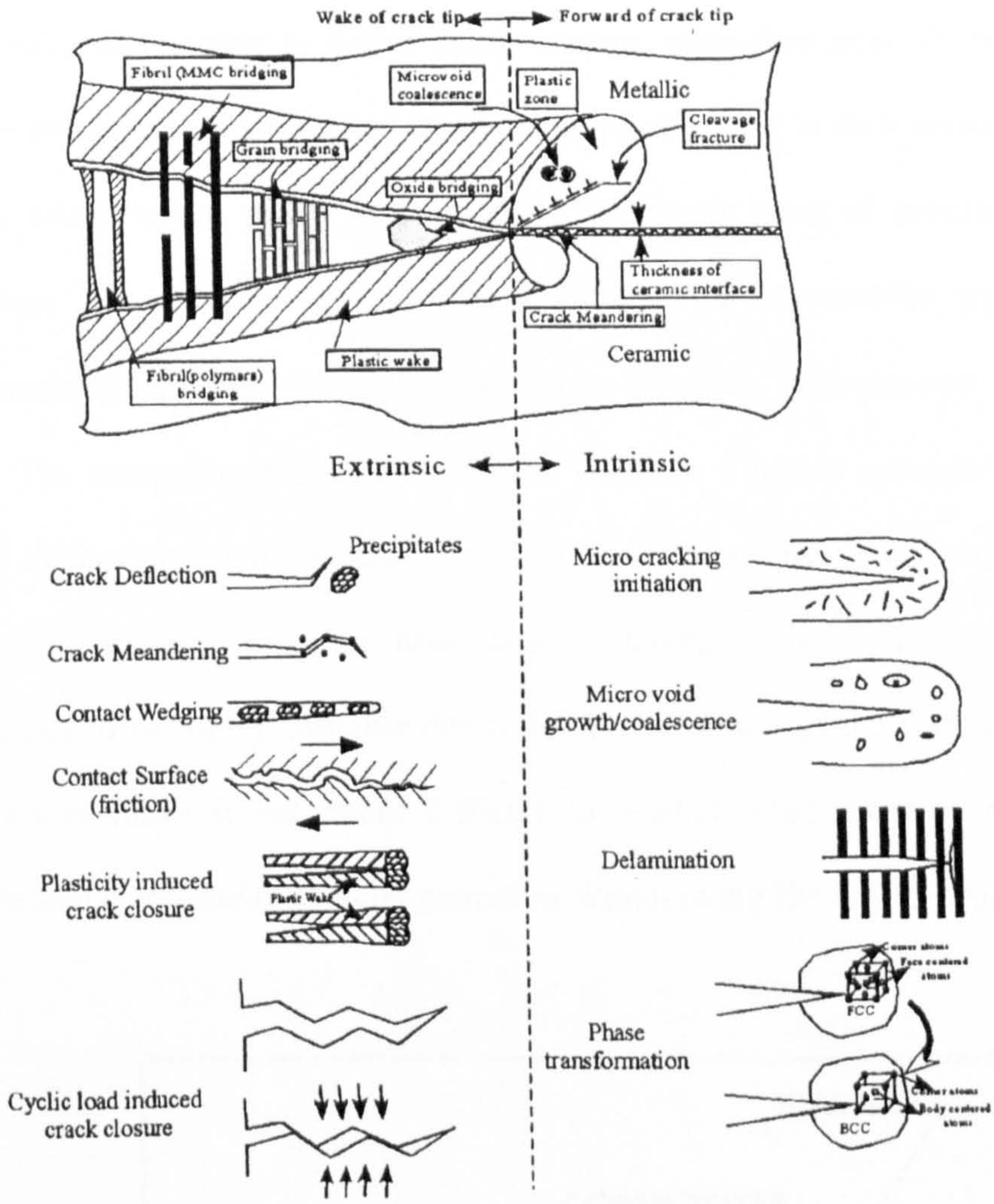

Figure 1.2: Intrinsic and Extrinsic Mechanisms[1]

If we now turn our attention from a single crack to damage accumulation throughout the material as a whole, the above observations can be used to explain the marked differences between ductile, isotropic materials such as metals and brittle, anisotropic materials such as composites. As shown in Figure 1.3, metals tend to exhibit a smooth progression of damage under cyclic loading. The initiation phase, during which microscopic cracks form and coalesce, tends to dominate the fatigue lifetime and involves an extremely gradual rate of damage size increase. This damage tends to be highly localised around a specific stress concentration. Whilst

there is a rapid increase in propagation rate prior to final failure, crack growth often remains sufficiently stable to detect during routine inspection intervals before this occurs. In composites, the situation is more complicated due to their anisotropy, the relatively brittle nature of the resin and the numerous types of potential failure mechanisms. These can occur either independently or sequentially and include matrix cracking, splitting along the resin/fibre interface, delamination and fibre fracture. The competing failure mechanisms result in a highly sporadic and non-localised increase in total damage accumulation with no clearly defined initiation and propagation stage. Also, the final stage of damage growth, just prior to final failure, tends to be highly unstable due to the brittle nature of the composite resin. These factors make it extremely difficult to predict what level of damage is allowable before replacing the component or withdrawing the entire structure from service.

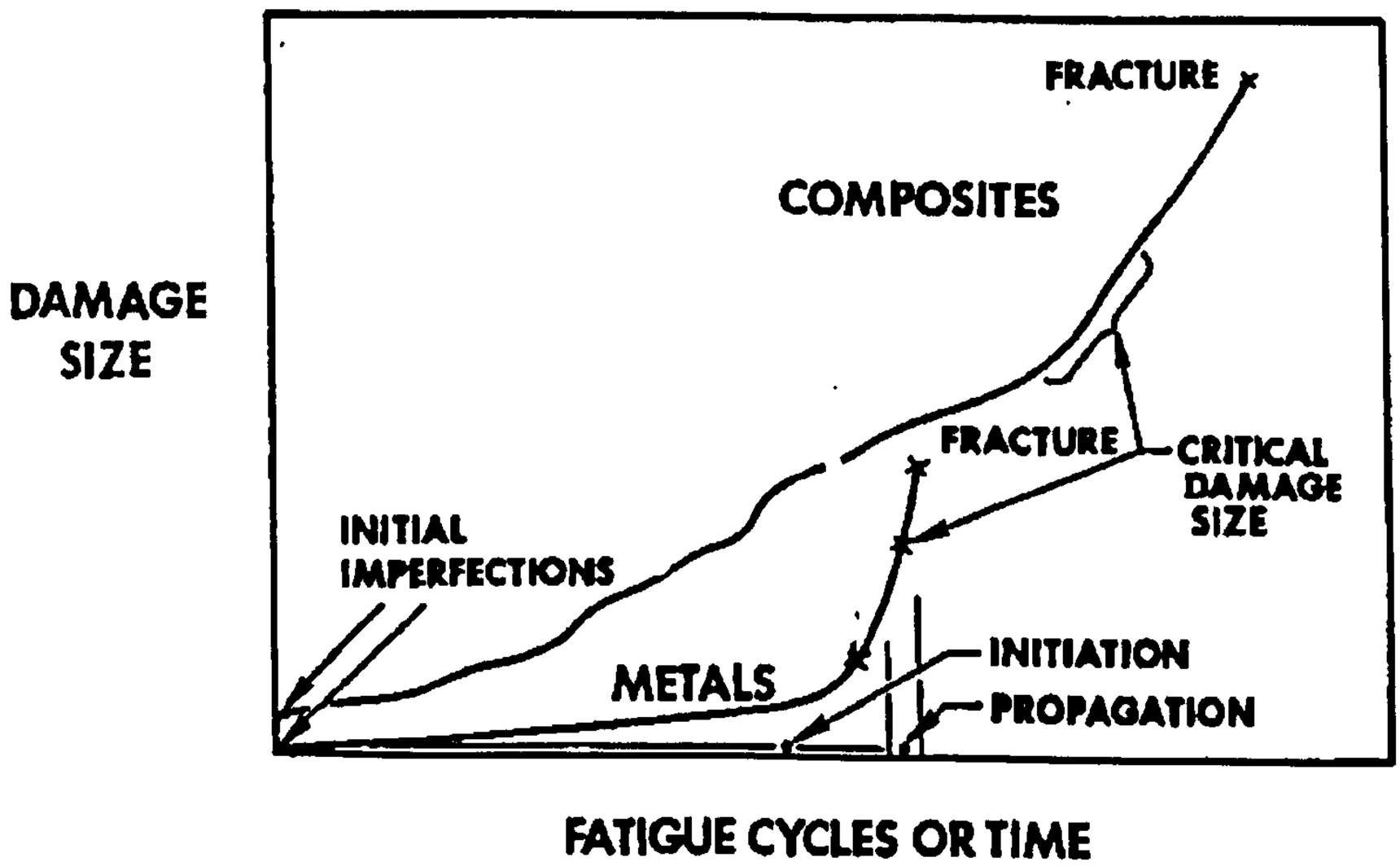

Figure 1.3: Comparison of damage progression in metals and composites[2]

1.1.3 Factors Affecting Fatigue Life

The design and certification process for a safety-critical structure must account for all factors influencing fatigue life. Figure 1.4 summarises these for bonded composite joints, which as discussed above, play a pivotal role in the design of optimised truss structures.

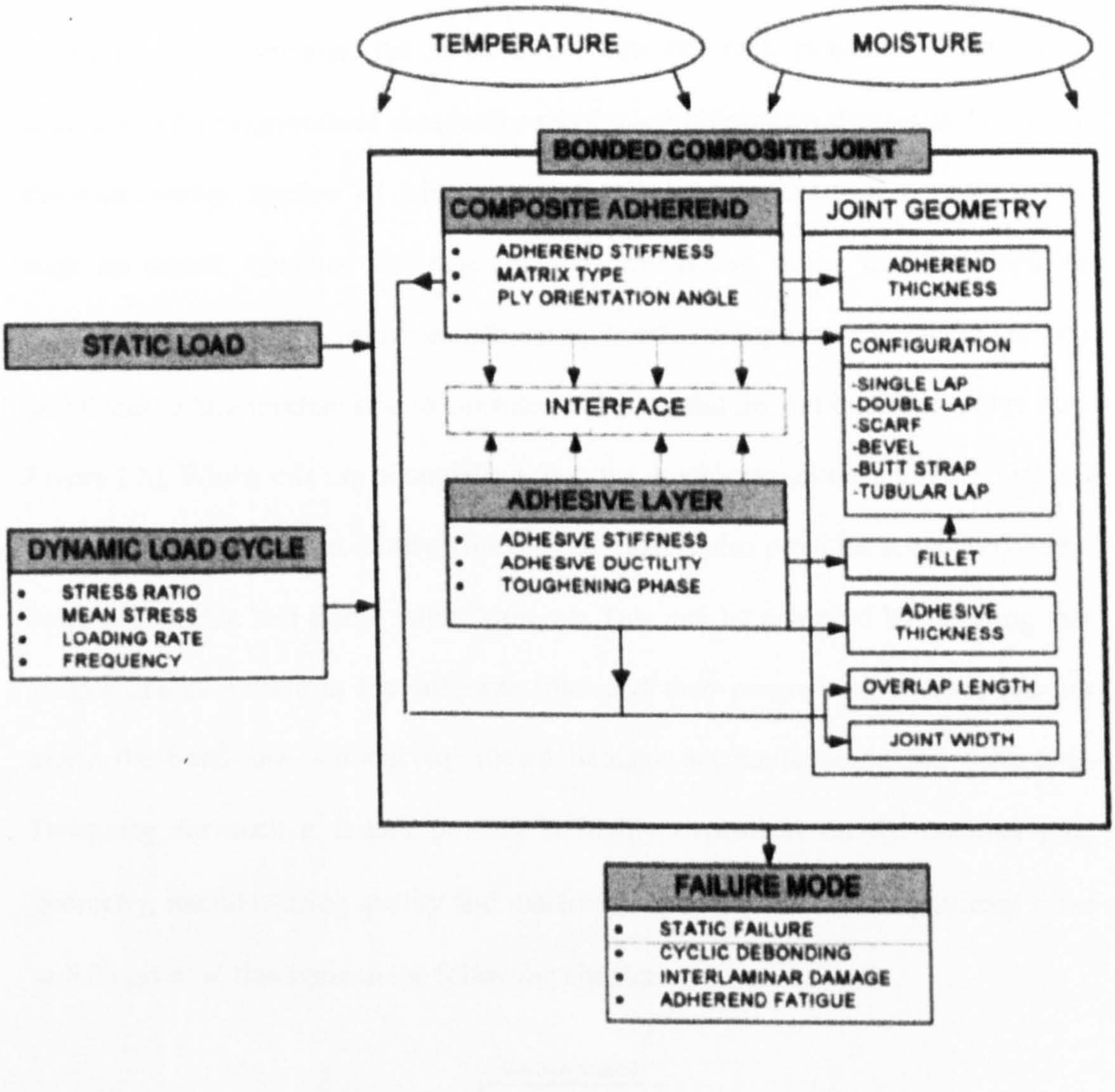

Figure 1.4: Factors affecting the fatigue life of an adhesively bonded composite joint[3]

The many factors influencing fatigue life are now discussed in more detail under 3 main categories:

i) Joint Geometry and Material Properties

ii) Fatigue Load Characteristics

iii) Environmental Conditions.

1.1.3.1 Joint Geometry and Material Properties

For any given applied load, the joint geometry and material properties determine the joint stress distribution and hence, play a significant role in damage progression. In particular, the location and rate of crack initiation is extremely sensitive to the magnitude of shear and peel (through-thickness) stresses at the end of the joint overlap. Section 1.1.2 has already detailed the various failure mechanisms, such as matrix cracking and delamination, which can occur in the composite adherends. If we now consider an adhesively bonded composite joint, there are two additional failure mechanisms to consider; cohesive failure and interface failure (see Figure 1.5). Whilst this can potentially add to the complexity of the situation, making damage progression even more difficult to analyse, it also provides scope to create a more predictable and stable failure process. This can be achieved by ensuring that fatigue cracks initiate in the adhesive fillet and then progress in a stable manner along the bond-line, without significant damage accumulation in the adherends. Designing for such a failure process is highly dependent on the detailed joint geometry, manufacturing quality and material properties, and more significant focus will be given to this issue in the following chapter.

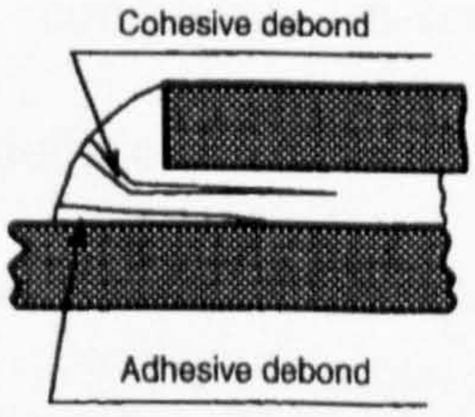

Figure 1.5: Cohesive and adhesive failure modes[4]

1.1.3.2 Fatigue Load Characteristics

In addition to the maximum load in each cycle, the following fatigue load characteristics can have a significant influence on the nature of damage development:

i) Stress-ratio (also known as R-ratio): This is defined as the algebraic ratio of the minimum to the maximum stress in one complete cycle, as shown in Figure 1.6. In conjunction with the maximum load in each fatigue cycle, R-ratio generally has the most significant effect on crack growth rates and significant attention is given to its effects in later chapters.

ii) Frequency: The impact of frequency on fatigue crack propagation rate (defined as the crack extension per load cycle) has been investigated in numerous studies. In their 2003 paper on this subject, Al-Ghamdi *et al.*[5] highlight that although the frequency sensitivity of crack propagation rate is material dependent, there is a tendency in many systems for the rate to increase as frequency decreases.

iii) Waveform Shape: This also affects the strain rate within each load cycle and can hence influence fatigue life. For example, at any given frequency, the strain rate within a sinusoidal waveform varies but remains constant for a triangular waveform.

iv) Variable Amplitude Loading: Although the majority of fatigue testing occurs under constant amplitude conditions, in-service structures are generally subjected to variable amplitude conditions. For many structures, standardised fatigue load spectrums representative of in-service life have been developed (e.g. TWIST for transport aircraft[6]). The order in which the variable amplitude cycles are applied can have a significant effect on damage accumulation[7]. Also,

the residual strength and fatigue life of composite laminates have been observed to decrease more rapidly when the loading sequence is repeatedly changed after only a few loading cycles[8].

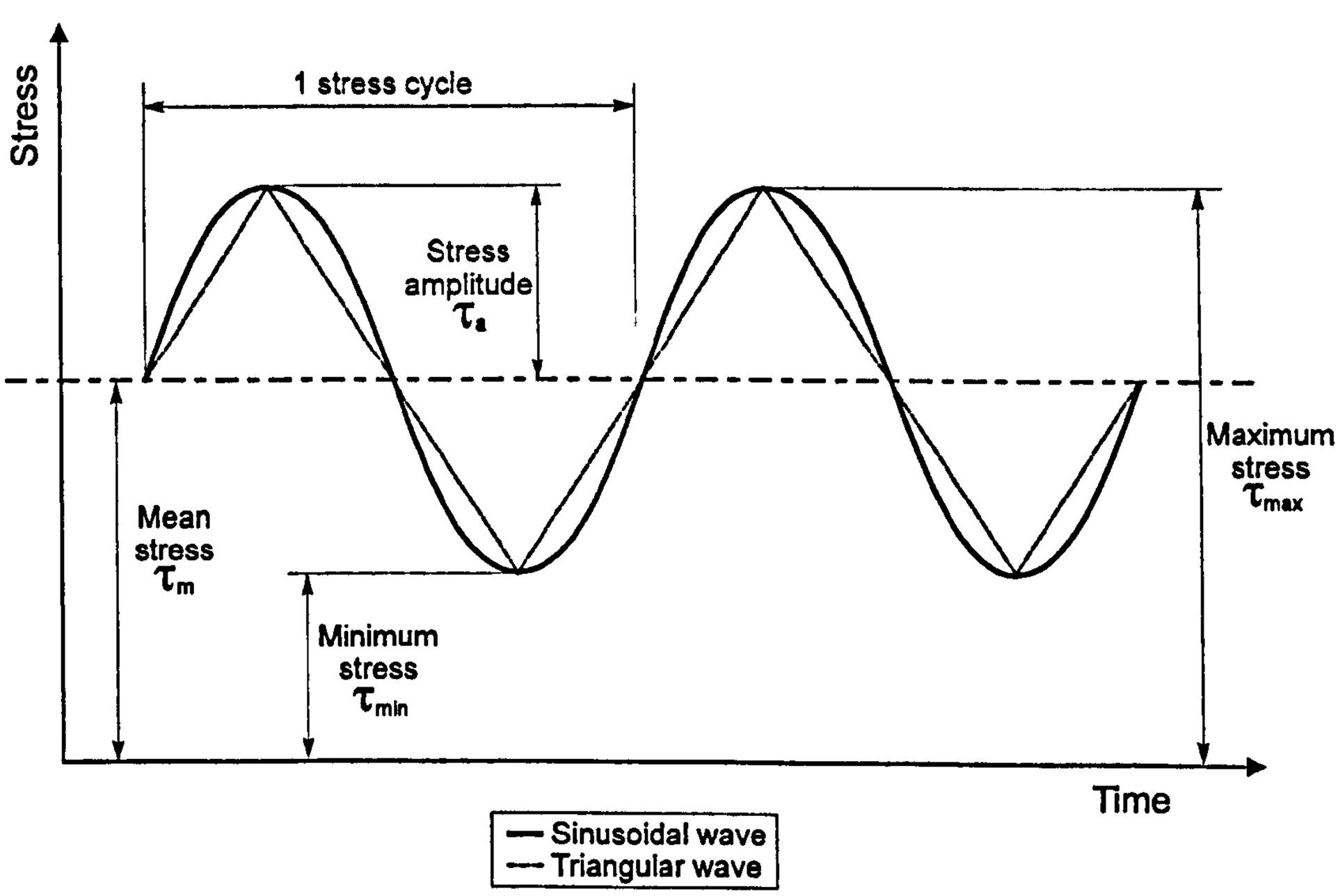

Figure 1.6: Fatigue Load Characteristics[9]

1.1.3.3 Environmental Conditions

Both the strength and fatigue behaviour of bonded joints are extremely sensitive to temperature and moisture. In their 2002 study on the fracture of composite bonded joints under fatigue loading, Ashcroft and Shaw[10] demonstrated that increasing temperature in the service range from -50°C to 90°C causes the fatigue threshold (i.e. the minimum load required for crack growth to occur) to increase. Also, the failure mode was observed to change from fracture within the composite adherends to cohesive failure of the adhesive.

Moisture can have a detrimental effect on both the adhesive and the adhesive/adherend interface, allowing interfacial failure at reduced fatigue load levels[3]. This is a particular problem if voids are present, since these can cause a relatively rapid ingress of water, enabling water pockets to develop along the interface[4].

1.1.4 Fatigue Design Requirements

Design and certification of a safety-critical composite structure requires a complex test and analysis programme, progressing from small scale coupon tests to validation of the full-scale article. An overview of the general 'building block' approach to this process is highlighted in Figure 1.7, showing the various design considerations, supporting technologies and test requirements involved. Physical testing imposes significant costs, especially under fatigue loading, where a typical test can take days to complete. As highlighted in section 1.3, there are many factors affecting fatigue life, and to test their relative influence at a structural level becomes prohibitively expensive. Efforts are made to remedy this by integrating physical testing with fatigue analysis techniques, but these are not sufficiently developed in composites to avoid imposing large reserve factors in the design process. This tends to result in an over-designed structure, in which strain levels are far below the fatigue threshold.

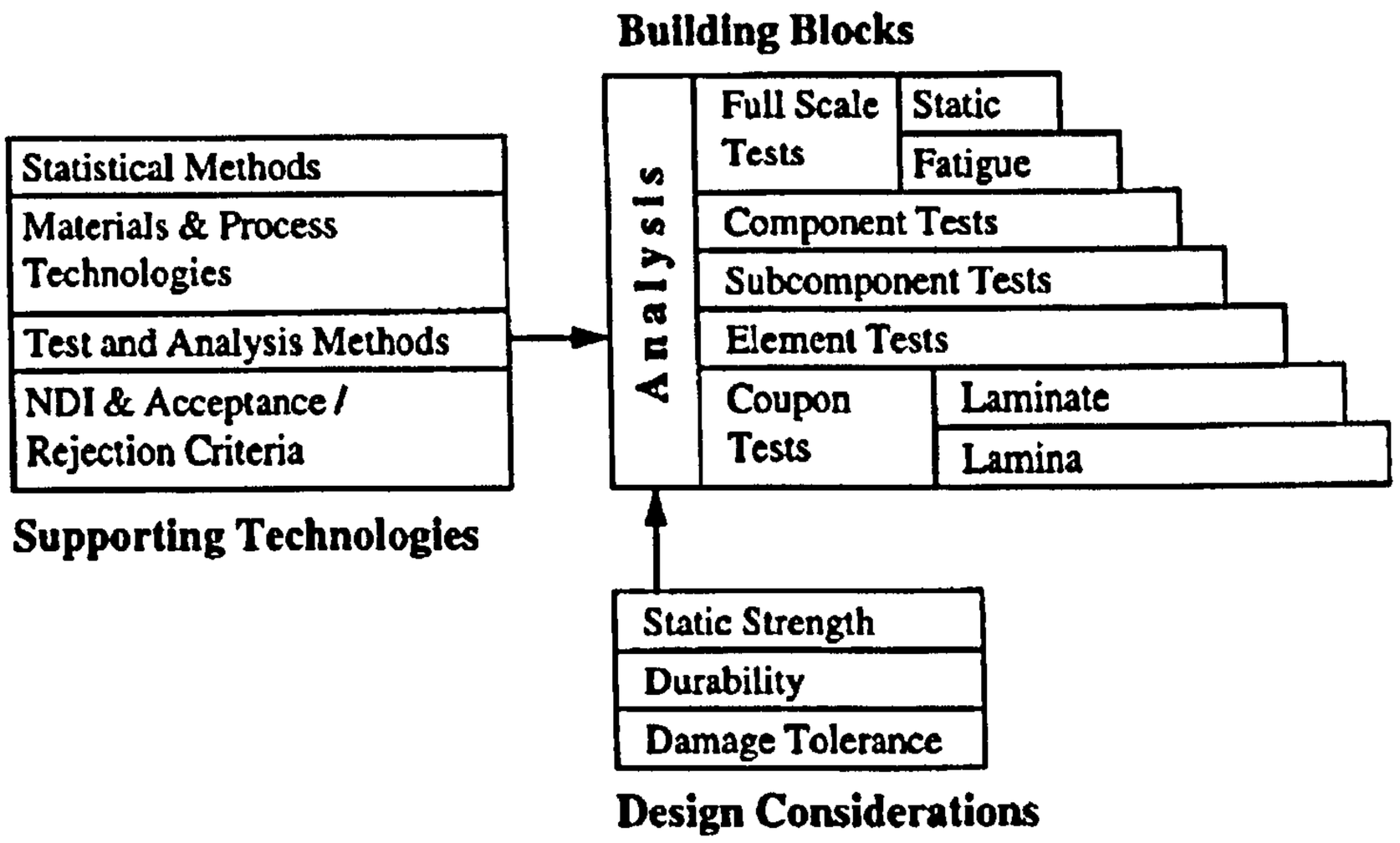

Figure 1.7: The Building Block approach to design and certification[11]

Referring specifically to the design of an adhesively bonded nodal joint, there are two potential fatigue design philosophies:

i) A 'no-growth' design approach, where strain levels remain sufficiently low to ensure that any initial damage in the structure does not grow during the in-service lifetime. The size and location of this initial damage is determined either by manufacturing deficiencies and the ability to detect these using NDT techniques, or potential impact events. Whilst the selection of a no-growth philosophy may be partly influenced by a lack of confidence in analytical fatigue models, it is also dependent on the nature of fatigue damage progression. For example, if cracks have a tendency to grow in an unstable manner, resulting in rapid failure once a specific strain level is exceeded, this approach is necessary regardless of our confidence in the available analysis techniques.

ii) A damage-tolerant design approach, where some crack growth is allowed, provided this can be detected before catastrophic failure. Adopting such an

approach relies on both an accurate fatigue analysis capability and a gradual rate of damage progression before final failure.

Whichever approach is adopted, fatigue analysis requires a detailed knowledge of the joint stress distribution and for a complex nodal joint geometry, this is only possible through finite element modelling. Therefore, it is essential that fatigue degradation and failure models can be integrated with finite element codes, in order for them to be an effective design tool.

1.1.5 Fatigue Modelling Techniques

Although various classifications of fatigue modelling approaches are possible, the present discussion groups them in three main categories. These are Constant-life Models, Residual Strength/Stiffness Models and Mechanistic Models, which is the classification method suggested by Degrieck *et al.* in their review of Fatigue Damage Modelling[12]. An explanation is given of the principles behind each modelling approach and how they can be applied to aid the design process.

1.1.5.1 Constant-Life Models

Constant-life models use information from Stress-life (S-N) diagrams. An S-N diagram is a plot of the maximum stress in each cycle against the number of cycles to failure, under constant amplitude fatigue loading, as shown in Figure 1.8.

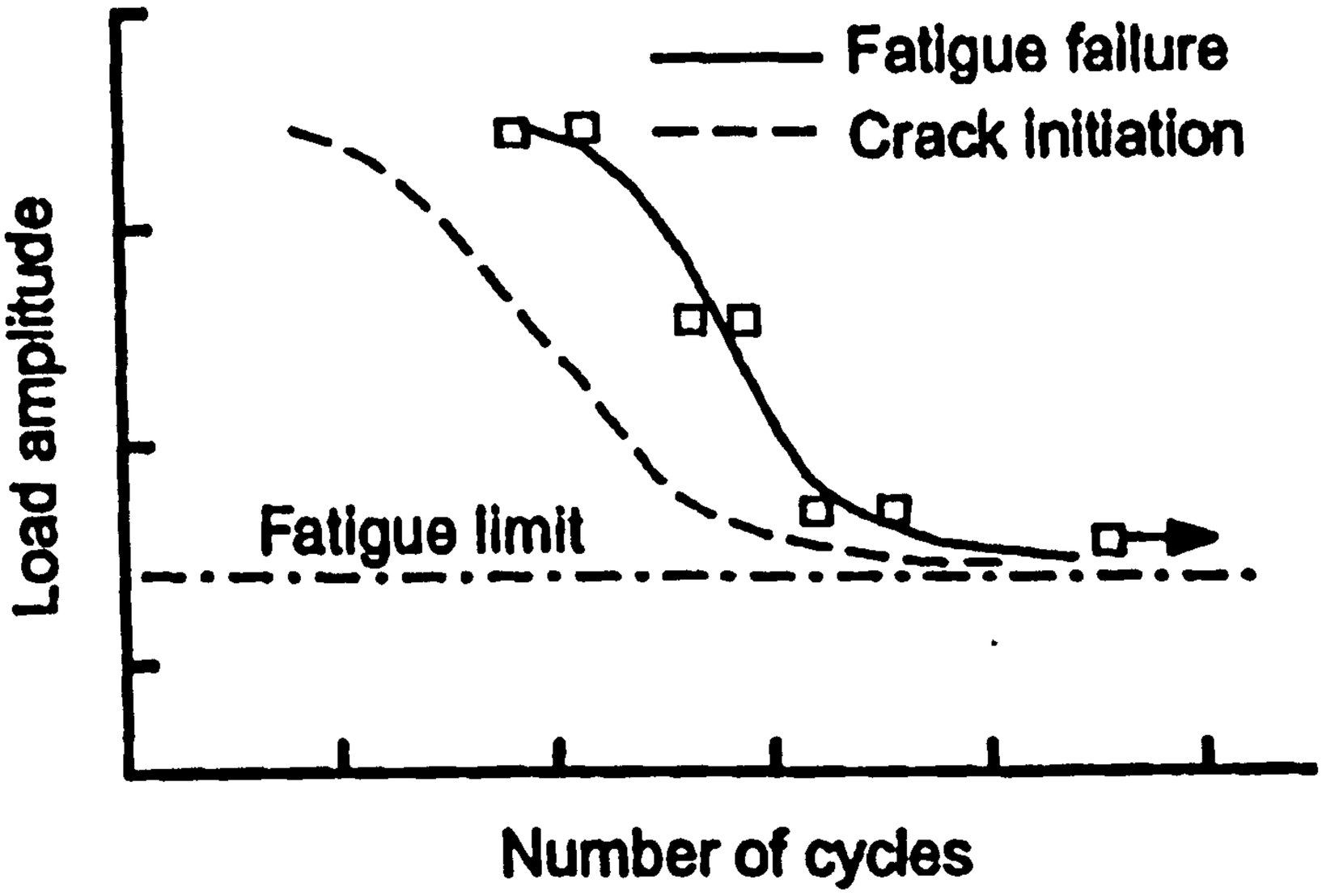

Figure 1.8: An S-N Diagram[4]

Each line on an S-N curve is only applicable to:

- A single R-ratio
- A specific laminate stacking sequence
- A specific specimen geometry (e.g. the presence of holes or notches cause stress concentrations from which fatigue cracks will initiate, greatly reducing total life)
- A single load distribution (e.g. uni-axial or bi-axial loading)

Constant-life models are entirely empirical and provide no information on the microscopic damage mechanisms leading to final failure. For example, no distinction is drawn between crack initiation and crack propagation lives. They also provide no information on how mechanical properties such as stiffness and strength degrade before final failure occurs. Various failure criteria are used to extract information from S-N curves and predict final failure. An example is the function developed by Harris and co-workers at Bath University[13], which is used to plot constant life

diagrams of the type shown in Figure 1.9. This enables the effect on fatigue life of varying R-ratio to be predicted.

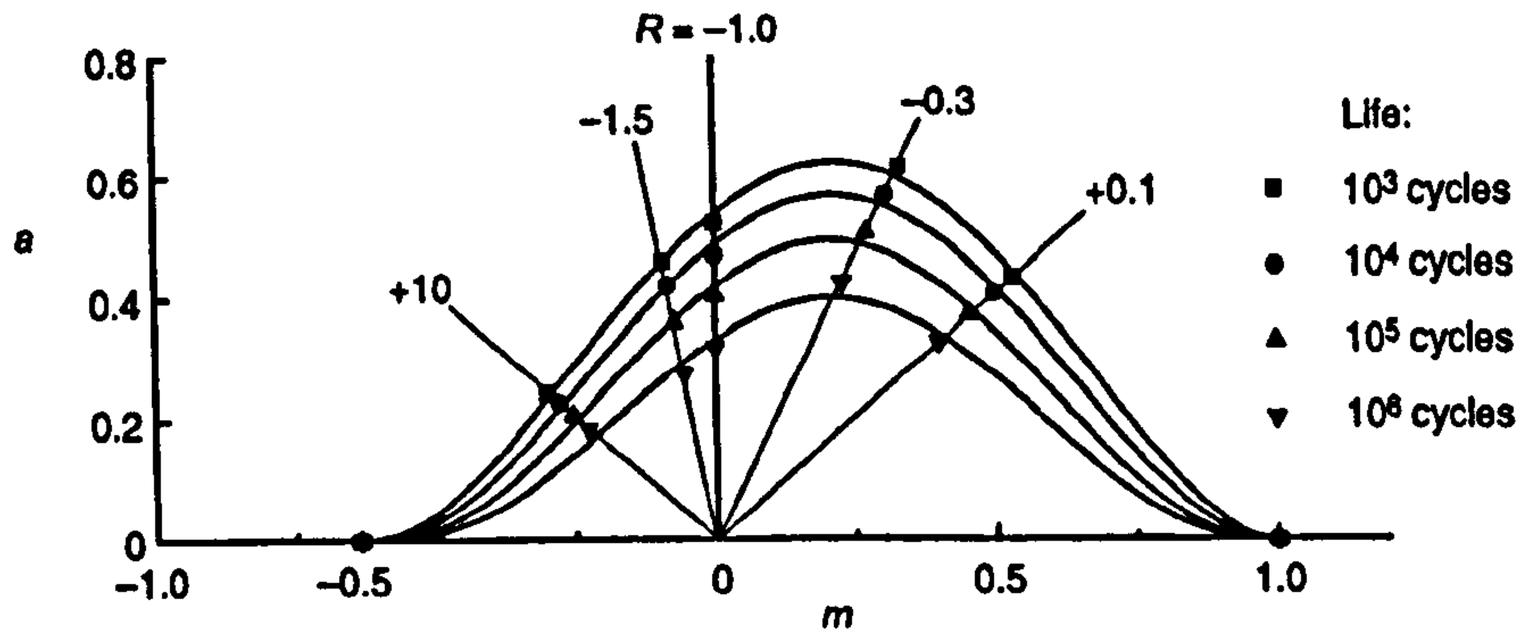

Figure 1.9: A typical Constant Life Diagram[13]

Each line of constant life satisfies the function:

$$a = f(1-m)^u(c+m)^v$$

where:

a = ratio of alternating stress to tensile strength

m = ratio of mean stress to tensile strength

c = ratio of compressive strength to tensile strength

f = a stress function which depends on the material but can generally be assumed constant at a value just above unity

u and v = material constants

The parameters u and v can be determined using the tensile and compressive static strengths and a single S-N curve generated at a specific R-ratio. The above function can then be used to predict the full constant life diagram.

1.1.5.2 Residual Strength/Stiffness Models

Residual strength/stiffness models provide information on the degradation of strength/stiffness up to the point of failure. Figure 1.10 below contrasts the typical stiffness degradation in a metal such as steel with that in a carbon-epoxy composite, under a constant amplitude fatigue load. Such information could be used to determine service lives of components based either on a minimum required stiffness (e.g. springs) or on a given percentage of total fatigue life (e.g. cables).

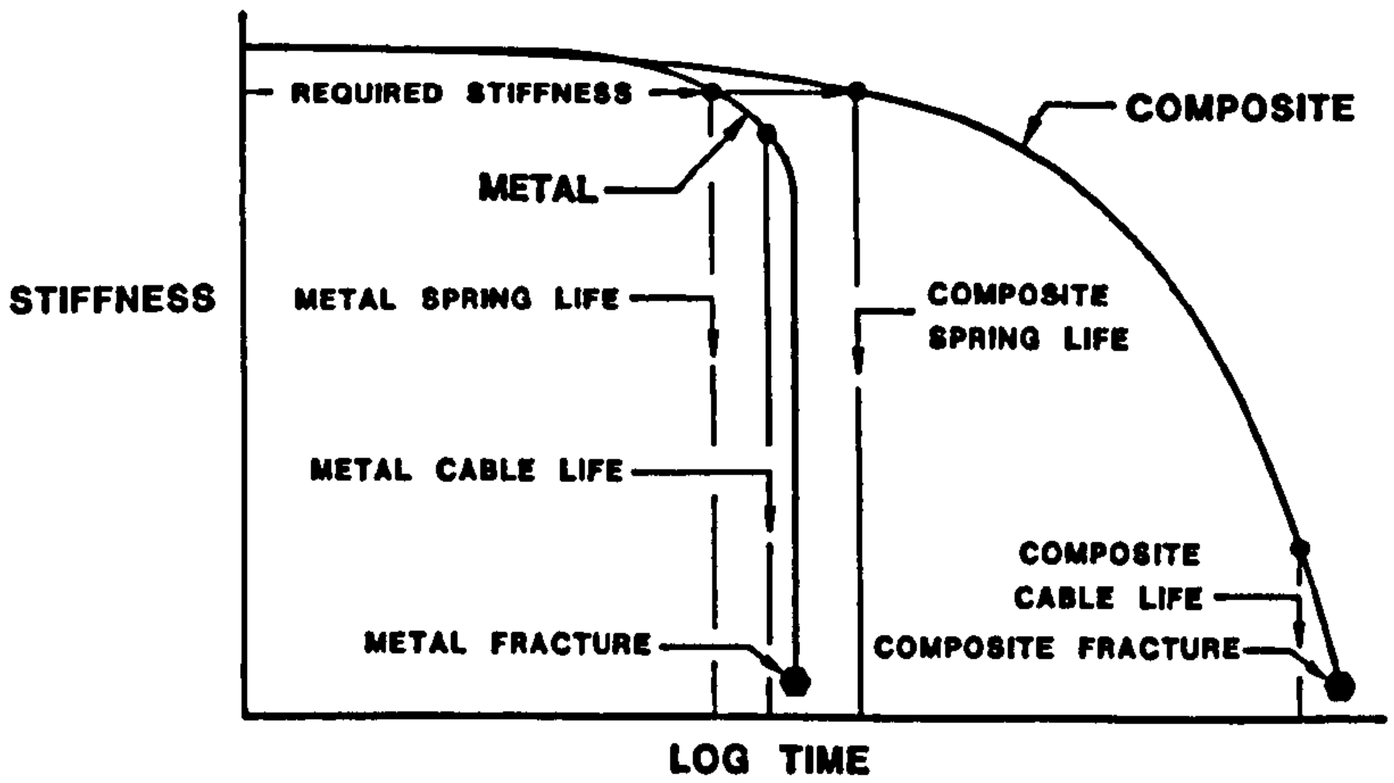

Figure 1.10: Typical Metal versus Composite Material Stiffness Behaviour in Fatigue[2]

Although the majority of residual strength/stiffness models are purely empirically based and provide no information on actual damage mechanisms, efforts are now underway to change this. For example, Tserpes *et al.*[14] have recently developed a residual strength model for CFRP laminates that accounts for seven different failure modes.

1.1.5.3 Mechanistic Models

Mechanistic models are those which describe the deterioration of a composite material in direct relation to specific damage processes (e.g. transverse matrix cracks, delamination). Relative to Constant-Life and Residual Strength/Stiffness

Models, Mechanistic Models are in their infancy and as highlighted by Gamstedt and Andersen[15], research is urgently required to develop such models for use by composite designers. This is motivated by their potential to provide the following design advantages relative to Constant-Life and Residual Strength/Stiffness models:

i) A reduced physical test requirement, enabling reduced product development costs. This is due to the potential to calibrate mechanistic models using results from small-scale coupon tests and then apply the same models in the numerical analysis of complex structures. Whilst constant-life and residual strength/stiffness models can reduce the empirical data requirement for a specific test geometry, they are not directly applicable if this changes. For example, constant-life models used at a laminate level cannot be applied at a structural design level due to the changes in stress state and potential failure mechanisms.

ii) Reduced design margins and the potential to adopt a damage-tolerant design approach, enabling a more light-weight structure. This is due to increased confidence in predicting both the nature and rate of damage progression.

Since a primary objective of this research project concerns the development of mechanistic models applicable to adhesive joints, further discussion on current methods is referred to later chapters.

1.2 Research Objectives

Motivated by the challenges associated with truss structure node design, fatigue failure analysis and the links established with the NOTS project, the main objectives of this research project were:

i) Identification of the most structurally efficient nodal joint designs and their typical failure modes. This was to be achieved through two means; a detailed review of relevant literature and the implementation of a fatigue test programme for the NOTS project.

ii) Development of a suitable mechanistic fatigue model, within a finite element code, for the analysis of nodal joints. A key requirement of this aim was to ensure a clear link between model input parameters and material data gained from standard, small-scale test coupons.

iii) Application of the model to the nodal truss joint developed within the NOTS project and recommendations concerning how the model can be integrated with the design process to enable a more optimised design solution and reduced physical test requirement. In order to address these objectives, the remainder of this thesis is structured as detailed in section 1.3.

1.3 Outline of Thesis

Chapter 2 presents a detailed investigation of nodal joint design and manufacture in composite truss structures. A review of typical joint stress distributions and fatigue failure mechanisms is supported by a detailed description of experimental results from the NOTS project.

In Chapter 3, potential fatigue failure laws for nodal joints are investigated. Focus is placed on modelling bond-line crack propagation and delamination between plies, which are key failure mechanisms in both the NOTS structure and other typical joint designs. This is supported by an investigation of methods for implementing fatigue laws within finite element codes. The chapter concludes with the selection of a cohesive zone model, coupled with a strain energy release rate based fatigue law,

as the most appropriate modelling technique for further development. This is subsequently achieved using interface elements, a specialised type of finite element, which can be placed along potential crack paths and used to simulate both crack initiation and propagation.

Chapter 4 presents a detailed analysis of the length and stress distribution of the numerical cohesive zone ahead of a crack tip, which is essential for subsequent development of the fatigue degradation law. Cohesive zone lengths and stress distributions are examined under mode I, mode II and mixed mode loading, whilst paying specific attention to the effects of mesh density and how this can be optimised. In addition, a technique is developed by which crack tip strain energy release rate can be extracted from the cohesive zone by integrating a crack tip interface element's traction-displacement response. This detailed analysis of the cohesive zone forms the basis for the development of an interface element fatigue degradation law, which is presented in chapter 5. Fatigue law inputs are directly linked to standard experimental test results and numerical model results are validated using mode I, mode II and mixed mode test specimens.

Chapter 6 demonstrates application of the fatigue model to structural applications, highlighting its potential use as an analytical design tool. A single-lap joint is analysed and results are compared with those gained by previous authors using the Virtual Crack Closure Technique (VCCT), an alternative method for analysing fatigue crack propagation. An analysis of the NOTS truss joint is then presented, where the increased structural complexity favours the use of interface elements over a VCCT analysis due to reduced computational expense.

Chapter 7 summarises the main conclusions of the research conducted. Limitations of the current fatigue model are discussed and recommendations provided concerning future development work and how the model can be integrated in the fatigue design process, potentially enabling a more optimised design solution and reduced physical test requirement.

2. Nodal Joint Design and Failure Mechanisms

2.1 Introduction

The previous chapter highlighted that nodal joint design has a significant impact on fatigue life, due to its direct influence on stress distribution and resulting crack growth paths. This is now considered in more detail, by examining the effects of both geometry and material properties on joint stress distribution and resulting failure mechanisms. Focus is placed on adhesively bonded joints, as opposed to mechanical fasteners, due to their ability to enable the least-weight design solution. Potential nodal manufacturing techniques are also examined, in order to assess the difficulties and constraints imposed on achieving optimised joint geometries. The chapter concludes with a detailed case study of the nodal joint developed as part of the NOTS project, drawing specific attention to fatigue considerations and the test programme undertaken. This serves to emphasise the severe challenges posed by nodal joint design and the need for improved manufacturing techniques and predictive failure models. Results from the NOTS fatigue test programme were used, in conjunction with common joint failure mechanisms identified in the literature, to guide the subsequent development of a predictive modelling capability.

2.2 Factors Affecting Joint Stress Distribution

Many of the design guidelines for adhesively bonded composite joints stem from the work performed by L.J. Hart-Smith in a series of NASA/Langley sponsored contracts of the early 1970's and also the U.S. Airforce's Primary Adhesively Bonded Structures Technology program of the mid 1970's. Fatigue failure is heavily influenced by the stress distribution across the joint, which for constant load is determined by two factors; geometry and the mechanical properties of the joint

constituents. Maximum fatigue life is gained by exploiting these factors to minimise stress concentrations where cracks can initiate. The following discussion provides an overview of how this is achieved, whilst also highlighting manufacturing constraints that hinder joint optimisation. Although mainly flat plate joints are discussed, on which most of the current literature is based, results from tubular joint studies are also presented.

2.2.1 Joint Geometry

There are many possible joint configurations and for flat plates, the most common of these are shown in Figure 2.1.

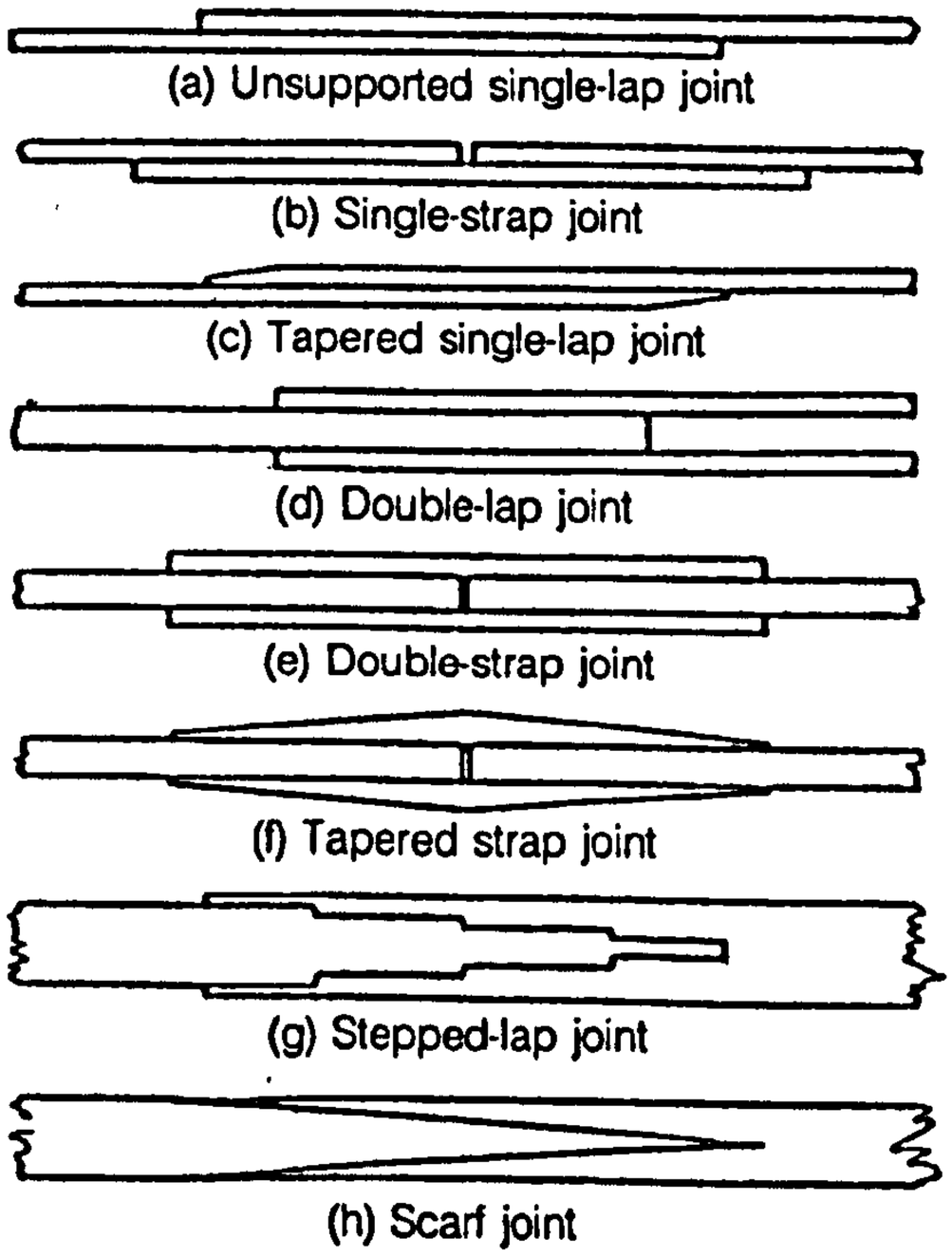

Figure 2.1: Types of Adhesive Joint[16]

When evaluating joint strength, both shear and peel stresses must be considered. As adherend thickness increases, different joint designs become

preferable for maximising joint efficiency (defined as joint strength divided by the strength of the weakest adherend), as shown in Figure 2.2.

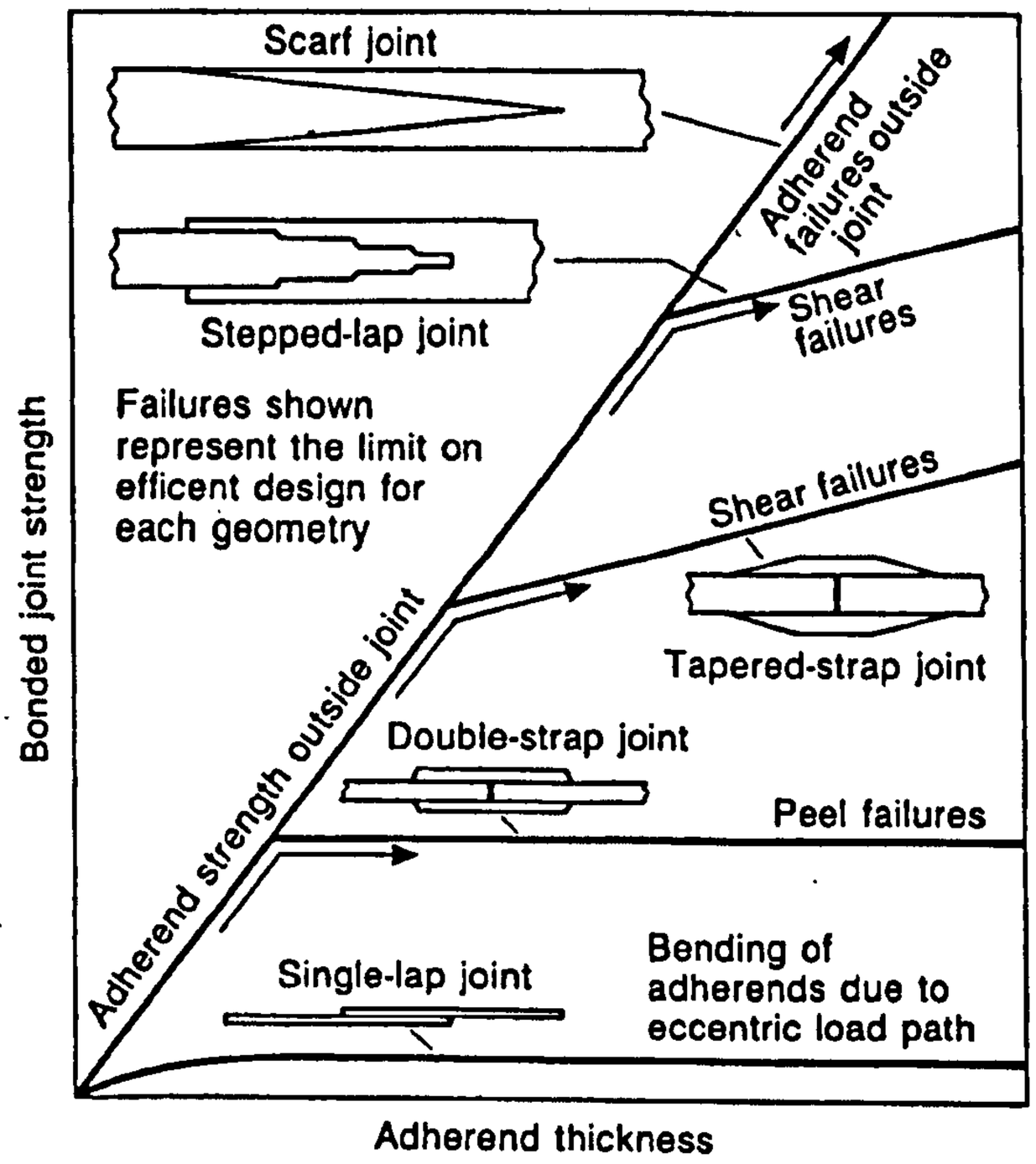

Figure 2.2: Relationship between joint geometry and potential bonded joint strength[16]

A single lap joint enables greatest ease of manufacture but is the least efficient configuration due to large shear and peel stresses at the ends of the joint overlap (see Figure 2.3). The high peel stresses result from the joint's eccentricity, which causes significant bending of the adherends.

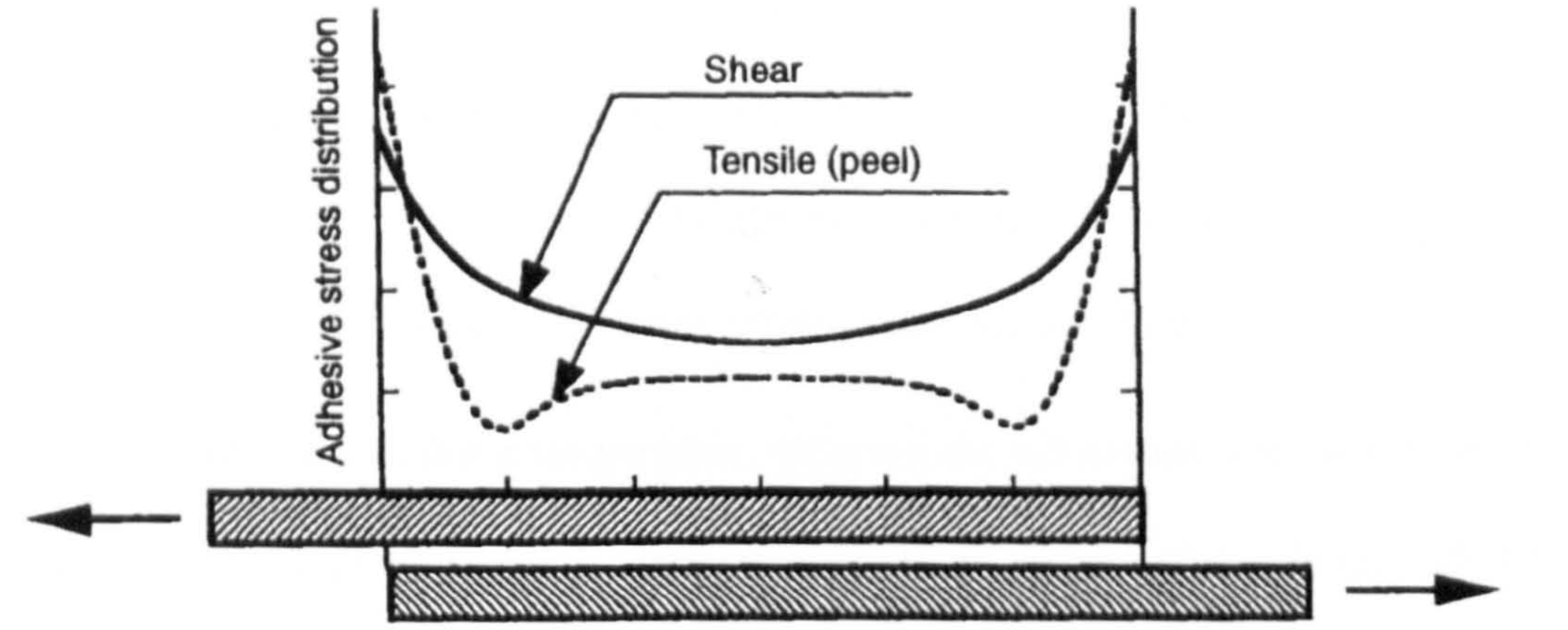

Figure 2.3: Shear and peel stress distributions across a single lap joint for a purely elastic adhesive response[4]

A symmetrical double-lap joint has reduced peel stress concentrations, but they are not eliminated due to the way load is transferred between the outer and inner adherends (see Figure 2.4). The shear stress distribution for a double-lap joint exhibits a similar form to that shown in Figure 2.3 for a single lap joint.

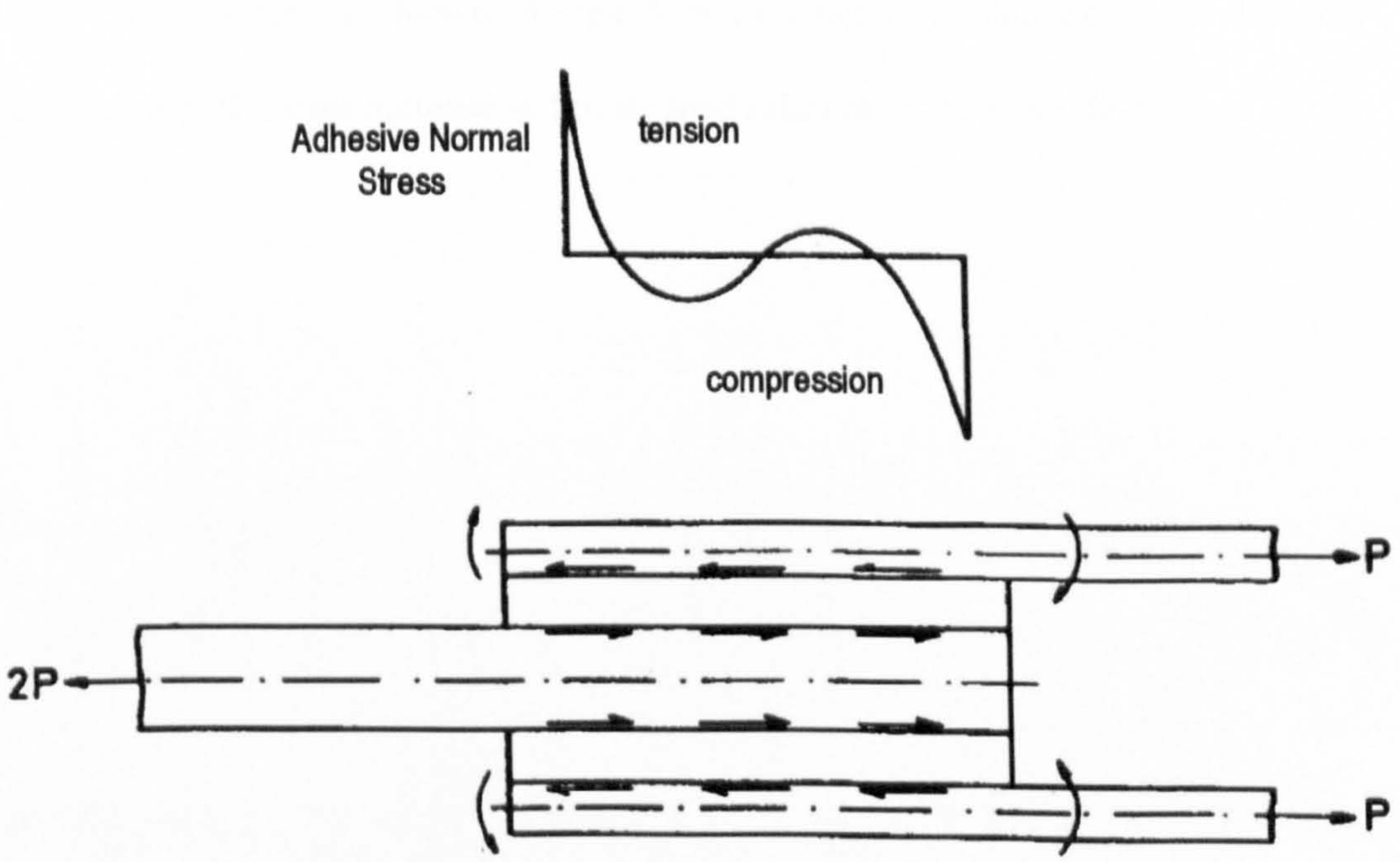

Figure 2.4: Peel stress distribution within a double lap joint[17]

Scarf joints are potentially the most structurally efficient configuration, enabling an even shear stress distribution and complete elimination of peel stresses. However, a uniform shear stress distribution increases the risk of creep failure unless care is taken to avoid the adhesive being stressed into the non-linear region.

In addition to joint configuration, tapering the adherends and including an adhesive fillet can greatly reduce stress concentrations. Adams *et al.*[17] investigated a series of adherend taper and fillet geometries on double lap joints, as shown in Figure 2.5. In joints 2 and 3, the outer adherends were modified by tapering, which reduces the maximum adhesive shear stress. The inclusion of a fillet reduces the peak maximum principal stress in the adhesive and the peak transverse stress in the central adherend. For example, a fillet angle of just under 35° reduces the maximum transverse stress to only one third of that in the basic design (i.e. no taper, no fillet). In the experiments conducted, design 5, with a tapered adherend and a 30° fillet, achieved a 3.07 factor increase in failure load relative to the basic design.

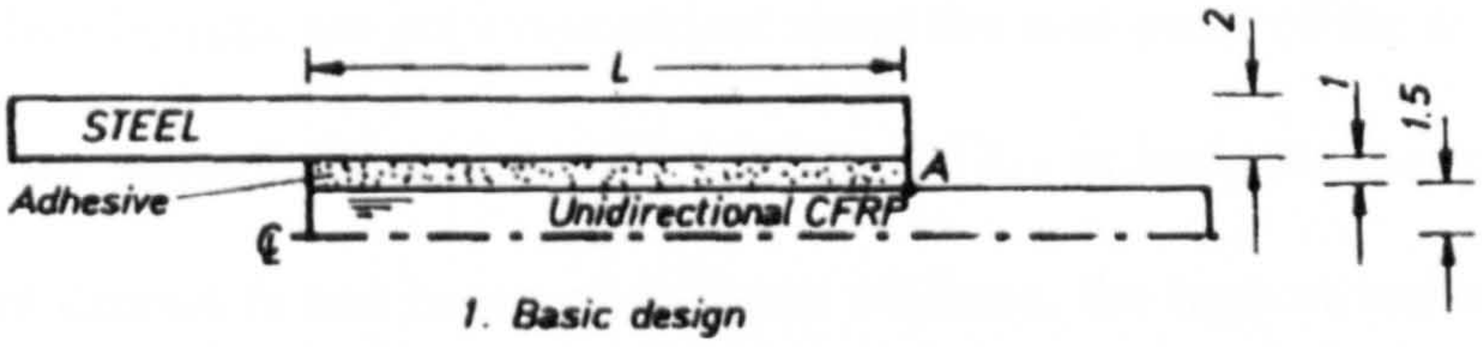

1. Basic design

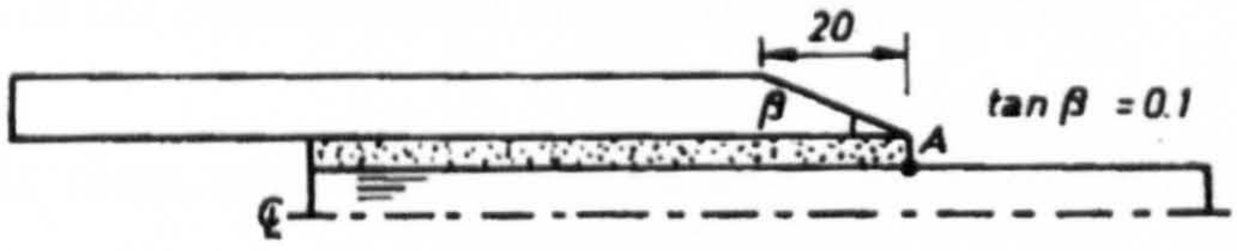

2. Outside taper

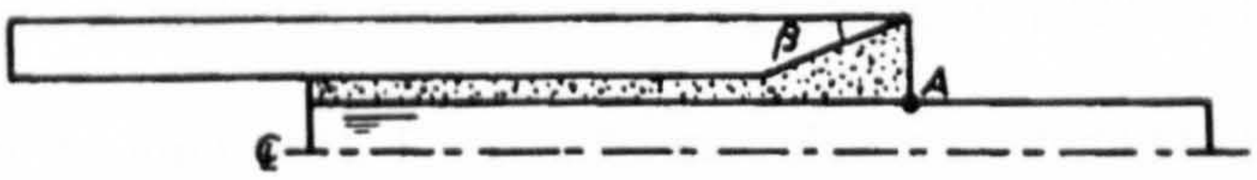

3. Inside taper

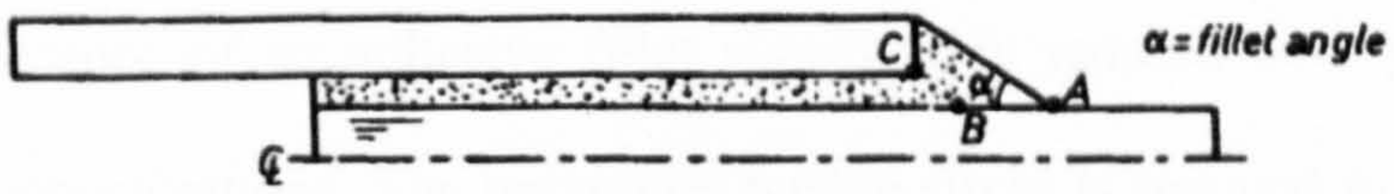

4. Adhesive fillet

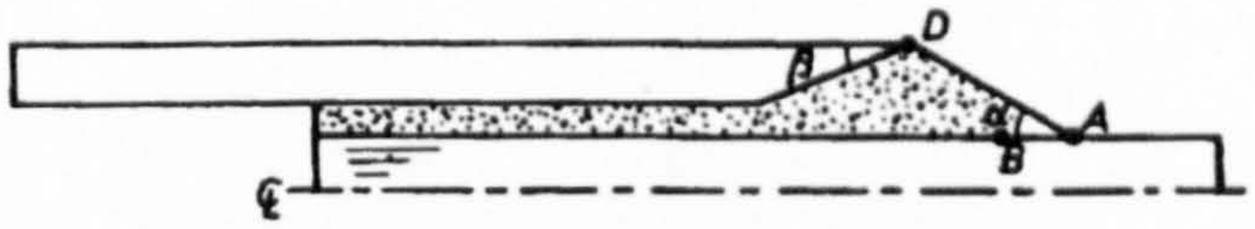

5. Inside taper and adhesive fillet

Figure 2.5: Adherend taper and fillet geometries tested by Adams *et al.*[17]

Assuming purely elastic behaviour of both the adherends and adhesive, shear and peel stresses in a tubular joint under a tensile axial load are of the form shown in Figure 2.6. The chart compares results from an analytical solution developed by Lubkin and Reissner in 1956 with those from a finite element model[17]. The Lubkin and Reissner solution applies purely to a square-edged joint (i.e. no adhesive fillet) whereas finite element results are presented for cases both with and without a fillet. Several important features should be noted from the chart:

i) Stress distributions are not symmetrical about the mid-point of the overlap, even though the tubes have equal wall thickness. This is because the tubes are of different diameters and hence of different stiffness, the highest stresses being at the end of the overlap where the smaller tube is loaded.

ii) There is close agreement between the Lubkin and Reissner solution and the square edged finite element model for the joint shear stress distribution.

iii) The Lubkin and Reissner solution significantly underestimates the peak peel stress at the joint ends. The maximum value is predicted to be 40% greater in the case of the square edged finite element solution.

iv) The presence of an adhesive fillet significantly reduces both peel and shear stress concentrations. The maximum tensile stress is reduced to less than 50% and the maximum shear stress to less than 70% of the Lubkin and Reissner values.

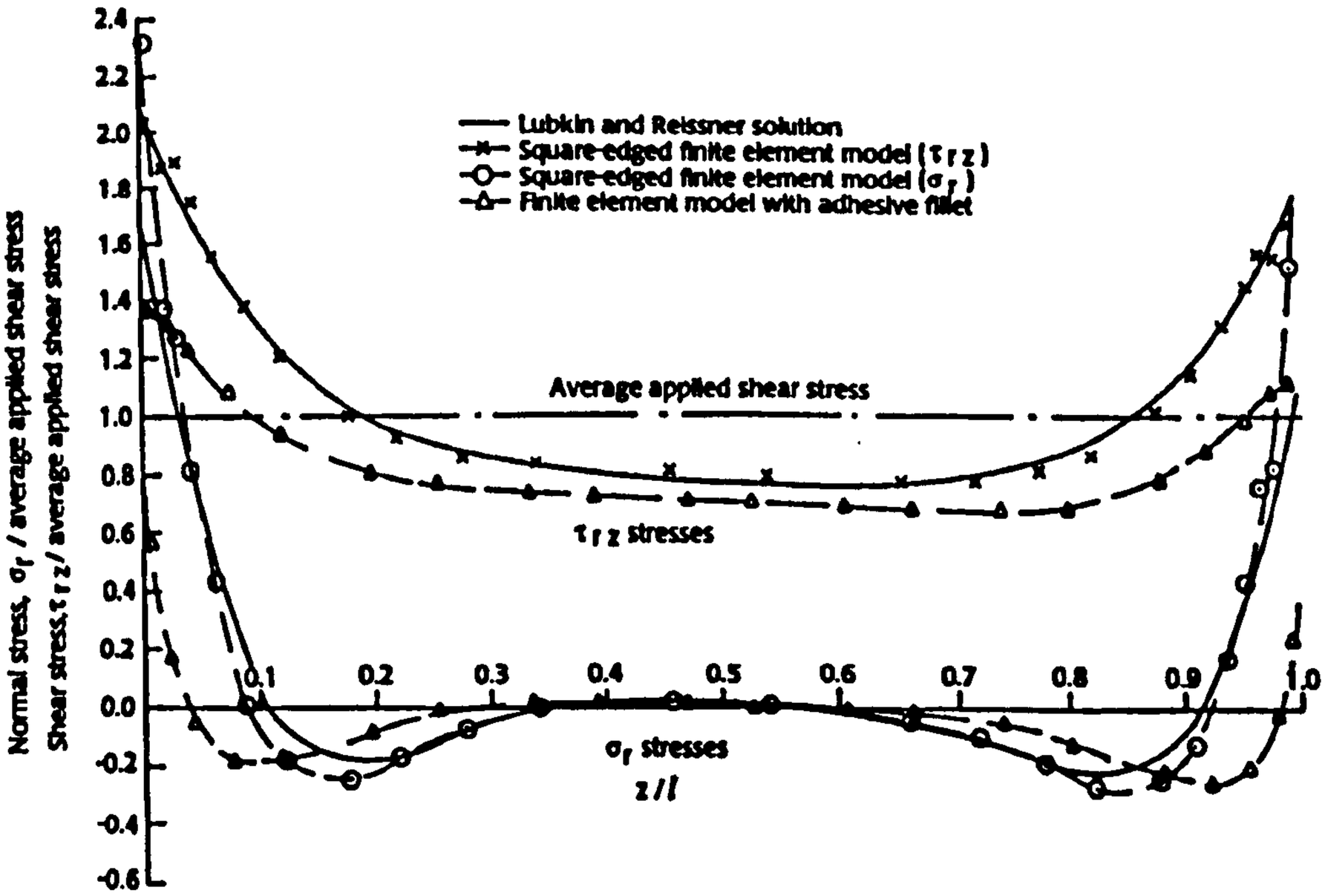

Figure 2.6: Shear and Peel Stress Distributions in a Tubular Lap Joint under Axial Tensile Load[17]

Although the above chart considers only axial loading, torsion and bending are also significant load cases for many tubular joints. Yang *et al.*[18] have developed an analytical 2-D model for composite tubular joints under bending using kinematics and constitutive relations. To verify the model, they conducted a finite element analysis using Abaqus and the results gained showed close agreement. Although this model can be used for parametric studies to reduce peak interfacial stresses, it cannot predict joint strength since it is a linear model and no failure criteria for the adhesive or resin matrix are included.

Until now, only an elastic response of both the adhesive and adherends has been considered. Whilst this may be valid for brittle materials, ductile materials can experience significant plastic deformation and this must be accounted for in any failure analysis. For example, a ductile adhesive exhibits the changes in shear stress distribution shown in Figure 2.7 for a double-lap joint loaded in tension. As load is increased, the adhesive at the joint ends eventually passes its elastic limit and begins to yield. The proportion of yielded adhesive gradually increases until the maximum adhesive shear strain is reached and the joint fails.

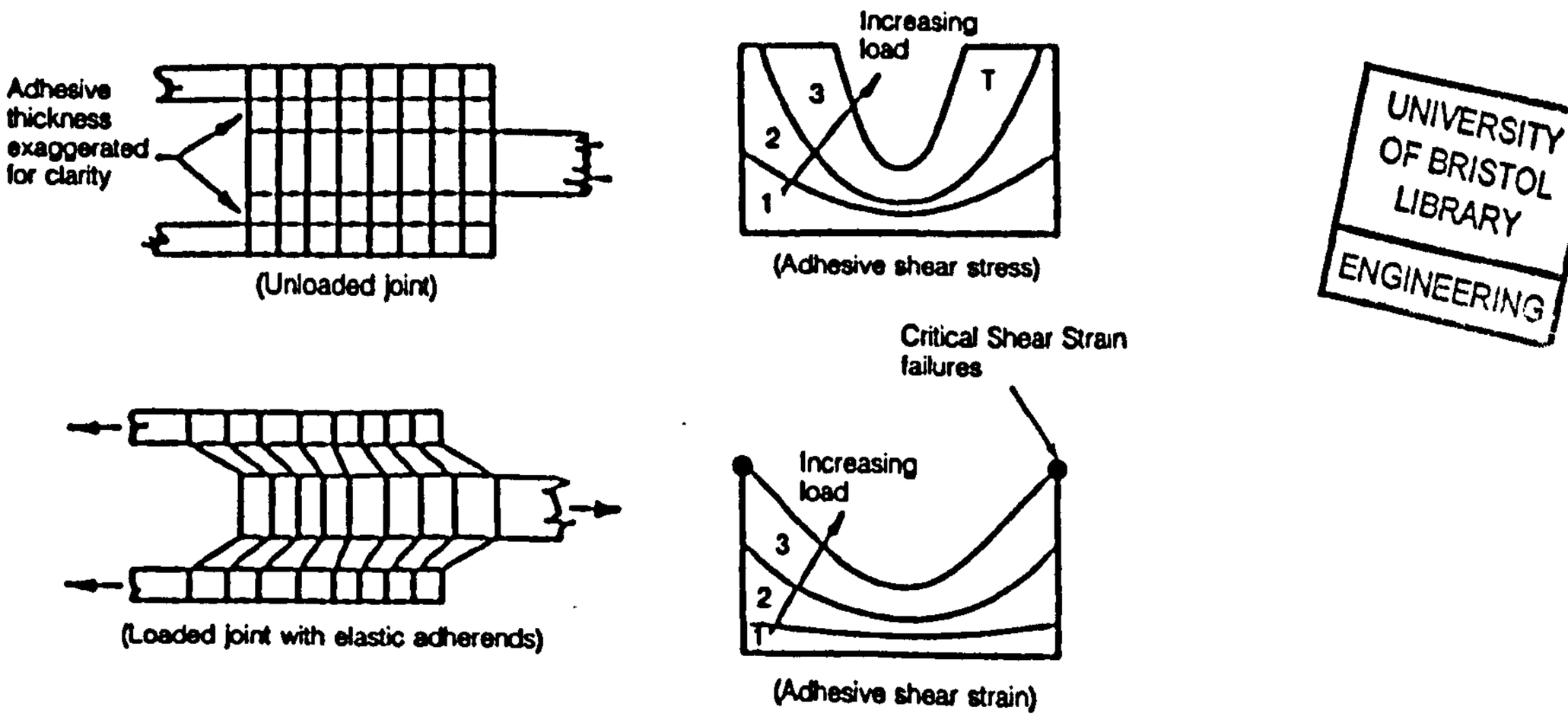

Figure 2.7: Shear Stress Distribution across double-lap joints as adhesive behaviour changes from purely elastic to elastic/plastic[16]

For a fatigue analysis, although global stresses will generally be well below the static failure strength, stress concentrations may still be sufficient to cause localised areas of plastic deformation.

2.2.2 Adherend Properties

The low through-thickness strength of polymer matrix composites gives even greater importance to the elimination of peel stresses than is the case with metallic adherends. This is highlighted in Figure 2.8, using the example of a double-lap joint, where the large peel stresses result in through-thickness failure of the central adherend.

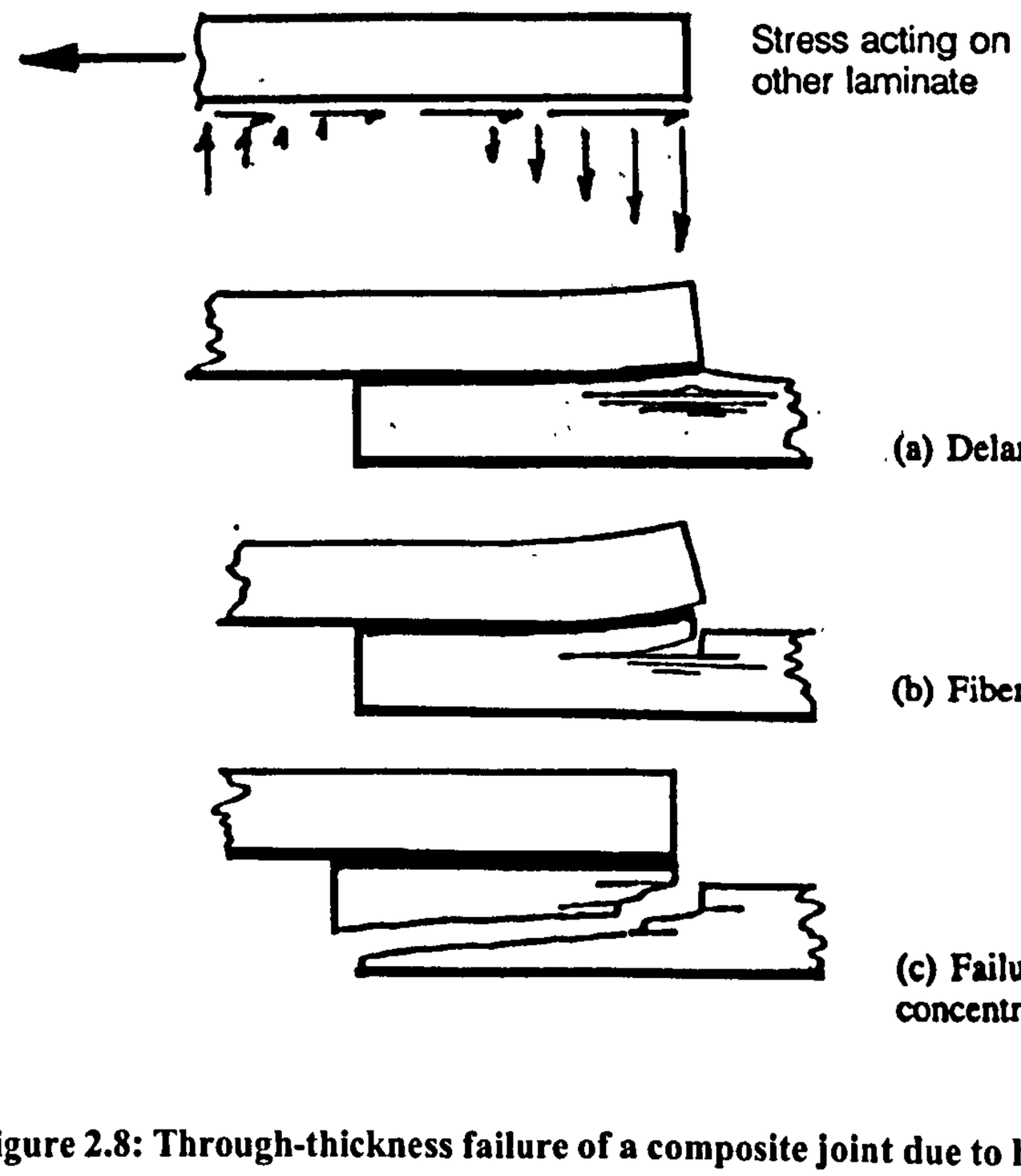

(a) Delamination

(b) Fiber breakage

(c) Failure initiated by local stress concentration and peak stress

Figure 2.8: Through-thickness failure of a composite joint due to high peel stresses combined with poor through-thickness strength[16]

The surface fibre orientation of laminates can also have a significant effect on the strength of adhesive joints. Placing fibres transverse to the load direction next to

the bond layer tends to seriously weaken the joint due to transverse cracking which develops in the resin[19].

All types of joint geometry are adversely affected by unequal adherend stiffness, where stiffness is defined as axial or in-plane shear modulus multiplied by adherend thickness[20]. This is highlighted by Figure 2.9, using the example of a double lap joint in which the stiffness of the central adherend is lower than the combined stiffness of the outer adherends. Under axial load, an unsymmetric adhesive shear stress distribution occurs, and the shear stress is increased at the end of the joint where the outer adherends terminate.

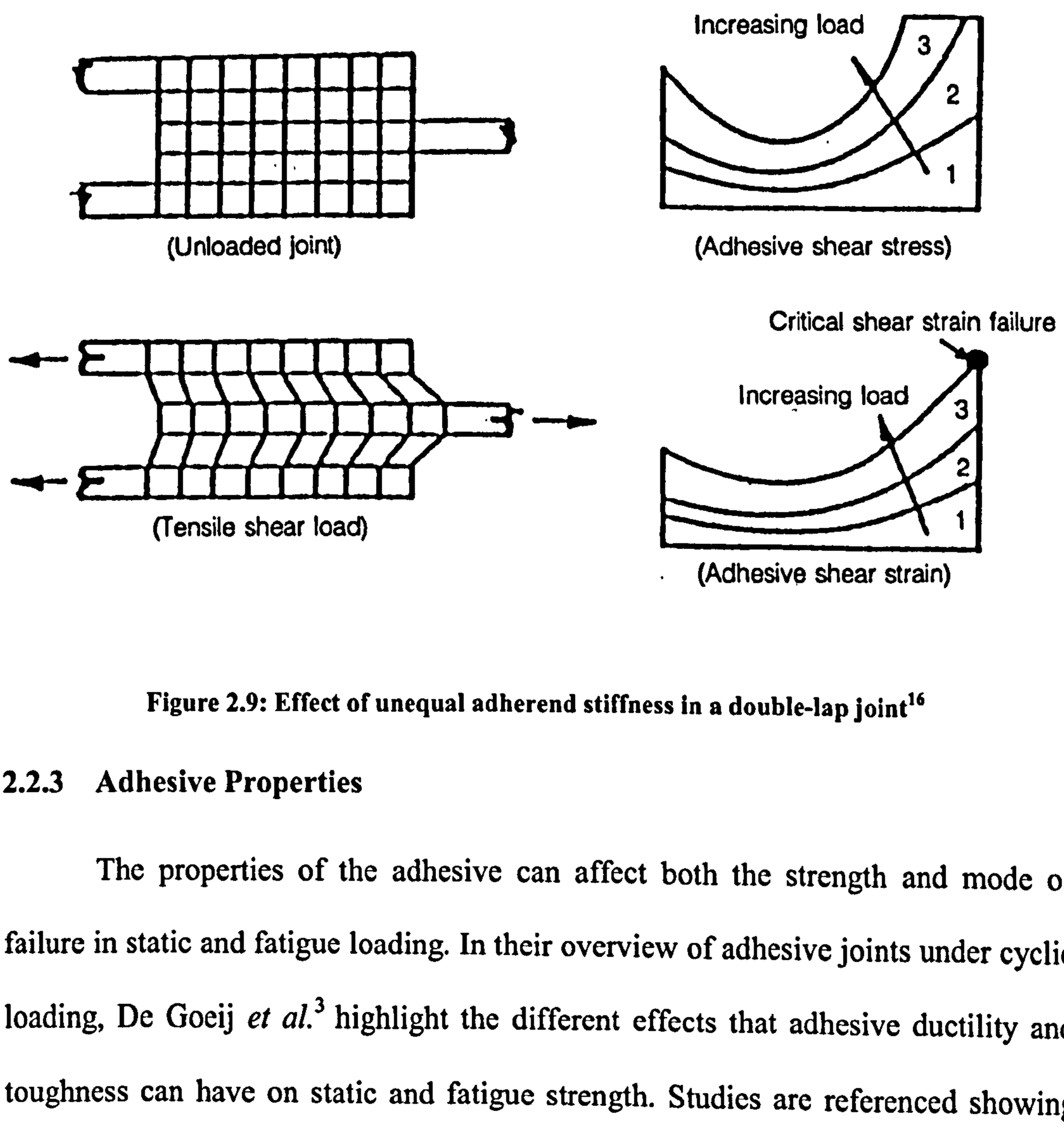

Figure 2.9: Effect of unequal adherend stiffness in a double-lap joint[16]

2.2.3 Adhesive Properties

The properties of the adhesive can affect both the strength and mode of failure in static and fatigue loading. In their overview of adhesive joints under cyclic loading, De Goeij *et al.*[3] highlight the different effects that adhesive ductility and toughness can have on static and fatigue strength. Studies are referenced showing

that although increased ductility can improve static strength due to increased fracture toughness, fatigue resistance may be lower due to hysteresis effects.

Bond-line thickness can also have a significant impact on static and fatigue strength. Increasing thickness improves the fracture resistance until a certain optimum thickness is reached. Any further increase in adhesive thickness from this point causes fracture resistance to decline[4].

The potential of using a variable modulus adhesive to improve the joint stress distribution has recently been investigated by Broughton and Fitton[21]. The most significant benefits were achieved in un-optimised adhesive joints, where failure occurs due to high peel stresses, at joint stresses considerably less than the adhesive shear strength. In such cases, the use of a variable modulus adhesive can change the mode of failure from through-thickness failure of the adherend to cohesive failure of the adhesive, providing a significant strength improvement. Work is yet to be performed on the fatigue behaviour of variable modulus adhesives.

2.2.4 Adherend/Adhesive Interface

If failure occurs along the interface between the adhesive and the composite (adhesive failure), the ultimate static strength is always lower than for failure within the adhesive itself (cohesive failure)[4]. There is also a severe reduction in the joint's fatigue resistance if failure occurs in an adhesive manner. Interfacial bond strength is largely dependent on the quality of surface preparation prior to bonding the adherends. When using a secondary bonding process, it is common practice to grit blast the adherend surfaces and then degrease with acetone to ensure a high bond strength.

2.3 Design Measures for Controlled Fatigue Crack Propagation

Before adhesive joints can become more widely accepted, their fatigue failure modes must be predictable and should result in a progressive rather than catastrophic failure. Crack growth can then be monitored using NDT techniques, allowing a residual joint lifetime to be calculated. This is not possible for sudden catastrophic failure mechanisms, since a small crack can propagate almost instantaneously and without warning through the joint.

A common failure mechanism in adhesive joints is for a crack to propagate into one of the adherends, resulting in sudden catastrophic interlaminar failure. A typical crack path for this failure case is shown in Figure 2.10.

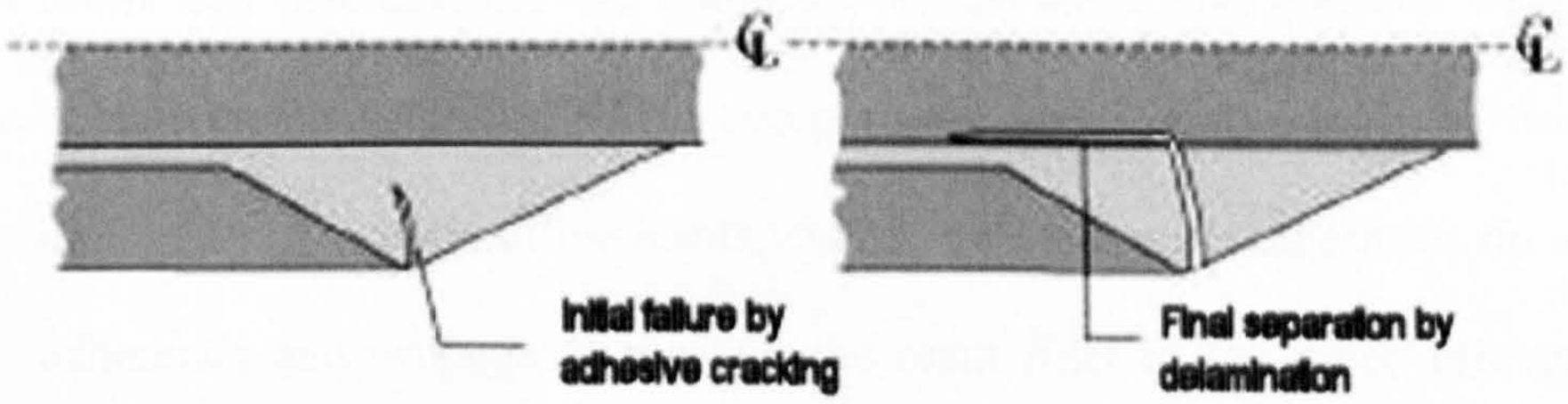

Figure 2.10: Typical crack path for interlaminar failure in a composite adhesive joint[22]

This failure mode is due to the low through-thickness strength of CFRP laminates and the brittle nature of the resin. For a tough adhesive, if the crack can be constrained within the bond-line, a progressive failure can be achieved, whereby the crack grows gradually under cyclic loading. A study at the University of Bristol (UoB)[22] considered numerous methods of providing stable crack propagation along the bond-line and these can be split into two main categories:

i) Increasing the through-thickness strength and/or delamination resistance of the adherend so that cracks within the adhesive will always propagate along the bond-line. Methods considered included through thickness stitching of the

adherends and the use of 3-D woven fabric adherends. Further information on the potential of 3-D woven fabrics to prevent crack propagation through the adherends will be provided in section 2.5, which discusses their use in the NOTS project.

ii) Inserting a thin layer of material into the adhesive to deflect cracks along the bond-line, thus preventing them from propagating into the adherends.

Experimental work focused on the second of these options and two types of crack deflection material were investigated; kapton film and nylon mesh. Pre-cured CFRP laminates were bonded to form a double lap joint, using a single part epoxy paste adhesive (3M EC3448). For some of the specimens, a layer of either Kapton film or Nylon mesh was inserted into the bond-line. Quasi-static and constant amplitude fatigue tests were then performed, to compare the behaviour of the modified and unmodified joints. For unmodified joints, cracks initiated at the outermost tip of one of the adherends and propagated through the resin fillet to the inner adherend, at which point the failure propagated as a delamination in the inner adherend (see Figure 2.10). The kapton film and nylon mesh were able to deflect the crack along the bond-line, preventing the occurrence of delamination. The crack path for the kapton film modified joint is shown in Figure 2.11.

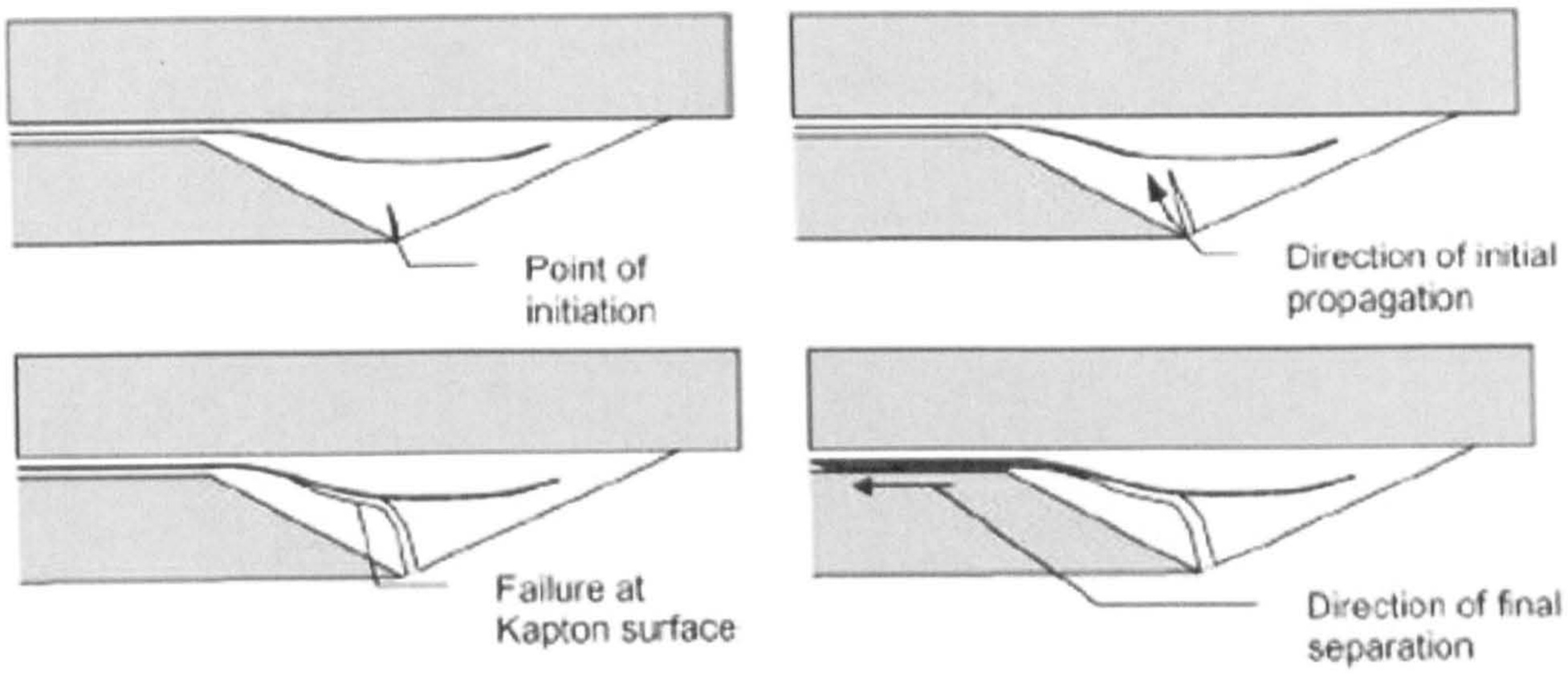

Figure 2.11: Crack propagation path for kapton film modified joint[22]

The interface between the adhesive and modifying layer was critical in effectively controlling joint failure. If the interfacial bond was too weak, it was found to separate prior to crack initiation at the point of peak strain in the adhesive. For a stronger interface, cracks initiated at the point of peak strain, as they would for an unmodified joint, but were then deflected upon reaching the interface.

2.4 Manufacturing Constraints

Although section 2.2 has demonstrated the ability to optimise joint stress distribution through careful design of the detailed geometry, manufacturing constraints often make such ideal solutions impractical. This is particularly apparent for tubular joints due to their complex 3-D geometries. Attention is now given to manufacturing options for bonded joints and the constraints placed on achieving optimised geometries.

Extensive research was conducted on nodal joint design and manufacture as part of the Innovative Approaches to Composite Structures (IACS) Programme at the University of Bristol in the late 1990's. The focus of this work was the development

of a carbon fibre truss structure for the fuselage of the Skylon spaceplane, which took the form shown in Figure 2.12.

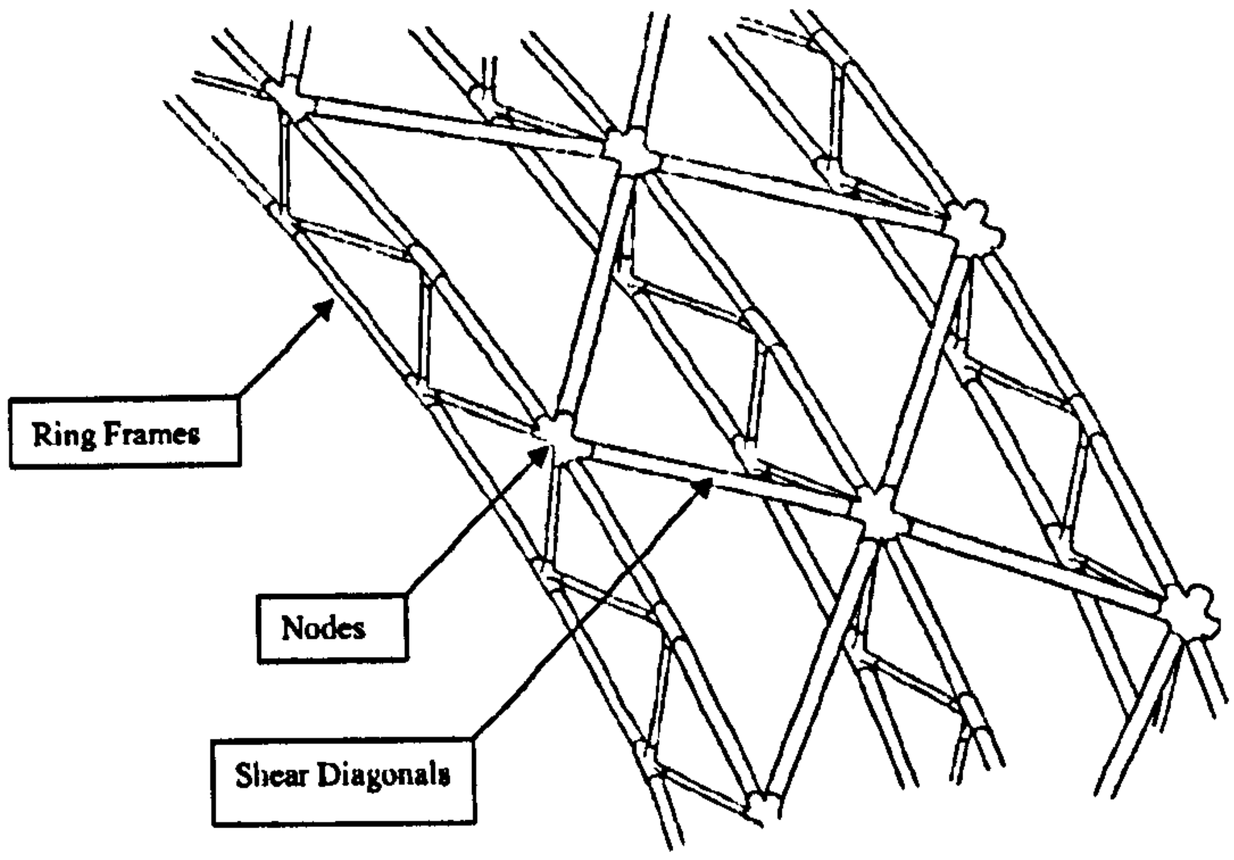

Figure 2.12: Fuselage structure of Skylon spaceplane[23]

Both cylindrical tubes and a honeycomb cored sandwich panel were considered as design options for the struts. Although the sandwich panel greatly simplified nodal design, this came at the expense of increased weight[24]. Consequently, significant effort was placed on developing bonded joints for composite tubes, using both metallic and composite nodes.

With respect to metallic nodes, work was undertaken on the development of a double-lap joint configuration, which as discussed above, can reduce the high peel stresses associated with a single-lap joint. Stress distribution can be further improved using a tapered mechanical seat joint and as part of the IACS programme, a study was conducted[25] to compare the manufacturing implications and resulting strength of these two design options.

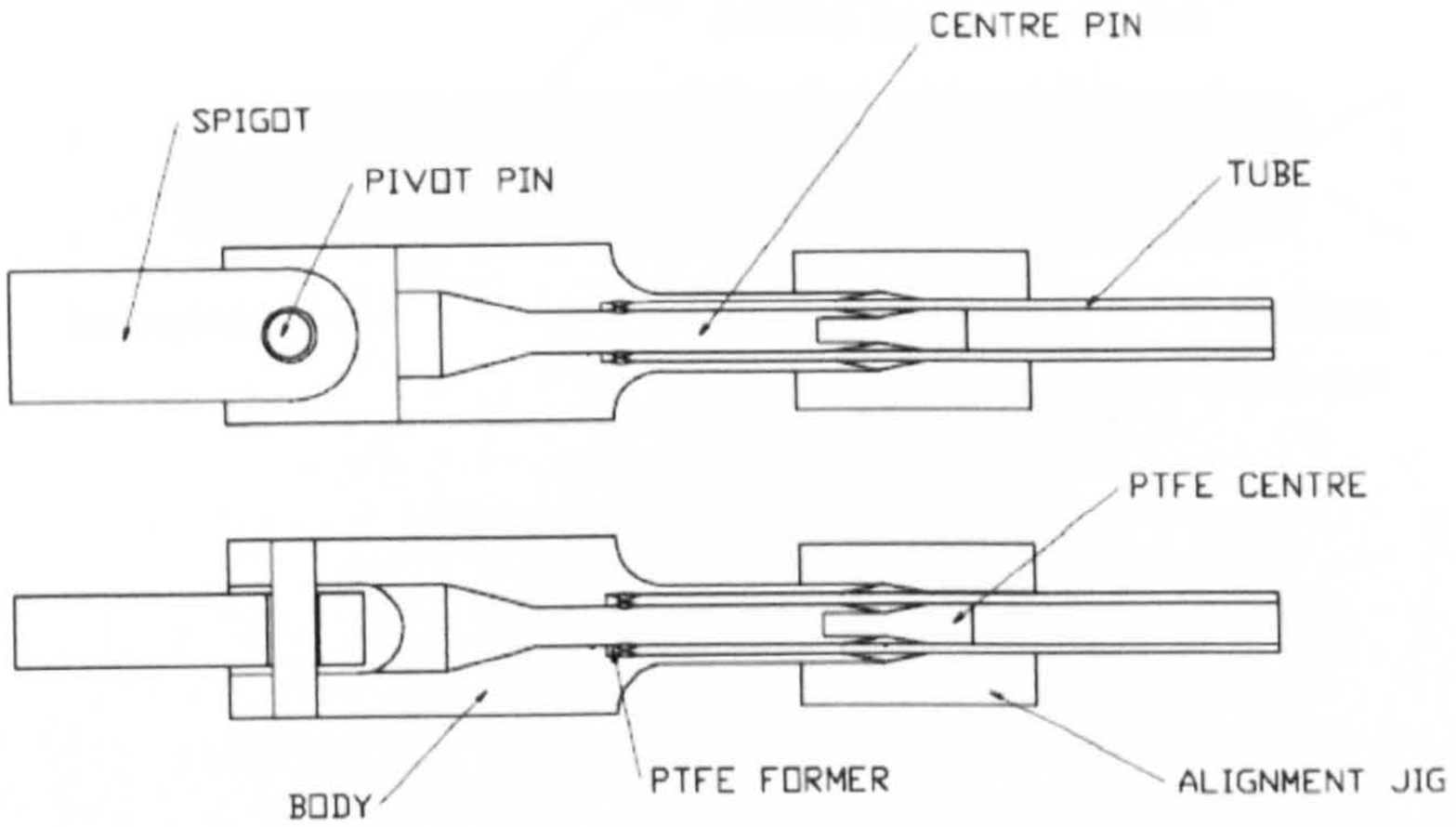

Figure 2.13: Tubular Double-Lap Joint Design[25]

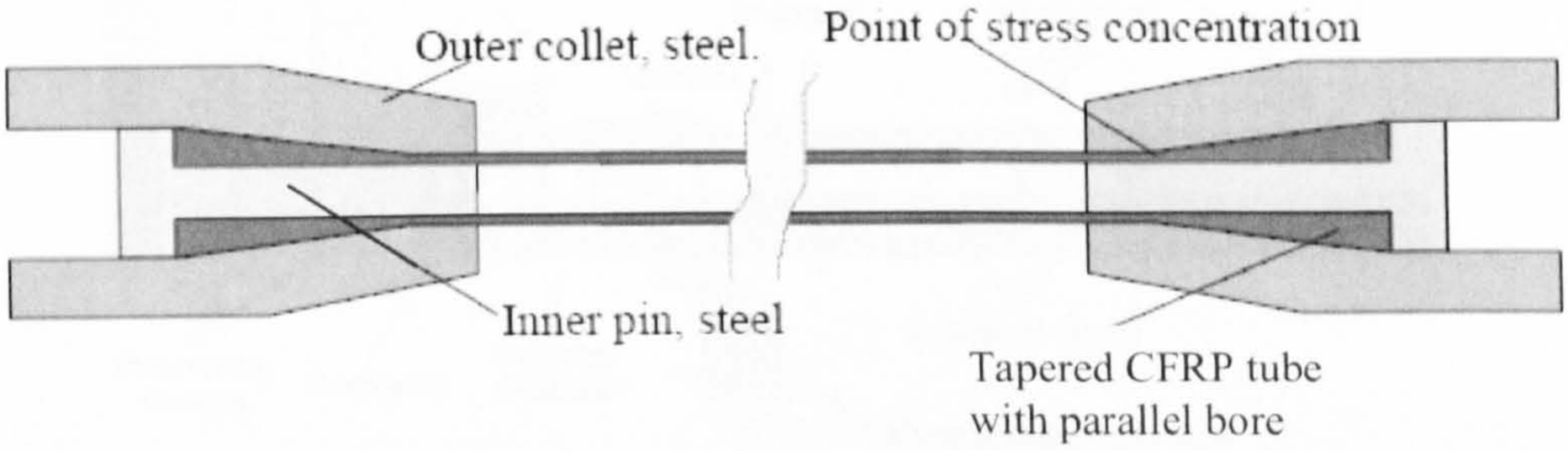

Figure 2.14: Tapered Mechanical Seat Joint Design[25]

As expected, the mechanical seat joint provided the greatest tensile strength, but at the expense of increased manufacturing complexity. The introduction of flares at the end of each tube significantly increases production costs because specialised tooling is required for each strut length. For tubes of constant cross-section, long lengths can initially be produced using filament winding or pultrusion (see Figure 2.15) and then cut to size accordingly, which is a far more economical process. Despite the greater ease of manufacture of the double-lap joint, it proved highly difficult to achieve the constant bond-line thickness and optimised fillet geometries required to minimise stress concentrations. Furthermore, it was recognised that the least-weight design solution could be realised using a fully composite node, for which these problems would be magnified.

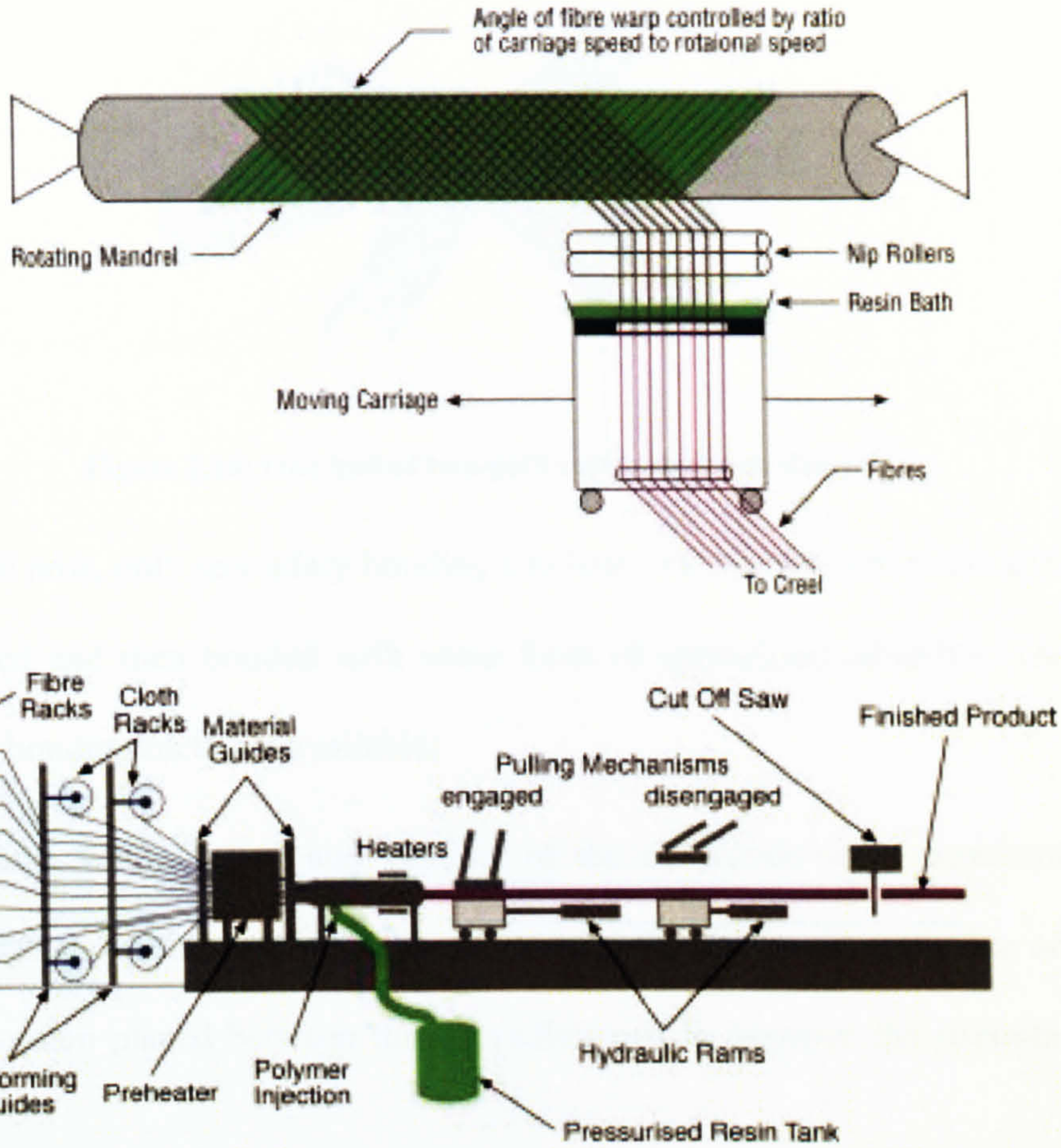

Figure 2.15: The Filament Winding (top) and Pultrusion (bottom) processes[26]

Composite node design was investigated through the development of a two-part composite shell bonded around tubular members, as shown in Figure 2.16. This provided a low-cost and low-weight alternative to the designs discussed above, which would be better suited to mass production[27]. Although bond strength was found to be lower, it was recognised that this could be improved by better surface preparation and a more refined geometry at the end of the joint.

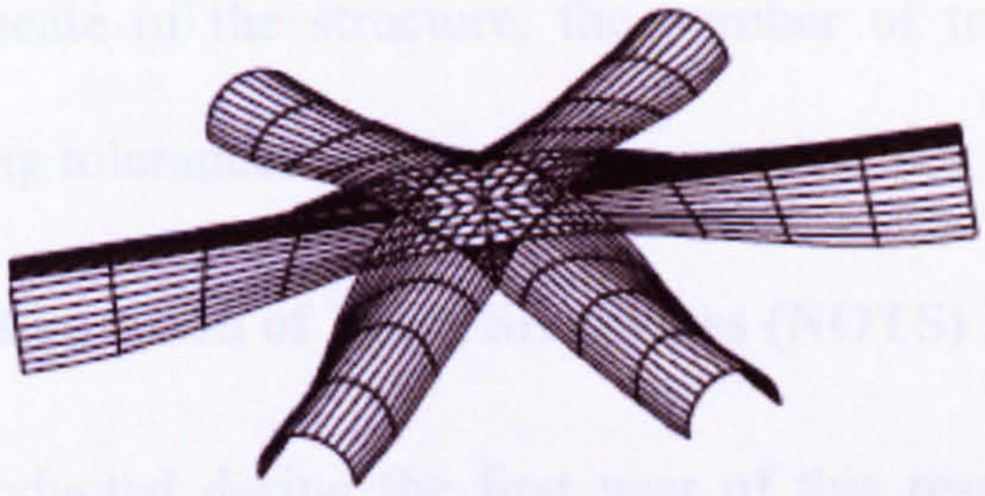

Figure 2.16: One half of two-part composite node design[27]

Until now, only secondary bonding has been considered, where the adherends are pre-cured and then bonded with some form of specialised adhesive. There are two further bonding methods available:

i) Co-curing, where curing and bonding of the adherends occur simultaneously. Although this bond can be made using only the composite resin, an adhesive film is often placed between the two adherends to improve the strength of the joint.

ii) Co-bonding, where one pre-cured adherend is bonded to a second adherend that undergoes curing at the same time. As for co-curing, the bond can rely purely on the composite resin or a separate adhesive film.

For a large, complex truss structure, co-curing is unlikely to be a practical option due to the expense and complexity of the required tooling. This is particularly so for tubular truss members, which as noted above, can be economically produced using techniques such as pultrusion and filament winding. For truss structures where all the truss members lie in the same 2-D plane, co-bonding pre-cured struts to an outer perimeter frame becomes a potential design option. Full details of this technique are provided in the following section and so are not repeated here. In such cases, the choice between secondary bonding and co-bonding is highly dependent on

factors such as the scale of the structure, the number of truss elements and the required manufacturing tolerances.

2.5 The Nodal Optimisation of Truss Structures (NOTS) Project

The work conducted during the first year of this research programme was driven primarily by the requirements of the NOTS project. This was a multi-partner Department of Trade and Industry – Aeronautics Research Programme (DTI-ARP) project, which was undertaken between 2003 and 2006, within the Faraday Advance Partnership. The overarching aim was to develop knowledge and technologies that would facilitate widespread use of composite trusses in civil aeronautic applications. The specific design focus of NOTS was the development of a fully composite truss structure to replace a conventional metallic aircraft wing rib. Use of a truss structure was motivated by the design solution produced by Altair, a structural optimisation package, when applied to the conventional rib. This is shown in Figure 2.17, together with key features of the final truss structure developed for manufacture.

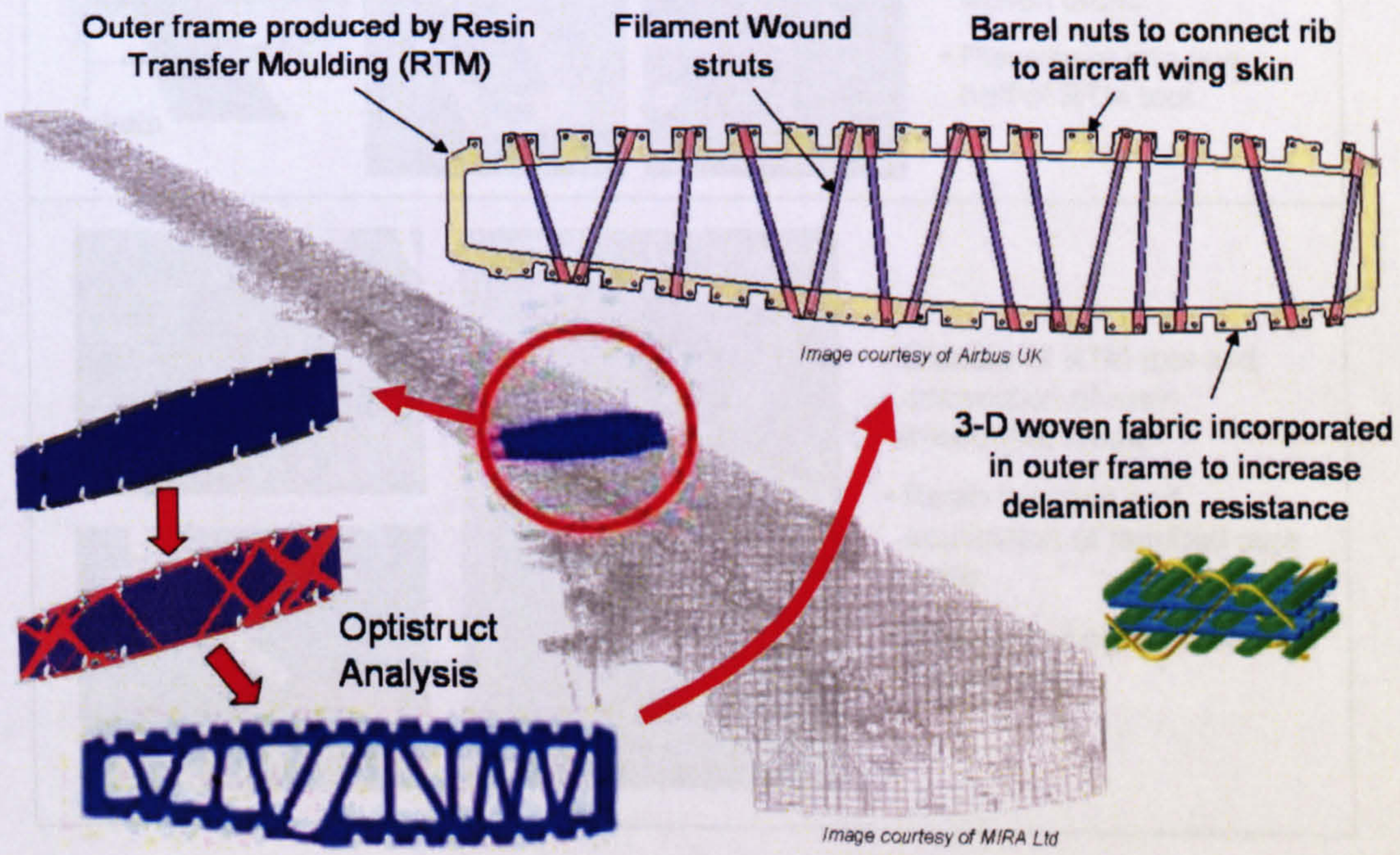

Figure 2.17: Development of the final truss design

Based on a detailed investigation of potential joining methods and the need to balance both light-weight design with a feasible manufacturing process, a co-bonded nodal joint was developed to connect the struts to the outer frame. A novel aspect of its design was the use of 3-D woven fabric to provide increased resistance to delamination, a common failure mechanism in conventional composite joints due to the high peel stresses at the ends of the joint overlap. The manufacturing process developed and used for the full-scale prototype is shown in Figure 2.18.

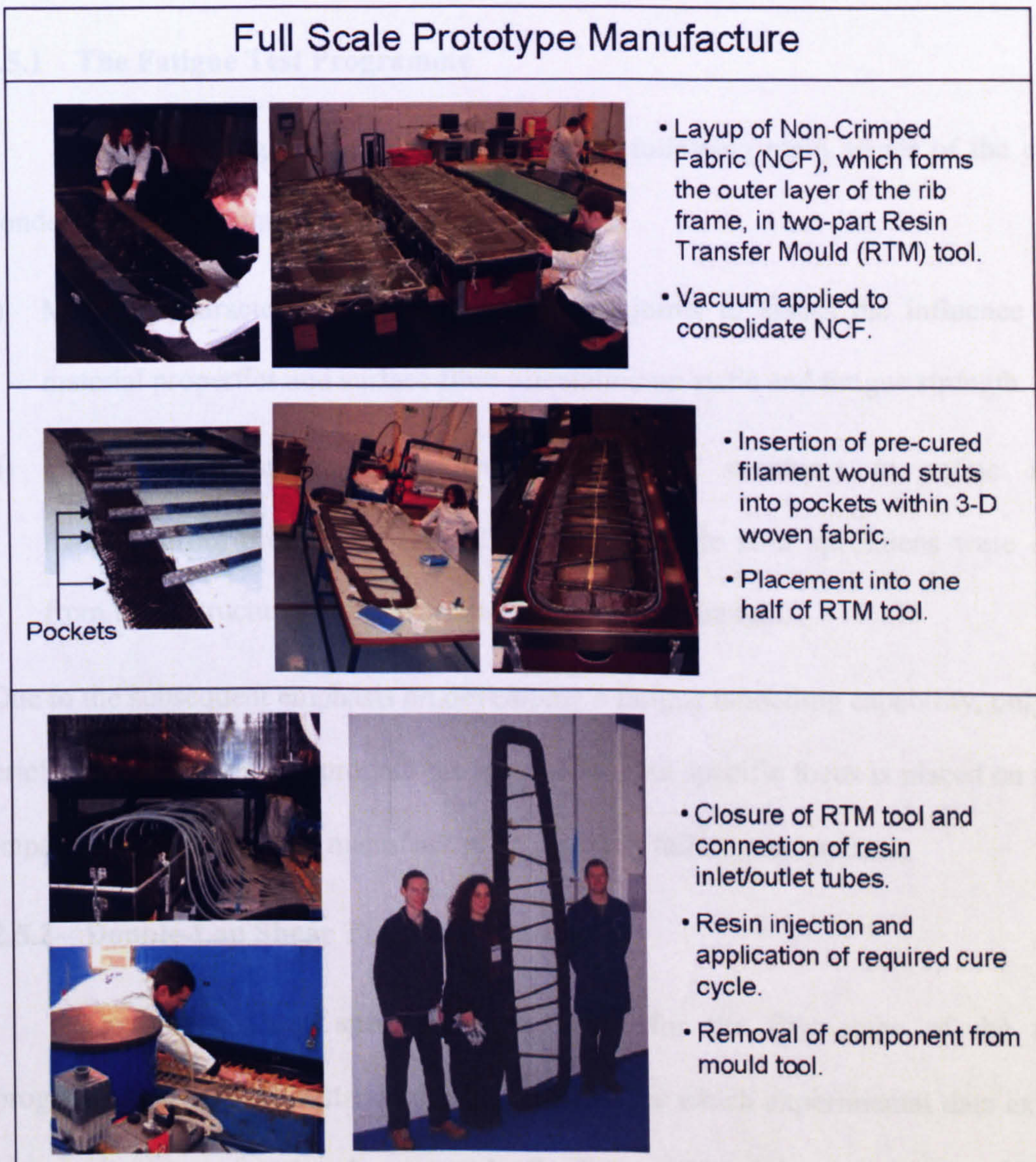

Figure 2.18: Manufacture of the full-scale NOTS prototype

The author's main roles within the NOTS project were as follows:

i) Design of a quasi-static and fatigue test programme, in collaboration with Oxford Brookes University, to evaluate the performance of the co-bonded joint.

ii) Implementation of the required fatigue tests within this programme and analysis of results.

iii) Evaluation of joint failure modes to guide future design and modelling requirements for co-bonded joints.

2.5.1 The Fatigue Test Programme

Fatigue testing was conducted during the following main stages of the co-bonded joint development process:

i) Material Characterisation, using double lap joints to assess the influence of material properties and surface fibre orientation on static and fatigue strength.

ii) Process development, using small-scale truss structures to refine the manufacturing process for the full-scale rib. Single strut specimens were cut from these structures to validate static and fatigue strength.

Due to the subsequent emphasis on developing a fatigue modelling capability, only a brief overview of the test programme is provided, but specific focus is placed on the impact of joint design and manufacture on resulting failure mechanisms.

2.5.2 Double-Lap Shear Tests

Double-lap shear specimens were used for the first stage of the test programme as they are a standard test specimen, for which experimental data exists on a wide range of material, resin and adhesive combinations. In planning the test procedure, both the British Standard for fatigue testing of structural adhesives in

tensile shear[28] and the National Physics Laboratory's (NPL's) Measurement Good Practice Guide on durability testing of adhesive joints[29] were consulted. Initially it had been intended to test the fatigue performance of the joint both with and without an adhesive film but this was not possible due to a shortage of test material. Quasi-static tensile tests performed on both joint types revealed no significant difference in strength[30]. Therefore, fatigue testing was performed only on resin bonded joints, due to the greater manufacturing simplicity this would provide in the full-scale structure.

The test specimens were prepared from a Double Lap Shear (DLS) moulding at Crompton Technology Group (CTG). This consisted of a central 3-D woven fabric adherend (5 layer angle interlock, 2.7mm thick) co-bonded to two pre-cured outer NCF adherends (2.6mm thick), as shown in Figure 2.19. Surface fibre orientation in both the central and outer adherends was parallel with the applied load direction.

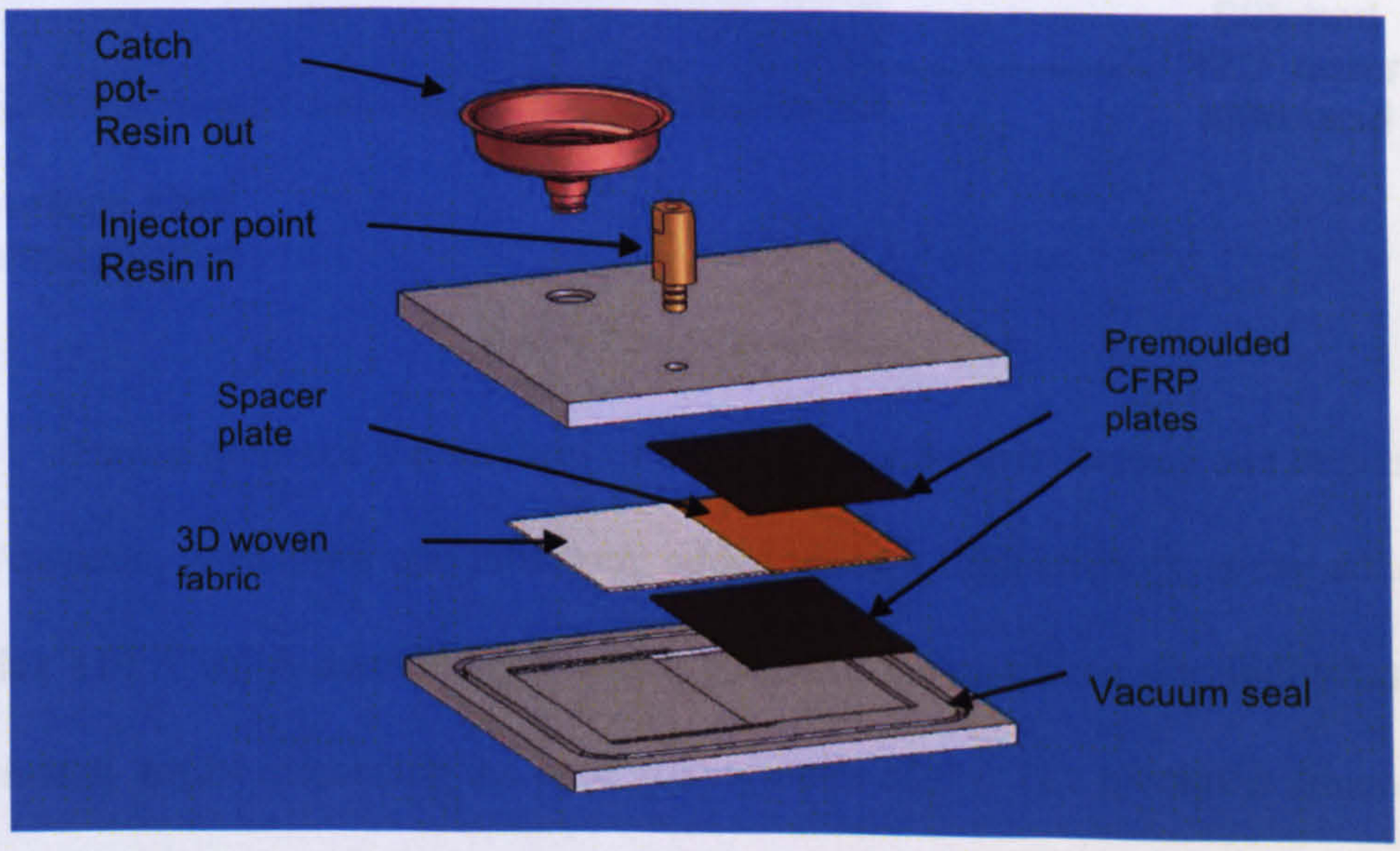

Figure 2.19: CTG mould for double-lap joint specimens

Significant features of the DLS moulding received from CTG (see Figure 2.20) were as follows:

a) Fibre misalignment in the woven fabric close to the bond-line (labeled A in Figure 2.20).

b) Fibre misalignment and resin-rich regions at the edges of the 3-D woven fabric adherend (labeled B in Figure 2.20).

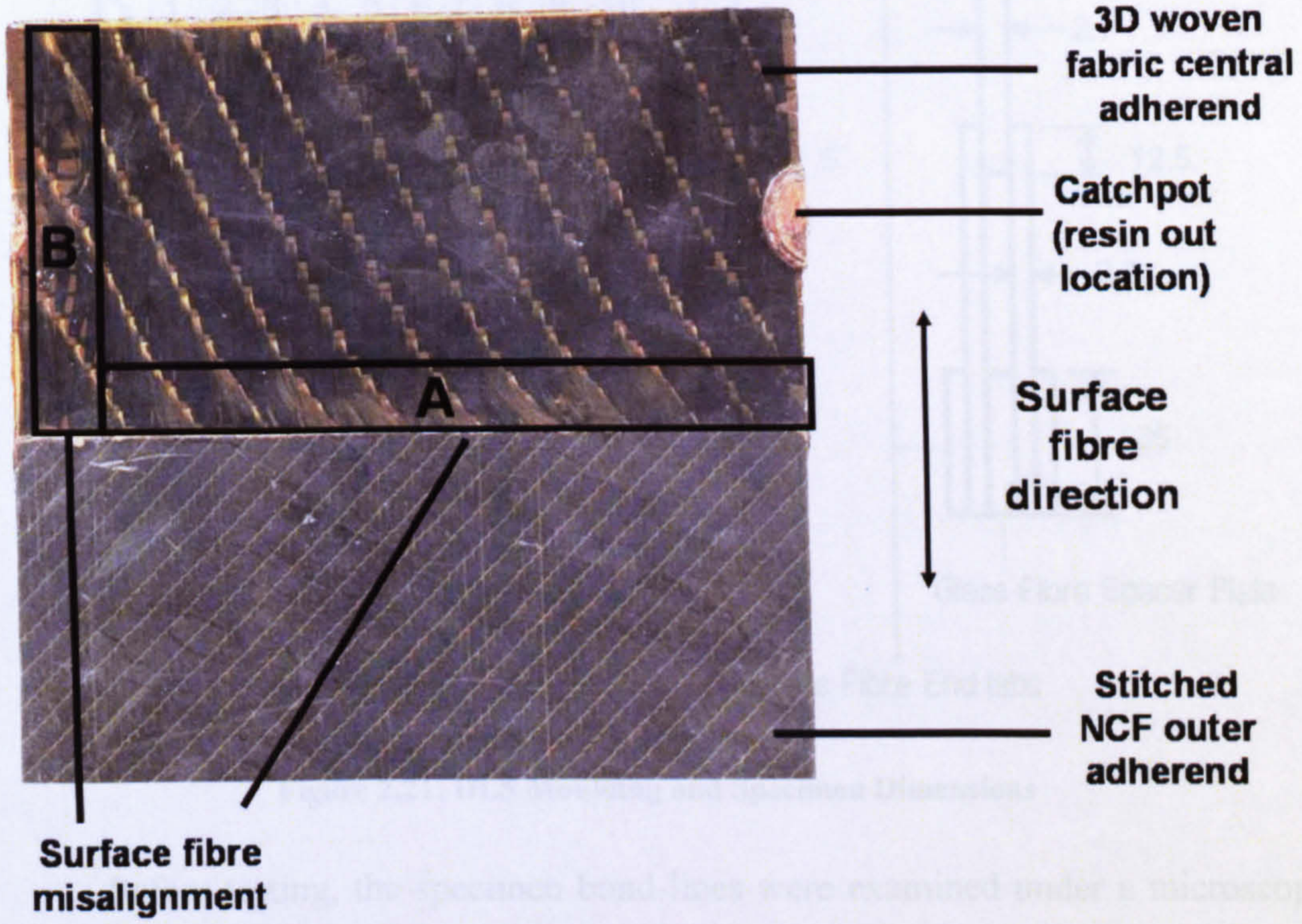

Figure 2.20: DLS moulding

Having prepared the surfaces of the moulding by grit blasting and degreasing with acetone, glass-fibre end tabs were added using a high-strength epoxy adhesive (Redux 810 A/B). A diamond saw was used to cut the moulding into individual test specimens, whilst discarding the poor quality outer edges. The specimen dimensions and the location of each specimen within the original moulding are shown in Figure 2.21. It should be noted that there was no adhesive fillet or adherend chamfer. Therefore, the joint geometry was that which gives the greatest potential for fatigue crack initiation at the free edge of the bond-line.

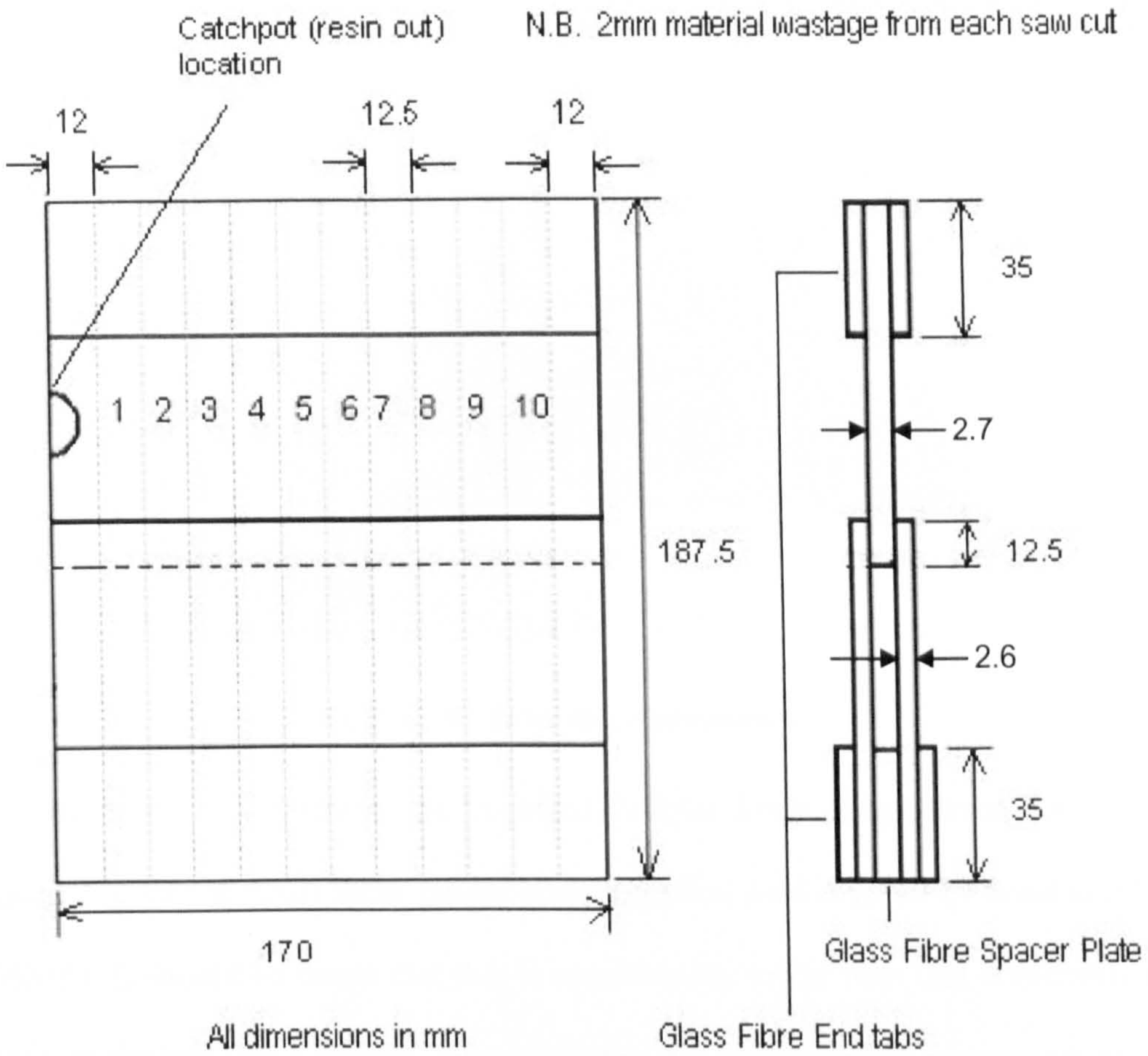

Figure 2.21: DLS Moulding and Specimen Dimensions

Before testing, the specimen bond-lines were examined under a microscope and Figure 2.22 shows the bond-line of specimen 6, revealing a large void within the 3-D woven fabric central adherend. This was a typical defect in all of the test specimens.

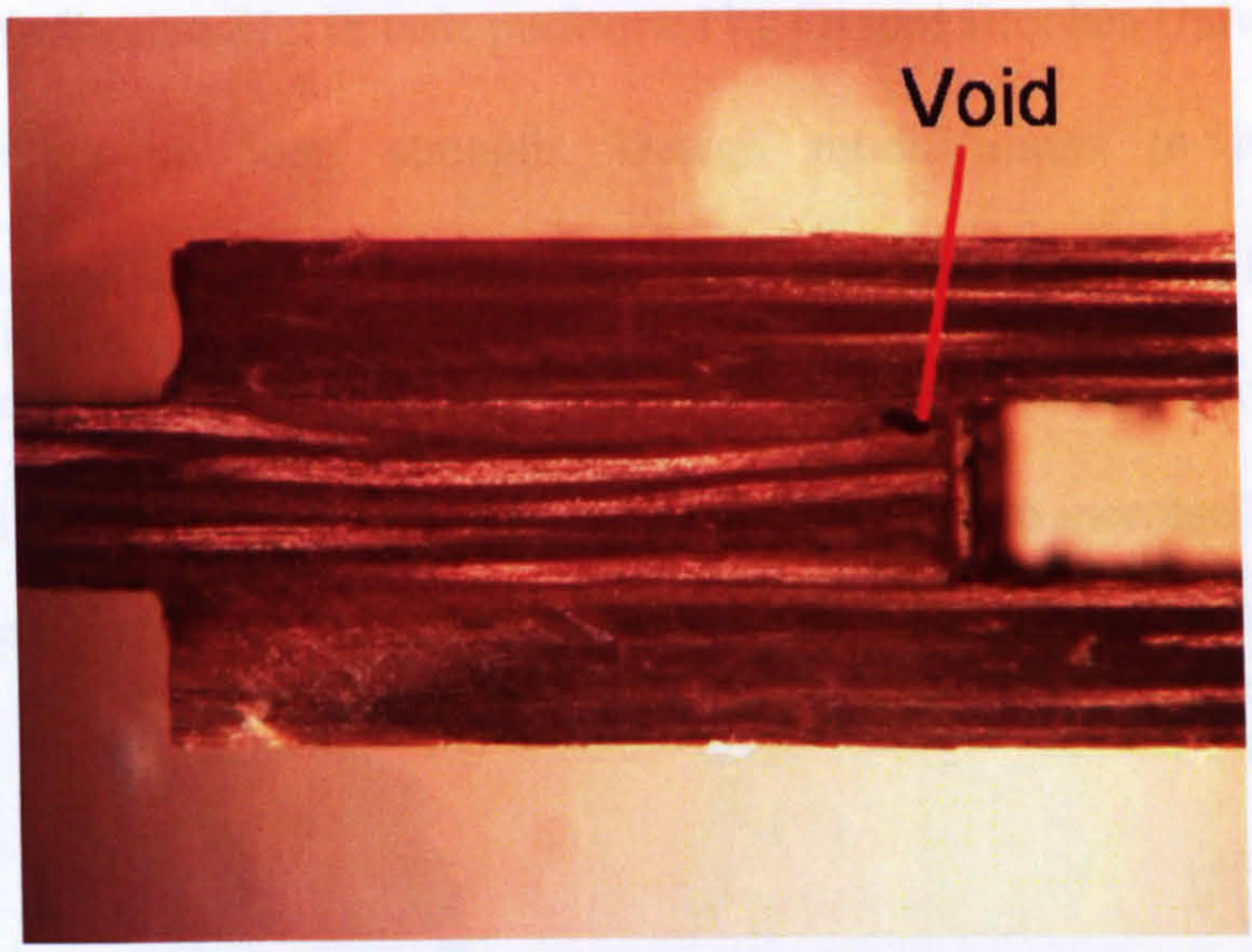

Figure 2.22: Bond-line of specimen 6

In order to determine the required fatigue loads, quasi-static tests were conducted, giving a mean shear failure stress (applied load divided by bond area) of 19.95MPa. It should be noted that this is considerably lower than that obtainable for a more optimised joint design. For example, an investigation performed at the University of Bristol in 1997[9] achieved a shear strength of approximately 45MPa in double-lap specimens. In this case, a secondary adhesive was used to bond pre-cured, uni-directional, carbon-fibre adherends. Stress concentrations were minimized by applying chamfers to the adherends and using adhesive fillets. Also, the stiffness of the central adherend was matched to that of the outer adherends. Therefore, although the NOTS structure requires a co-bonded joint, this previous University of Bristol study highlights the significant strength improvements obtainable from design features such as chamfers, adhesive fillets and stiffness matched adherends.

Post-failure inspection of the quasi-static specimens revealed crack propagation to occur via fibre tow failure in both the NCF and 3-D woven fabric (Figure 2.23). There was no evidence of interfacial/cohesive failure, which explains

why use of an adhesive film in tests performed by Oxford Brookes University had no significant effect on joint strength. Design modifications to reduce stress concentrations and hence increase strength (e.g. chamfers, adhesive fillets, stiffness matched adherends), may result in a change of failure mode from interlaminar to interfacial failure. In such a case, use of an adhesive film to increase bond strength may be beneficial.

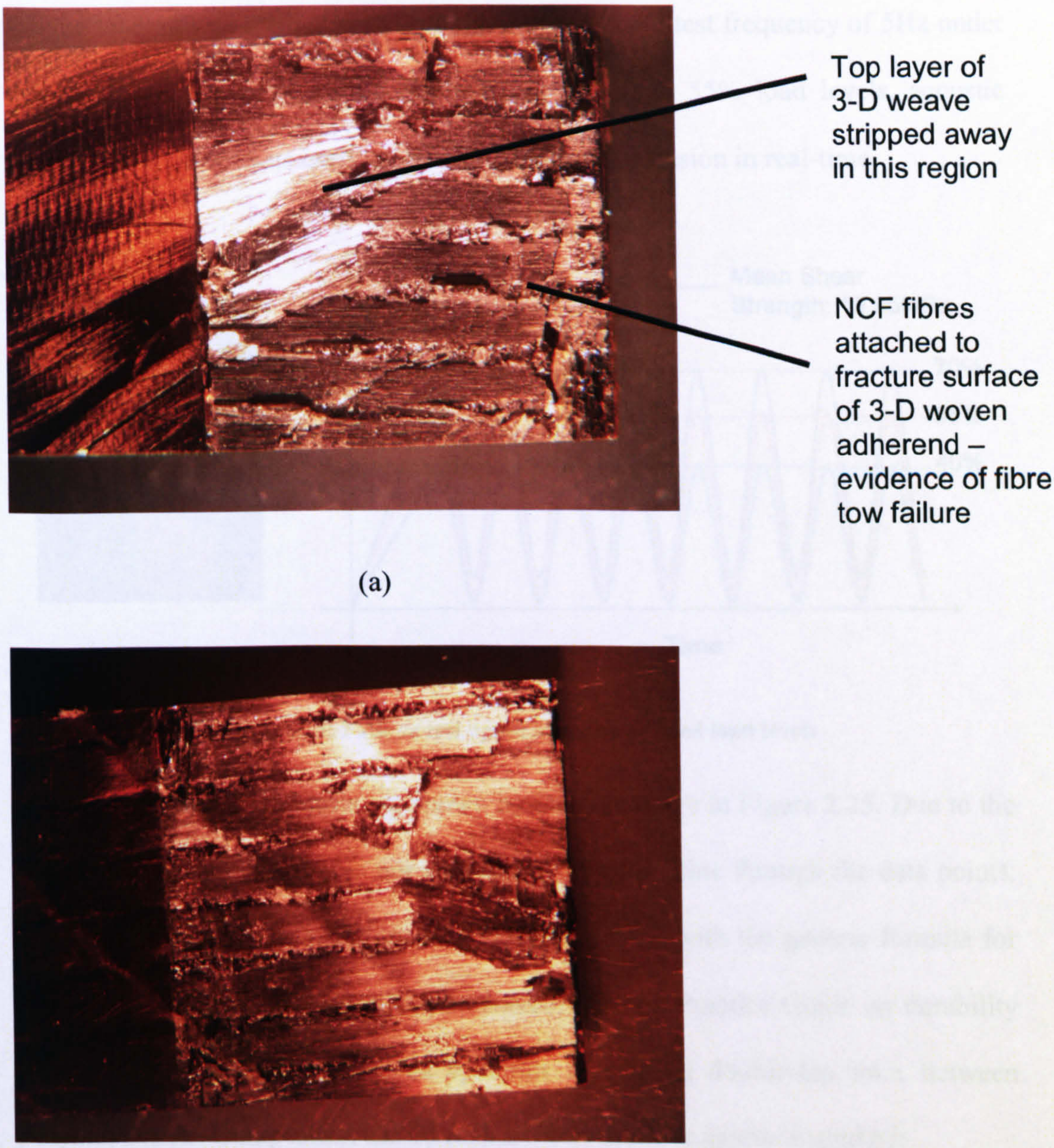

Figure 2.23: Fracture surfaces of central 3-D woven fabric (a) and outer NCF (b) adherends for one of the quasi-static test specimens

Fatigue tests were performed under load control at 40%, 55% and 70% of the mean quasi-static failure strength. 2 specimens were tested at each load level, giving 6 data points (The remaining two specimens had to be discarded, due to premature fracture caused by problems with test machine setup/operation). Tension-tension

fatigue loading was applied with an R-ratio of 0.1 and a test frequency of 5Hz under ambient conditions. For specimens tested at 70% and 55% load levels, acoustic emission equipment was used to monitor damage progression in real-time.

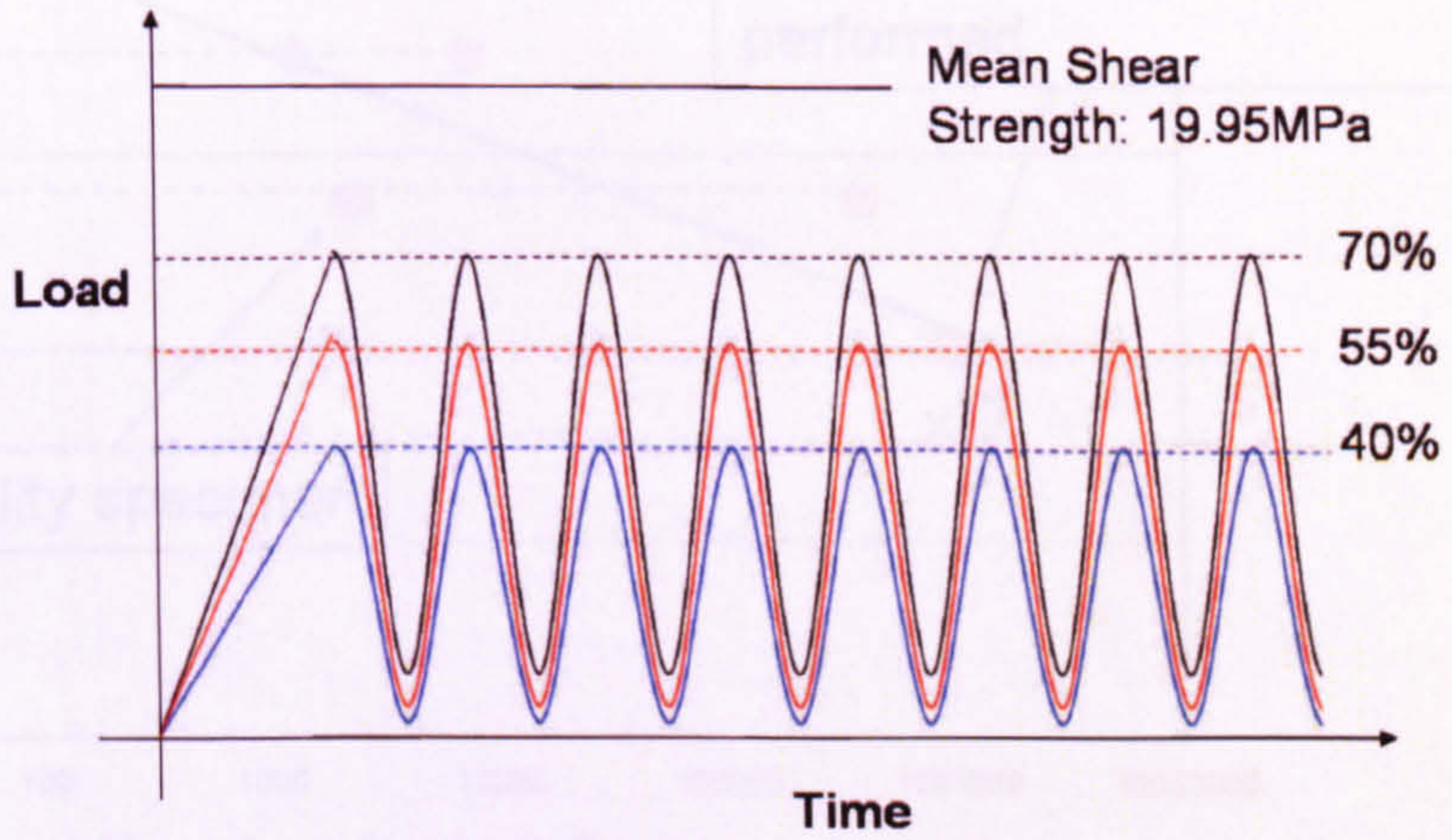

Figure 2.24: Fatigue test apparatus and applied load levels

Results from the fatigue tests are shown by the S-N curve in Figure 2.25. Due to the shortage of specimens, it was not possible to fit a trendline through the data points. However, the results gained appear broadly consistent with the generic formula for S-N curves published in the NPL Measurement Good Practice Guide on durability testing of adhesive joints[29]. This specifies that for a double-lap joint between Polymer Matrix Composites, the normalized S-N curve is approximated by:

$$P_{MAX}/P_0 = 1 - 0.097 \log N_f \qquad \text{(Eqn. 2.1)}$$

where N_f is the number of cycles to failure, P_{MAX} is the maximum load applied to the specimen and P_0 is the ultimate strength of identically conditioned specimens measured at the fatigue test loading rate.

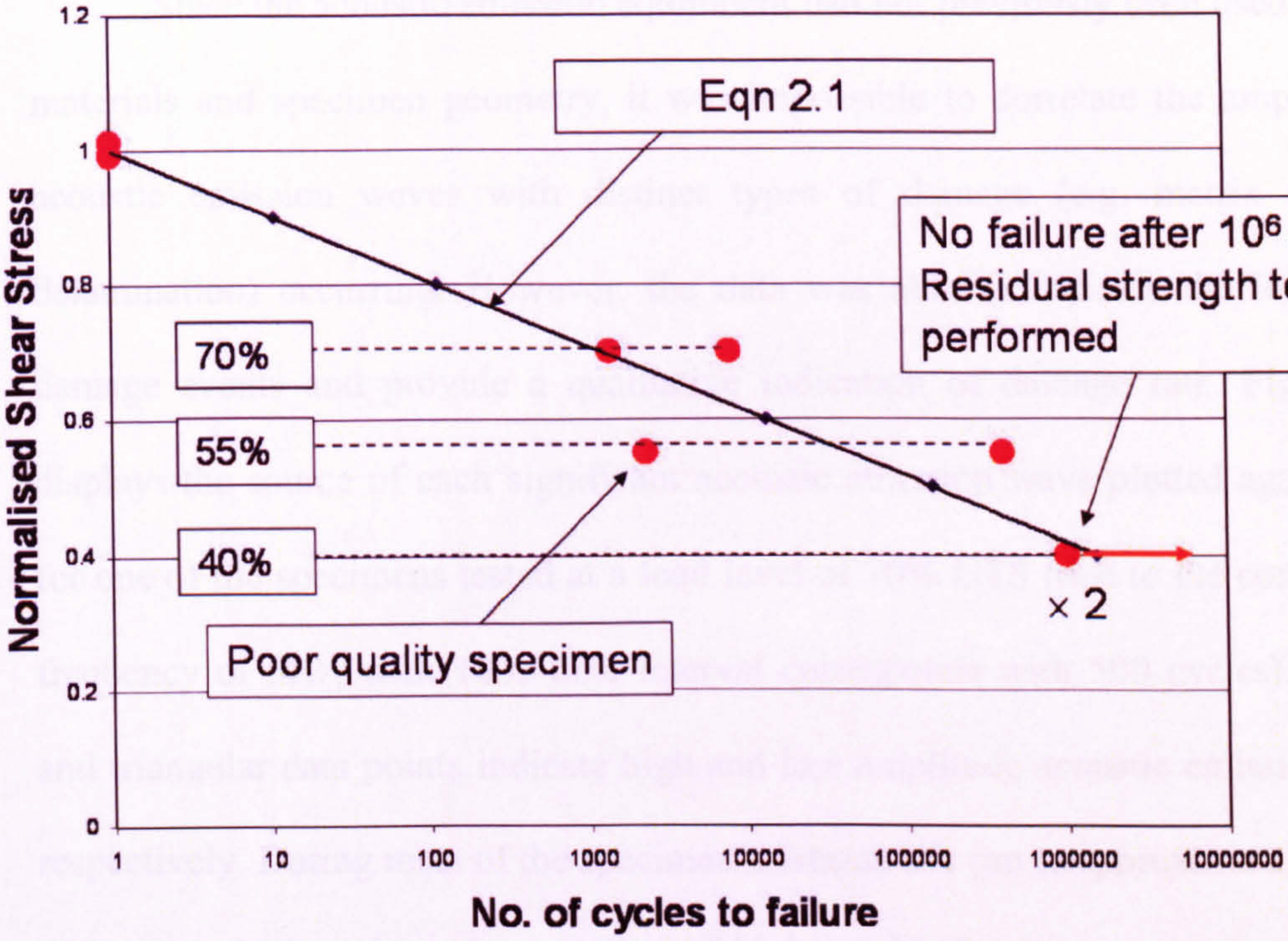

Figure 2.25: S-N Curve for DLS Specimens

The fracture surfaces of specimens that failed in fatigue indicated that as for the quasi-static specimens, cracks propagated close to the bond-line but within the adherends, as opposed to along the bond interface. Visual inspection during testing revealed no stable crack growth and it appears that crack propagation occurred in a sudden, unstable manner.

The specimens tested at 40% UTS showed no visible signs of damage after 10^6 fatigue cycles and rather than fatiguing for an indefinite time, it was believed more beneficial to perform residual strength tests. A mean shear strength of 20.14MPa for the two fatigued specimens compared to 19.95MPa for the un-fatigued specimens indicated no deterioration in strength, suggesting that the fatigue threshold lies somewhere between the 40% and 55% load levels. The fracture surfaces again indicated crack propagation through fibre tows close to the bond-line.

Since the acoustic emission equipment had not previously been used on these materials and specimen geometry, it was impossible to correlate the amplitude of acoustic emission waves with distinct types of damage (e.g. matrix cracking, delamination) occurring. However, the data was able to indicate the location of damage events and provide a qualitative indication of damage rate. Figure 2.26 displays the source of each significant acoustic emission wave plotted against time for one of the specimens tested at a load level of 70% UTS (due to the constant test frequency of 5Hz, each 100s time interval corresponds with 500 cycles). Circular and triangular data points indicate high and low amplitude acoustic emission waves respectively. During most of the specimen's fatigue life (up to approximately 1200s - 6000 cycles), there is a concentration of high amplitude waves emitted close to the bond-line, within the 3-D woven fabric central adherend. This suggests that the most significant damage events occured in this region, which is likely to be due to the large through-thickness stresses at the end of the overlap. Prior to final failure, there is no obvious concentration of hits in the bond region and the results give no indication of how cracks propagated through the joint. A similar pattern of acoustic emission damage events was recorded for the other specimens monitored.

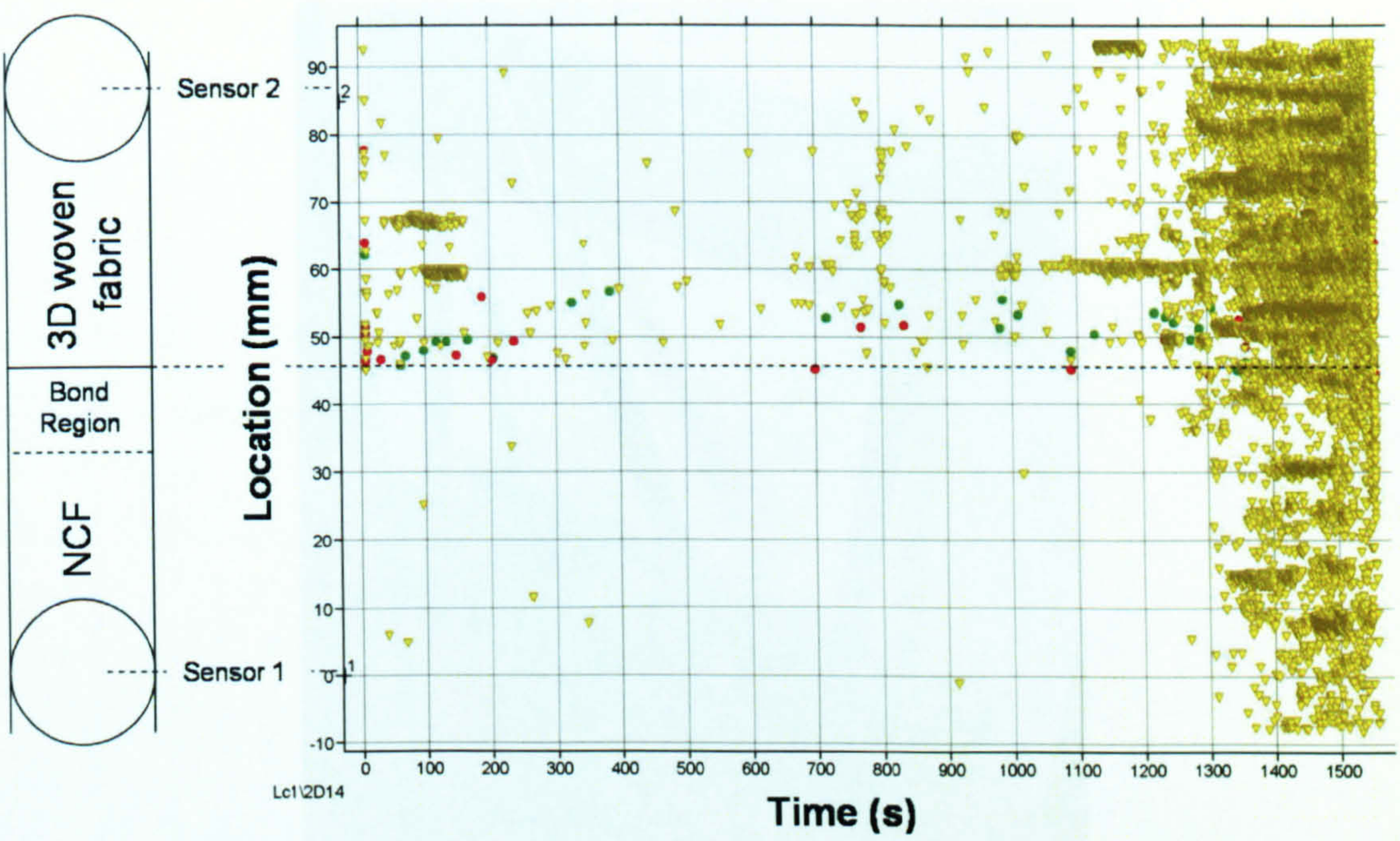

Figure 2.26: Acoustic emission events recorded for specimen tested at 70% load level

2.5.3 Single Strut Tests

Before progressing to the manufacture and test of a full-scale rib, the strength of the co-bonded joint between the struts and 3-D woven fabric frame was investigated using single strut specimens. For this to be achieved in conjunction with development of the final manufacturing process, a small-scale truss structure, referred to as S2, was designed incorporating all the key features of the full-scale rib (see Figure 2.27). This was manufactured using an identical process to that previously shown for the full-scale prototype (see Figure 2.18), with the exception of smaller scale tooling.

Figure 2.27: The S2 Structure

A diamond saw was used to cut the two vertical struts from the moulding in order to form two test specimens, as shown in Figure 2.28. In order to replicate the proposed method of connecting the full-scale NOTS rib to an aircraft wing skin, loading on the single strut specimens was applied through barrel nuts. Holes were drilled in the outer frame for the barrel nuts to be inserted (see Figure 2.28) and specialised test fixtures were designed and manufactured to enable this method of loading in the servohydraulic test machine (see Figure 2.29).

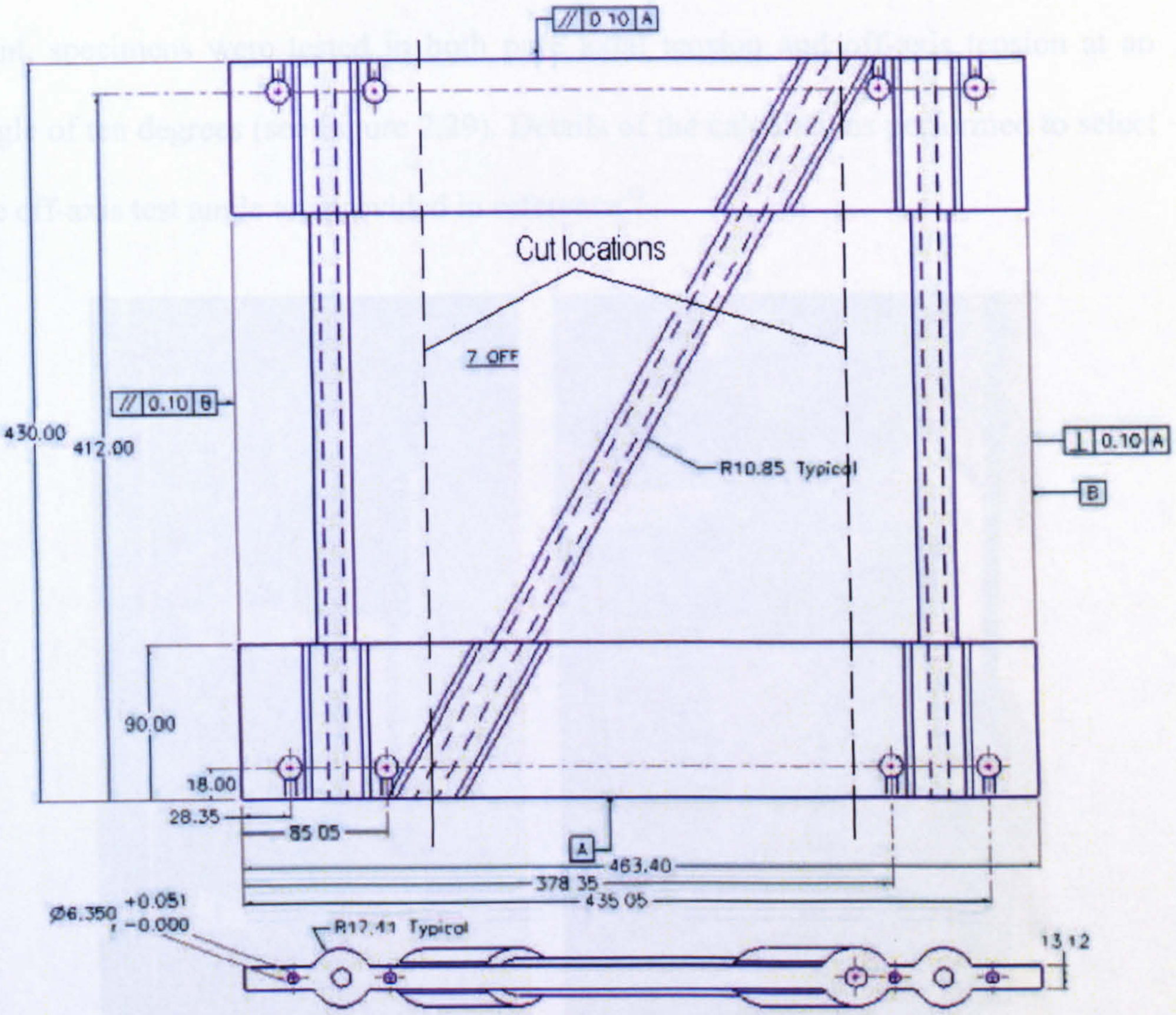

Dimensions in mm

Figure 2.28: Cut locations and barrel nut hole positions in S2 structure

In order to determine the type and magnitude of loads that should be applied to the single strut specimens, results from a NASTRAN model of the full scale rib developed by MIRA were consulted. The model was analysed under three critical loadcases supplied by Airbus:

a) Maximum Shear Load

b) Maximum Pull-off Load

c) Maximum Bending

Results from the analyses showed that whilst torsional loads in the struts would be negligible, significant axial and bending loads would exist. In order to investigate the relative effects of axial and bending loads on the static and fatigue strength of the

joint, specimens were tested in both pure axial tension and off-axis tension at an angle of ten degrees (see Figure 2.29). Details of the calculations performed to select the off-axis test angle are provided in reference[31].

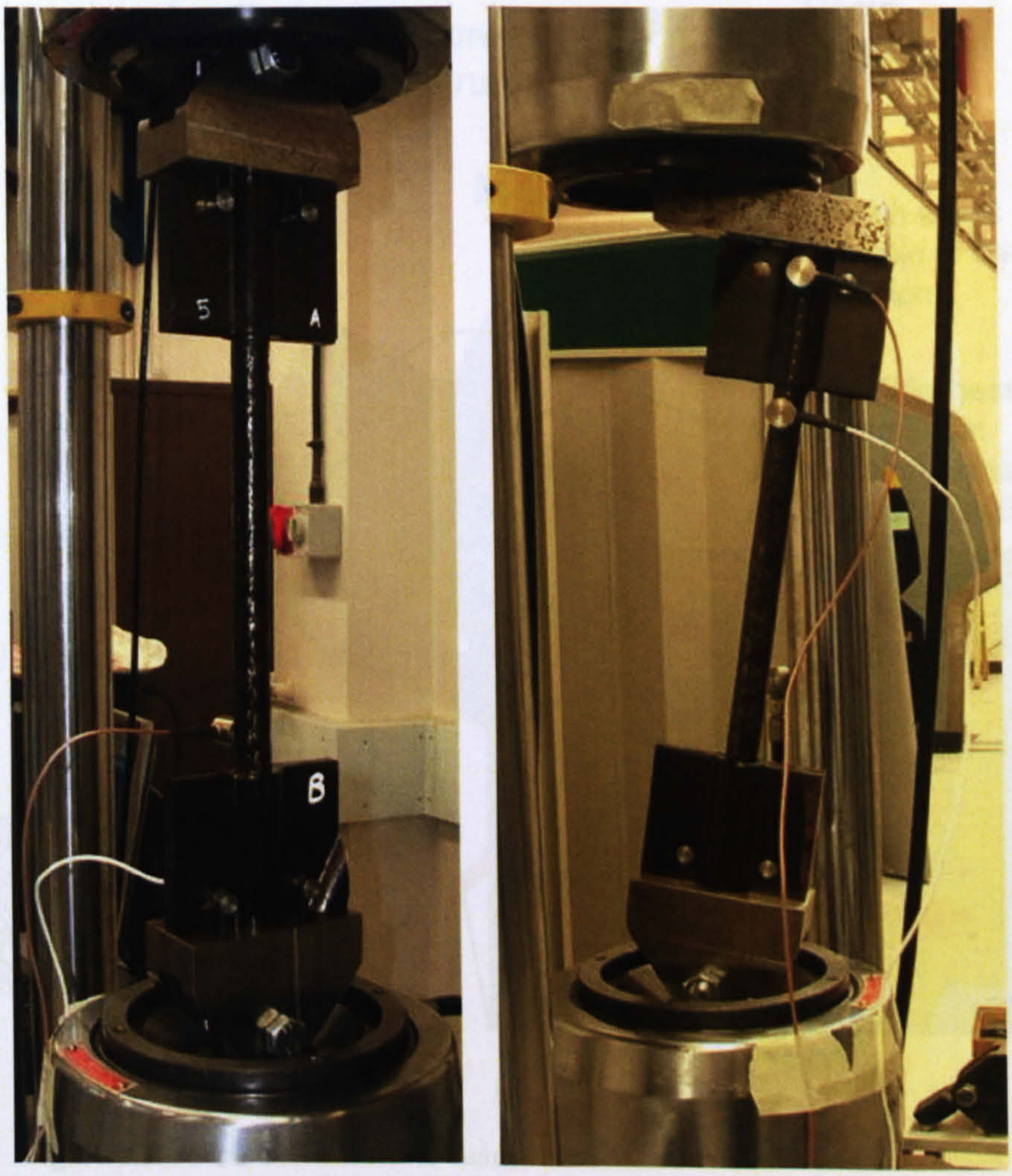

Figure 2.29: Pure axial (left) and off-axis (right) load configurations

Under bending load, the bond-line region most susceptible to crack initiation/propagation is the resin rich area where the 3-D woven fabric separates to surround the strut. Therefore, to ensure conservative test results, the specimen was orientated so that maximum stress due to bending occurred in this region, as shown in Figure 2.30.

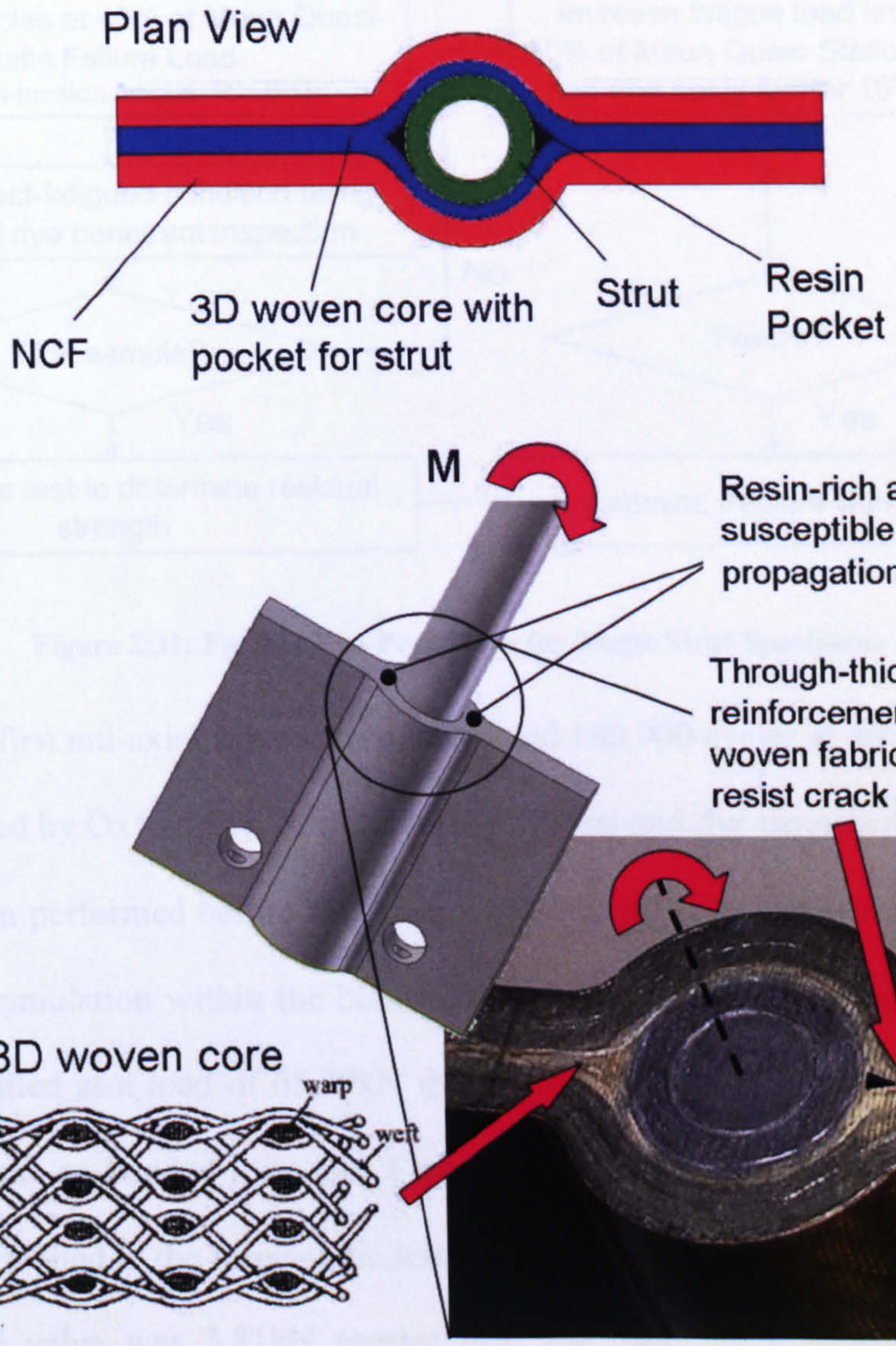

Figure 2.30: Strut orientation to ensure maximum stress in resin rich areas

Due to severe material shortages within the NOTS programme, fatigue testing could only be performed on 4 single strut specimens, 2 in a pure tension configuration and 2 in an off-axis configuration. This prevented the acquisition of a full S-N curve and to maximise the fatigue data obtainable, the procedure shown in Figure 2.31 was followed for each loading configuration. Acoustic emission equipment was again used to monitor the location of damage events real-time during testing.

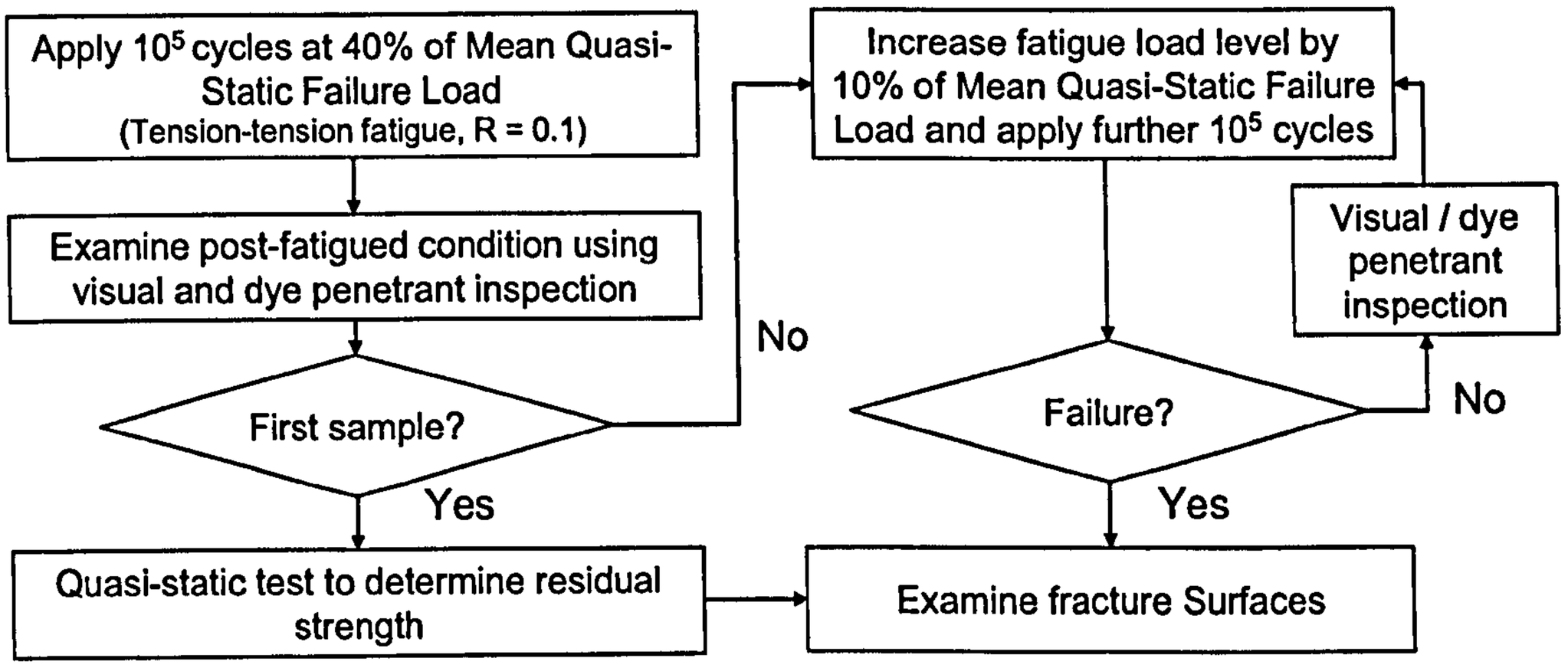

Figure 2.31: Fatigue Test Procedure for Single Strut Specimens

The first uni-axial test specimen survived 100,000 cycles at 40% of the mean UTS recorded by Oxford Brookes University. Visual and dye penetrant inspection of the specimen performed before and after testing revealed no significant evidence of damage accumulation within the bond-line region. In the residual strength test, the specimen failed at a load of 65.29kN through delamination of the filament wound strut along the co-bonded joint (see Figure 2.32). This failure mode was consistent with that exhibited in the quasi-static tests performed by Oxford Brookes[30]. Since the failure load value was 3.81kN greater than the mean UTS recorded by Oxford Brookes, it appeared that no reduction in strength had resulted from the applied fatigue loading.

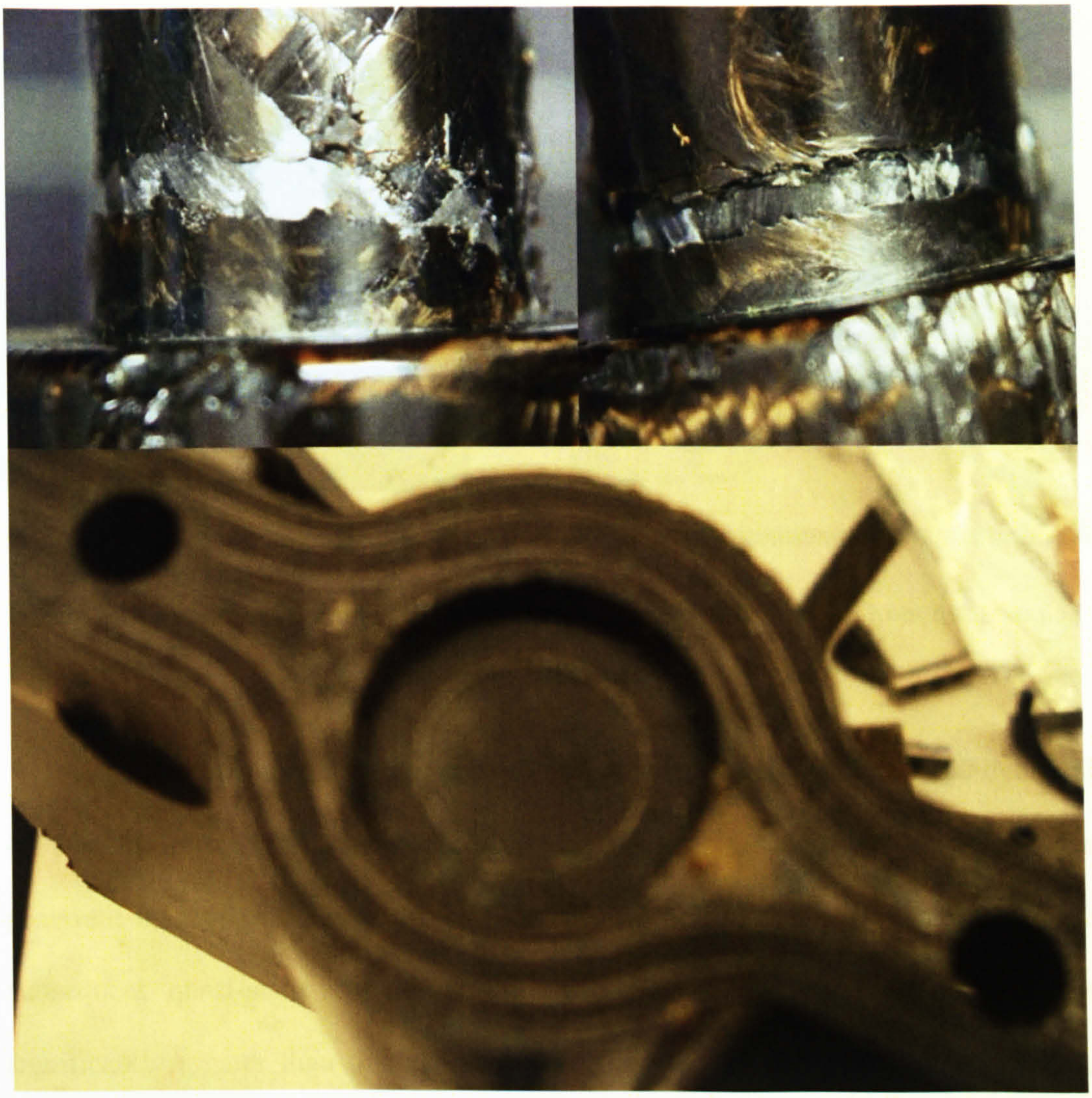

Figure 2.32: Fracture surfaces of first uni-axial test specimen after residual strength test

For the second uni-axial test specimen, failure occurred after 42,000 load cycles at 40% of the mean UTS, via tear-out of one of the barrel nuts through the RTM frame, as shown in Figure 2.33. This is likely to be due to the high level of delamination and voidage present within the RTM frame, which was detected by C-scan inspection performed at Airbus prior to testing.

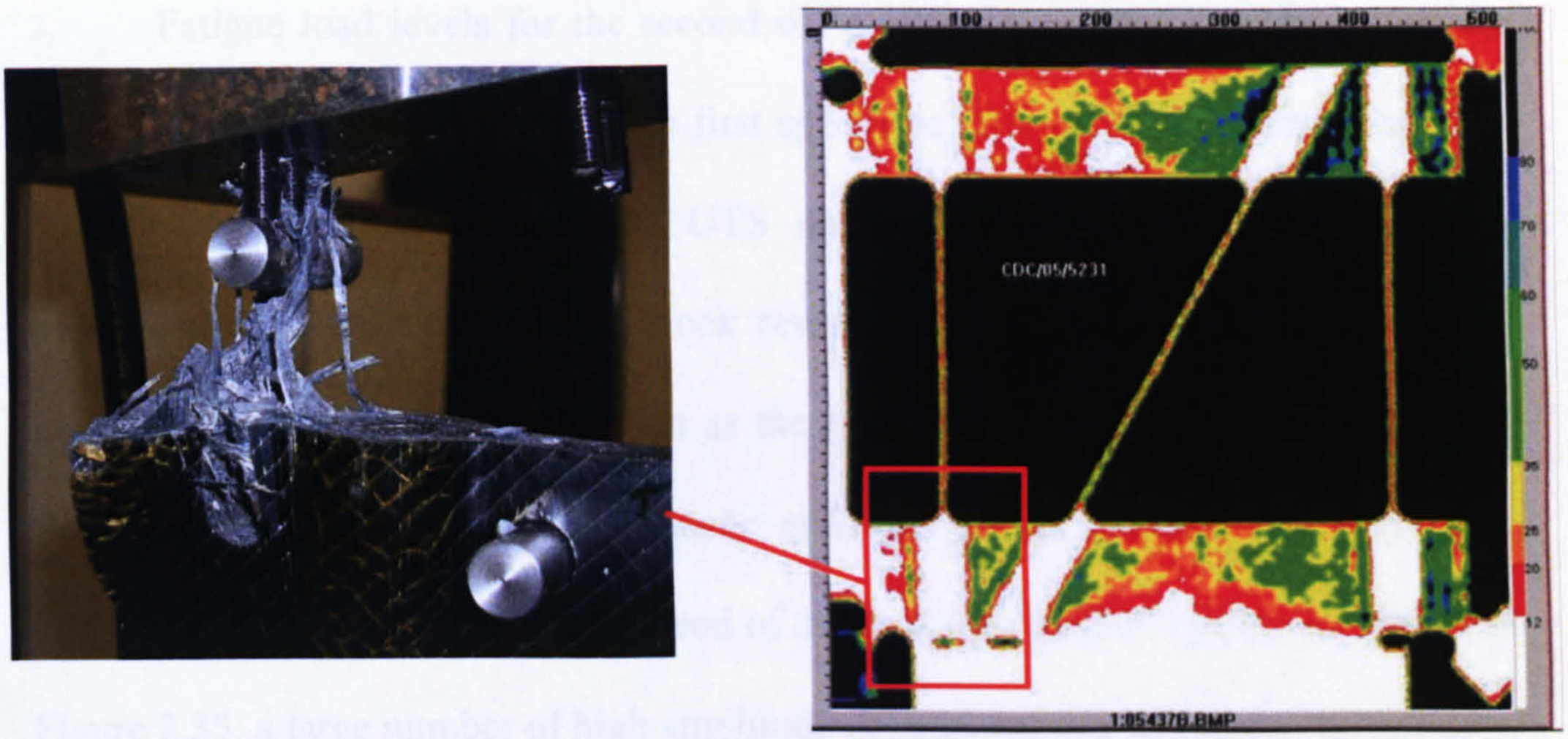

Figure 2.33: Failure of second uni-axial test specimen and evidence of significant delamination in pre-test C-scan

The first off-axis test specimen survived fatigue loading for 100,000 cycles at 40% of the mean UTS recorded by Oxford Brookes University and visual / dye penetrant inspection revealed no significant evidence of crack growth. During the subsequent quasi-static residual strength test performed, the failure load was significantly greater than that recorded by Oxford Brookes and a different failure mode was observed, as shown in Figure 2.34. This is believed to be due to differences in the off-axis test fixtures used at the two Universities.

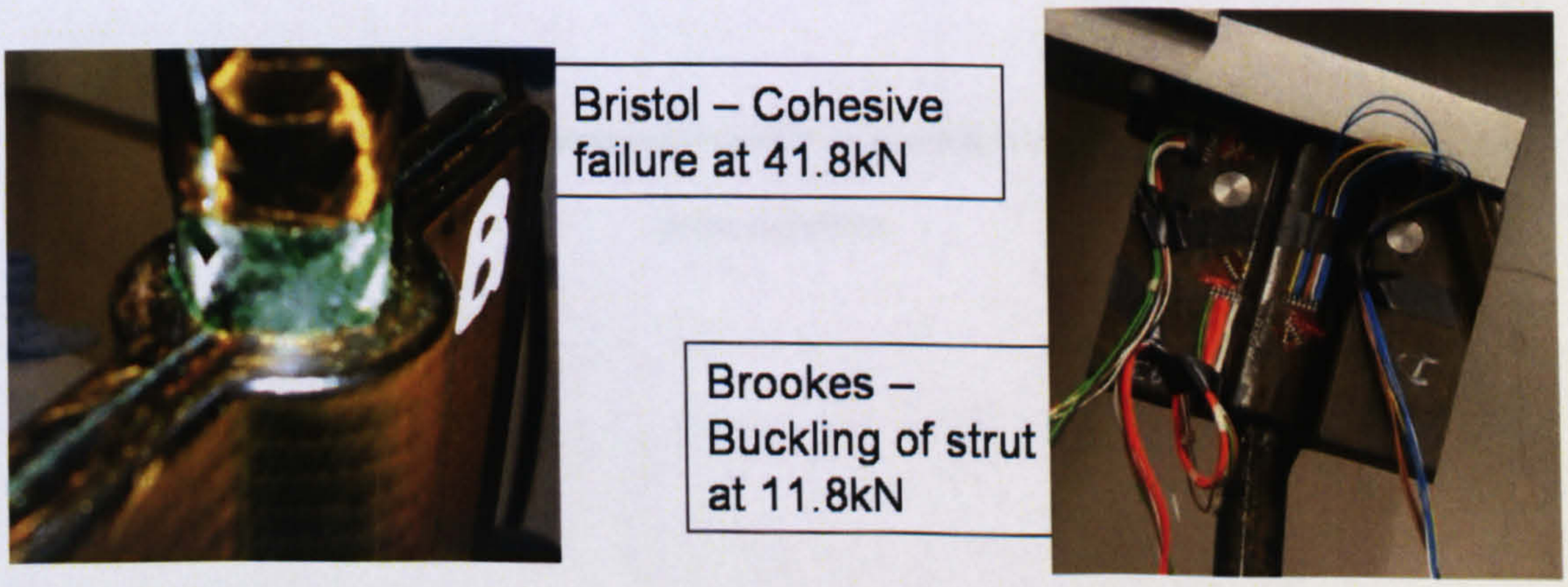

Figure 2.34: Differences in failure mechanism and load for off-axis strut specimens tested at Bristol and Oxford Brookes

Fatigue load levels for the second off-axis test specimen were based on the ultimate failure load recorded for the first specimen. The second specimen survived 100,000 cycles at 40% and 50% UTS and visual / dye penetrant inspection performed after each cyclic load block revealed no significant evidence of crack growth. However, it was evident that as the fatigue load level increased, so too did the frequency and amplitude of acoustic emission events recorded. At 60% UTS, bond-line failure occurred at the top end of the strut after 14,200 cycles. As shown in Figure 2.35, a large number of high amplitude damage events, shown by the red dots, were recorded across the bond-line prior to final failure. Inspection of the fracture surfaces revealed the failure mode to be a combination of interfacial/cohesive failure and strut delamination.

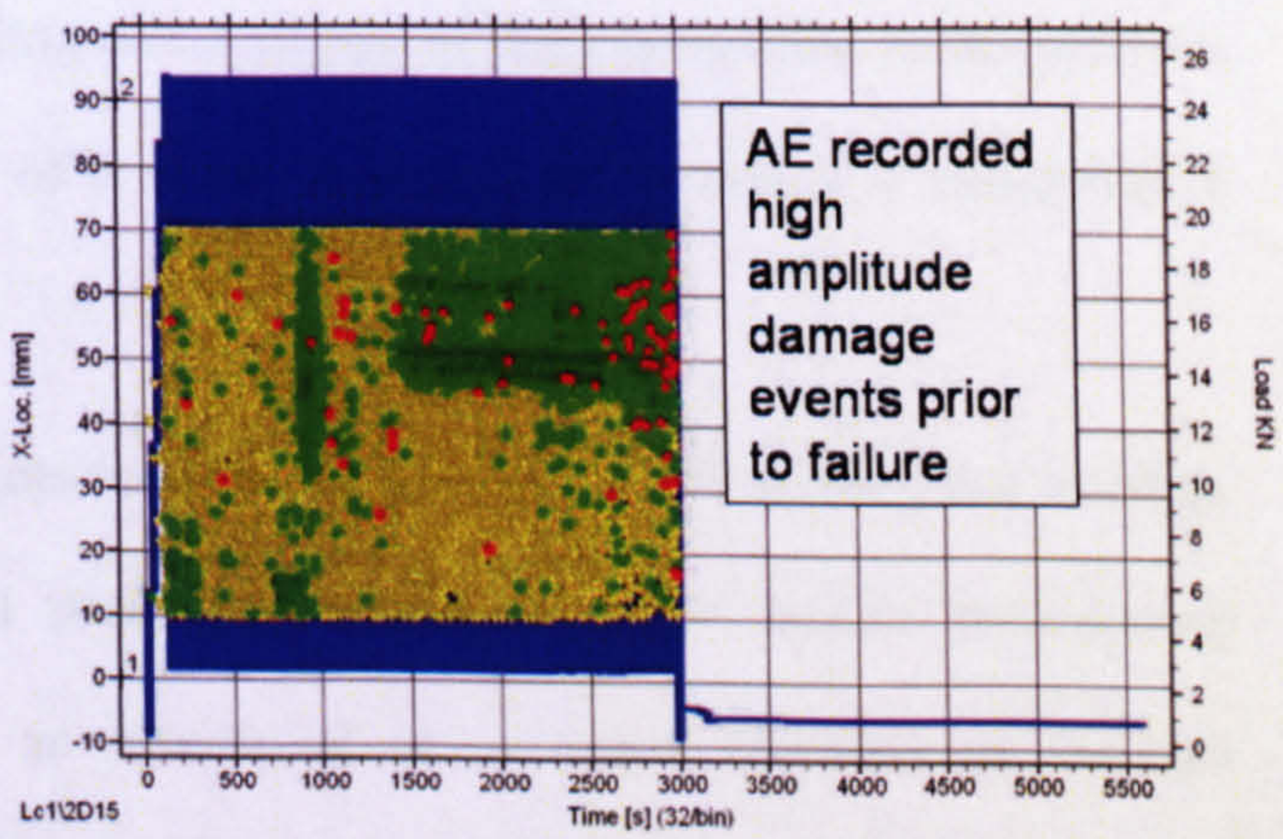

Figure 2.35: Acoustic emission events recorded along bond-line region of off-axis test specimen prior to failure

2.6 Conclusions

The NOTS project, in conjunction with a detailed literature review, has demonstrated the severe difficulties in achieving optimised joint geometries in bonded tubular truss structures. These tend to favour a single-lap joint configuration, particularly when using a composite node, which offers the least-weight design solution and the potential to reduce the residual stress problems associated with bonding composite tubes to metallic end fittings. Whilst the high peel and shear stress concentrations at the ends of the joint overlap can be alleviated using design features such as tapered adherends and adhesive fillets, these are difficult to manufacture to a consistent standard. This is particularly apparent at the innermost end of a tubular nodal joint, which is difficult to access and impossible to visually inspect. Therefore, failure modelling and analysis of fully composite nodal joints is likely to require the assumption of a square-edged joint to ensure a conservative design approach.

Fatigue failure in such joints tends to initiate at the end of the joint overlap, where maximum shear and peel stress concentrations occur, before propagating either along the bond-line (in an interfacial or cohesive manner) or through delamination in the adherends. Therefore, in developing a mechanistic fatigue modelling capability, focus should be placed on these failure mechanisms. In the case of the NOTS project, fibre-tow failure was also evident but it is believed that this could be avoided through improved design and manufacture. Due to the brittle nature of composite resins, failure predominantly occurs in an instantaneous manner with no stable crack propagation phase, particularly in the case of co-bonded joints. This necessitates a no-growth design philosophy, where fatigue stress levels remain sufficiently low to ensure that a crack will not propagate during the in-service

lifetime of the structure. This requires an analysis of both the potential size and most critical location of the assumed starter-crack. Size is generally determined either by potential manufacturing defects or damage resulting from in-service impact. For example, bond-line voids, such as those evident in the co-bonded NOTS joints can act as starter cracks. Evaluating their potential size is highly dependent on the resolution of NDT techniques used for quality assurance. For a square-edged single lap joint, the most critical crack location is at the end of the joint overlap, where the maximum shear and peel stress concentrations occur. Therefore, it may be necessary to insert a starter crack at the end of the joint overlap, when evaluating the fatigue life of such designs.

Despite the limitations discussed above, future design and manufacturing developments are likely to give potential for a more stable failure process. For example, the development of 3-D woven fabrics to resist delamination in composite adherends will favour bond-line failure and in the case of secondary bonding, this can be designed to occur in a stable manner using a ductile adhesive. Therefore, as well as allowing for a no-growth design philosophy, the fatigue model should also give potential to predict crack growth rates, enabling a damage-tolerant design approach. Such an approach will be further promoted by the development of structural health monitoring systems, using techniques such as acoustic emission, to detect and monitor crack growth during the in-service life of the structure. The remainder of this thesis describes the work undertaken in developing a predictive fatigue modelling capability to address the needs outlined.

3. Fatigue Model Requirements and Selection of a Cohesive Zone Approach

As highlighted in chapter 1, mechanistic fatigue models are those which describe damage accumulation in direct relation to specific failure processes (e.g. transverse matrix cracks, delamination), hence providing the following advantages over Constant-Life and Residual Strength/Stiffness models:

i) The models can be calibrated using data from small scale coupon tests and then directly applied at a structural level.

ii) The ability to model crack initiation and growth enables a more accurate prediction of a structure's safe remaining lifetime, allowing for reduced design margins and a more optimised solution. For example, potential exists to apply a damage tolerant design philosophy whereby, once initial damage is detected, the remaining safe lifetime can be calculated and an appropriate inspection interval scheduled.

The previous chapter has shown that for bonded composite joints, cracks will generally form at the ends of the joint overlap, where the highest stress concentrations exist, before propagating either along the bond-line or between plies. For complex geometries, difficulties in ensuring defect free manufacture and precise adhesive fillet geometries mean that the crack initiation phase is highly variable and can be extremely short. To ensure a conservative fatigue life analysis, this necessitates the assumption of an initial defect/crack at a critical location, which is generally where maximum stress concentrations exist. Therefore, focus is placed on developing a predictive modelling technique for the crack propagation phase, which for adhesive joints, is defined as shown in Figure 3.1.

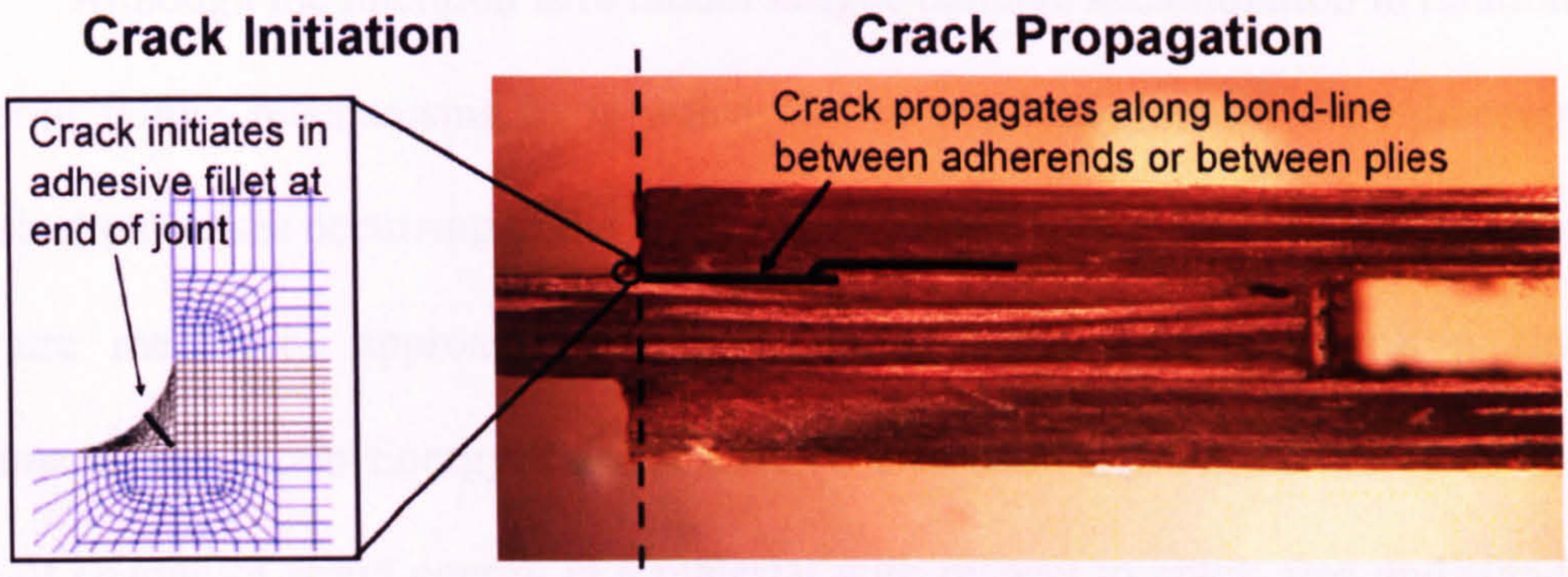

Figure 3.1: Distinction between initiation and propagation in adhesive joints

Although only the most basic 2-D case is shown above, the model must be applicable to the complex 3-D geometries typically found in structural joints. The stresses in such geometries can only be accurately analysed using numerical techniques. Hence, there are two key stages in developing the required modelling tool; identifying an appropriate crack growth model and then integrating this with a numerical code, which is discussed in sections 3.1 and 3.2 respectively.

3.1 The Application of Fracture Mechanics to Analyse Fatigue Crack Growth

A crack can propagate via 3 separate crack extension modes; opening (mode I), forward-shear (mode II) and parallel-shear (mode III), as shown in Figure 3.2. Unless significant torsion is present, it will generally be subjected to a mixture of mode I opening and mode II in-plane shear loading.

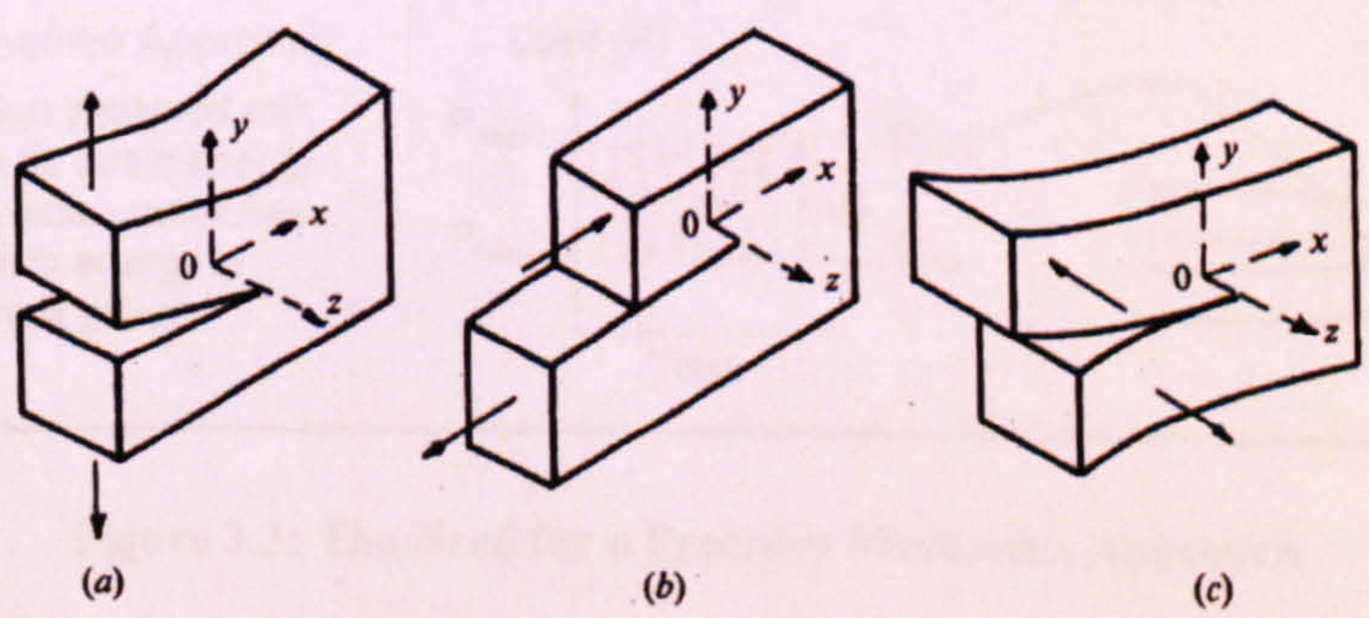

Figure 3.2: Mode I (a), Mode II (b) and Mode III (c) Crack Extension[32]

Although the intention is to model fatigue damage accumulation in relation to specific failure mechanisms, it is unfeasible to explicitly model the microscopic physical processes occurring at the crack tip. For this reason, it is common to adopt a fracture mechanics approach and to associate these processes with a single parameter, the Strain Energy Release Rate (G), as shown in Figure 3.3. This is the rate of change of strain energy in a material with respect to crack area and standard methods for calculating this parameter, using both experimental data and numerical methods are detailed in sections 3.1.1 and 3.2.1 respectively. Under fatigue loading, we are interested in both the maximum strain energy release rate in each cycle, G_{max}, and the variation in strain energy release rate between the peak and trough of each cycle, ΔG, given by:

$$\Delta G = G_{max} - G_{min} \qquad \text{(Eqn. 3.1)}$$

where G_{min} is the minimum strain energy release rate in each cycle.

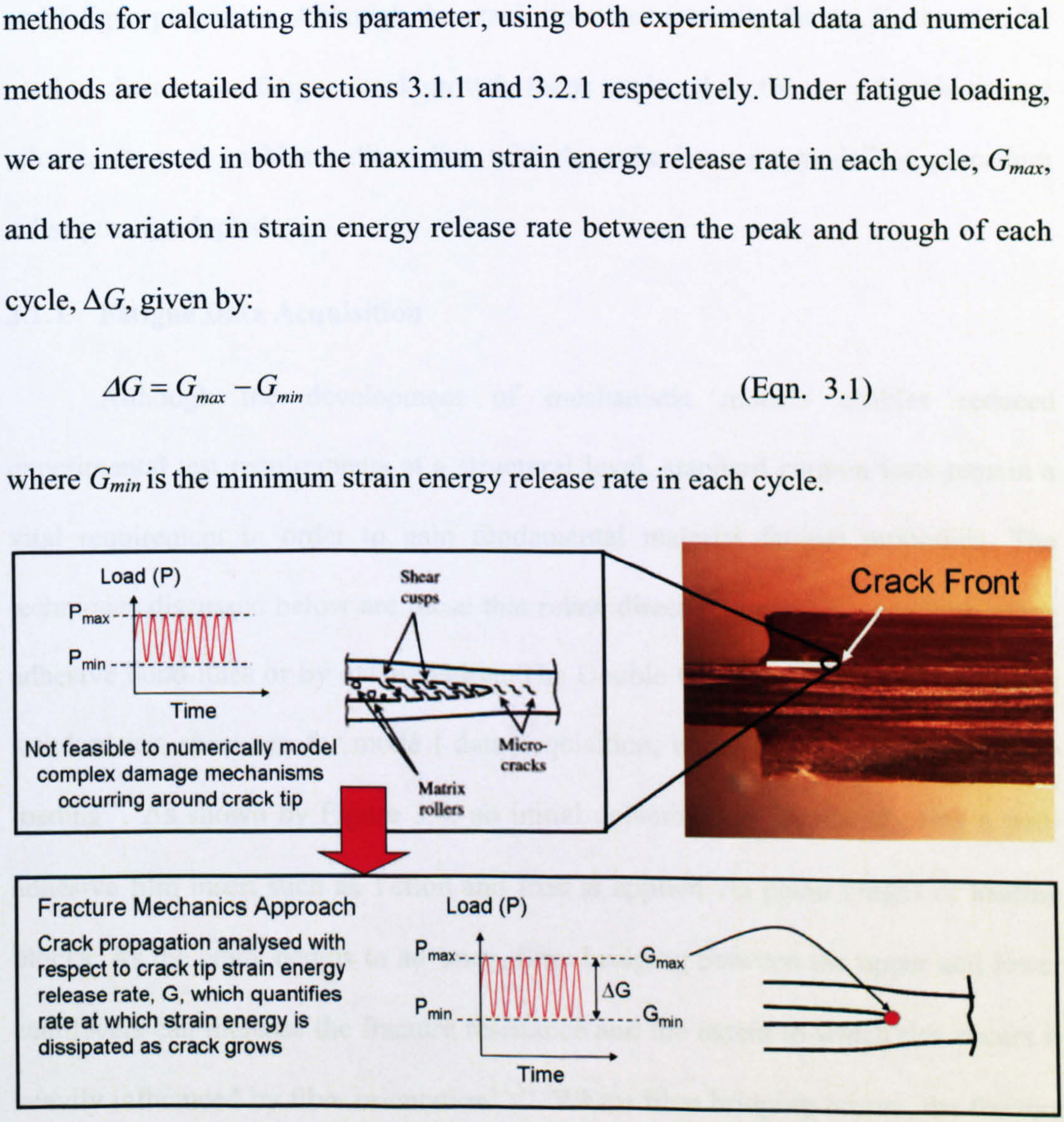

Figure 3.3: The Need for a Fracture Mechanics Approach

The strain energy release rate can be split into separate mode I and mode II components and the ratio of these has a significant influence on the rate of crack growth. Before examining methods used to characterise crack growth rate, a brief overview is provided of the experimental techniques available to gain strain energy release rate and crack growth rate data under mode I, mode II and mixed mode loading. Common specimens are used both for gaining static fracture toughness data and fatigue properties. Although the crack tip stress intensity factor, K, can also be used to characterise fatigue crack growth, focus is placed on the use of strain energy release rate as it enables a direct link with the cohesive zone modelling procedure subsequently adopted.

3.1.1 Fatigue Data Acquisition

Although the development of mechanistic models enables reduced experimental test requirements at a structural level, standard coupon tests remain a vital requirement in order to gain fundamental material fatigue properties. The techniques discussed below are those that relate directly to crack propagation along adhesive bond-lines or by delamination. The Double Cantilever Beam (DCB) is the standard test specimen for mode I data acquisition, under both static[33] and fatigue loading[34]. As shown by Figure 3.4, an initial delamination is created using a non-adhesive film insert such as Teflon and load is applied via piano hinges or loading blocks. As the crack begins to advance, fibre bridging between the upper and lower cantilevers can increase the fracture resistance and the extent to which this occurs is heavily influenced by fibre orientation[33,34]. Where fibre bridging occurs, the fracture toughness recorded at initial crack advance, before fibre bridging becomes significant, should be used for conservative results in a predictive model. Care must also be taken in selecting an appropriate film to generate the initial delamination, as

the precise crack geometry can significantly affect the measured fracture toughness value[35]. These considerations are equally important for the mode II and mixed mode tests. In composites with significant through-thickness reinforcement, modified versions of the standard test method, such as the addition of doubler plates, are necessary in order to extract fracture toughness properties before failure of the specimen arms[36,37].

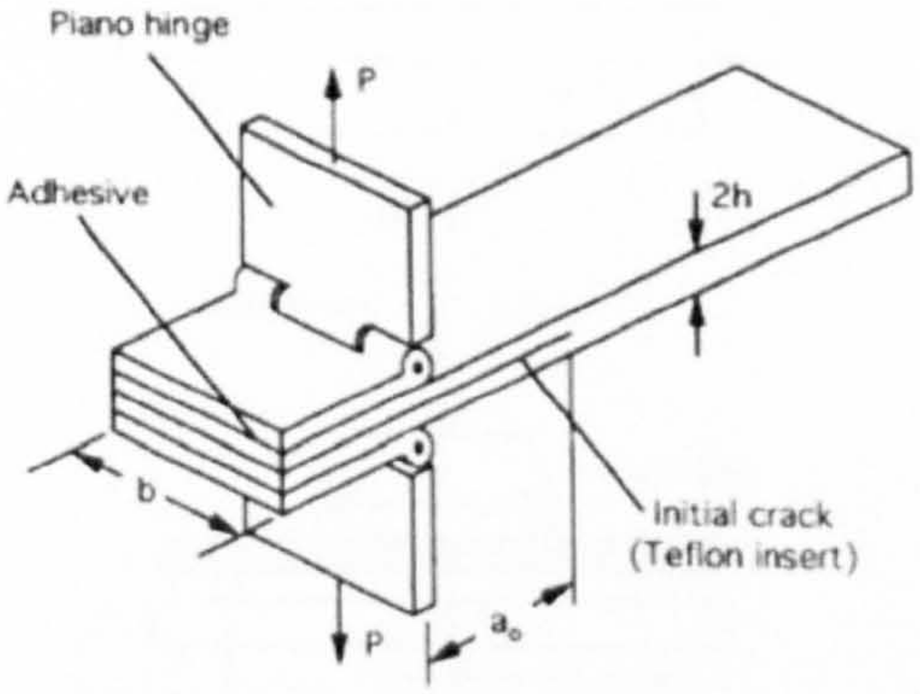

Figure 3.4: The Mode I DCB[33]

For mode II loading, a standard is yet to be specified and a variety of specimens are used, including the End Loaded Split (ELS)[38], the 3 point End Notched Flexure (ENF) and 4 point ENF[37] (see Figure 3.5). The 4 point ENF is becoming increasingly common because unlike the ELS and 3 point ENF, crack growth is stable under displacement control[39].

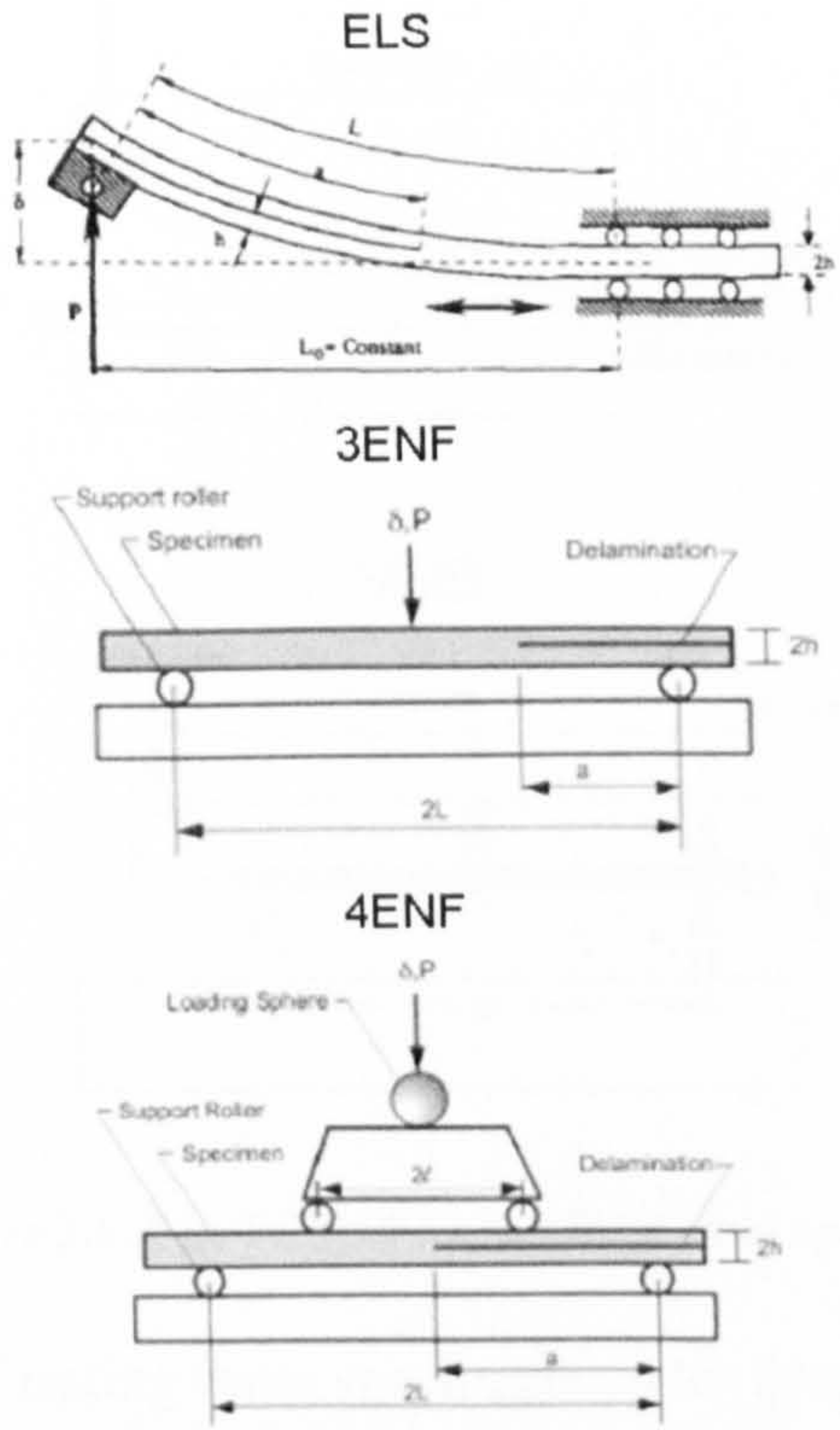

Figure 3.5: The Mode II ELS[38], 3ENF and 4ENF[37] specimens

For mixed mode testing, options include the Fixed Ratio Mixed Mode specimen[38] and Mixed Mode Bending (MMB) test, now an ASTM standard[40] (see Figure 3.6). Although the FRMM can produce a variety of mode-ratios, this relies on changing the relative thickness of the upper and lower cantilevers[38]. The MMB has become the most commonly used specimen as it combines the loading methods of the DCB and 3ENF tests and means that a single set of test apparatus and specimen geometry can be used to generate data for all pure and mixed-mode load conditions[40].

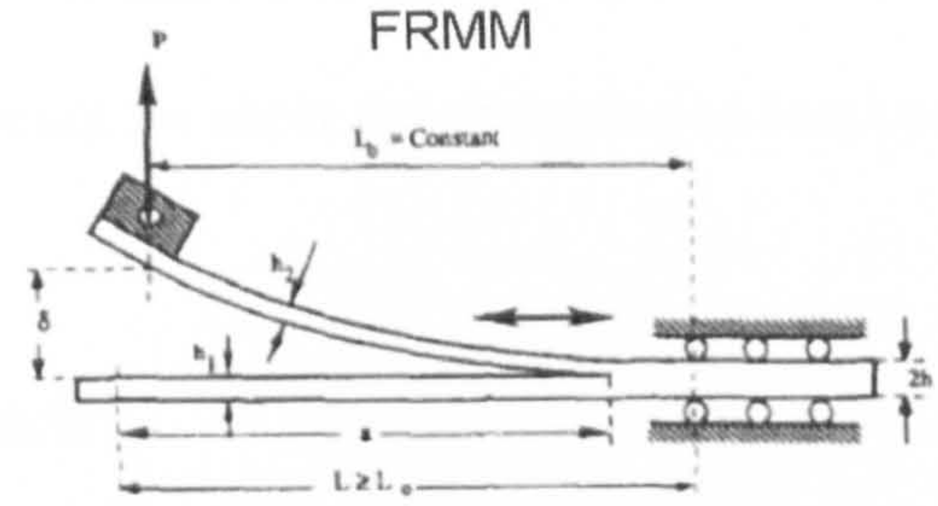

Figure 3.6: The FRMM[38] and MMB[37] test specimen

The objective of testing these specimens under fatigue loading is generally to acquire a plot of crack growth rate against strain energy release rate. For this to be achieved, fatigue loading is usually applied under displacement control, allowing a complete crack growth rate curve to be gained from each specimen tested[10]. Crack extension can be measured either manually (e.g. with an instrumented travelling microscope[41]), or by measuring the electrical resistance of a metallic foil bonded to the side of the specimen and designed to tear coincidentally with the crack[42].

Various analysis methods can be applied to convert load/displacement data to strain energy release rate[33,37,43], all of which can be related back to the following equation:

$$G = \frac{P^2}{2b}\frac{dC}{da} = \frac{P}{2b}\frac{d\delta}{da}\bigg|_{P=constant} \qquad \text{(Eqn. 3.2)}$$

where P is the applied load, δ is the displacement at the point of load application, b is the specimen width and C is the specimen compliance. Specimen compliance is

either measured directly, or calculated using simple beam theory, with a crack length correction factor to account for shear deformation and local deformations around the crack tip[37].

3.1.2 Paris Law Models

For specimens or structures containing initial cracks and subject to fatigue loading, two questions must be addressed:

i) Is the maximum strain energy release rate in each fatigue cycle sufficient for the crack to grow?

ii) If so, at what rate will the crack grow?

Crack growth is commonly represented using a plot of G_{max} or ΔG against cyclic crack growth rate (da/dN) data. When plotted on a log-log scale, this data generally exhibits the trend shown in Figure 3.7, where the fatigue crack growth rate can be split into 3 distinct regions; a threshold region, a linear region and an unstable region. The two extremes of the trendline correspond with the threshold strain energy release rate, G_{th}, below which no crack growth occurs and the fracture toughness, G_C, at which instantaneous, unstable crack growth occurs.

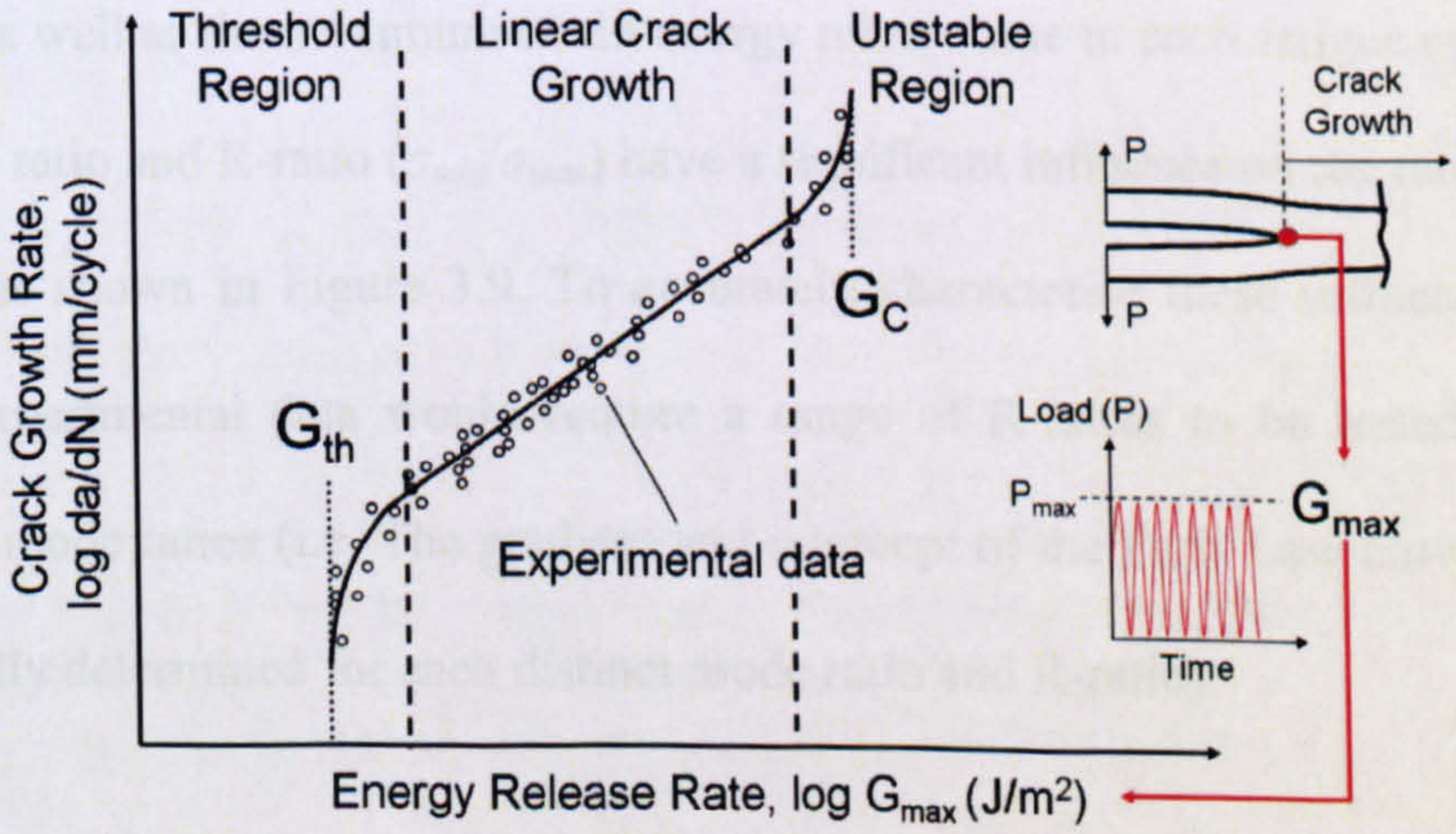

Figure 3.7: Typical fatigue crack growth rate curve

Although models have been developed to represent the threshold and unstable regions[44], it is common to neglect these two extremes of the curve and to characterise the whole data-set using the linear Paris-Law (see Figure 3.8), where strain energy release rate is expressed in terms of either G_{max} or ΔG:

$$\frac{\partial a}{\partial N} = C G_{max}^{\ m} \qquad \text{(Eqn. 3.3)}$$

$$\frac{\partial a}{\partial N} = C \Delta G^{m} \qquad \text{(Eqn. 3.4)}$$

C and m are constants determined by fitting the Paris-law to the experimental data.

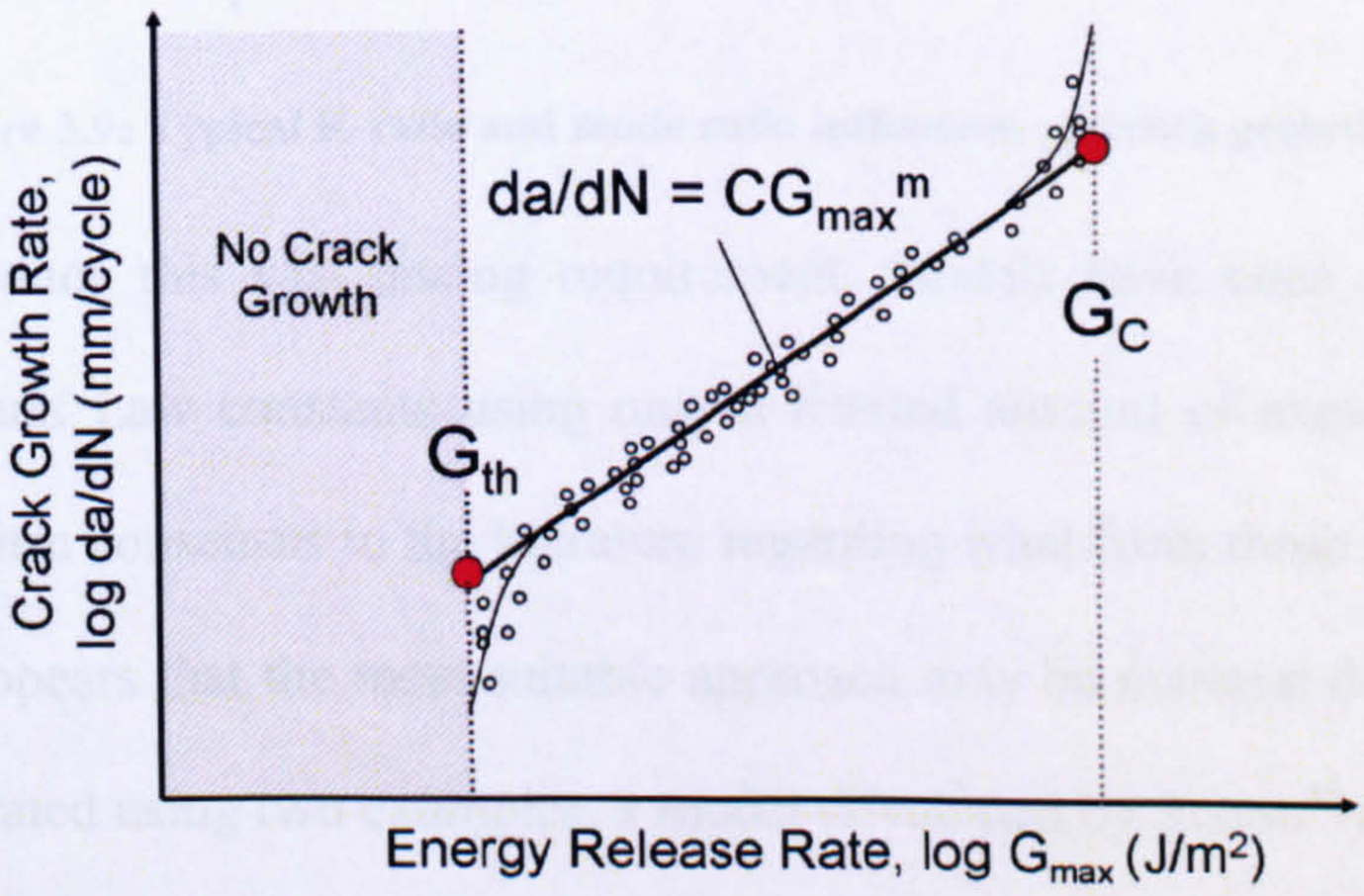

Figure 3.8: The Paris Law Curve

As well as the maximum strain energy release rate in each fatigue cycle, both the mode ratio and R-ratio ($\sigma_{min}/\sigma_{max}$) have a significant influence on the rate of crack growth, as shown in Figure 3.9. To accurately characterise these influences using purely experimental data would require a range of R-ratios to be tested at many different mode ratios (i.e. The gradient and intercept of the Paris Law curve must be empirically determined for each distinct mode ratio and R-ratio).

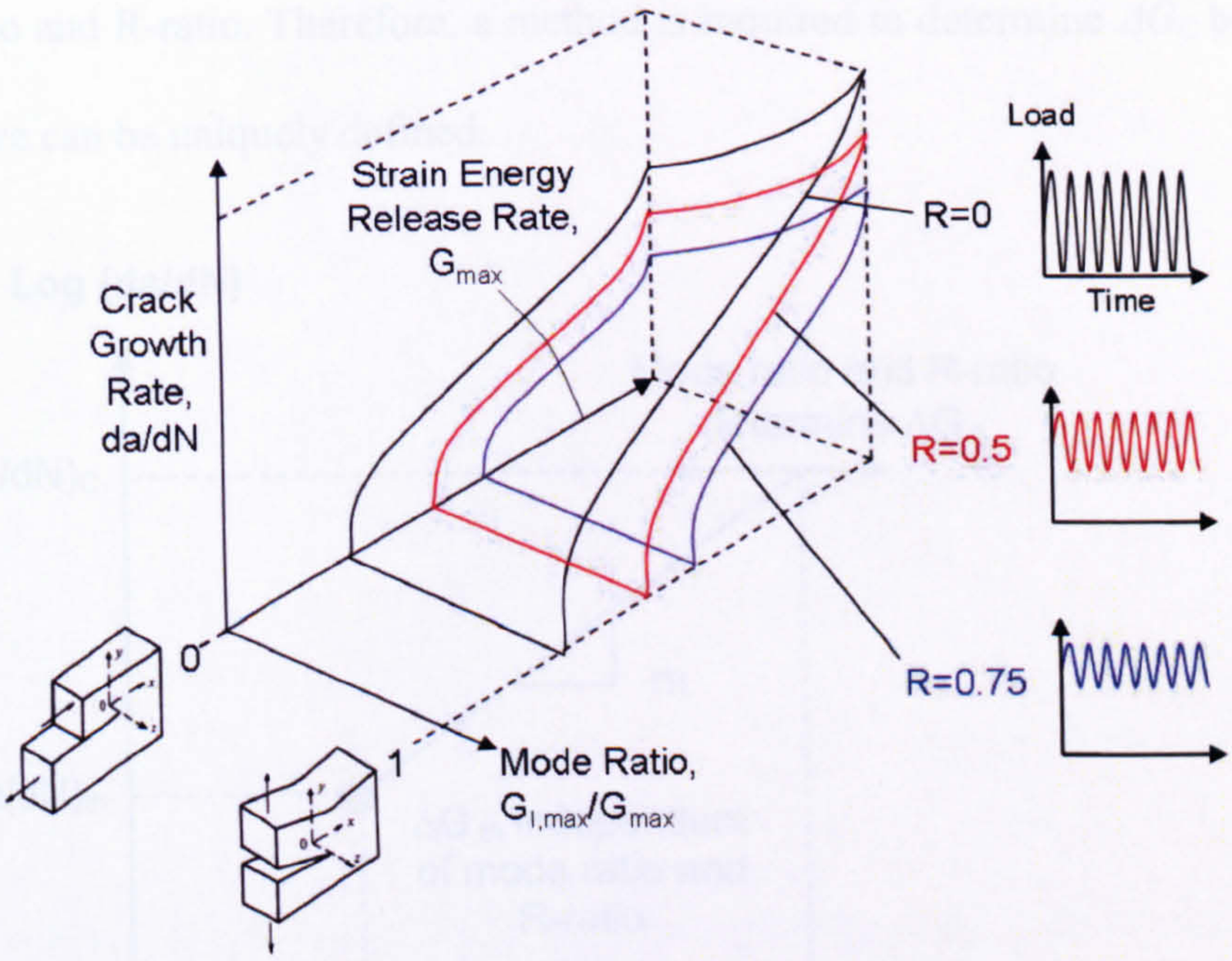

Figure 3.9: Typical R-ratio and mode ratio influences on crack growth rate

To reduce this vast testing requirement, models have been developed for predicting Paris Law constants using only a limited amount of experimental data. There is no firm consensus in the literature regarding what form these models should take and it appears that the most suitable approach may be material dependent. This is now illustrated using two examples, a model developed by Schon[45] and another by Blanco et al.[46], both of which are based on the Paris Law relationship (equations (3.3) and (3.4)), but use very different assumptions to calculate the coefficient, C, and exponent, m.

The fatigue delamination model developed by Schon[45] requires only 5 experimental parameters, which are gained from pure mode I and mode II fatigue tests. Schon refers to experimental evidence suggesting that cracks begin to propagate at a value of ΔG, which is independent of both R-ratio and mode ratio. This provides a single fixed point on the Paris curve, ΔG_{th}, as shown in Figure 3.10. The value of ΔG at which unstable crack growth occurs, ΔG_C, is dependent on both

mode ratio and R-ratio. Therefore, a method is required to determine ΔG_C before the Paris curve can be uniquely defined.

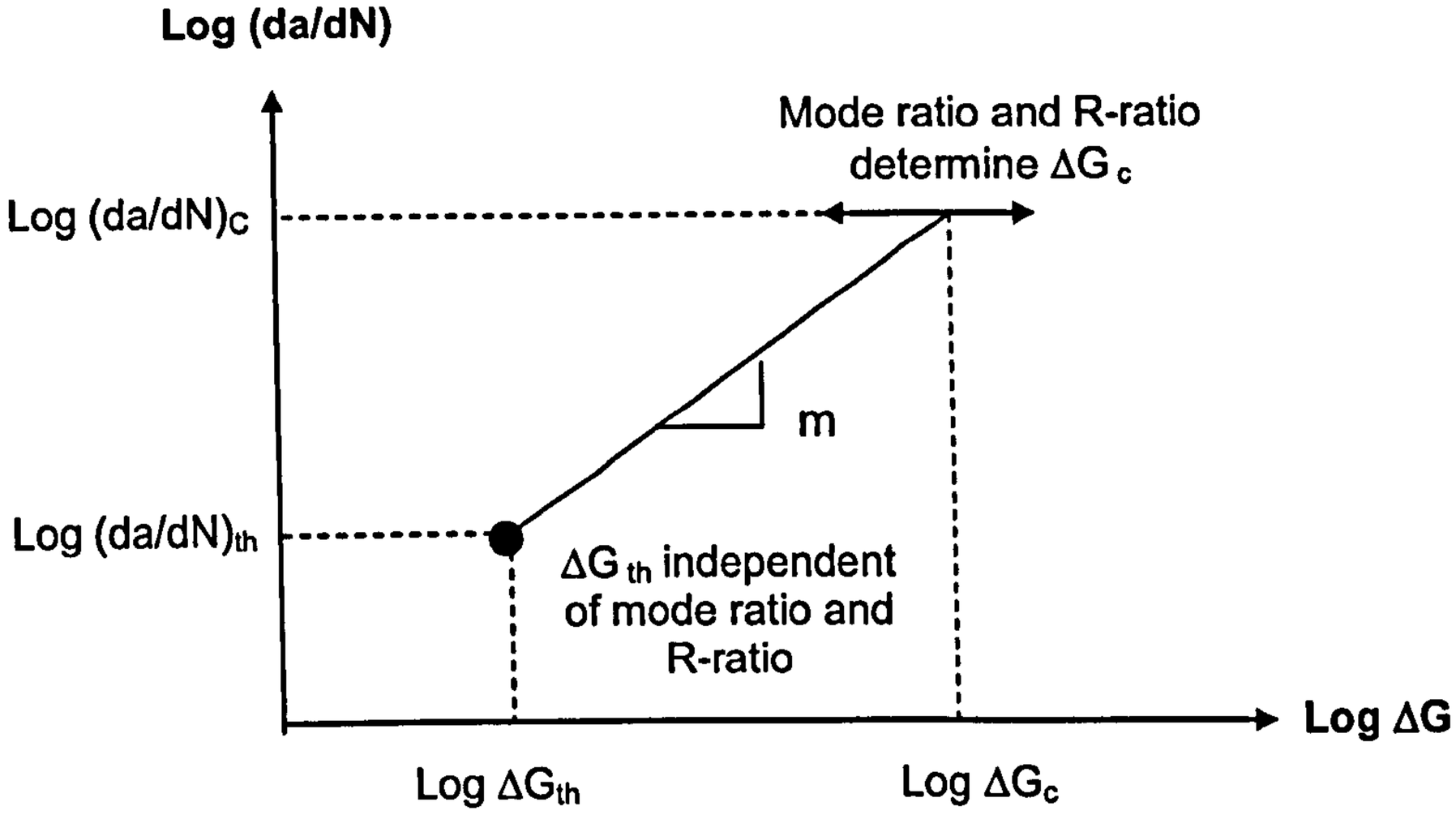

Figure 3.10: Paris-law plot highlighting that ΔG_{th} is independent of mode ratio and R-ratio, whilst ΔG_C is dependent on both of these parameters

In order to generate another fixed point on the Paris curve, Schon uses experimental evidence suggesting that the strain energy release rate value at which unstable crack propagation occurs, G_C, is dependent on mode ratio but independent of R-ratio. This enables use of a static failure criterion, based on strain energy release rate, to determine G_C. Schon uses a linear failure criterion of the form:

$$G = G_C \text{ when: } \frac{G_I}{G_{IC}} + \frac{G_{II}}{G_{IIC}} = 1 \qquad \text{(Eqn. 3.5)}$$

Assuming tension-tension fatigue loading (i.e. positive R-ratio), G_C can be converted to ΔG_C using the cyclic load's R-ratio, R[45]:

$$\Delta G_C = G_C(1 - R^2) \qquad \text{(Eqn. 3.6)}$$

There are now two fixed points available on the plot of *da/dN* against ΔG and these can be used to calculate the Paris Law coefficient, *C,* and exponent, *m,* in equation (3.4).

$$m = \frac{log\left[\left(\frac{da}{dN}\right)_c\right] - log\left[\left(\frac{da}{dN}\right)_{th}\right]}{log[\Delta G_c] - log[G_{th}]} \qquad \text{(Eqn. 3.7)}$$

$$C = \frac{\left(\frac{da}{dN}\right)_{th}}{(\Delta G_{th})^m} \qquad \text{(Eqn. 3.8)}$$

To apply Schon's technique, only the parameters GI_C, GII_C, $(da/dN)_C$, ΔG_{th} and $(da/dN)_{th}$ must be empirically determined. This means that only pure mode I and mode II fatigue tests are required to generate a Paris Law curve for any given mode-ratio and R-ratio.

Blanco *et al.*[46] have recently developed a new Paris Law model requiring at least one set of mixed mode data, in addition to pure mode I and mode II data. The need for mixed mode data was motivated by experimental evidence for HTA/6376C showing that as mode ratio varies from pure mode I to pure mode II, the Paris Law exponent, *m*, initially increases before reaching a mode ratio of approximately 50%, at which point it begins to decrease. For the Paris Law coefficient, *C*, the opposite trend was found to be true, as shown in Figure 3.11. These findings contradict the assumption made in many other Paris Law models, including Schon's, that a continuously increasing/decreasing variation in *C* and *m* occur between pure mode I and mode II loading. Blanco *et al.* compared their model with a range of other models proposed in the literature for calculating Paris Law parameters at any given mode ratio and found it gave significantly improved accuracy.

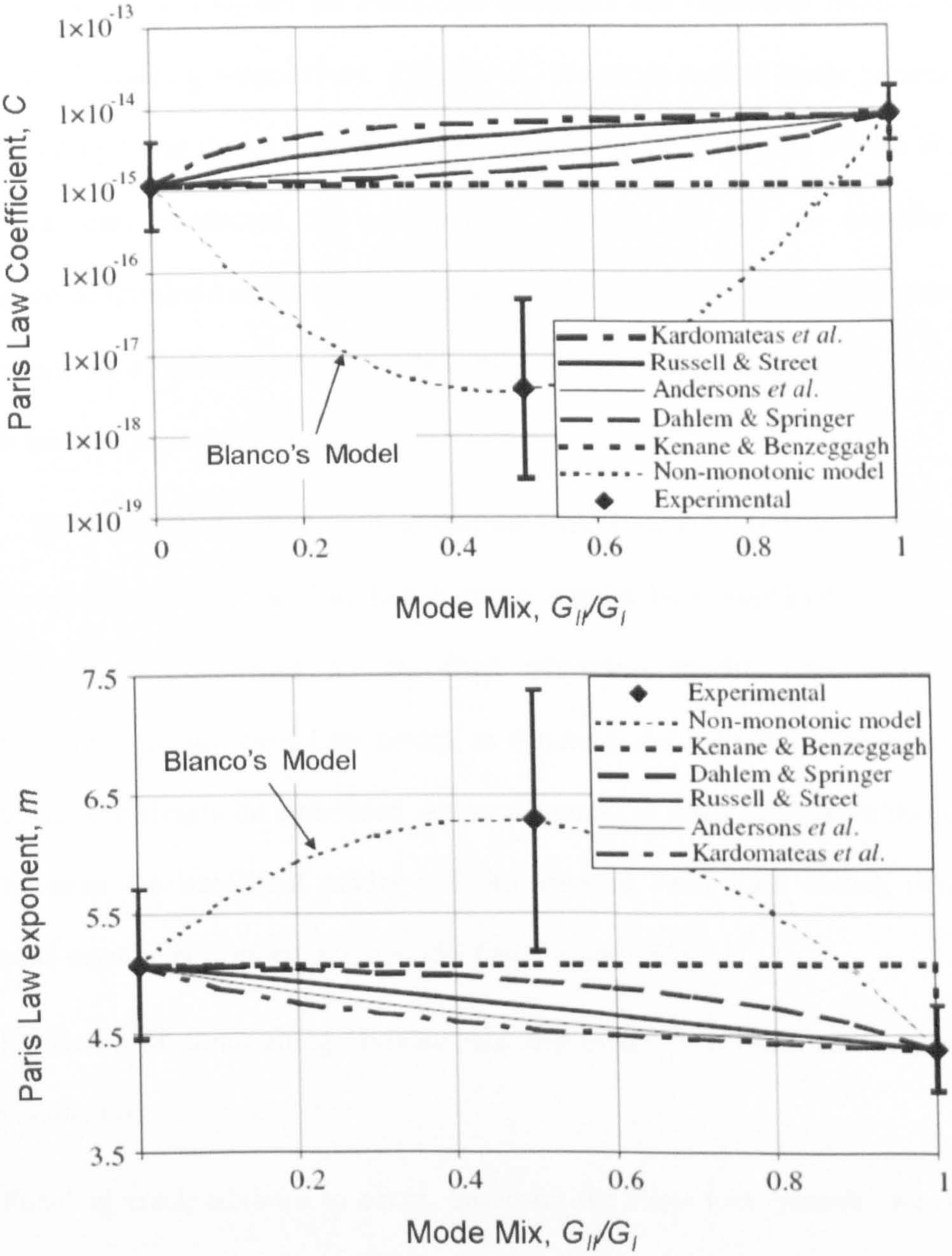

Figure 3.11: Variation in Paris Law Constants for HTA/6376C[46]

Using Blanco's model, the Paris Law constants, C and m, are given by:

$$\log C = \log C_I + \left(\frac{G_{II}}{G}\right)\log C_m + \left(\frac{G_{II}}{G}\right)^2 \log \frac{C_{II}}{C_m C_I} \qquad \text{(Eqn. 3.9)}$$

$$m = m_I + m_m\left(\frac{G_{II}}{G}\right) + (m_{II} - m_I - m_m)\left(\frac{G_{II}}{G}\right)^2 \qquad \text{(Eqn. 3.10)}$$

where C_I, m_I, C_{II} and m_{II} are the Paris Law constants and exponents under mode I and mode II loading respectively. C_m and m_m are extra mixed mode parameters determined by curve fitting experimental data. It should be noted that Blanco *et al.*'s study was only conducted for one specific R-Ratio and did not consider the evaluation of threshold strain energy release rate. However, it clearly highlights that at least one set of mixed mode test data is vital to ensure that an accurate Paris Law can be gained for all mode ratios.

The purpose of outlining these various Paris Law models is to highlight the importance of providing a clear link between results from standard experimental tests and input parameters for the final numerical model. This will enable compatibility with any Paris Law model, as equations for calculating the Paris Law parameters can simply be embedded within the code. In order to provide this direct link between the numerical model and the selected Paris Law model, two key functions must be performed in the model (see Figure 3.12):

i) Extraction of strain energy release rate and mode ratio from crack tip output parameters.

ii) Enabling crack advance to occur, based on the Paris Law growth rate, whilst monitoring the accumulated number of load cycles.

Potential methods for achieving these aims are examined in the following section.

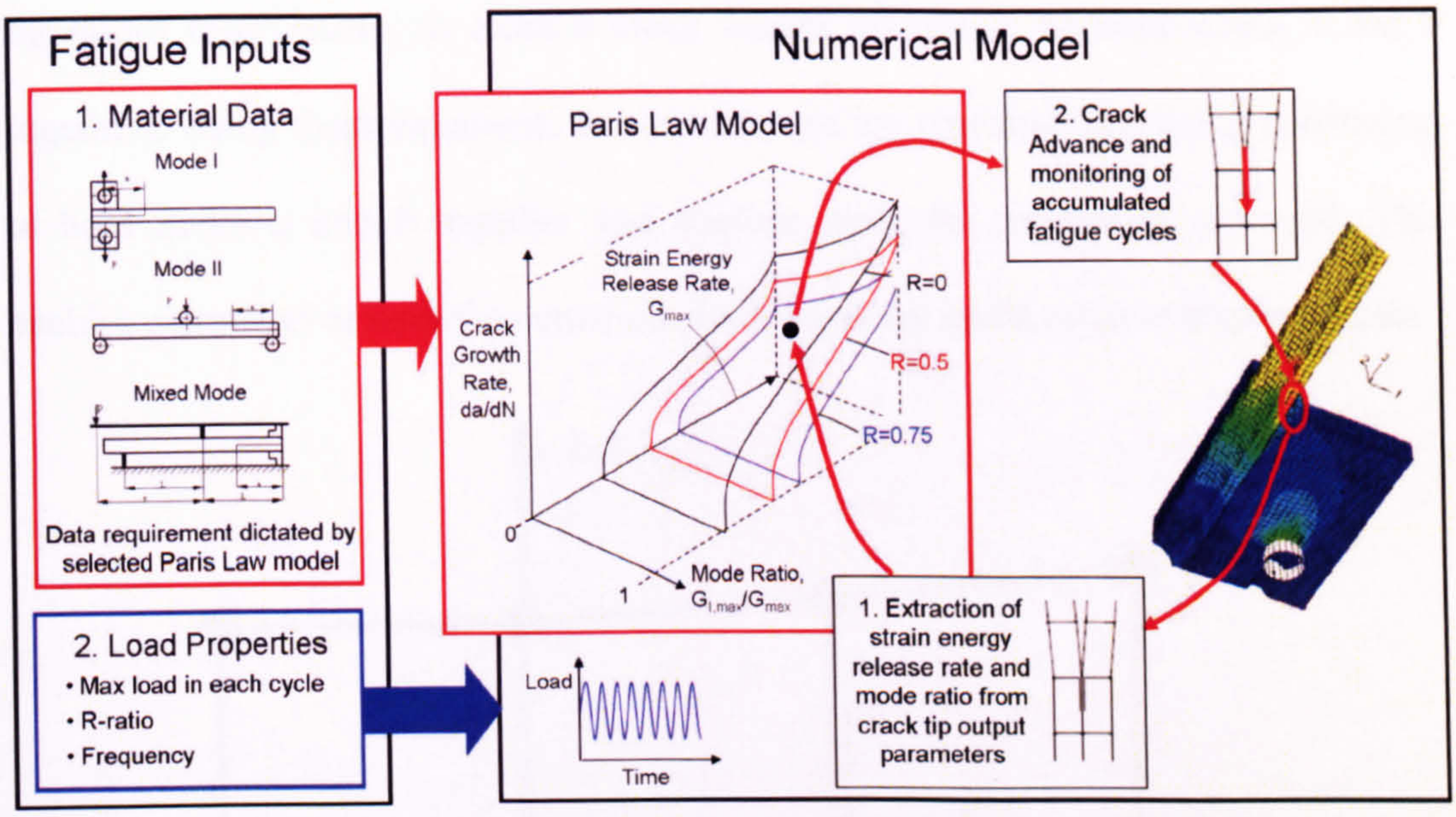

Figure 3.12: Linking the Numerical Model to a Paris Law Model

3.2 Numerical Methods for Analysing Bond-Line Failure and Delamination

3.2.1 The Virtual Crack Closure Technique

The Virtual Crack Closure Technique (VCCT)[47] has become widely used in finite element models for calculating the separate mode I, mode II and mode III strain energy release rate components at a crack tip. It is based on the work done to close the crack and relies on having initially coincident nodes along potential crack growth paths, which can then be released to simulate crack growth. Taking a simple 2-D case involving only mode I and mode II components (see Figure 3.13), G_I and G_{II} are given by:

$$G_I = \frac{F}{2\Delta l}(v_a - v_b) \qquad \text{(Eqn. 3.11)}$$

$$G_{II} = \frac{T}{2\Delta l}(u_a - u_b) \qquad \text{(Eqn. 3.12)}$$

where u and v are displacements in the x and y directions respectively (at nodes a and b, denoted by subscripts), and T and F are the forces required in the x and y

directions respectively, to close a crack length of Δl (i.e. to hold nodes a and b together). Using these equations, two model runs are required; one using constraints to hold nodes *a* and *b* together and another with the constraints removed. This enables extraction of both the constraint forces and the nodal relative displacements.

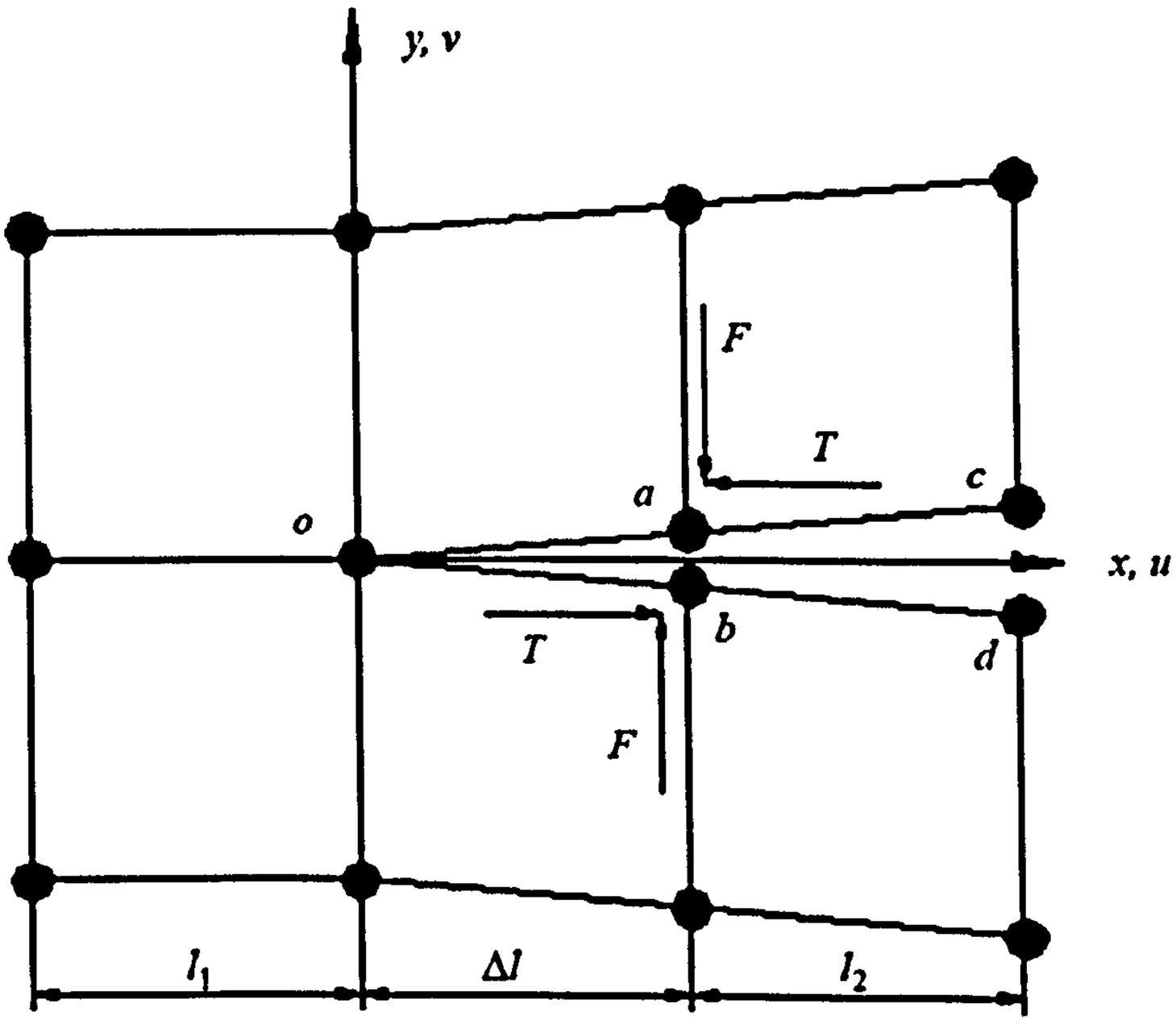

Figure 3.13: The Virtual Crack Closure Technique[48]

The Virtual Crack Closure Technique can be combined with the Paris Law to analyse fatigue crack growth using the following numerical integration procedure:

i) A Finite Element (FE) model of the joint is produced, with an initial crack inserted at the required location, for example, at the edge of the adhesive fillet.

ii) A static analysis of the joint is performed, using the maximum load in each fatigue cycle.

iii) Strain energy release rate and mode ratio are extracted from the model using the Virtual Crack Closure Technique.

iv) The Paris Law is used to calculate the crack propagation rate.

v) The number of fatigue cycles, *dN*, required to advance the crack by a small increment, *da*, is determined, using the relationship $dN = da/(da/dN)$. The crack increment is chosen small enough to ensure convergence of the solution.

vi) The crack length and number of fatigue cycles are updated in the model ($a = a + da$, $N = N + dN$).

vii) Stages (ii) to (vi) are repeated until the strain energy release rate reaches its critical value or the crack reaches its maximum defined limit.

Techniques based on this procedure have been applied by numerous authors to predict the fatigue propagation life of adhesive joints. Abdel-Wahab *et al.*[49] studied double lap and single lap joint specimens under constant amplitude loading. The joints were tested and modelled both with and without adhesive fillets. For joints with adhesive fillets, the predicted fatigue life was found to be very conservative because the crack initiation phase, which formed a large proportion of total fatigue life, was neglected. Hoyt *et al.*[50] applied a similar technique to analyse fatigue crack propagation in a skin-stiffener T-joint and a bonded single lap joint. Quaresimin *et al.*[51] have combined the VCCT for analyzing propagation life with a separate stress based crack initiation model to develop a total fatigue life analysis capability for bonded joints. Deobald *et al.*[52,53] have recently developed a new Virtual Crack Closure based technique, using specialized 'interface elements' placed along potential delamination paths. Due to the very strong links with the Cohesive Zone Modelling approach subsequently described, a full description of this technique is referred to section 3.2.2.

Mesh density must be carefully chosen in both the VCCT procedures detailed above and the Cohesive Zone models subsequently described. Whilst a fine mesh is important for accurate strain energy release rate extraction, potential problems can arise from an oscillating singularity that occurs between bi-material interfaces for very small mesh sizes[54].

3.2.2 Cohesive Zone Modelling using Interface Elements

Cohesive-Zone Models (CZM's) represent the variation in stresses (tractions) acting over the region of a crack known as the process zone, where the surfaces are separating. In finite element analysis, CZM's are implemented using interface elements, which are specialised elements that can simulate both crack initiation and propagation. Over recent years, they have become increasingly used for modelling composites, particularly in relation to delamination[55,56,57,58,59,60,61] and adhesive bond-line failure[62,63,64,65]. In a 3-D model, interface elements can take the form of either discrete elements, placed between initially coincident nodes, or continuum elements assigned with either zero or a very small initial thickness, as shown in Figure 3.14.

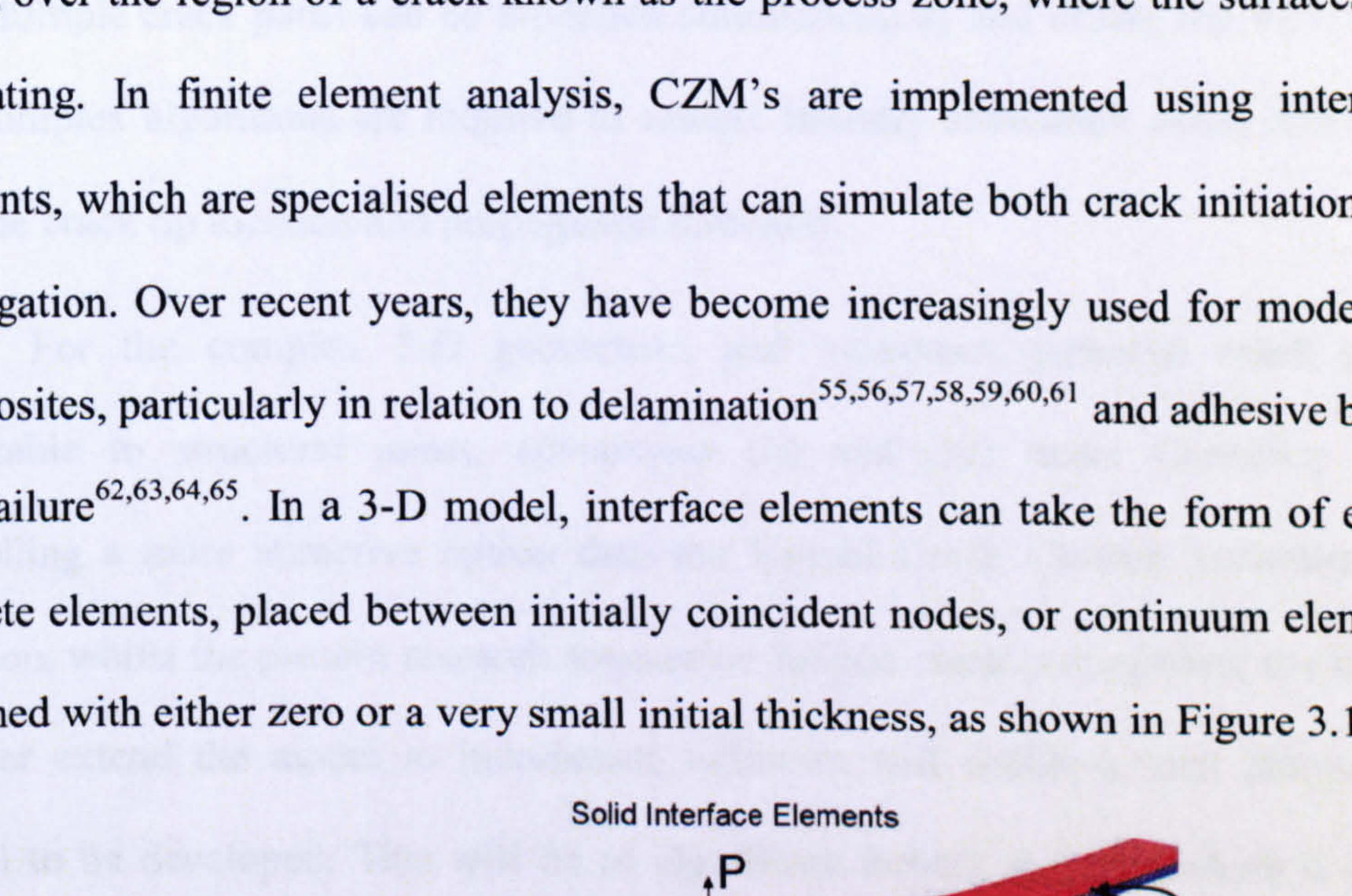

Figure 3.14: Composite Delamination in a DCB using interface elements

Compared with the Virtual Crack Closure Technique, CZM's offer the following advantages:

i) The potential to model both crack initiation and crack propagation in a single coherent simulation.

ii) The direction of crack propagation does not need to be known in advance and cracks have the potential to propagate along any path where interface elements are placed[66].

iii) Multiple crack paths can be modelled simultaneously and unlike the VCCT, no complex algorithms are required to release initially coincident nodes and track the crack tip location and propagation direction.

For the complex 3-D geometries and numerous potential crack paths applicable to structural joints, advantages (ii) and (iii) make Cohesive Zone Modelling a more attractive option than the Virtual Crack Closure Technique. In addition, whilst the present research focuses on fatigue crack propagation, the ability to later extend the model to incorporate initiation will enable a total fatigue life model to be developed. This will be of significant benefit in cases where it is not necessary to assume an initial pre-crack, for example, when a tapered adhesive fillet can be ensured and the initiation stage forms a significant portion of total fatigue life. For these reasons, the present research has focused on the development of a cohesive zone fatigue model. Before describing this in detail, background is provided on the principles behind cohesive zone modelling and current fatigue laws implemented by other authors using interface elements.

An interface element's behaviour is governed by a traction-displacement curve, relating element stress (traction) to mode I (opening) and mode II (shear)

nodal displacements. For simplicity, the current examples relate only to mode I loading but traction-displacement curves for mode II and mixed mode loading will be fully detailed in the following chapter. Although a variety of geometric shapes can be used for the traction-displacement curve[67], a bi-linear form is commonly implemented for modelling composite delamination (see Figure 3.15). This consists of the following main features:

i) An initial elastic region until reaching a maximum stress (σ_{max}), which represents the interfacial strength.

ii) A subsequent softening region until zero stress is reached and element failure occurs.

iii) The total area enclosed by the curve is equal to the fracture toughness of the material.

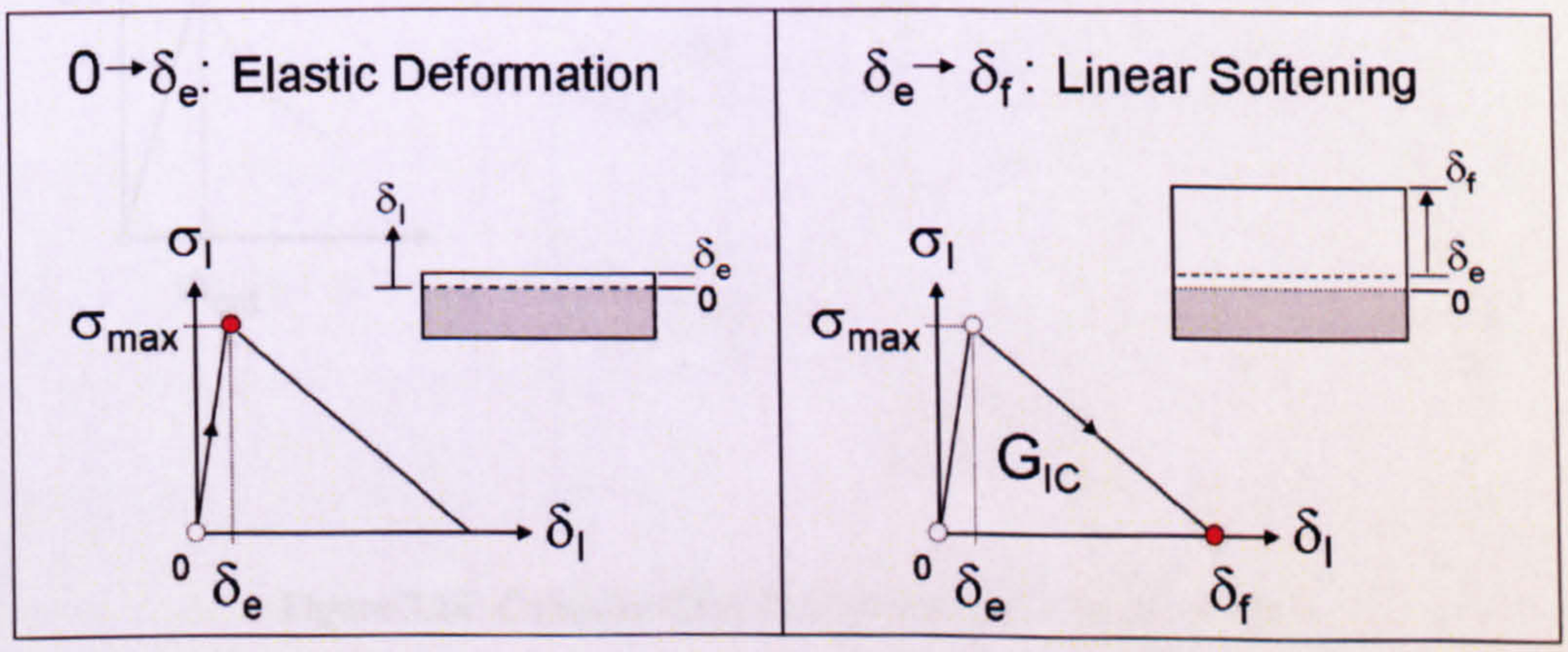

Figure 3.15: Main features of the bi-linear traction-displacement curve for pure mode I loading

Ahead of a numerical crack tip, interface elements within the cohesive zone experience irreversible deformation (i.e. region δ_e-δ_f on the traction-displacement response shown in Figure 3.15). Figure 3.16 illustrates the development of this zone, using the example of a mode I DCB subject to a linearly increasing tip displacement.

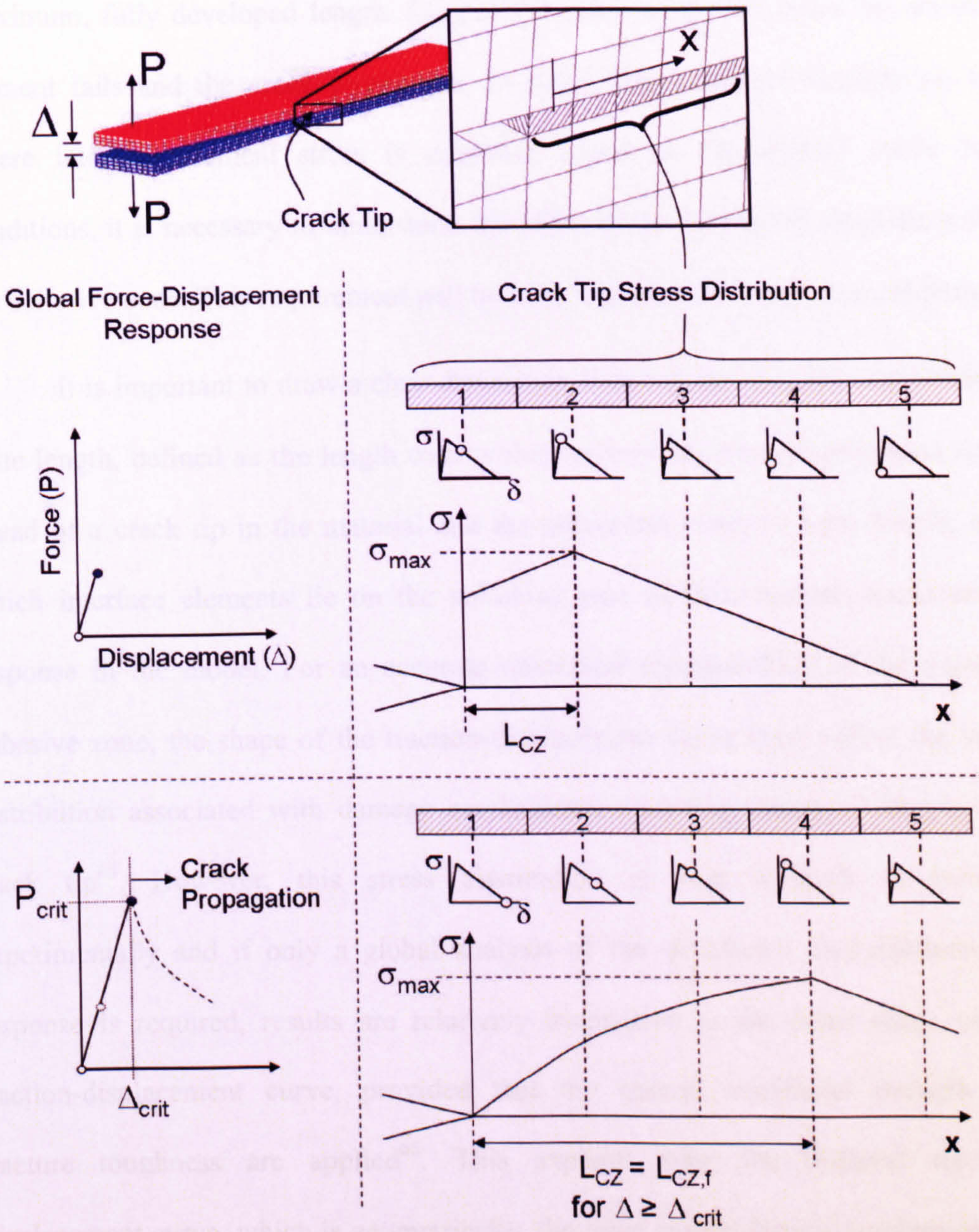

Figure 3.16: Cohesive Zone Development in a mode I DCB

As displacement initially increases, the interface element adjacent to the crack tip rapidly reaches its maximum interfacial strength and moves into the softening region of the traction-displacement response. As tip displacement increases further, adjacent elements also undergo irreversible deformation, allowing a cohesive zone length to be defined, over which stress increases up to the maximum interfacial strength some distance ahead of the crack tip. The cohesive zone reaches its

maximum, fully developed length, $L_{CZ,f}$, at the point where the crack tip interface element fails and the crack propagates. In developing a fatigue degradation law where interface element stress is degraded based on the applied cyclic load conditions, it is necessary to understand the effect of the law on all elements within the cohesive zone. This requirement will be fully addresses in subsequent chapters.

It is important to draw a clear distinction between the true physical cohesive zone length, defined as the length over which irreversible damage processes occur ahead of a crack tip in the material and the numerical cohesive zone length, over which interface elements lie on the softening part of their traction-displacement response in the model. For an accurate numerical representation of the physical cohesive zone, the shape of the traction-displacement curve must reflect the stress distribution associated with damage mechanisms occurring ahead of the physical crack tip[68]. However, this stress distribution is very difficult to measure experimentally and if only a global analysis of the structure's load-displacement response is required, results are relatively insensitive to the exact shape of the traction-displacement curve, provided that the correct interfacial strength and fracture toughness are applied[66]. This explains why the bi-linear traction-displacement curve, which is geometrically, the most simple form to implement, has become commonly used for delamination analyses[59,60,61]. Furthermore, once a crack has initiated in a structure and a cohesive zone exists, results are relatively insensitive to the exact value of interfacial strength and only the fracture toughness value is of critical importance[66]. It should, however, be noted that if significant plastic deformation occurs around the crack tip and a detailed analysis of this region is required, then the shape and interfacial strength of the traction-displacement curve are of increased importance. Shet and Chandra highlighted this by comparing bi-

linear, exponential and trapezoidal curves, demonstrating that the choice of shape significantly influences the plastic zone around the crack tip[68].

Although the majority of interface element studies have focused purely on quasi-static failure cases, several techniques have been developed over recent years to extend their application to fatigue analyses. These generally involve the introduction of a fatigue damage variable into the interface element formulation, which degrades element strength or stiffness based on the number of elapsed cycles. However, there is considerable variation in the damage variable function and the methods used to simulate cyclic loading. A brief overview is now provided to demonstrate potential approaches and challenges faced when implementing fatigue degradation laws in cohesive zone models.

Roe and Siegmund[69] embedded a fatigue degradation law within an exponential form of the interface element traction-displacement curve. As fatigue loading occurs, the accumulated strain within each interface element is monitored on a cycle-by-cycle basis and used to degrade the interface element stiffness until complete element failure occurs, as shown in Figure 3.17.

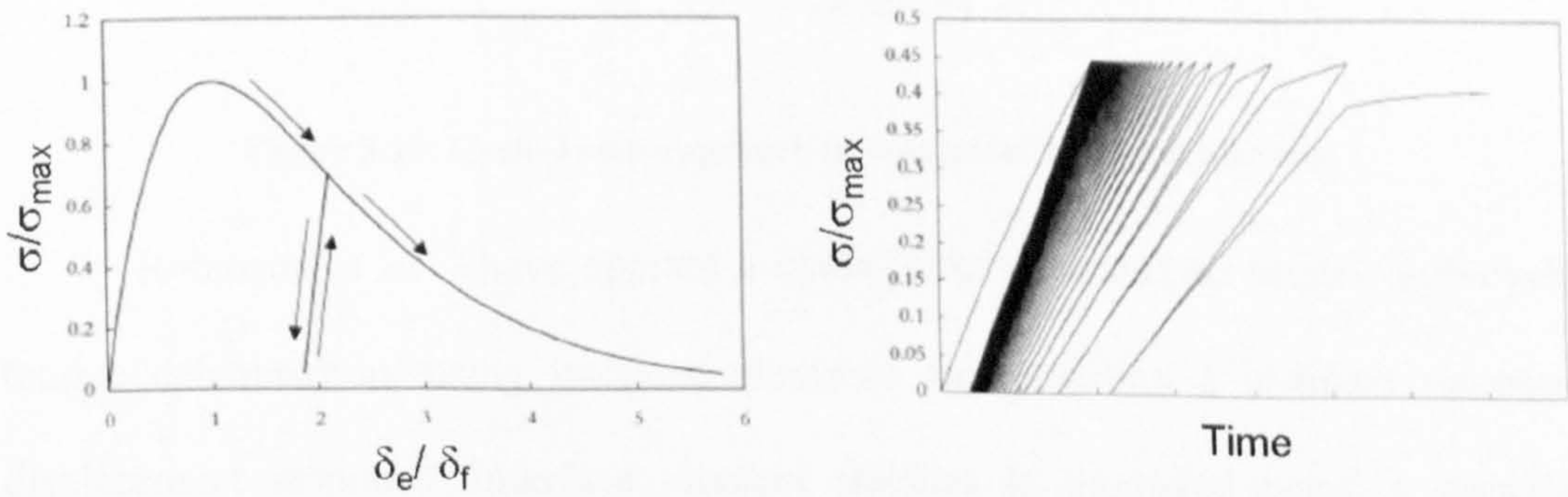

Figure 3.17: Siegmund's exponential traction-displacement curve (left) and the concept of a cycle-by-cycle approach to interface element stiffness degradation (right)[69]

Yang *et al.*[70] and Nguyen *et al.*[71] have also developed cohesive zone fatigue models that enable damage to occur on a cycle-by-cycle basis based on unloading-reloading hysteresis. Whilst tracking loading and unloading of each interface element using a cycle-by-cycle approach enables R-ratio and variable amplitude effects to be accounted for, it imposes a significant computational cost for modelling high cycle fatigue and is likely to be prohibitively expensive in large 3-D models.

This problem can be remedied by adopting a cycle-jump strategy, which relies on maintaining a constant numerical load, whilst implementing a fatigue law that assumes the existence of cyclic loading, as shown in Figure 3.18.

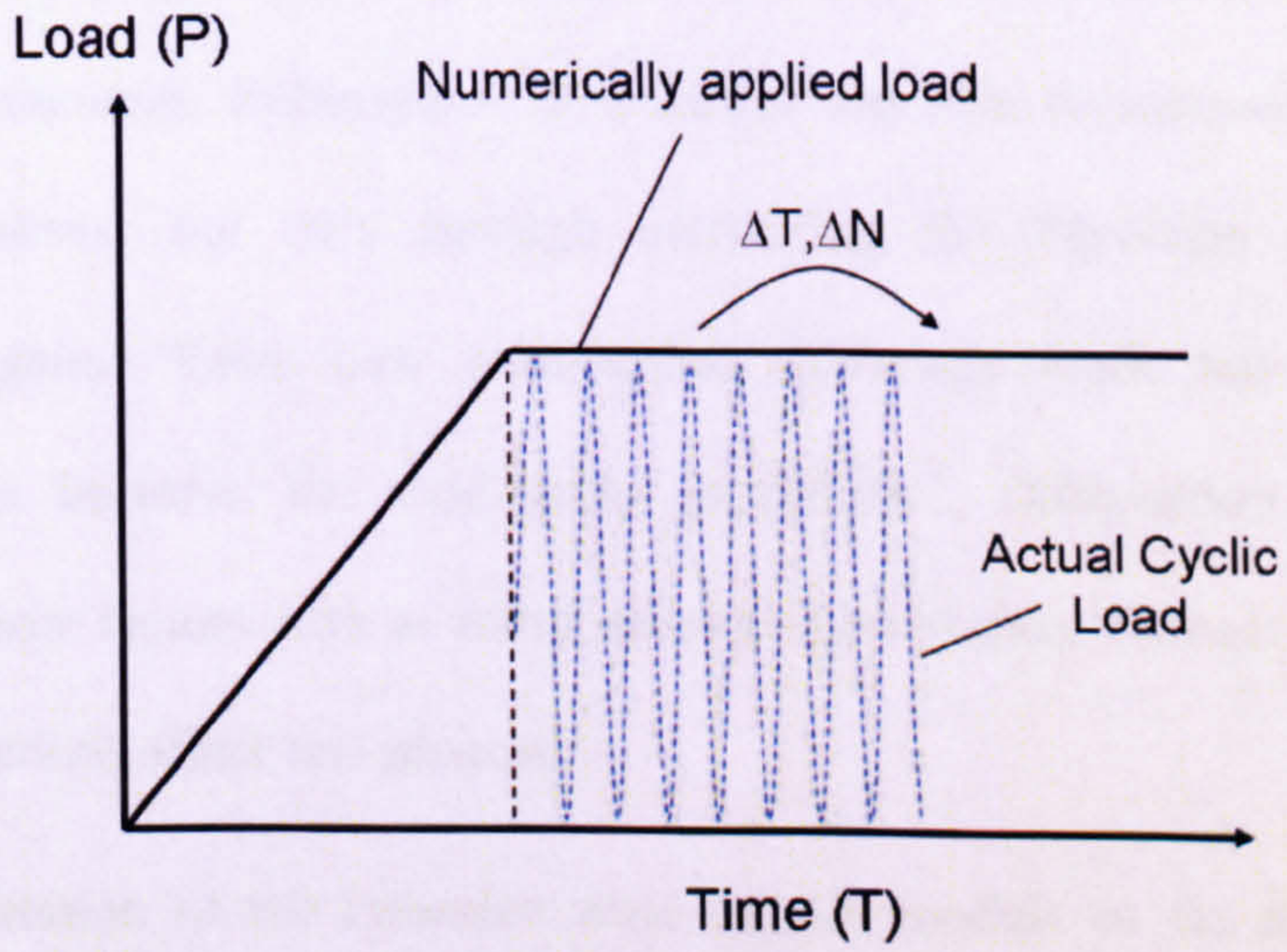

Figure 3.18: Cycle-Jump approach to numerical fatigue modelling

Robinson *et al.*[72] have applied a cycle-jump approach to model high-cycle fatigue delamination, using interface elements incorporating a bi-linear traction-displacement response. Interface element traction is degraded using a damage parameter, D, which includes both a quasi-static and fatigue damage component, as shown in Figure 3.19.

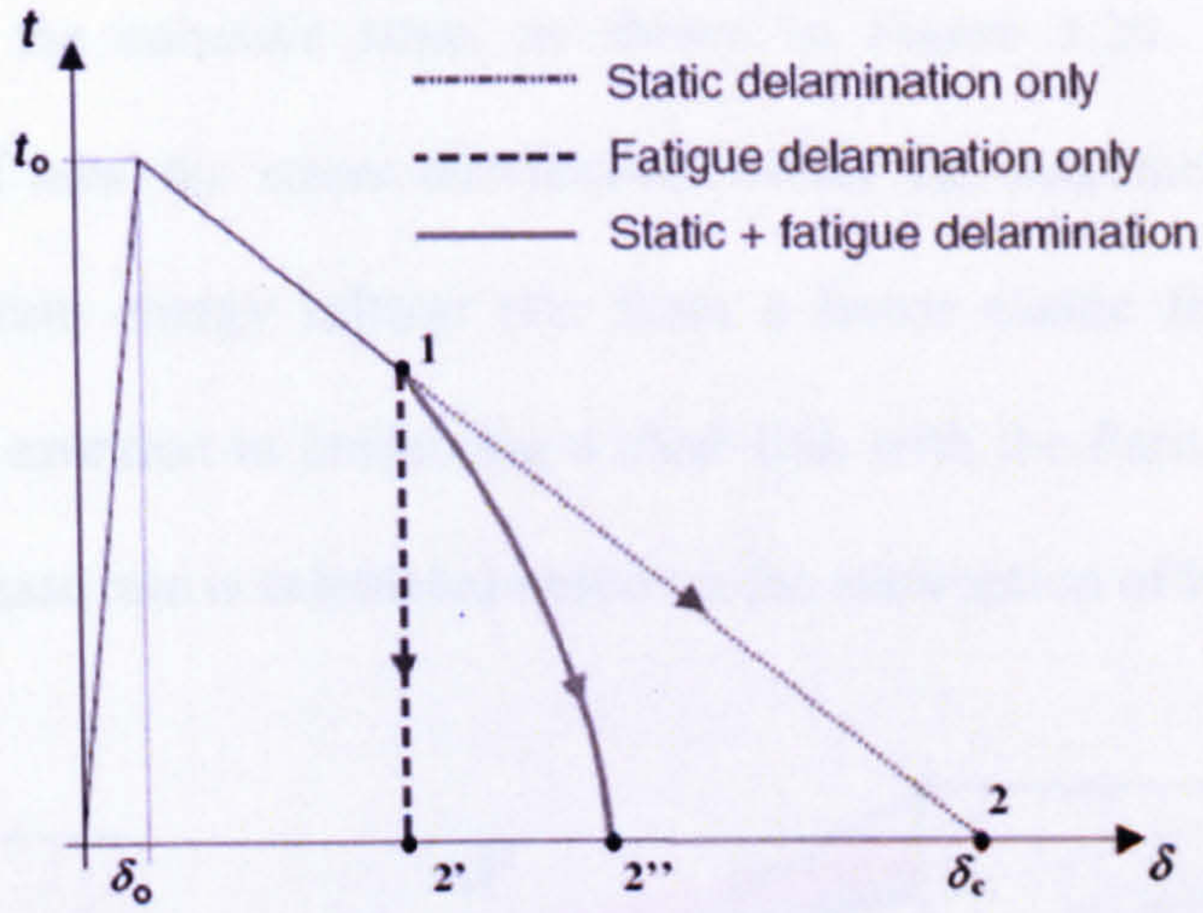

Figure 3.19: Effect of combined static and fatigue damage on the interface element response[72]

The fatigue damage component is calculated based on a fatigue damage model originally proposed by Peerlings *et al.*[73] for use in a continuum damage mechanics framework. Robinson *et al.*'s model was able to successfully reproduce Paris Law curves, but only through calibrating the Peerlings damage model parameters against Paris Law parameters. Although work has recently been undertaken to improve the calibration procedure[74], information has not been provided on how factors such as mesh density and interface element properties (e.g. maximum traction) affect this process.

A limitation of the cohesive zone fatigue models so far discussed is that calibration factors with no clear physical meaning are required in order to reproduce Paris Law crack growth rates. Turon *et al.*[75,76] have recently developed a new fatigue damage law which aims to provide a direct link between model input parameters and the Paris Law. This relies on the ability to calculate the length of the numerical cohesive zone and as highlighted by their studies, further research is required to establish the most appropriate formulae for achieving this. A need also exists to investigate how an accurate value of strain energy release rate can be extracted from

elements within the cohesive zone, as shown in Figure 3.20. This requires an understanding of how the stress distribution within the non-linear cohesive zone relates to the strain energy release rate from a linear elastic fracture mechanics analysis. This is essential in preserving a clear link with the Paris curve, for which strain energy release rate is calculated based on the assumption of linear elasticity.

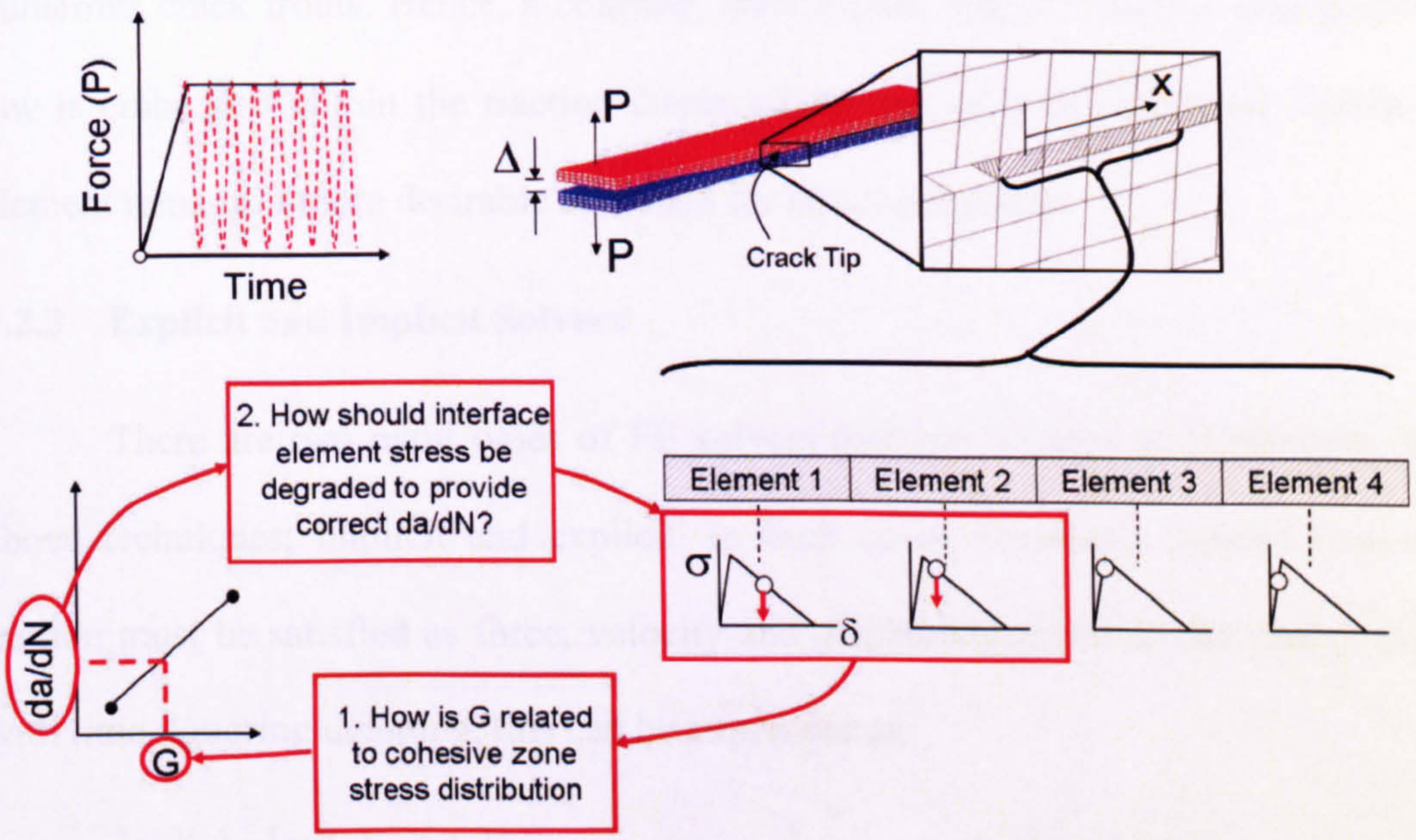

Figure 3.20: Linking a cohesive zone model to the Paris Law

Deobald *et al.*[52,53] have recently developed an interface element fatigue model that avoids the need to include cohesive zone length within the damage formulation, hence overcoming the difficulties described above. The model uses specialised interface elements, capable of extracting strain energy release rate using VCCT principles. Hence, when an element lies adjacent to a numerical crack tip, a crack growth rate can be calculated using the Paris Law. The number of cycles required for the element to fail can then be calculated based on the element's area. This enables cracks to be incrementally advanced whilst counting the accumulated number of fatigue cycles. Unlike the previous VCCT methods discussed, the use of

interface elements enables a strength based initiation criterion to be included and cracks can propagate along any path where the elements are placed. However, an algorithm is still required to monitor the location of crack tip elements and incrementally delete these to advance the crack. This makes the method very computationally expensive to implement in complex 3-D models containing numerous crack fronts. Hence, a cohesive zone model, where a fatigue degradation law is embedded within the traction-displacement law of each individual interface element remains a more desirable approach for structural joints.

3.2.3 Explicit and Implicit Solvers

There are two main types of FE solvers that can be used to implement the above techniques; implicit and explicit. In both cases, Newton's Second Law of motion must be satisfied as force, velocity and displacement within the model vary with time. Ignoring damping, this can be expressed as:

$$[M]\{\ddot{x}\}+[K]\{x\}=\{f_{ex}\} \qquad \text{(Eqn. 3.13)}$$

where $[M]$ and $[K]$ are the system mass and stiffness matrices and $\{\ddot{x}\}$, $\{x\}$ and $\{f_{ex}\}$ are the nodal accelerations, displacements and external force vectors respectively. In an implicit solution, global equilibrium is first achieved by iteration, following which local element variables are evaluated. Although this involves the formation and inversion of large matrices, the process is ideally suited to static or quasi-static analyses, where there is a requirement to converge on the final solution using the minimum number of load steps.

An explicit analysis involves evaluating local variables directly without the need for global equilibrium calculations. Whilst the solution procedure is less

complex than for an implicit approach, very small time-steps are required to prevent significant numerical errors developing[77].

The VCCT numerical integration procedures discussed above can be more efficiently handled using implicit methods. This is because they involve performing a linear elastic static analysis for each discrete increment of crack extension. Using the cohesive zone approach, in which there is progressive crack extension as interface elements degrade and fail within a single continuous analysis run, the choice between implicit and explicit time integration becomes less clear. For quasi-static cohesive zone analyses using interface elements, several researchers have recently selected an explicit approach in order to avoid stability problems, such as snap-back and snap-through, commonly encountered in implicit analyses[60,61,78]. However, to the author's knowledge, none of the existing cohesive zone fatigue models have been implemented using explicit time integration and the challenges of doing so are yet to be detailed. Addressing this need will also enable further enhancement of an interface element developed at the University of Bristol, for use within the explicit solver 'LS-Dyna'. This has been successfully used to model quasi-static failure in notched composites[61] and its formulation has recently been further developed to predict the effect of through-thickness compressive stress on delamination[79]. Extending its application to high-cycle fatigue will provide potential to model impact events, followed by subsequent fatigue failure, within a single coherent simulation.

3.3 Summary of Fatigue Model Requirements

The current chapter has highlighted the importance of the Paris Law for characterising fatigue delamination and bond-line failure in composite materials. For

this reason, it is vital that the final numerical fatigue model can be easily calibrated using Paris Law parameters from standard experimental tests. The Virtual Crack Closure Technique is a proven method for achieving this aim, allowing strain energy release rate and mode ratio to be directly extracted from the numerical model, hence providing a direct link with the Paris Law. However, this technique will only allow the crack to advance along pre-defined paths and complex algorithms are required to incrementally advance cracks by releasing initially coincident nodes. For complex 3-D geometries, which may contain numerous and curved crack fronts, Cohesive Zone Modelling using interface elements offers a more computationally efficient approach. This is because a fatigue damage formulation can be directly embedded within the traction-displacement response of each element, eliminating the need for a global algorithm to release initially coincident nodes and allow cracks to advance. In addition, cracks can grow along any path where interface elements are placed and the direction of propagation does not need to be known in advance.

Existing interface element fatigue models have demonstrated promising results, but have highlighted the need for an improved knowledge of the length, stress distribution and extraction of strain energy release rate from the cohesive zone. This is essential in preserving a direct link between the Paris Law and input parameters for the numerical fatigue model. The subsequent research aims to provide a detailed understanding of the cohesive zone, before using this to develop a new interface element fatigue degradation model. The work is performed using the explicit finite element solver 'LS-Dyna', allowing the development of interface elements previously used for quasi-static analyses at the University of Bristol. Use of an explicit code is ideally suited to modelling impact and subsequent fatigue loading

within a single coherent simulation and can avoid stability problems, such as snap-back and snap-through, commonly encountered in implicit analyses.

4. The Numerical Cohesive Zone: A Detailed Analysis

4.1 Introduction

The previous chapter introduced the concept of a cohesive zone and demonstrated the development of this zone for a DCB under pure model I loading. It also highlighted the importance of extracting strain energy release rate from the cohesive zone, in order to provide a direct link between the numerical fatigue model and the Paris Law. Based on a detailed investigation of cohesive zone development, which has also been presented in the international journal, Engineering Fracture Mechanics[80], the current chapter demonstrates how this can be achieved by integrating the traction-displacement response of interface elements directly adjacent to the crack tip. The accuracy of strain energy release rate values obtained is highly dependent on having a minimum number of elements within the fully developed cohesive zone length. Consequently, predictive formulae for cohesive length are required in order to design a finite element mesh that achieves the correct balance between ensuring accurate results, whilst minimising computational expense. As will be shown in the following chapter, the need for such formulae is strengthened by the inclusion of cohesive zone length in the fatigue degradation law. It is shown that there is no clearly established technique for predicting cohesive zone length and significant work remains to refine the accuracy of existing methods. Details are provided of initial work undertaken to achieve this aim and recommendations provided concerning future development. The studies conducted have used the bi-linear interface element formulation developed at the University of Bristol and before presenting a detailed analysis of the cohesive zone, a brief overview of this formulation is provided.

4.2 Interface Element Formulation

The interface elements used for this research take the form of solid hexahedral elements with a small initial thickness, which are governed by a bi-linear constitutive law. This was developed from the University of Bristol's discrete interface element formulation, which has been successfully implemented to model both matrix cracking and delamination within notched composites using the explicit finite element code 'LS-Dyna'[61,79].

The formulation can be illustrated using a single three-dimensional map by representing the normal opening mode (mode I) on the 0 - σ - δ_{normal} plane, and the transverse shear mode (mode II) on the 0 - σ - δ_{shear} plane, as shown in Figure 4.1. The triangles 0 - $\sigma_{I,max}$ - $\delta_{I,f}$ and 0 - $\sigma_{II,max}$ - $\delta_{II,f}$ are the bi-linear responses in pure opening mode and in pure shear mode respectively. Any point on the 0 - δ_{normal} - δ_{shear} plane represents a mixed-mode relative displacement.

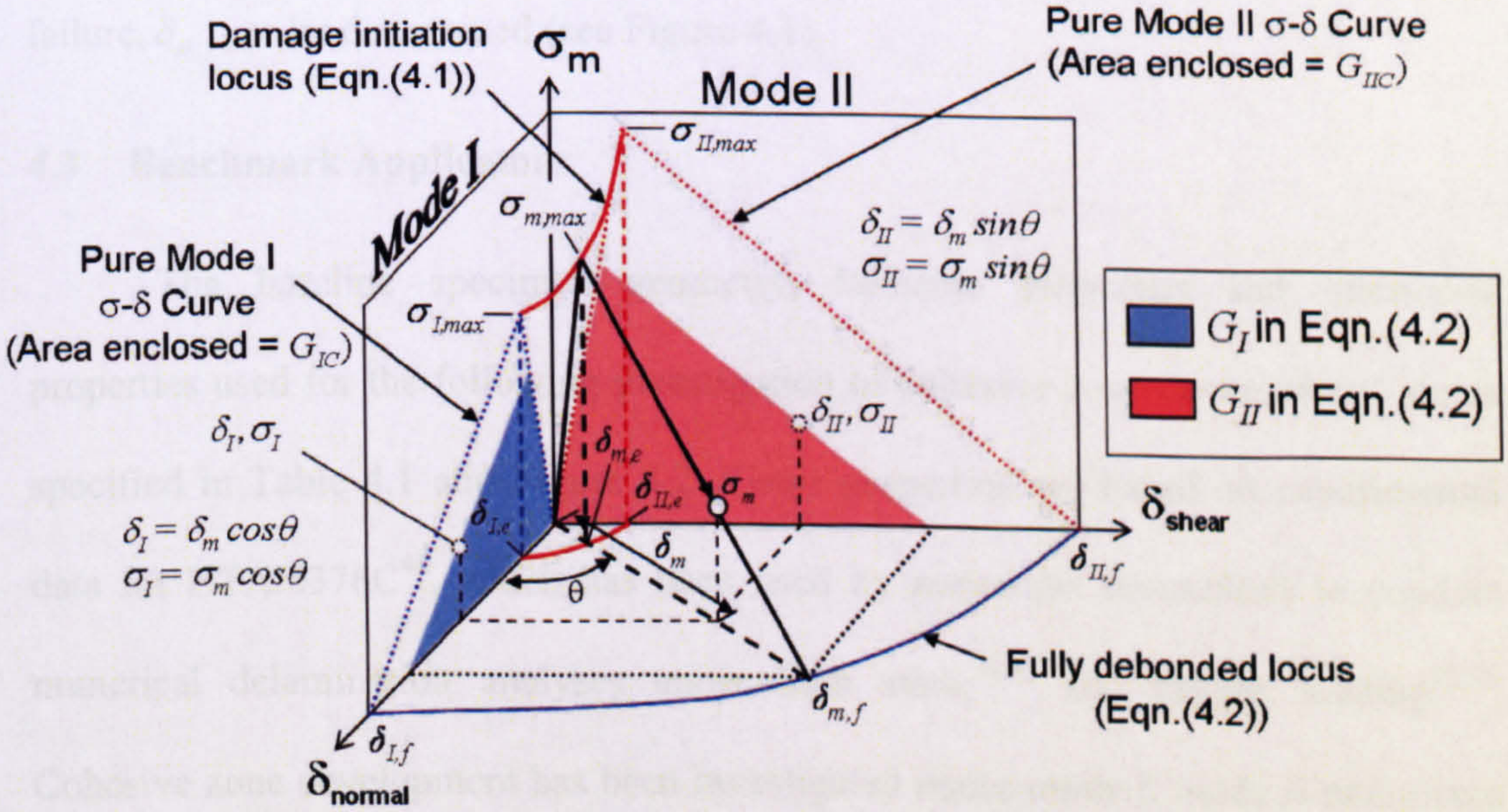

Figure 4.1: The bi-linear mixed mode softening law

The mixed mode damage onset displacement, $\delta_{m,e}$, and interfacial strength, $\sigma_{m,max}$, are calculated using a quadratic damage onset criterion:

$$\sqrt{\left(\frac{max(\sigma_I,0)}{\sigma_{I,max}}\right)^2+\left(\frac{\sigma_{II}}{\sigma_{II,max}}\right)^2}=1 \qquad \text{(Eqn. 4.1)}$$

The mixed mode failure displacement corresponding to complete decohesion is calculated using the following power law failure criterion:

$$\left(\frac{G_I}{G_{IC}}\right)^{\alpha}+\left(\frac{G_{II}}{G_{IIC}}\right)^{\alpha}=1 \qquad \text{(Eqn. 4.2)}$$

where $\alpha \in (1.0 \sim 2.0)$ is an empirical parameter derived from mixed-mode tests, G_{IC} and G_{IIC} are critical energy release rates for pure mode I (opening) and pure mode II (shear) respectively. A value of $\alpha=1$ has been assumed in all the numerical studies presented within this thesis. Equation (4.2) allows the fully debonded locus, represented by the relative displacement corresponding to complete interface failure, $\delta_{m,f}$, to be determined (see Figure 4.1).

4.3 Benchmark Applicatons

The baseline specimen geometry, laminate properties and interfacial properties used for the following investigation of cohesive zone development are as specified in Table 4.1 and Figure 4.2. These properties are based on experimental data for HTA/6376C[41], which has been used by numerous researchers to conduct numerical delamination analyses under both static[78,81] and fatigue loading[72,75]. Cohesive zone development has been investigated under mode I, mode II and mixed mode loading, using the DCB, 3 Point End Notched Flexure (3ENF) and Fixed Ratio Mixed Mode (FRMM) specimens respectively. The details of each model, including

boundary conditions and properties of the numerical interface are shown in Figure 4.3. It should be noted that the mode II interfacial strength of 60MPa is significantly higher than that of 30MPa[72,75] and 40MPa[78,81] applied by previous authors. As fully discussed in reference [80], this is necessary to perform an accurate quasi-static load-displacement analysis of the 3ENF and FRMM specimens.

Mass-scaling was applied to maintain reasonable computational run times of a few hours and a global damping factor of 5 was applied to remove high frequency oscillations. Accurate results were maintained by ensuring that the kinetic and damping energy remained negligible compared to the strain energy absorbed by the specimen.

Table 4.1: Material Properties for HTA6376/C

Laminate Properties		**Interfacial Properties**	
E_{11} (MPa)	120,000	G_{IC} (N/mm)	0.26
$E_{22} = E_{33}$ (MPa)	10,500	G_{IIC} (N/mm)	1.002
$G_{12} = G_{13}$ (MPa)	5,250	$\sigma_{I,max}$ (MPa)	30
G_{23} (GPa)	3,480	$\sigma_{II,max}$ (MPa)	60
$\nu_{12} = \nu_{13}$	0.3	K_I (N/mm^3)	1×10^5
ν_{23}	0.51	K_{II} (N/mm^3)	1×10^5

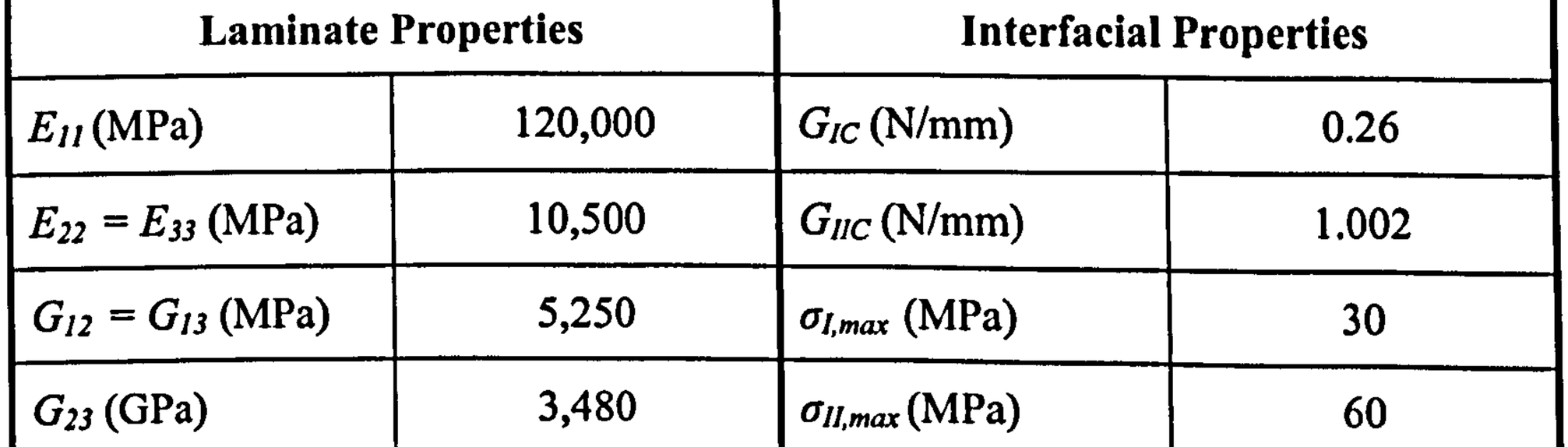

Figure 4.2: Specimen Geometry

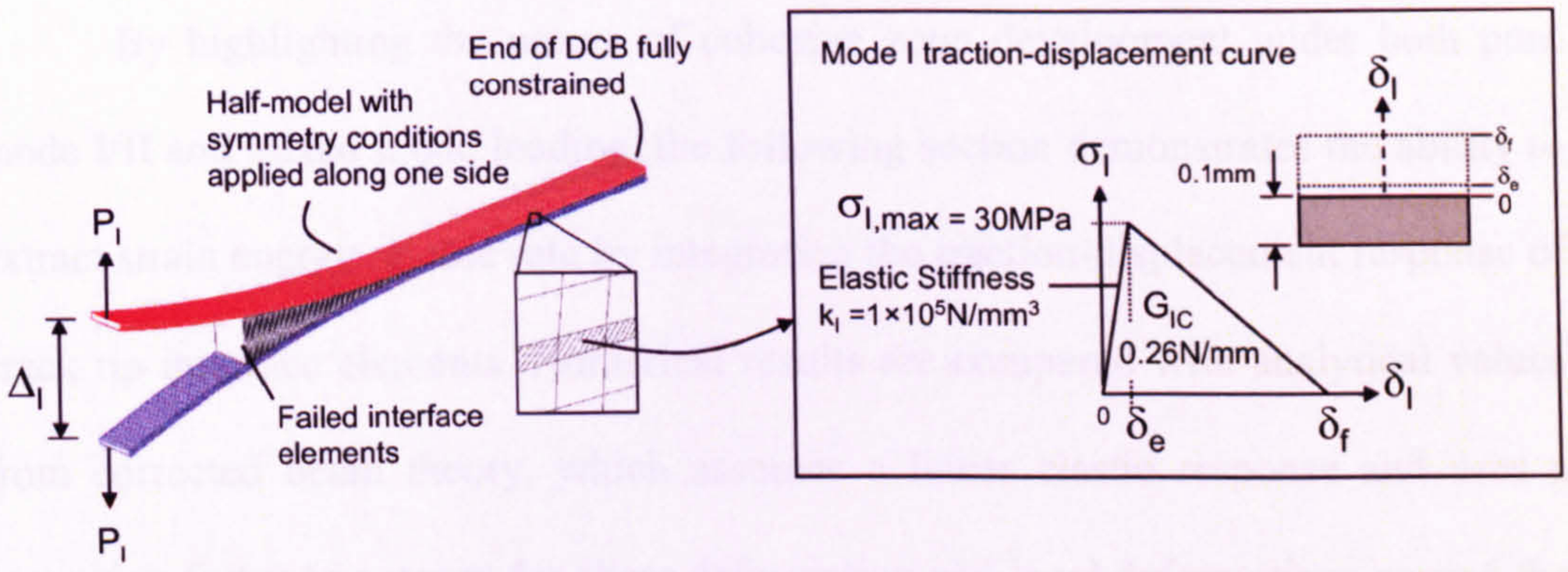

(a) Mode I DCB

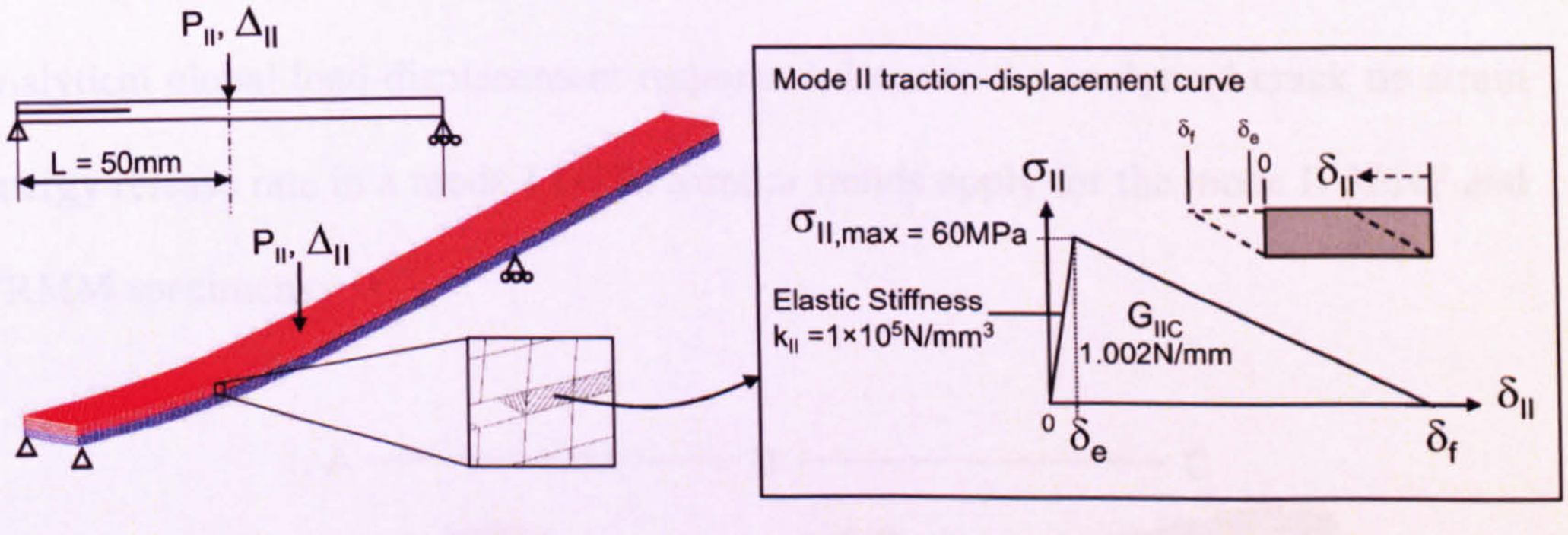

(b) Mode II 3ENF

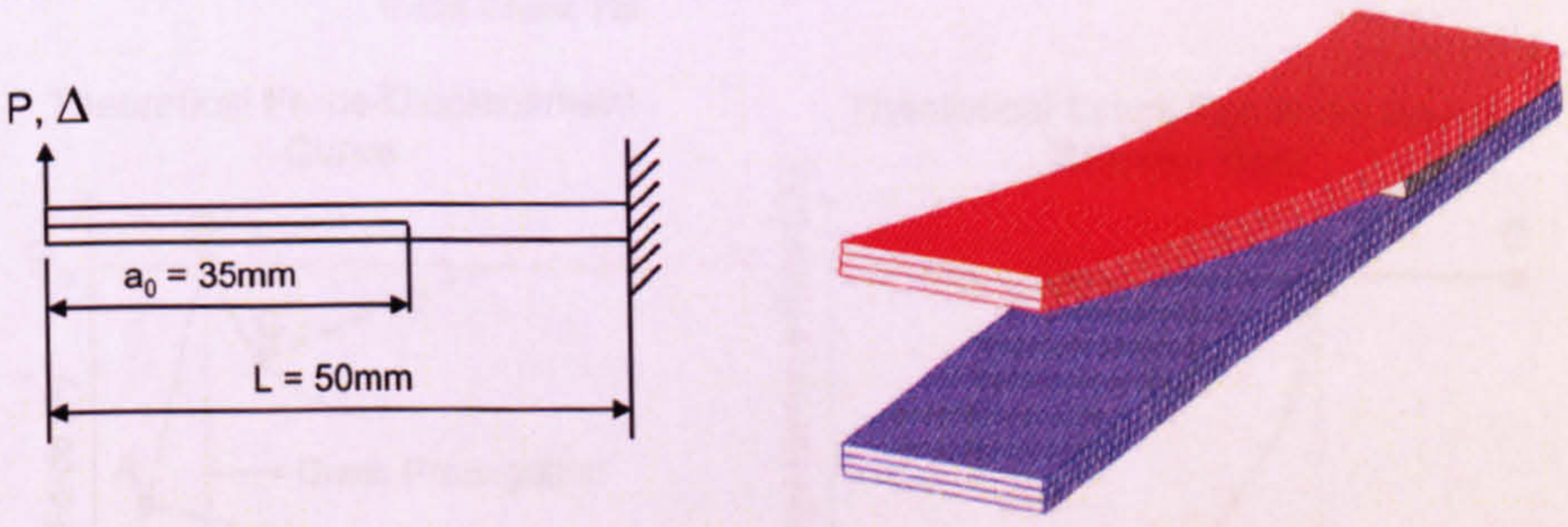

(c) FRMM

Figure 4.3: Finite Element models of benchmark specimens

4.4 Cohesive Zone Development and Strain Energy Release Rate Extraction

By highlighting the nature of cohesive zone development under both pure mode I/II and mixed mode loading, the following section demonstrates the ability to extract strain energy release rate by integrating the traction-displacement response of crack tip interface elements. Numerical results are compared with analytical values from corrected beam theory, which assumes a linear elastic response and uses a correction factor to account for shear deformation and local deformations around the crack tip (see Appendix A for details of calculations). Figure 4.4 illustrates how the analytical global load-displacement response relates to the analytical crack tip strain energy release rate in a mode I DCB. Similar trends apply for the mode II 3ENF and FRMM specimens.

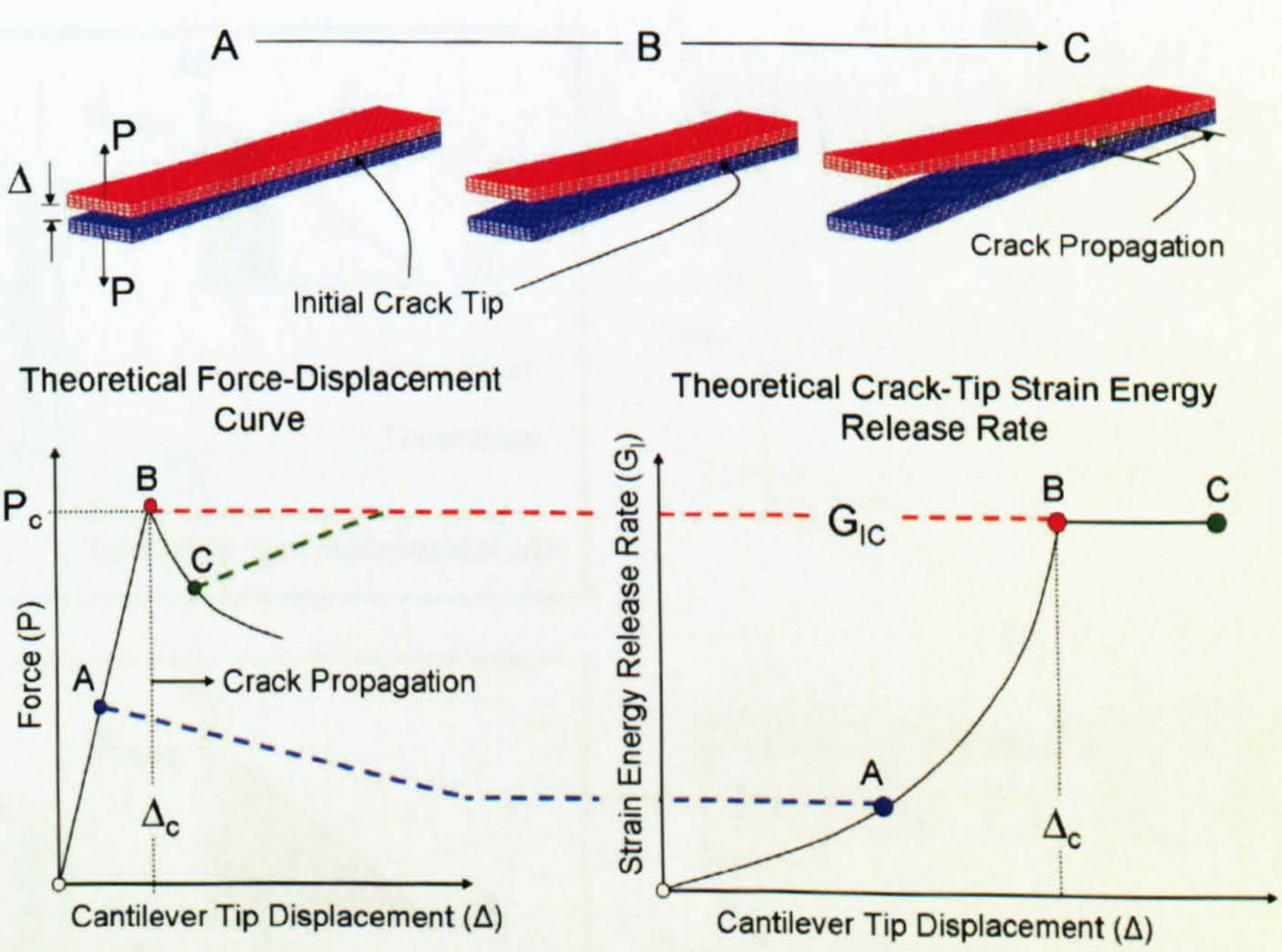

Figure 4.4: Analytical Load-Displacement and Crack Tip Strain Energy Release Rate curves for the mode I DCB

Although the development of a cohesive zone violates the assumption of linear elasticity, investigating the nature of cohesive zone development revealed that integrating the traction-displacement response of a crack tip interface element provides a reasonably close match to the strain energy release rate from corrected beam theory. This technique is demonstrated in Figure 4.5, again using the example of the DCB under a linearly increasing displacement.

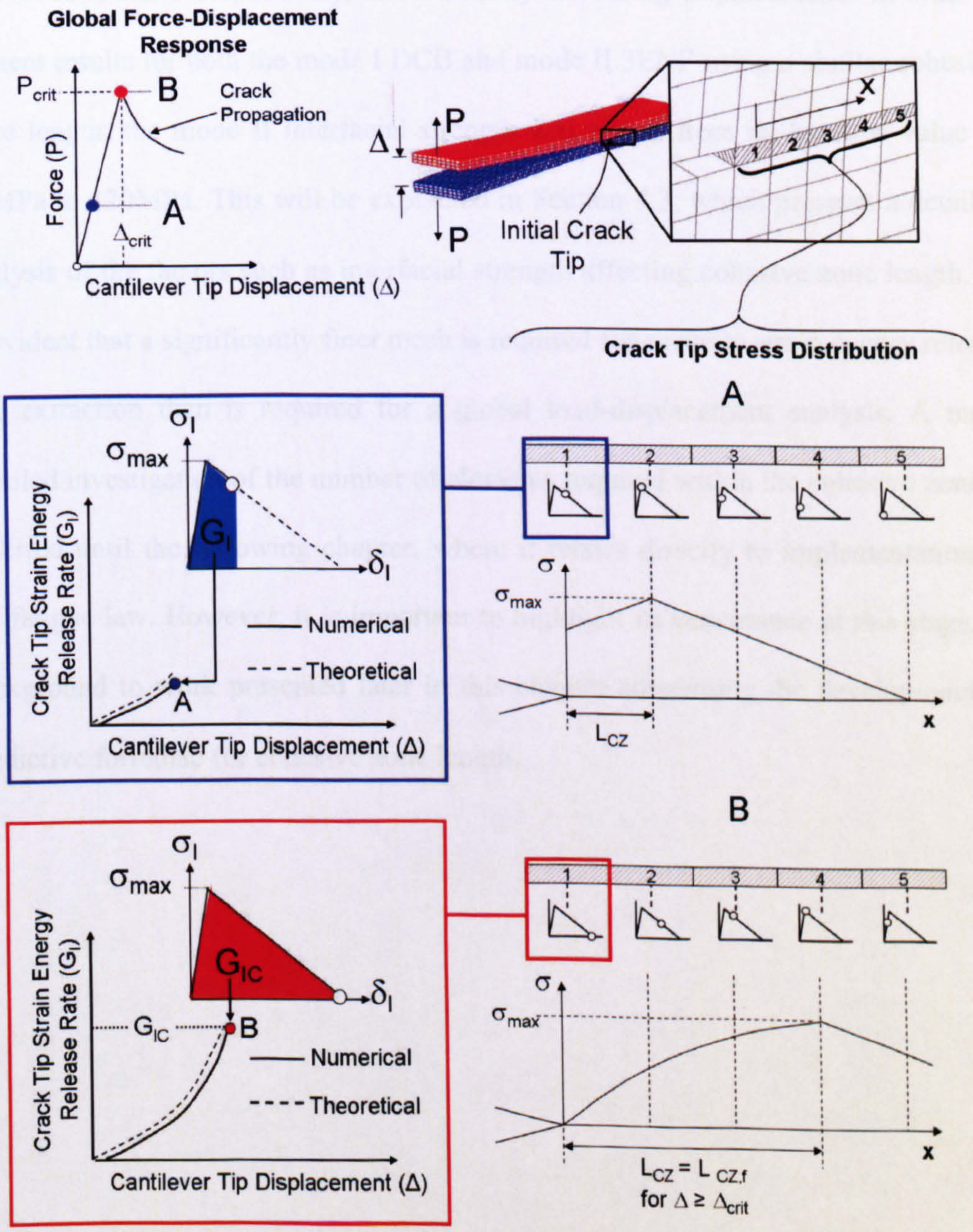

Figure 4.5: Strain Energy Release Rate Extraction

At the point at which the crack tip element fails, the cohesive zone reaches its fully developed length, $L_{CZ,f}$. The number of interface elements that exist within this fully developed cohesive zone length, defined throughout this thesis as the ratio $L_{CZ,f}/L_{el}$, where L_{el} is the element length in the direction of crack propagation, has a very strong influence on the accuracy of strain energy release rate extraction. This is demonstrated in Figure 4.6 and Figure 4.7, using results gained for the mode I DCB and mode II 3ENF respectively, under linearly increasing displacements. In order to present results for both the mode I DCB and mode II 3ENF using a similar cohesive zone length, the mode II interfacial strength was raised from its baseline value of 60MPa to 120MPa. This will be explained in Section 4.3, which presents a detailed analysis of the factors such as interfacial strength affecting cohesive zone length. It is evident that a significantly finer mesh is required for accurate strain energy release rate extraction than is required for a global load-displacement analysis. A more detailed investigation of the number of elements required within the cohesive zone is deferred until the following chapter, where it relates directly to implementation of the fatigue law. However, it is important to highlight its importance at this stage, as background to work presented later in this chapter concerning the development of predictive formulae for cohesive zone length.

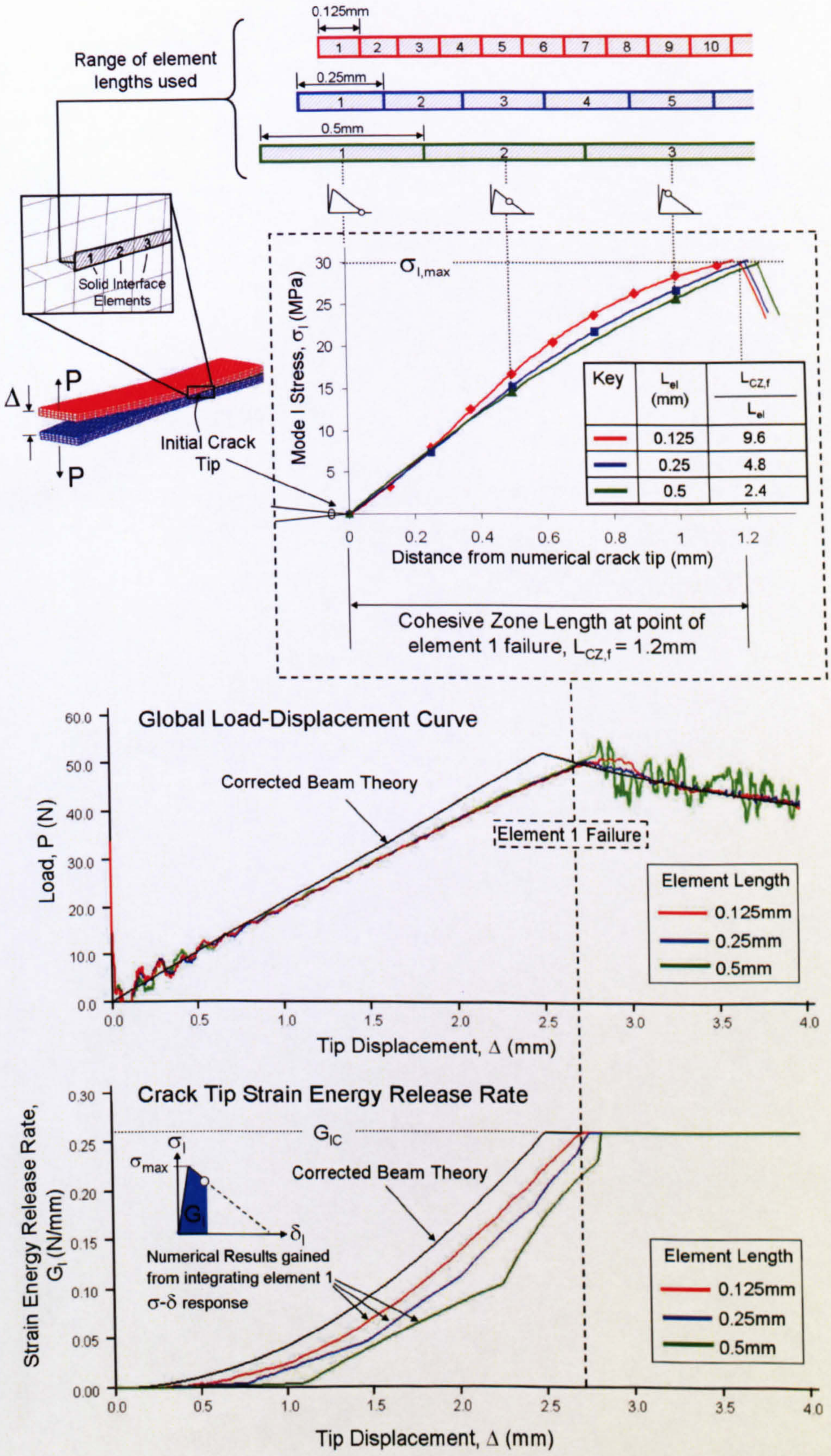

Figure 4.6: Mode I DCB Numerical Results

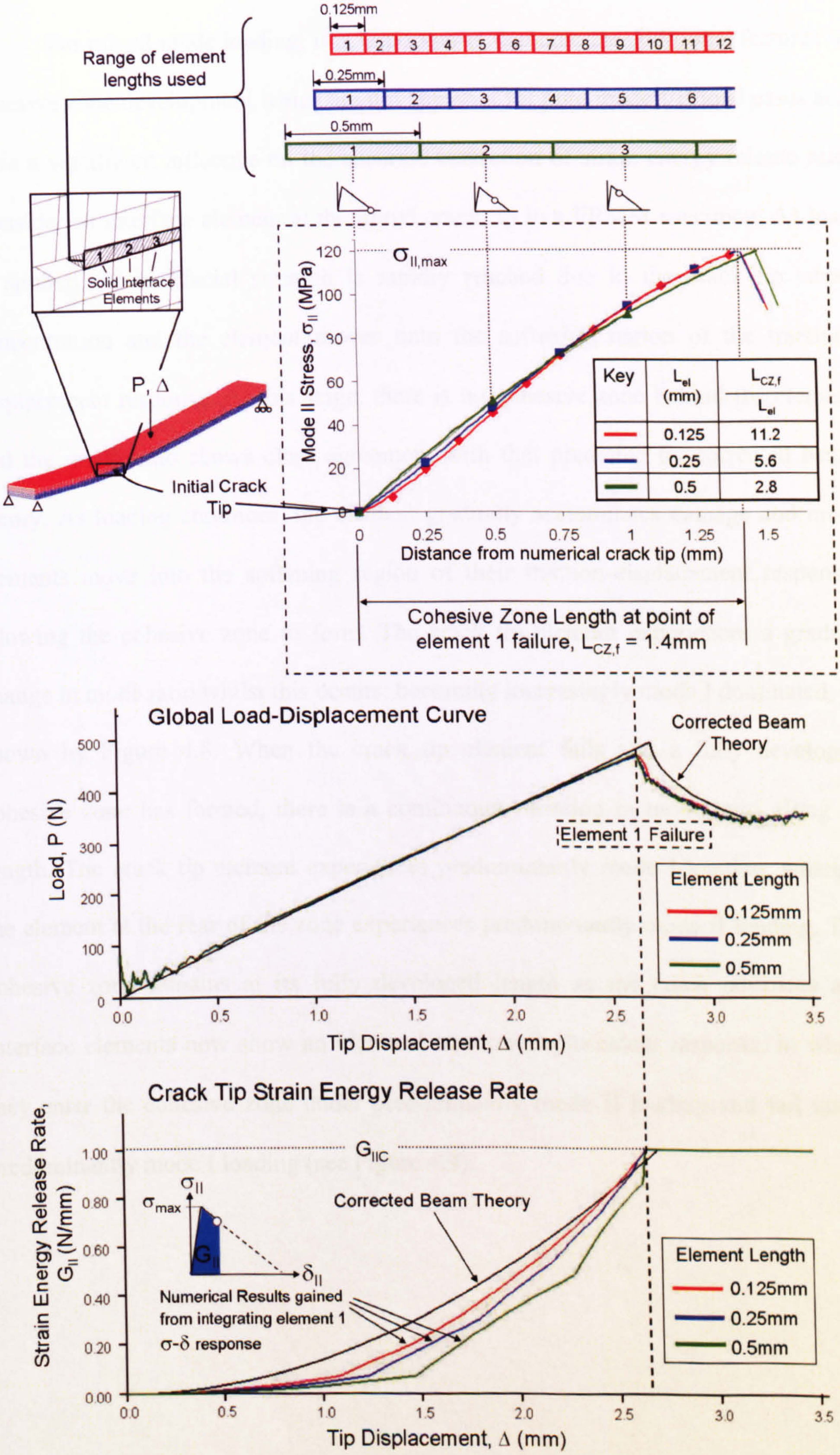

Figure 4.7: Mode II 3ENF Numerical Results

For mixed mode loading, it is important to demonstrate additional features of cohesive zone development which are not apparent for pure mode I/II load cases and have a significant influence on the accurate extraction of strain energy release rate. Consider an interface element at the initial crack tip in a FRMM specimen. As load is applied, its interfacial strength is rapidly reached due to the crack tip stress concentration and the element moves onto the softening region of the traction-displacement response. At this stage, there is no cohesive zone behind the element and the mode ratio shows close agreement with that predicted by corrected beam theory. As loading continues, the element gradually accumulates damage and more elements move into the softening region of their traction-displacement response, allowing the cohesive zone to form. The crack tip element experiences a gradual change in mode ratio whilst this occurs; becoming increasingly mode I dominated, as shown by Figure 4.8. When the crack tip element fails and a fully developed cohesive zone has formed, there is a continuous variation in mode ratio along its length. The crack tip element experiences predominantly mode I loading, whereas the element at the rear of the zone experiences predominantly mode II loading. The cohesive zone remains at its fully developed length as the crack advances and interface elements now show an identical traction-displacement response, in which they enter the cohesive zone under predominantly mode II loading and fail under predominantly mode I loading (see Figure 4.9).

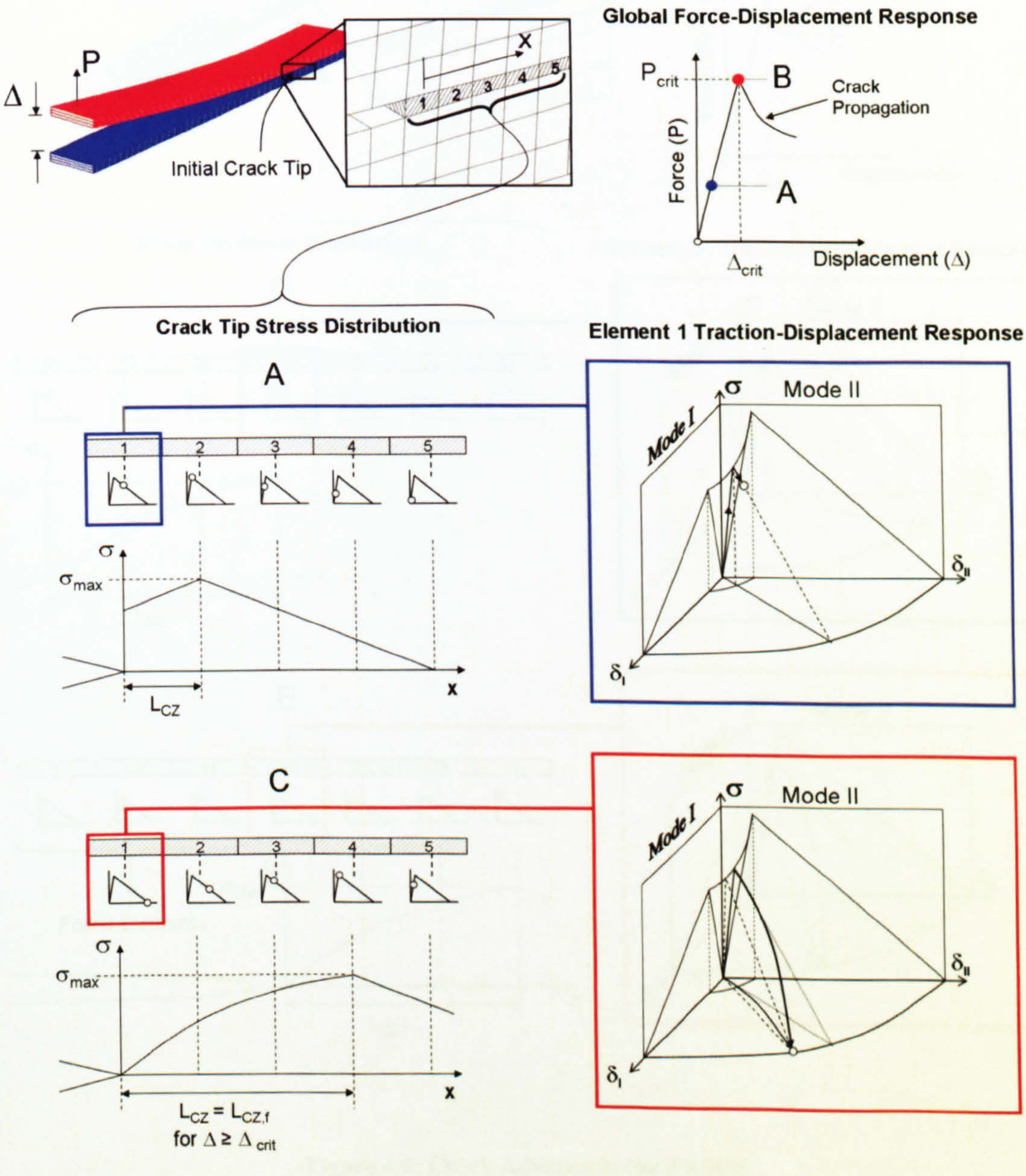

Figure 4.8: Cohesive Zone Development in the FRMM

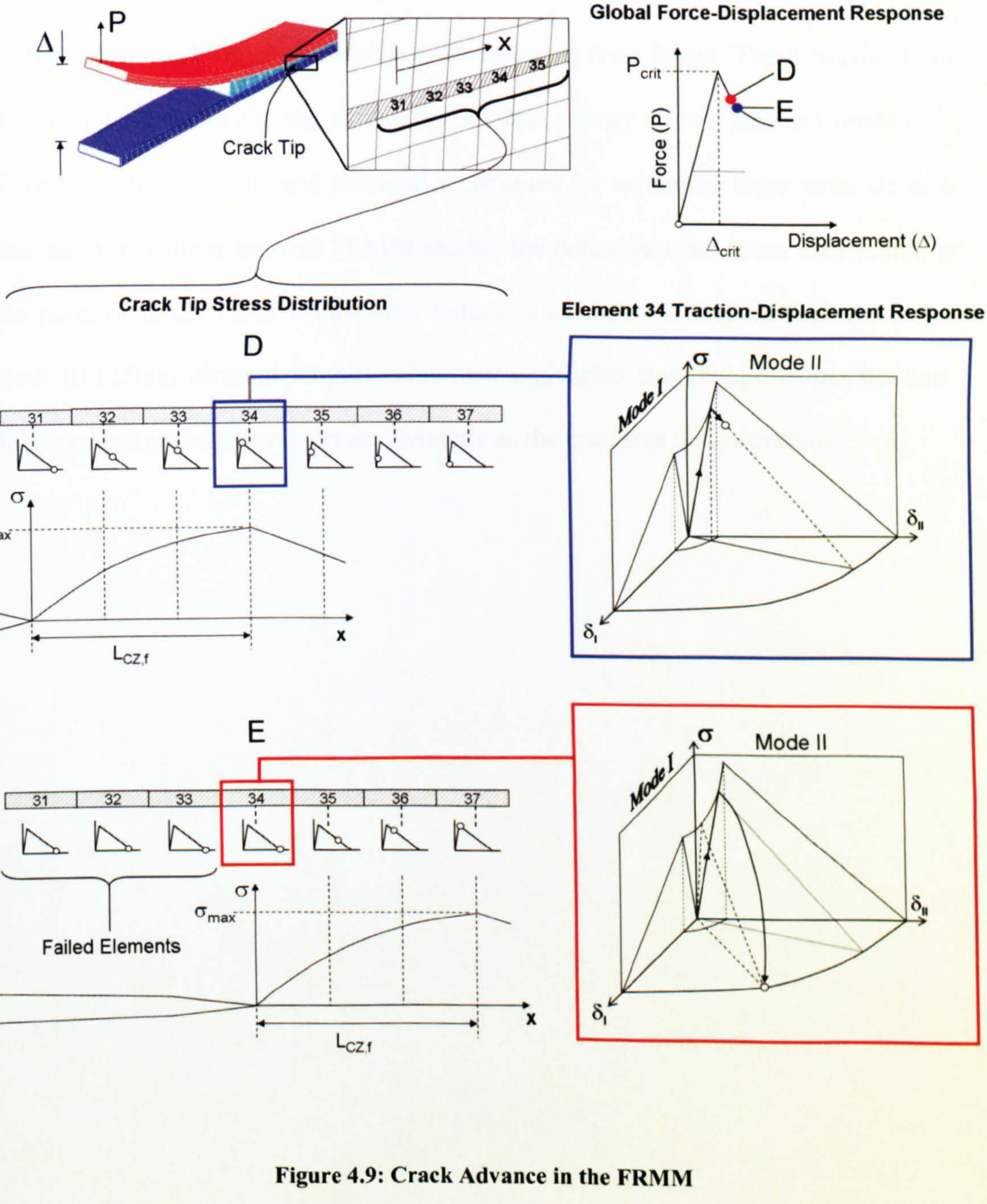

Figure 4.9: Crack Advance in the FRMM

It is important to emphasise that the traction-displacement response of elements entering the fully developed cohesive zone is significantly different to that of the initial crack tip element before the cohesive zone forms. These trends are of significant importance to the extraction of strain energy release rate and mode ratio from the cohesive zone, and potential techniques for achieving these aims are now discussed. For the numerical FRMM model, the cohesive zone stress distribution at the point of initial crack tip element failure is as shown in Figure 4.10 for a fine mesh (0.125mm element length). This also highlights the change in the traction-displacement response of interface elements as the cohesive zone develops.

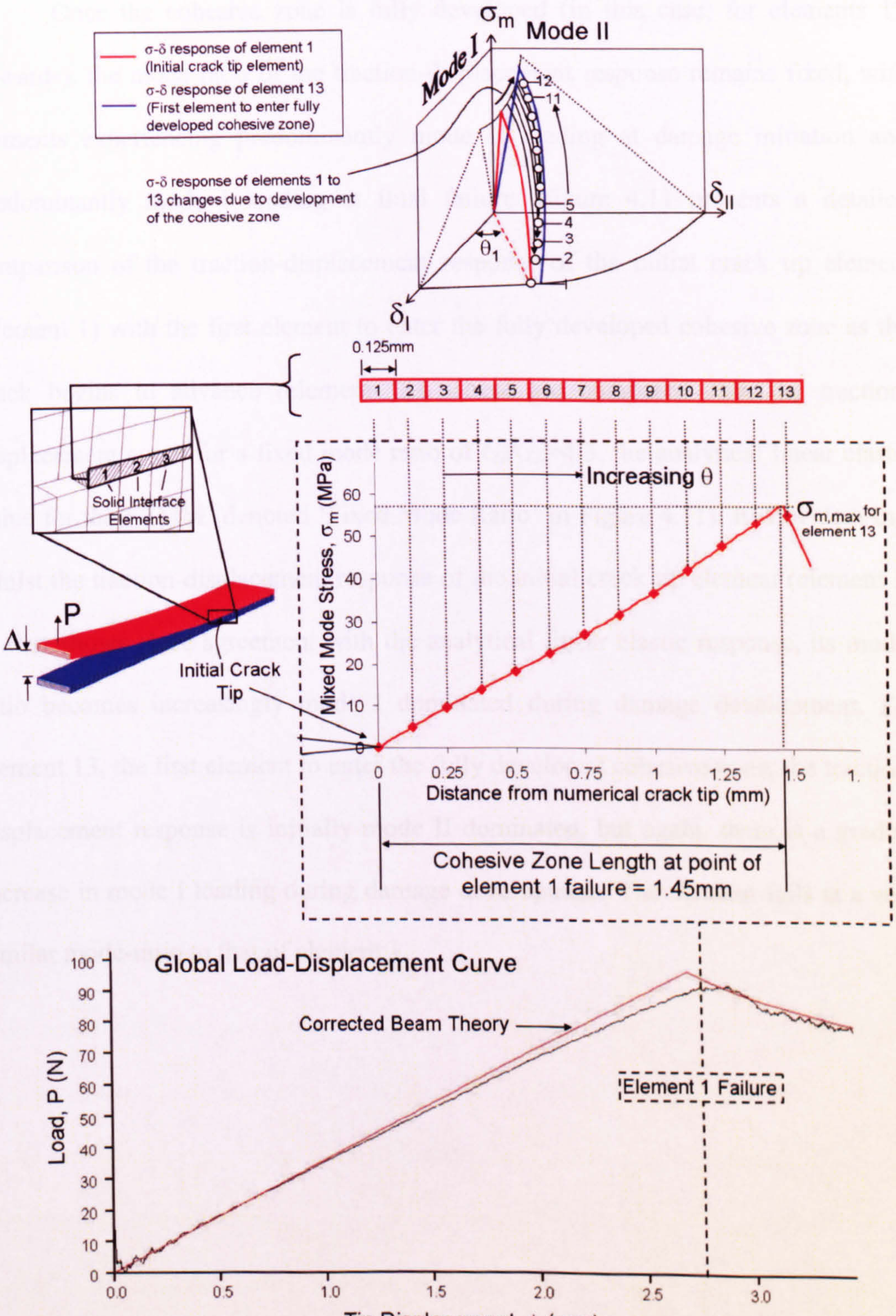

Figure 4.10: Cohesive Zone Stress Distribution of FRMM specimen at point of initial crack tip element failure

Once the cohesive zone is fully developed (in this case, for elements 13 onwards), the mode ratio of the traction-displacement response remains fixed, with elements experiencing predominantly mode II loading at damage initiation and predominantly mode I loading at final failure. Figure 4.11 presents a detailed comparison of the traction-displacement response of the initial crack tip element (element 1) with the first element to enter the fully developed cohesive zone as the crack begins to advance (element 13). These are compared with the traction-displacement curve for a fixed mode ratio of G_I/G_{II}=4/3, the analytical linear elastic value for the FRMM (denoted 'Fixed Mode Ratio' in Figure 4.11). It is evident that whilst the traction-displacement response of the initial crack tip element (element 1) at first shows close agreement with the analytical linear elastic response, its mode-ratio becomes increasingly mode I dominated during damage development. For element 13, the first element to enter the fully developed cohesive zone, the traction-displacement response is initially mode II dominated, but again, there is a gradual increase in mode I loading during damage development. The element fails at a very similar mode-ratio to that of element 1.

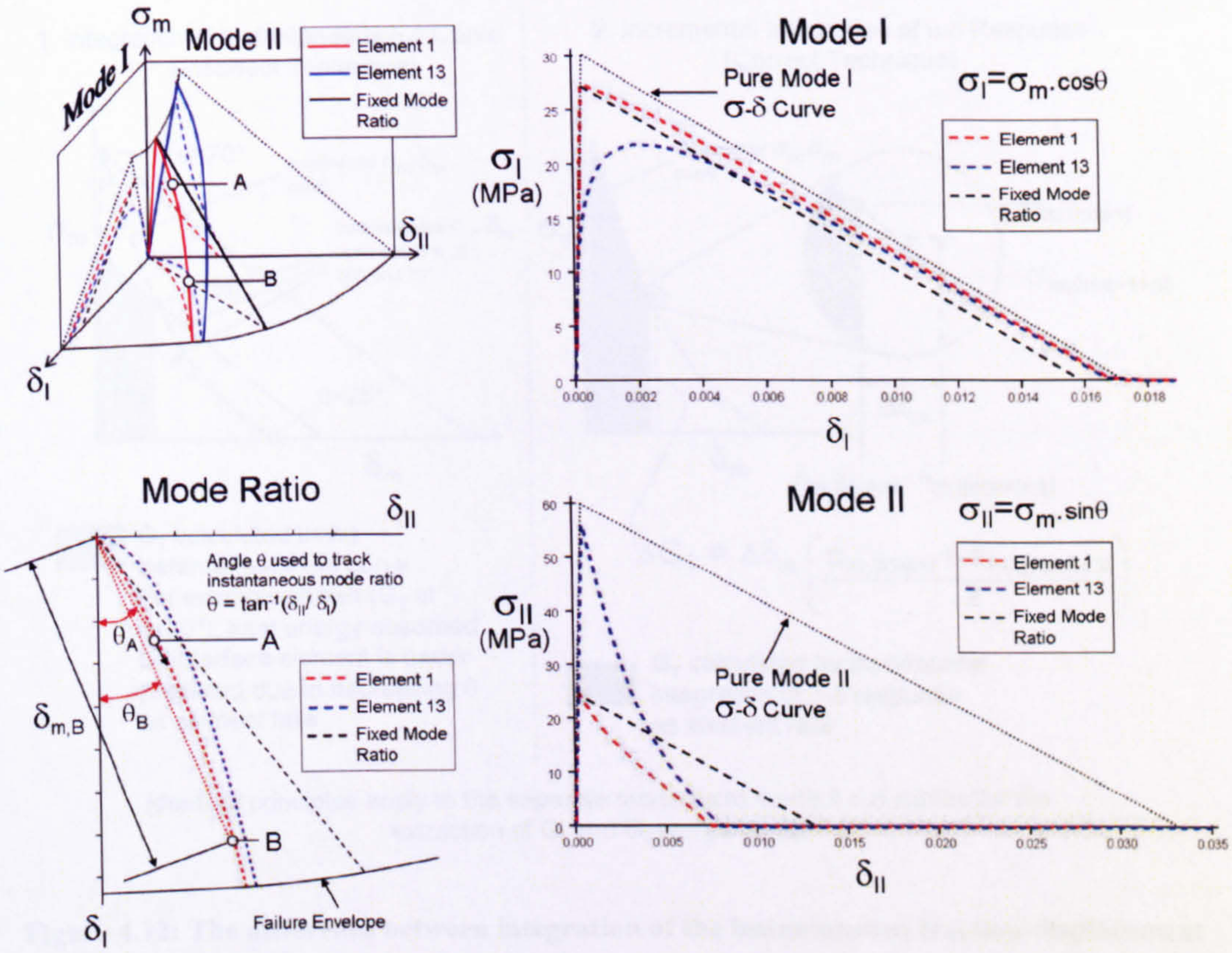

Figure 4.11: Traction-displacement response of elements 1 and 13 for the FRMM specimen

These trends can be explained by analysing the energy absorbed as the cohesive zone develops. Prior to doing so, it is important to define the exact technique that must be used for accurate strain energy release rate extraction. Under pure mode I/II loading, there is no variation in mode-ratio and strain energy release rate can be extracted either by performing an incremental integration procedure after each time-step, or by integrating the instantaneous traction-displacement response (the difference between these two techniques is clarified in Figure 4.12). However, for mixed-mode load cases, where a variation in mode-ratio occurs as the element fails, these two techniques yield significantly different results (see Figure 4.12) and as will now be demonstrated, only the incremental integration procedure enables an accurate strain energy release rate to be extracted.

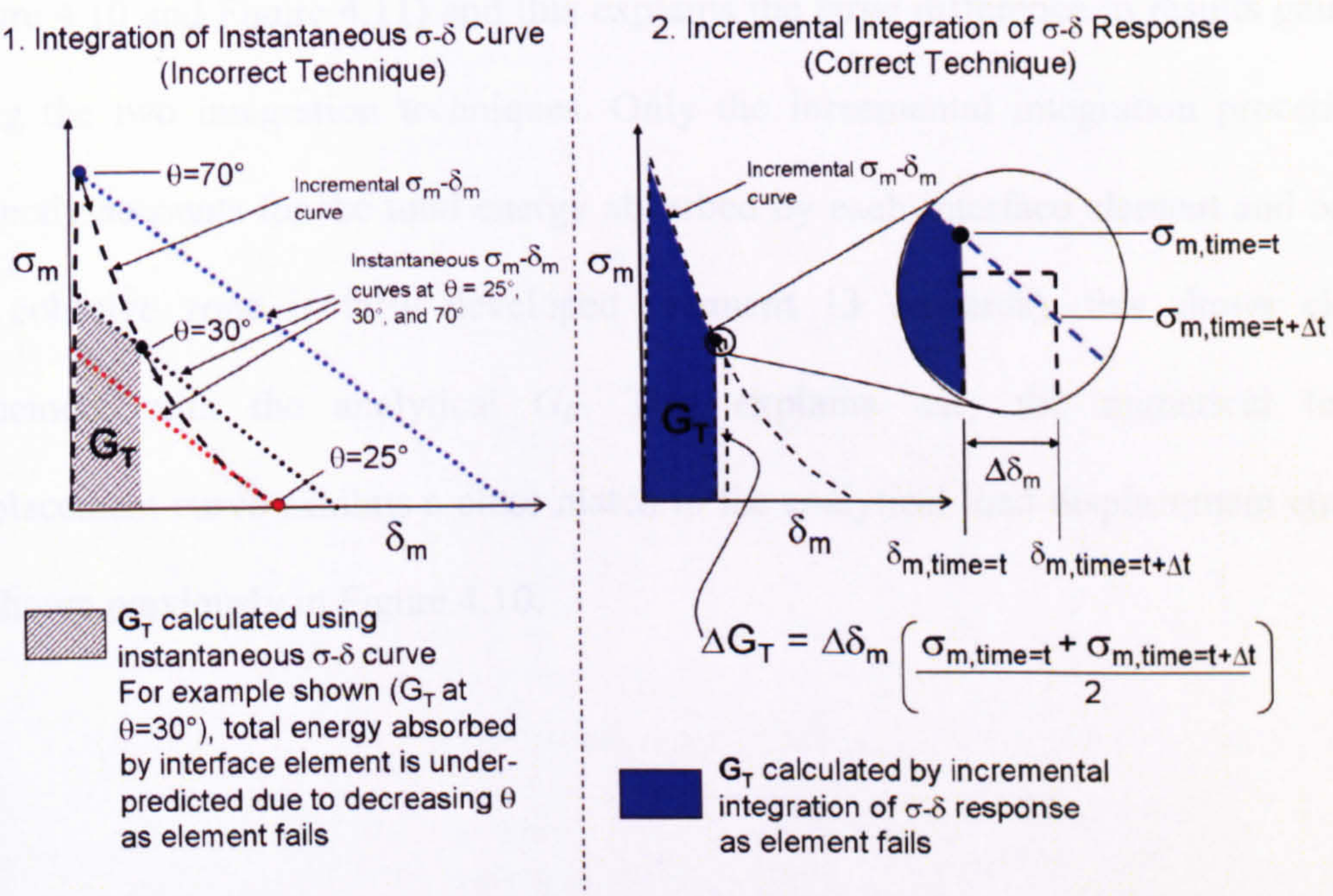

Figure 4.12: The difference between integration of the instantaneous traction-displacement response and incremental integration

Figure 4.13 presents a comparison of results gained using the two integration techniques for the FRMM specimen. If only the initial crack tip element is considered, similar results are obtained using each technique, since this element experiences a relatively small change in mode ratio during damage development. Before a significant cohesive zone develops behind the initial crack tip element, the mode ratio shows close agreement with the analytical linear elastic value. Therefore, the numerical strain energy release rate results initially show reasonable agreement with corrected beam theory. As the cohesive zone develops, the crack tip element experiences an increasing G_I/G_{II} ratio. For both integration techniques, this results in a significantly lower total G_C value calculated by the model relative to the analytical solution from corrected beam theory. Elements behind the initial crack tip element show a far more significant variation in mode ratio during damage development (see

Figure 4.10 and Figure 4.11) and this explains the large difference in results gained using the two integration techniques. Only the incremental integration procedure correctly accounts for the total energy absorbed by each interface element and once the cohesive zone is fully developed (element 13 onwards), this shows close agreement with the analytical G_C. This explains why the numerical load-displacement curve exhibits a close match to the analytical load-displacement curve, as shown previously in Figure 4.10.

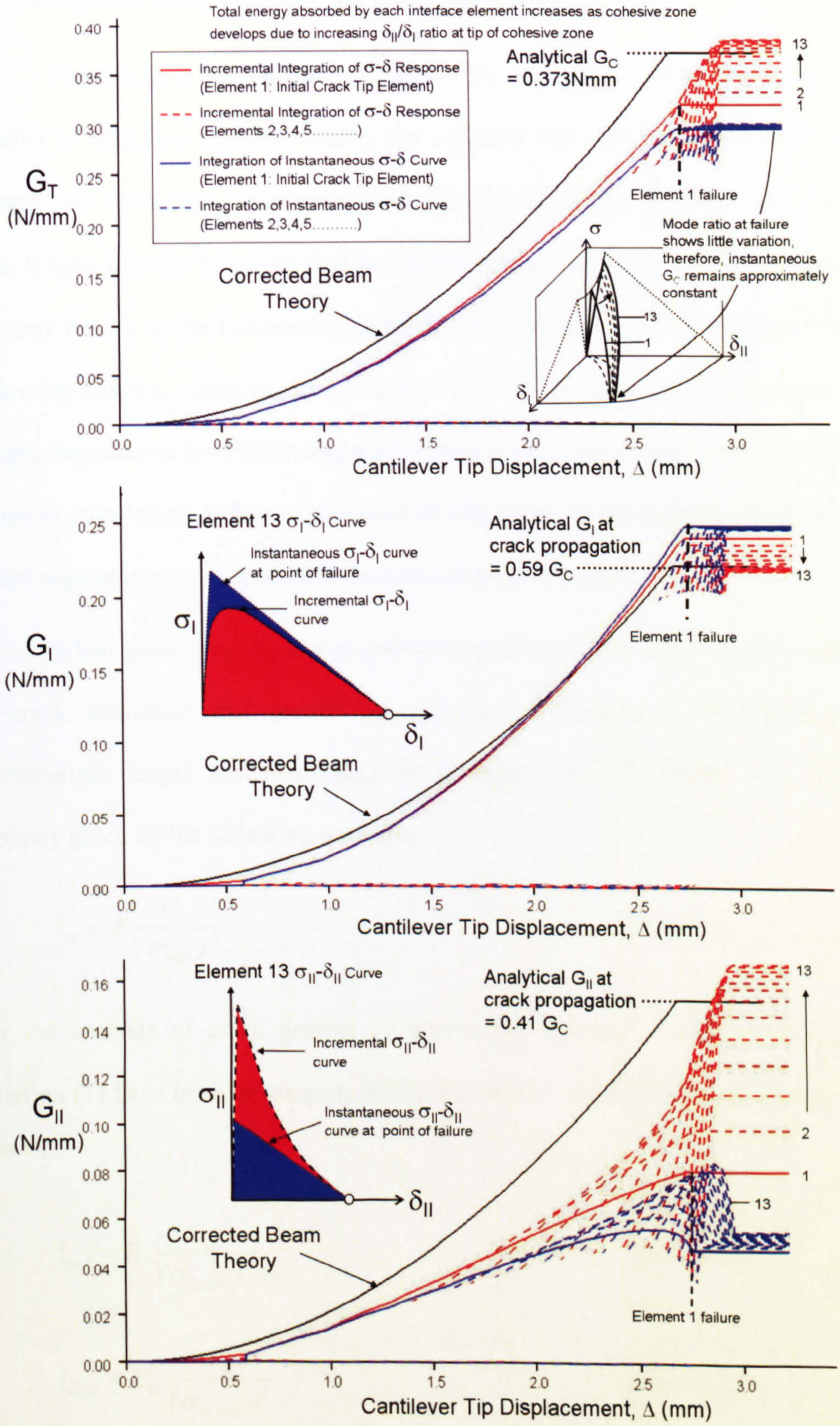

Figure 4.13: Strain Energy Release Rate Results for FRMM specimen (element length = 0.125mm)

4.5 Predictive Formulae for Cohesive Zone Length

The previous section has highlighted the importance of having a minimum number of interface elements within the cohesive zone for accurate strain energy release rate extraction. This necessitates having predictive formulae for cohesive zone length, in order to ensure that the correct balance is achieved between ensuring accurate results whilst minimising computational expense. As will be shown in the following chapter, cohesive zone length is also an important parameter within the fatigue degradation law. Following a brief review of existing methods used to predict cohesive zone length and an explanation of why these are inadequate, progress made in developing improved predictive formulae is now discussed.

When pioneering the use of cohesive zone models in finite element analyses of crack formation and growth in concretes, Hillerborg *et al.*[82] presented a characteristic length parameter (l_{ch}) for isotropic materials, which is a material property given by the following equation:

$$l_{ch} = E\frac{G_C}{(\sigma_{max})^2} \qquad \text{(Eqn. 4.3)}$$

For the analysis of crack growth in orthotropic materials, modified versions of equation (1) have been developed, which for mode I and mode II loading are given by[66,83]:

$$l_{ch,I} = E_I^{'}\frac{G_{IC}}{(\sigma_{I,max})^2} \qquad \text{(Eqn. 4.4a)}$$

$$l_{ch,II} = E_{II}^{'}\frac{G_{IIC}}{(\sigma_{II,max})^2} \qquad \text{(Eqn. 4.4b)}$$

where E' is an equivalent elastic modulus (MPa) for orthotropic materials, whose value depends on the material's longitudinal modulus, transverse modulus, shear modulus, depth and whether plane stress or plane strain conditions exist[66]. This replaces the isotropic elastic modulus in equation (4.3). The procedure for calculating E' is provided in Appendix B.

Values equal to or close to the characteristic length have since been suggested by several authors[66,83,84] for predicting the fully developed numerical cohesive zone length, $L_{CZ,f}$, and hence, required mesh density, in finite element analyses. The present study highlights that the characteristic length can significantly over-predict the maximum numerical cohesive zone length. This finding is consistent with existing analytical solutions for cohesive zone length. For example, Planas and Elices[85] have compared fully developed cohesive zone lengths in remotely loaded, isotropic, infinite bodies resulting from rectilinear, linear and exponential softening traction-displacement laws. They found the cohesive zone length to be given by $(\pi/8)$ l_{ch}, 0.731 l_{ch} and 2.92 l_{ch} for rectilinear, linear and exponential softening laws respectively. This strong dependence of cohesive zone length on traction-displacement curve shape has also been shown by Smith[86], who developed closed form cohesive zone length solutions for a range of power law curves. One of these curves was a close approximation of the linear softening law and similar results to those of Planas and Elices were gained.

There are several significant differences between these analytical solutions for cohesive zone length and the present numerical study. All the examples quoted are based on the development of cracks in isotropic materials, but as highlighted by Yang *et al.*[83,83] and shown by the calculation procedure for E' in equations (4.4a) and (4.4b), when analysing cohesive zone length in orthotropic materials, the elastic

modulus in the characteristic length equation becomes a function of the material's longitudinal modulus, transverse modulus, shear modulus, depth and plane stress or plane strain conditions. In Turon *et al.*'s previous study[84], the value of *E'* was assumed equal to the transverse modulus when predicting cohesive zone length. The present study highlights the importance of including the additional parameters listed above in the calculation of cohesive zone length for orthotropic materials.

Furthermore, the analytical traction-displacement curves discussed above prescribe maximum cohesive traction at zero crack opening displacement. However, when implementing a cohesive zone law in a numerical model, it is necessary to have an initial rising part of the traction-displacement curve, which is generally taken as linear to simulate the elastic response of the interface until the point of damage initiation.

Finally, the above analytical solutions are for infinite bodies, where material depth has no influence on cohesive zone length. For analysis of composite delamination and bond-line failure, it is critical that the effects of specimen thickness on cohesive zone length are studied, due to the slender nature of typical laminates. Williams and Hadavinia[87] conducted an analytical investigation of cohesive zone models applied to a slender DCB specimen, incorporating a range of traction-displacement laws. Their work was motivated by developing analytical solutions for the equivalent crack length in a purely elastic material, as opposed to the length of the cohesive zone. Based on previous studies of crack bridging models[88,89], Cox and Yang proposed modified forms of the characteristic length equations for infinite bodies, which they suggest should be used for estimating cohesive zone length in slender laminates, with centred cracks, under mode I and mode II loading respectively[66]:

$$l_{ch,slender,I} = \left(E'_I \frac{G_{IC}}{(\sigma_{I,max})^2} \right)^{\frac{1}{4}} h^{\frac{3}{4}} \qquad (4.5a)$$

$$l_{ch,slender,II} = \sqrt{\left(E'_{II,slender} \frac{G_{IIC}}{(\sigma_{II,max})^2} \right) h} \qquad (4.5b)$$

where h is the laminate half-thickness and $E'_{II,slender}$ is a mode II equivalent elastic modulus for a slender body, which takes a different form to that used in equation (4.4b) (see Appendix B). The mode I equivalent elastic modulus takes the same form as that used in equation (4.4a). These formulae are based on the assumption that the characteristic length parameter, l_{ch}, provides an accurate prediction of cohesive zone length in an infinite body, which as previously discussed, is not necessarily the case. In addition, no guidance is provided concerning what constitutes a slender laminate.

No numerical studies have been presented to validate the accuracy of equations (4.4) and (4.5) across a range of material properties, structural geometries and load conditions. The present investigation addresses this need by investigating whether these equations are applicable to numerical cohesive zone lengths and under what conditions each formula provides the greatest level of accuracy.

Figure 4.14 shows the effects on $L_{CZ,f}$ of independently varying E', G_C, σ_{max} and h for the benchmark HTA6376/C mode I, DCB model, using a consistent element length of 0.125mm. (N.B. As shown in Appendix B, E' is influenced by E_{11}, E_{33} and G_{13}, therefore, each of these parameters has been independently varied). Due to the uncertainties surrounding the accuracy of existing predictive formulae highlighted in the introduction, a scaling factor, M, has been applied to equations (4.4) and (4.5), to try and identify the best fit to numerical results.

When comparing the numerical results with equations (4.4a) and (4.5a) (i.e. the characteristic cohesive zone lengths, $l_{ch,I}$ and $l_{ch,slender,I}$, in infinite and slender bodies respectively), it was apparent that both formulae significantly over-predict the numerical cohesive zone length. As a result, using these formulae for mesh design risks the application of a mesh that is too coarse to accurately extract crack tip strain energy release rate. It was identified that applying $M = 0.5$ to equation (4.5a), which accounts for the influence of specimen depth, provides a reasonable and generally conservative correlation with the numerical results across most of the parameter ranges investigated. In cases where material properties result in a very short cohesive zone length (e.g. high interfacial strength, low shear modulus, low transverse modulus), equation (4.4a), which takes no account of structural depth, begins to exhibit a closer match to the numerical results. Again, it is necessary to use $M = 0.5$ in order to gain a close match with the numerical results. It is apparent that this value falls between the analytical solutions for cohesive zone lengths in infinite bodies of $M = \pi/8$ and $M = 0.731$, for rectilinear and linear softening traction-displacement laws respectively[85]. Equations (4.4a) and (4.5a), with a scaling factor of $M = 0.5$ applied, have been plotted on Figure 4.14 to highlight the trends discussed.

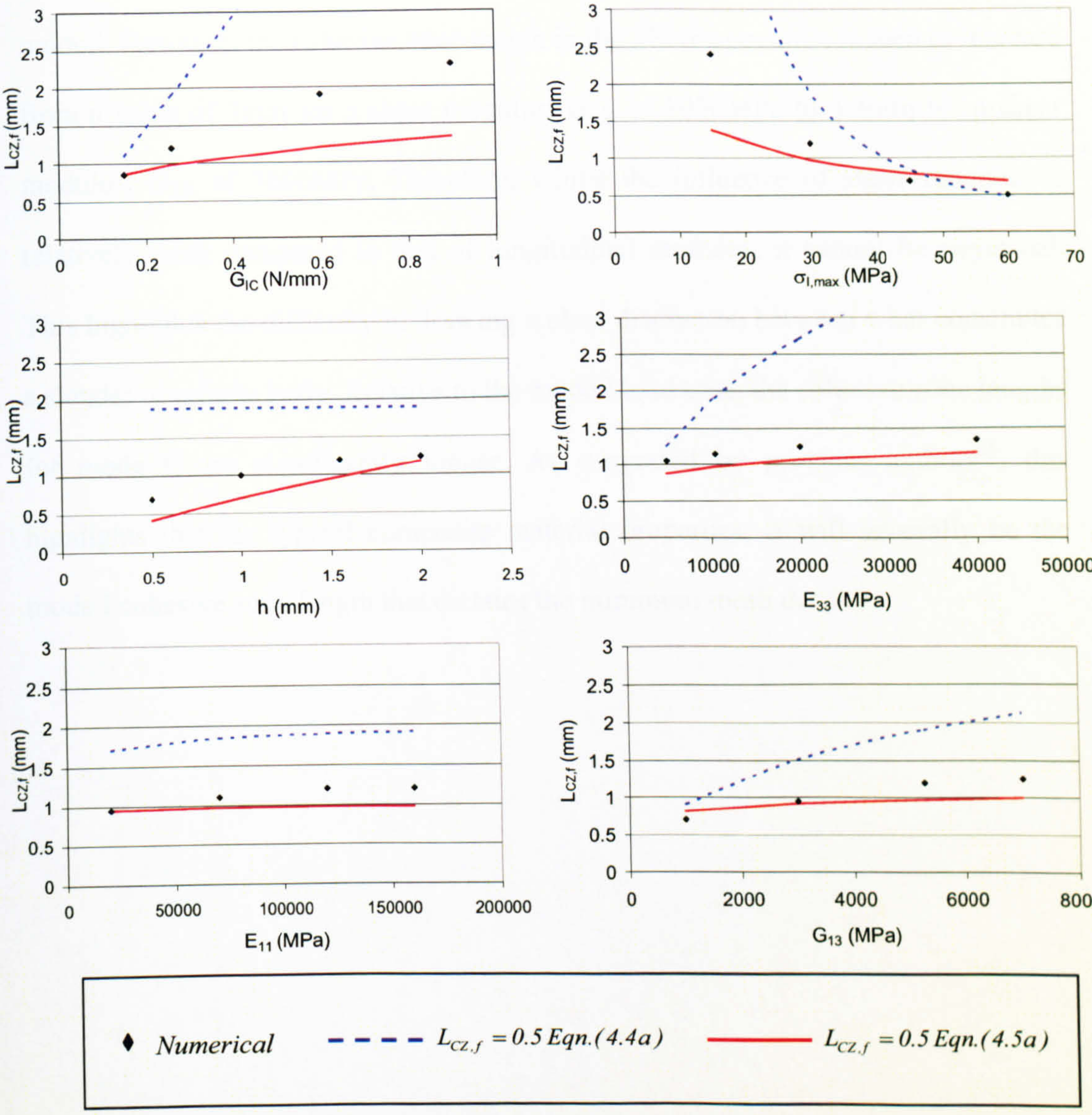

Figure 4.14: Effect of material properties and depth on mode I cohesive zone length for the HTA6376/C benchmark DCB model

Very similar observations can be made for the mode II cohesive zone length results shown in Figure 4.15, for an element length of 0.25mm. Again, equation (4.5b), which accounts for structural depth, generally provides the best correlation with numerical results, but it is necessary to apply $M = 0.5$ to gain a close match. Previous work by Massabo and Cox[89] has shown that the equivalent mode II modulus in the characteristic length equation for slender bodies, $E'_{II,slender}$, takes the same value as the longitudinal modulus, E_{11}, and is influenced by no other elastic

moduli. However, the cohesive zone length in the 3ENF specimen is seen to increase from a value of 3mm for a shear modulus, G_{13}, of 1000MPa to 4.3mm for a shear modulus, G_{13}, of 7000MPa. Therefore, whilst the influence of shear modulus is relatively weak compared to that of longitudinal modulus, it cannot be neglected. This highlights the difficulty in drawing a clear distinction between what constitutes a slender or infinite body. Relative to the mode I load case, the cohesive zone lengths for mode II are significantly longer. As suggested by previous authors[66], this highlights that for typical composite material properties, it will generally be the mode I cohesive zone length that dictates the minimum mesh density.

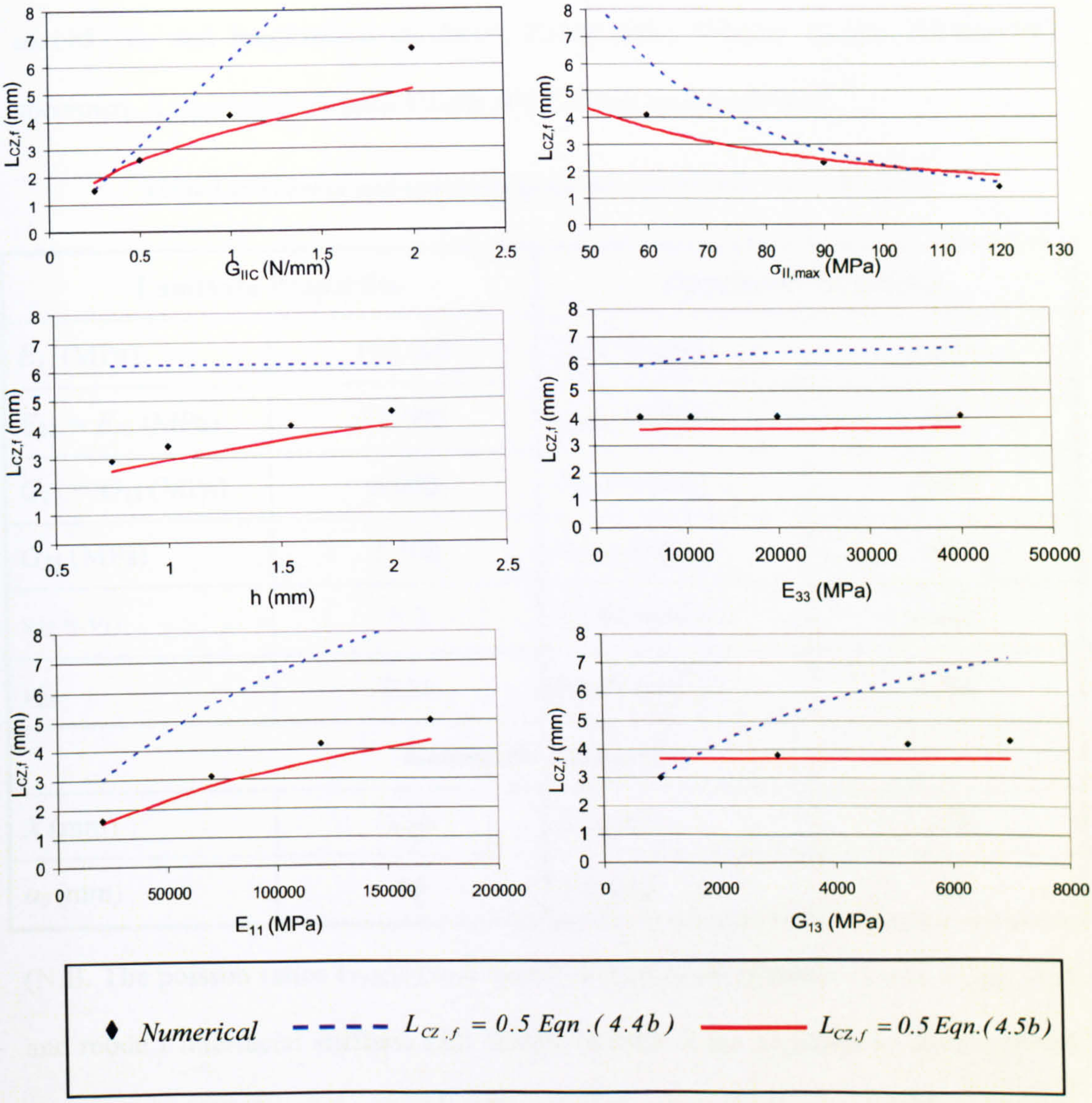

Figure 4.15: Effect of material properties and depth on mode II cohesive zone length for the HTA/6376C benchmark 3ENF model

In order to investigate the accuracy of equations (4.4) and (4.5) in situations where the structural depth has a less significant influence, an additional mode I DCB model was created, using the specimen geometry and material properties shown in table 2. This is based on data provided in reference [84] for a T300/977-2 specimen, which has a significantly increased mode I fracture toughness, G_{IC} (+74%), interfacial strength, $\sigma_{I,max}$ (+200%), specimen depth, h (+32%), initial crack length,

a_0 (+57%), and longitudinal modulus, E_{11} (+25%), relative to the HTA/6376C specimen. A consistent element length of 0.125mm was again used.

Table 4.2: Material and geometric properties for T300/977-2 DCB model

Laminate Properties		**Interfacial Properties**	
E_{11} (MPa)	150,000	G_{IC} (N/mm)	0.352
$E_{22} = E_{33}$ (MPa)	11,000	$\sigma_{I,max}$ (MPa)	60
$G_{12} = G_{13}$ (MPa)	6,000	G_{IIC} (N/mm)	1.002
G_{23} (MPa)	3,700	$\sigma_{II,max}$ (MPa)	60
$\nu_{12} = \nu_{13}$	0.3	K_I (N/mm^3)	1×10^5
ν_{23}	0.51	K_{II} (N/mm^3)	1×10^5
Geometric Properties			
X (mm)	150	h (mm)	1.98
a_0 (mm)	55	B (mm)	20

(N.B. The poisson ratios (ν_{12},ν_{13},ν_{23}), mode II interfacial properties (G_{IIC}, $\sigma_{II,max}$, K_{II}) and mode I interfacial stiffness (K_I) shown in table 2 are identical to those applied for the HTA/6376C specimen. All other properties are consistent with those shown in reference [84] for a T300/977-2 mode I DCB specimen.)

Figure 4.16 highlights that for these material properties, the specimen depth has a much less significant influence across the range of parameters investigated and equation (4.4a) frequently gives a more accurate prediction of numerical cohesive zone length than equation (4.5a). Again, it is necessary to apply $M = 0.5$ to gain a close match to the numerical results. Only for cases where the variation of a material property significantly extends the cohesive zone length, such as reduced interfacial strength or increased fracture toughness, does equation (4.5a) provide the best

correlation. It is always the minimum of the two analytical values, provided by equations (4.4a) and (4.5a) respectively, which provides the closest match to numerical results.

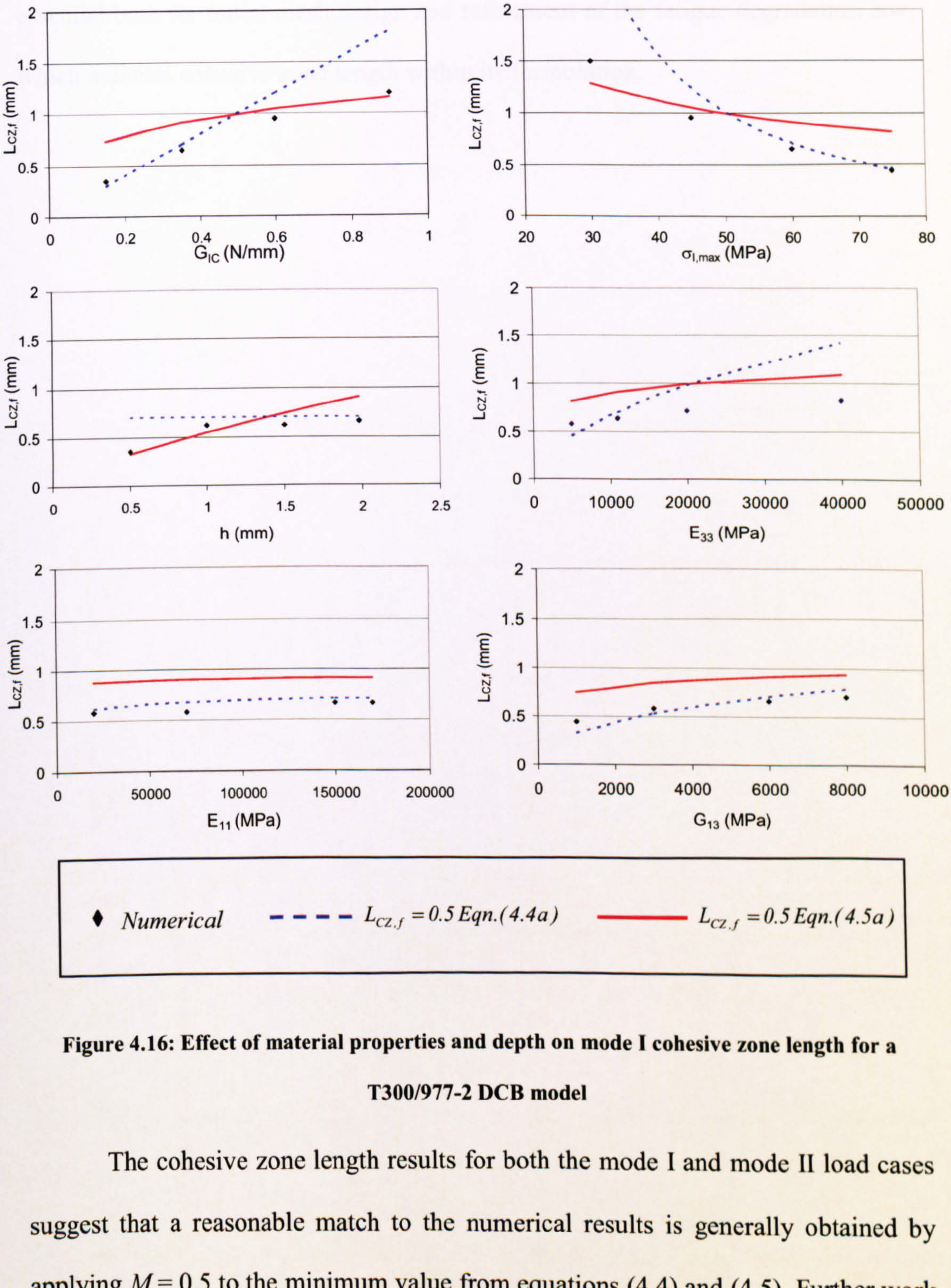

Figure 4.16: Effect of material properties and depth on mode I cohesive zone length for a T300/977-2 DCB model

The cohesive zone length results for both the mode I and mode II load cases suggest that a reasonable match to the numerical results is generally obtained by applying $M = 0.5$ to the minimum value from equations (4.4) and (4.5). Further work

remains to investigate appropriate values of M for alternative traction-displacement laws and for a wider range of crack lengths and structural geometries. The following chapter will demonstrate why predictive formulae for cohesive zone length are essential both for initial mesh design and refinement of the fatigue degradation law, which includes cohesive zone length within its formulation.

5. Fatigue Model Development and Implementation

5.1 Introduction

The previous chapter has indicated that it is possible to gain an accurate value of crack tip strain energy release rate by integrating the traction-displacement response of the element directly adjacent to the numerical crack tip. This gives potential to develop a fatigue degradation law which uses the extracted strain energy release rate to enable a rate of element failure and crack propagation based on the Paris law. There are several significant challenges that must be addressed in allowing this to occur:

1. Simulating cyclic loading within the explicit finite element code LS-Dyna.

2. Defining a minimum required mesh density in order to extract an accurate strain energy release rate value. This is found to be dependent on the length of the cohesive zone, which will be discussed at length in section 5.4. The results presented extend the author's previous work[80] to define the minimum number of interface elements required within the cohesive zone for an accurate global load-displacement analysis.

3. Implementing a fatigue degradation law that is insensitive to mesh density and the number of elements within the cohesive zone once an accurate strain energy release rate is extracted. Due to the desire to implement the fatigue law in complex structural geometries, which may have numerous crack fronts, this must be possible without the computational expense of crack path following algorithms.

Progress made in developing an interface element fatigue degradation algorithm which addresses these challenges is now detailed.

5.2 Benchmark Models

The fatigue algorithm is developed under mode I, mode II and mixed mode loading and validated using a DCB, 4 point ENF and mixed mode specimen in which $G_I = G_{II}$. These specific specimens were selected for two reasons; they enable results gained to be compared with those of previous authors[72,75] and in each case, load can be applied in a manner that provides a constant crack tip strain energy release rate independent of crack length.

For the mode I DCB, a constant crack tip strain energy release rate is achieved by applying a moment, M, to the cantilever tips, as shown in Figure 5.1(a). The magnitude of the strain energy release rate, G_I, is given by[72]:

$$G_I = \frac{M^2}{BEI} \qquad \text{(Eqn. 5.1)}$$

For the mode II 4ENF,

$$G_{II} = \frac{3P^2c^2}{16BEI} \qquad \text{(Eqn. 5.2)}$$

where P and c are the load and length defined in Figure 5.1(b). For the mixed mode case, an identical model to the mode I DCB is used but it is necessary to apply moments of different magnitudes to the two cantilever tips to achieve a mode-ratio of 50%, as shown in Figure 5.1(c). The ratio between the two applied moments, ρ, is given by:

$$\rho = \frac{1 - \frac{\sqrt{3}}{2}}{1 + \frac{\sqrt{3}}{2}} \qquad \text{(Eqn. 5.3)}$$

The strain energy release rates are given by:

$$G_I = G_{II} = \frac{3}{4\left(1+\frac{\sqrt{3}}{2}\right)^2}\frac{M^2}{BEI} \qquad \text{(Eqn. 5.4)}$$

The baseline geometry and material properties (HTA/6376C carbon/epoxy) for the specimens are consistent with those used for the cohesive zone length studies in chapter 4 (refer to figure 4.2 and table 4.1).

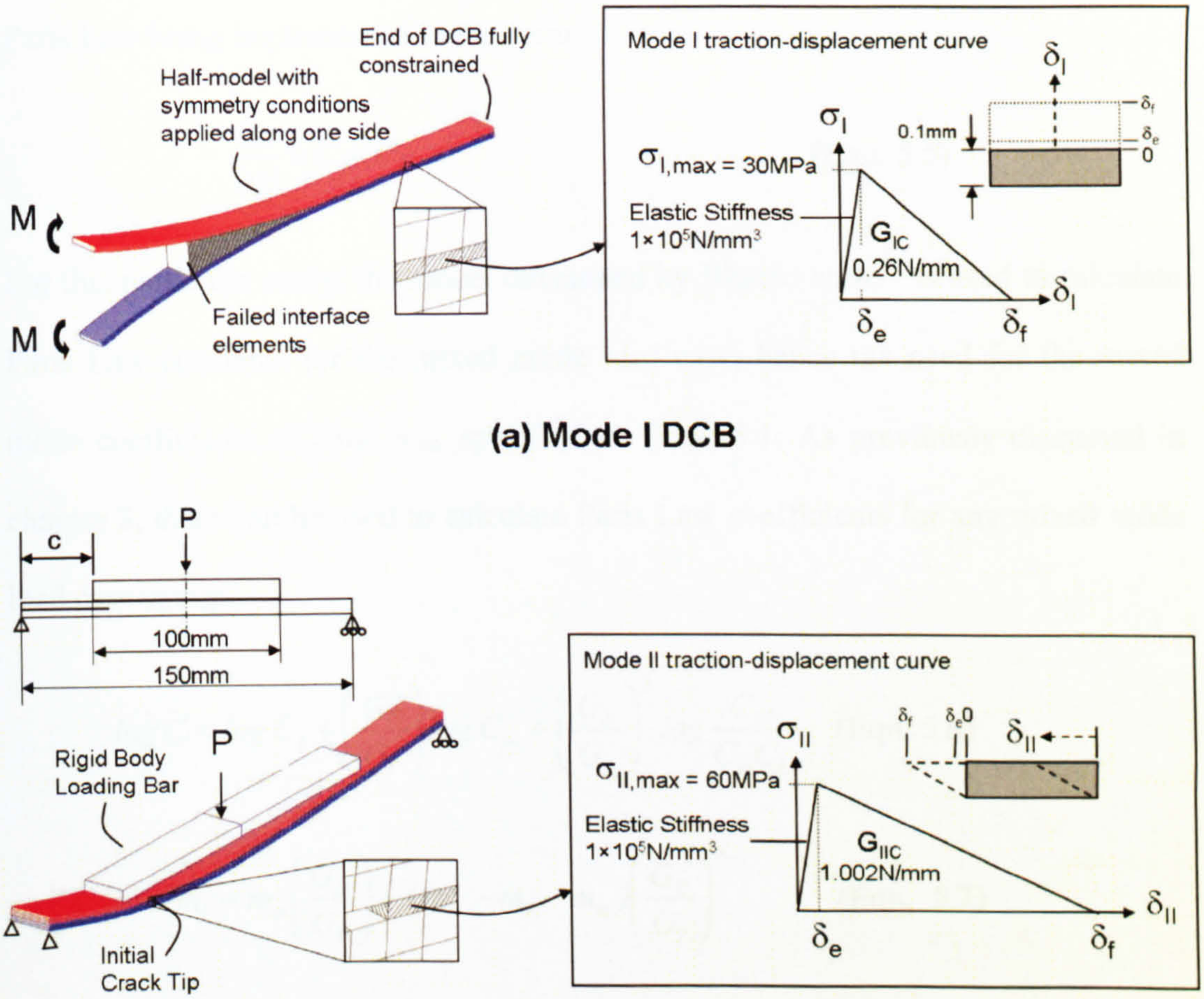

Figure 5.1: Benchmark Models used for Fatigue Law Development

Fatigue properties for HTA/6376C are as shown in Table 5.1 and apply to the Paris Law being implemented in the form:

$$\frac{\partial a}{\partial N} = C\Delta G^m \qquad \text{(Eqn. 5.5)}$$

For this particular study, the model developed by Blanco *et al.*[46] is used to calculate Paris Law constants for the mixed mode load case, hence the need for the mixed mode coefficients, C_m and m_m, specified in Table 5.1. As previously discussed in chapter 3, these can be used to calculate Paris Law coefficients for any mixed mode load case using:

$$\log C = \log C_I + \left(\frac{G_{II}}{G_T}\right)\log C_m + \left(\frac{G_{II}}{G_T}\right)^2 \log\frac{C_{II}}{C_m C_I} \qquad \text{(Eqn. 5.6)}$$

$$m = m_I + m_m\left(\frac{G_{II}}{G_T}\right) + (m_{II} - m_I - m_m)\left(\frac{G_{II}}{G_T}\right)^2 \qquad \text{(Eqn. 5.7)}$$

where G_T, G_I and G_{II} are the total, mode I and mode II strain energy release rates respectively, which are extracted from the interface element traction-displacement response, as previously detailed in chapter 4, section 4.4.

Table 5.1: Fatigue Properties of HTA/6376C[46]

C_I $(mm/cycle)(N/mm)^{-m}$	C_{II} $(mm/cycle)(N/mm)^{-m}$	C_m $(mm/cycle)(N/mm)^{-m}$
2.1	0.12	436000
m_I	m_{II}	m_m
5.09	4.38	5.48

By substituting the mixed mode coefficients, C_m and m_m, into equations (5.8) and (5.9) respectively, the theoretical Paris Law coefficients for a mode ratio of 50% ($G_I = G_{II}$) are found to be $C_{50} = 26.38$ (mm/cycle)(N/mm)$^{-m}$ and $m_{50} = 6.28$. It is important to note that since the fatigue algorithm developed is directly related to the Paris Law through the extraction of strain energy release rate, an alternative Paris Law model can easily be implemented by modifying the section of the code where the Paris Law constants are calculated. This will be demonstrated in the following chapter on Fatigue Law Applications.

5.3 Mesh Design for Fatigue Law Application

Before development of the fatigue damage algorithm can occur, there is a need to define the minimum mesh density required for an accurate value of strain energy release rate to be extracted from crack tip interface elements. This study is now performed by applying a linearly increasing load to the benchmark specimens detailed above. Load control is used for consistency with the fatigue simulations subsequently presented. In each case, the theoretical relationship between applied load and crack tip strain energy release rate (equations (5.3), (5.4) and (5.6)) is compared with numerical results from integrating the traction-displacement response of the crack tip interface element. As shown in Figure 5.2, the principles of this process are identical to those discussed in chapter 4, where specimens were subject to a linearly increasing displacement. The only difference is that under a linearly increasing load, there is no stable propagation phase and instantaneous failure occurs once the critical propagation load is exceeded. Results are presented for various mesh densities and are discussed in relation to the number of elements within the fully developed cohesive zone length at the point of initial crack propagation, L_{CZf}.

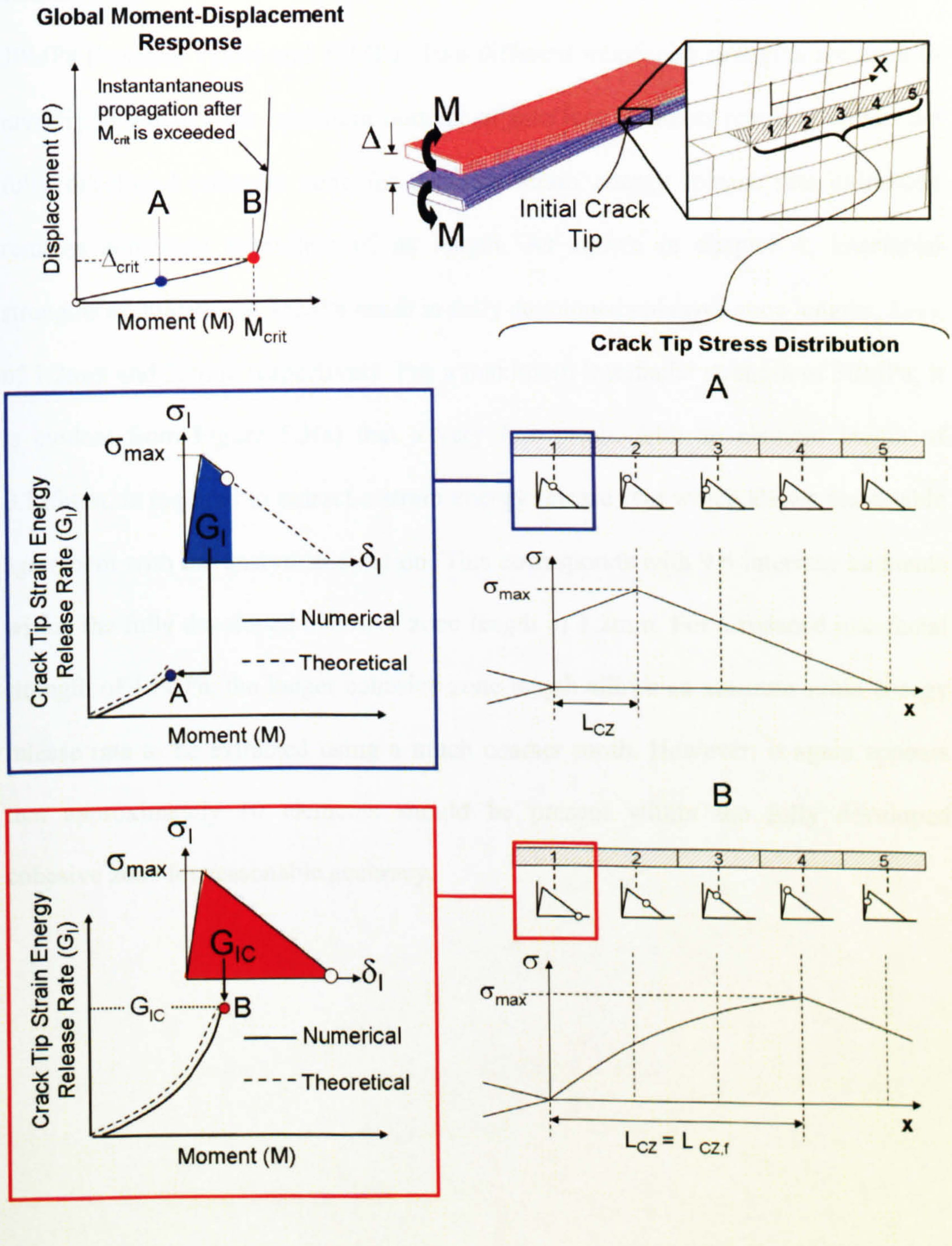

Figure 5.2: Strain energy release rate extraction from the DCB model under a linearly increasing applied moment

For the mode I DCB, strain energy release rate extraction is compared for element lengths of 0.125mm, 0.25mm and 0.5mm at mode I interfacial strengths of 30MPa (baseline value) and 15MPa. Two different interfacial strengths are used to investigate whether the minimum number of interface elements required within the fully developed cohesive zone for accurate strain energy release rate extraction remains consistent regardless of its length. As shown in chapter 4, interfacial strengths of 30MPa and 15MPa result in fully developed cohesive zone lengths, $L_{CZ,f}$, of 1.2mm and 2.4mm respectively. For a maximum interfacial strength of 30MPa, it is evident from Figure 5.3(a) that a very fine mesh, with an element length of 0.125mm, is required to extract a strain energy release rate which shows reasonable agreement with the analytical solution. This corresponds with 9.6 interface elements within the fully developed cohesive zone length of 1.2mm. For a reduced interfacial strength of 15MPa, the longer cohesive zone length allows an accurate strain energy release rate to be extracted using a much coarser mesh. However, it again appears that approximately 10 elements should be present within the fully developed cohesive zone for reasonable accuracy.

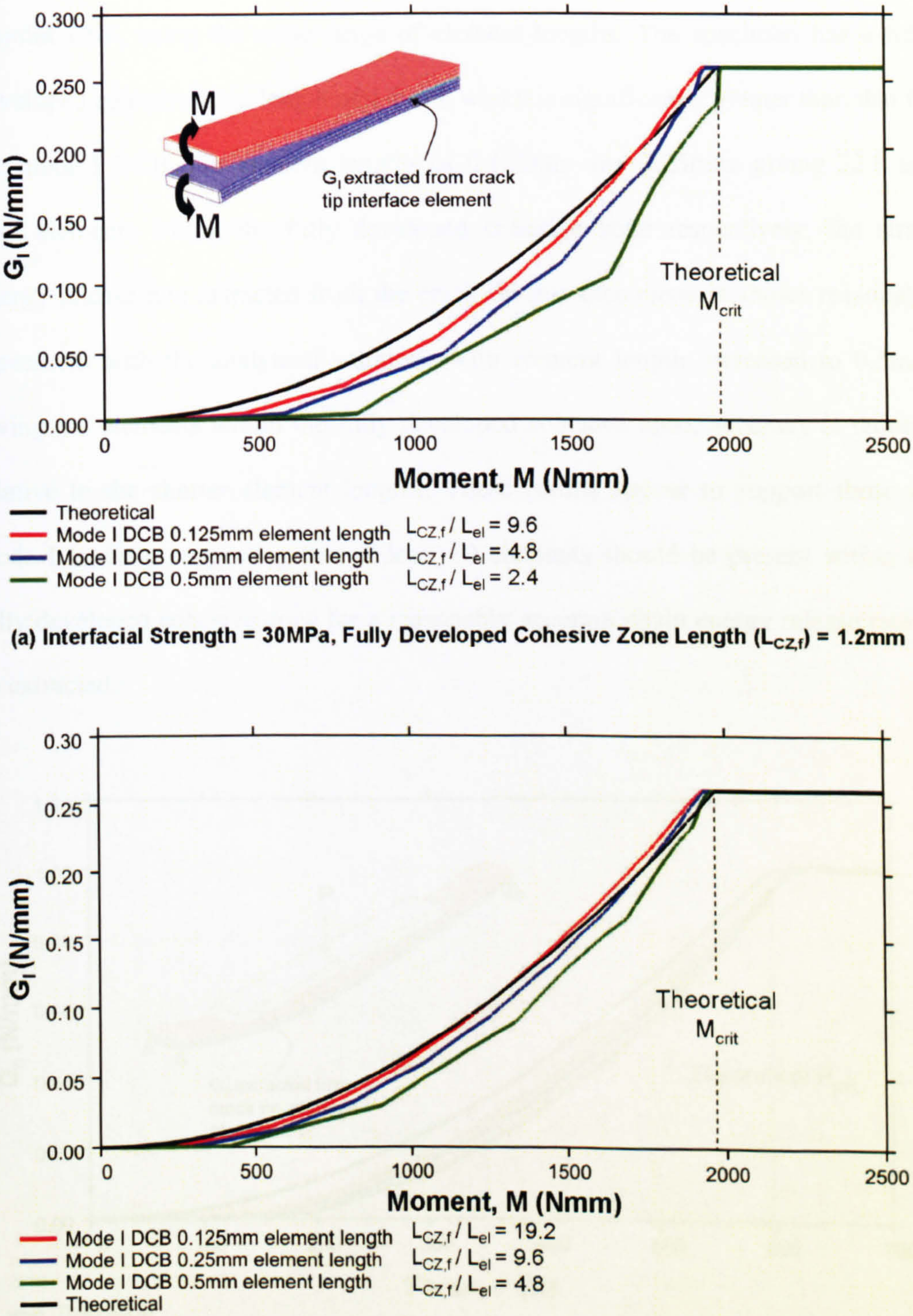

(a) Interfacial Strength = 30MPa, Fully Developed Cohesive Zone Length ($L_{CZ,f}$) = 1.2mm

(b) Interfacial Strength = 15MPa, Fully Developed Cohesive Zone Length ($L_{CZ,f}$) = 2.4mm

Figure 5.3: Mode I strain energy release rate extraction from crack tip element

Figure 5.4 shows strain energy release rate extraction results for the mode II 4 point ENF, using the same range of element lengths. The specimen has a fully developed cohesive zone length of 4.1mm, which is significantly greater than that for the mode I DCB. For element lengths of 0.125mm and 0.25mm, giving 32.8 and 16.4 elements within the fully developed cohesive zone respectively, the strain energy release rate extracted from the crack tip interface element shows reasonable agreement with the analytical solution. With element length increased to 0.5mm, giving 8.2 elements within the fully developed cohesive zone, accuracy is reduced relative to the shorter element lengths. These results appear to support those for mode I loading, suggesting that at least 10 elements should be present within the fully developed cohesive zone for a reasonably accurate strain energy release rate to be extracted.

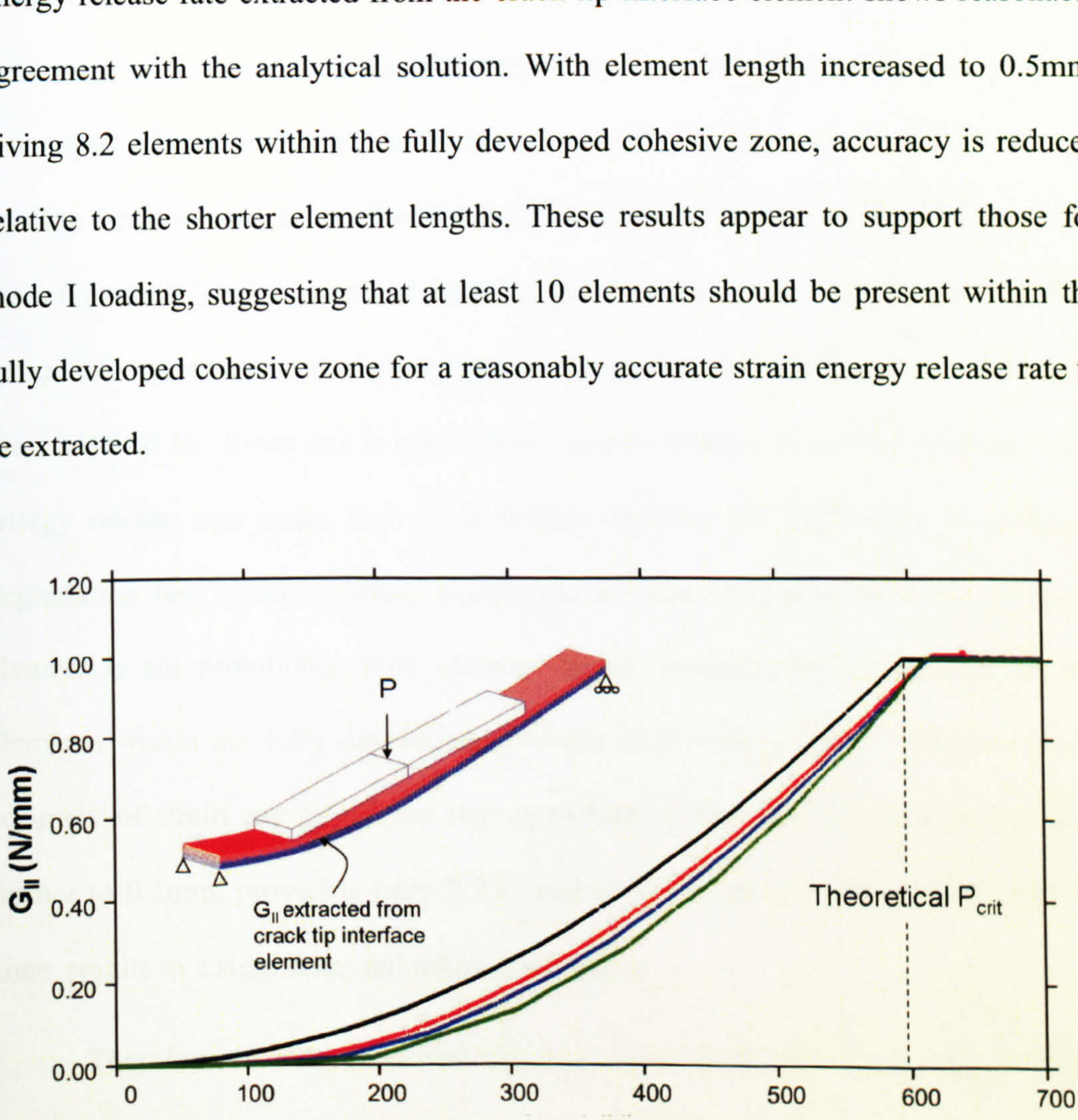

Figure 5.4: Mode II strain energy release rate extraction from crack tip element

Figure 5.5 shows the total strain energy release rate, G_T, extracted from the crack tip interface element in the mixed mode specimen, again using the same range of element lengths. For the shortest element length of 0.125mm (12.8 elements within the fully developed cohesive zone length of 1.6mm), the integrated G_T extracted from 14 interface elements behind the initial crack tip element are also displayed, to emphasise that the total integrated strain energy release rate at failure only matches the analytical fracture toughness, G_C, once the cohesive zone is fully developed. This is due to the variation in mode ratio that elements experience during damage development, as detailed in chapter 4, section 4.4. Despite this characteristic, the integrated G_T value extracted from the initial crack tip interface element exhibits reasonable agreement with the analytical solution until its point of failure at 85% of the analytical G_C. Since this is significantly greater than an allowable crack tip strain energy release rate under high-cycle fatigue loading, the application of a fatigue degradation law based on strain energy release rate extraction from the crack tip element is not prohibited. With element length increased to 0.25mm, giving 6.4 elements within the fully developed cohesive zone, only a minor reduction in the accuracy of strain energy release rate extraction occurs. Increasing element length further to 0.5mm, providing only 2.2 elements within the fully developed cohesive zone, results in a significant reduction in accuracy.

Therefore, in order to ensure that a reasonably accurate strain energy release rate is extracted from the crack tip interface element regardless of mode-ratio, it appears necessary to ensure that at least 10 interface elements are present within the fully developed cohesive zone length.

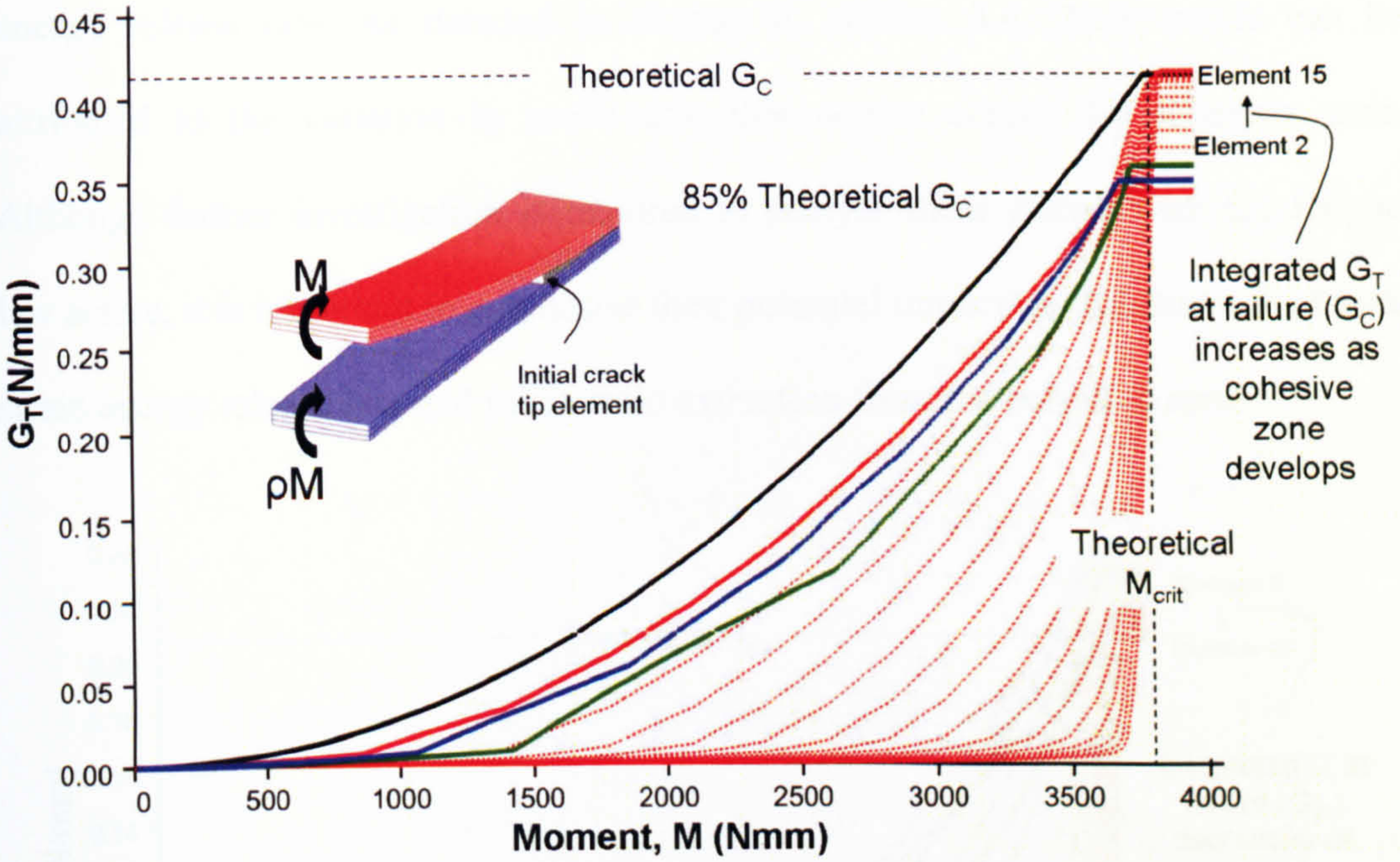

Figure 5.5: Mixed Mode strain energy release rate extraction (GI=GII specimen)

For mixed mode load cases, it is also necessary to analyse the separate mode I and mode II components of strain energy release rate in order to calculate the required rate of crack advance using the Paris Law model. Figure 5.6 displays the integrated G_I and G_{II} strain energy release rate components extracted from the mixed mode specimen's crack tip element for the three distinct element lengths. For consistency with Figure 5.5, G_I and G_{II} components for the 14 elements behind the initial crack tip element are also shown for the shortest element length of 0.125mm. This again highlights that it is only when the cohesive zone has become fully developed that the integrated G_{IC} and G_{IIC} values exhibit reasonable agreement with the analytical solutions. For the crack tip element, the mode I strain energy release rate extracted from the model becomes increasingly greater than the analytical solution as damage development occurs. The opposite trend is true for mode II strain

energy release rate. As detailed in chapter 4, section 4.4, these trends can be attributed to the variation in mode-ratio that occurs across the cohesive zone. Although further investigation is required to analyse these effects with the fatigue law active, it is important to emphasise their potential impact on the accuracy of both strain energy release rate and mode-ratio extraction from the cohesive zone.

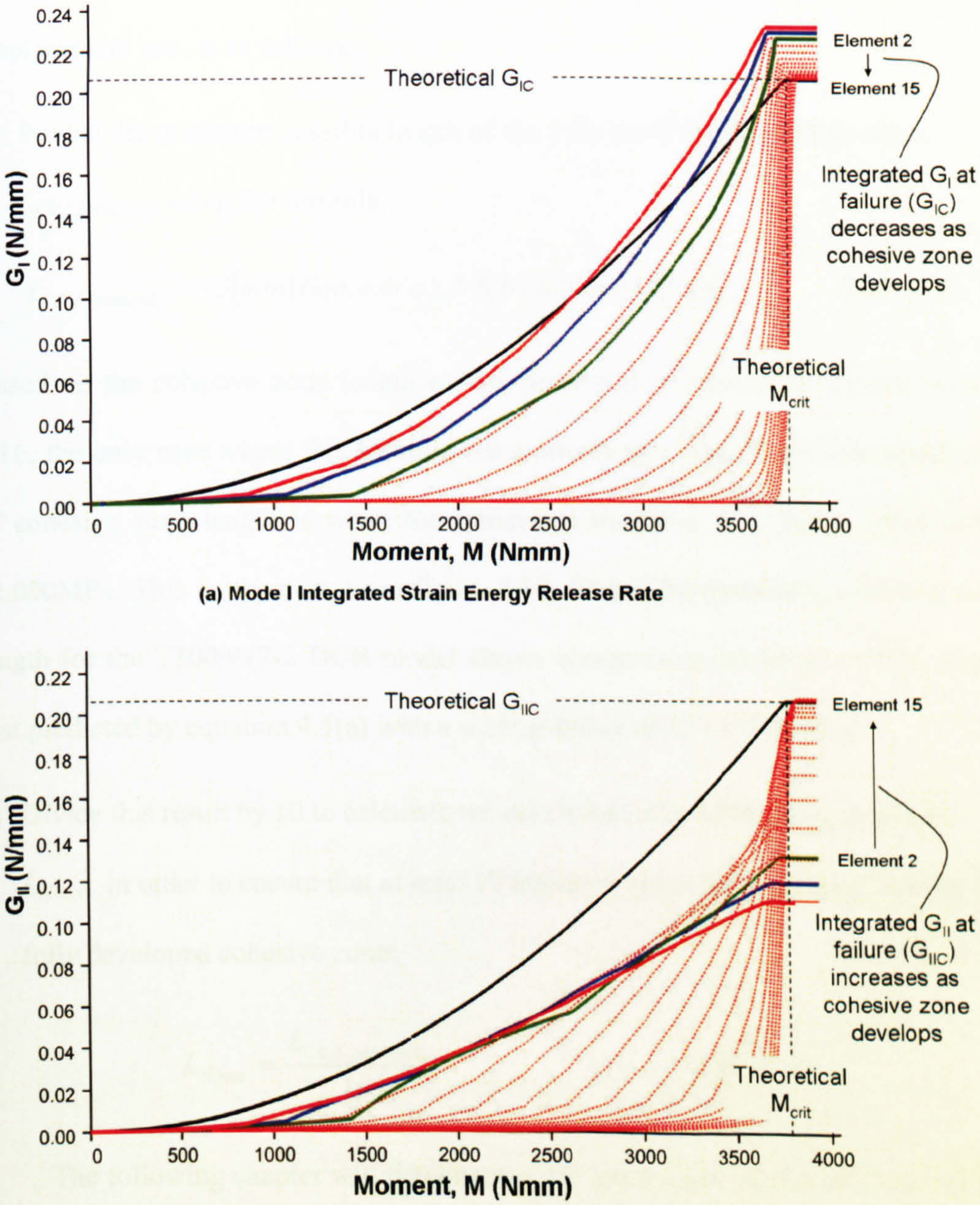

Figure 5.6: Mode I/II strain energy release rate components for mixed mode specimen

In summary, the results presented suggest that in order to extract a reasonably accurate value of strain energy release rate from the crack tip element, the mesh density should be such that a minimum of ten elements exist within the fully developed cohesive zone. Combining these results with the predictive formulae developed for cohesive zone length in chapter 4, section 4.4, the proposed mesh design strategy for a general mixed mode load case, when using a bi-linear traction-displacement law, is as follows:

i) Predict the minimum possible length of the fully developed cohesive zone, $L_{CZ,f,predicted}$, using the formula,

$$L_{CZ,f,predicted} = 0.5[min(Eqn.4.4(a),4.4(b),4.5(a),4.5(b))] \qquad \text{Eqn. (5.8)}$$

Based on the cohesive zone length results presented in chapter 4, figures 4.14 to 4.16, the only case where this formula risks providing a significant over-prediction of cohesive zone length is when the transverse modulus, E_{33}, has a value above 12,000MPa. This is apparent from figure 4.16, where the numerical cohesive zone length for the T300/977-2 DCB model shows a maximum variation of 30% below that predicted by equation 4.5(a) with a scaling factor of $M = 0.5$ applied.

ii) Divide this result by 10 to calculate the maximum allowable element length, $L_{el,max}$, in order to ensure that at least 10 interface elements are present within the fully developed cohesive zone:

$$L_{el,max} = \frac{L_{CZ,f,predicted}}{10} \qquad \text{Eqn. (5.9)}$$

The following chapter will demonstrate the application of this process in finite element mesh design for typical structural applications.

5.4 Fatigue Simulation within an Explicit Code

As previously highlighted in chapter 3, there are two potential methods of modelling interface element damage accumulation under fatigue loading within a numerical code:

i) Tracking loading/unloading and degrading stiffness on a cycle-by-cycle basis.

ii) Applying a cycle-jump strategy, where the applied numerical load remains constant and interface element strength is degraded based on a discrete number of elapsed cycles after each model time-step.

For high-cycle fatigue, a cycle-jump strategy offers a more computationally efficient approach, avoiding the need to continually monitor loading/unloading hysteresis for what could extend to hundreds of thousands of cycles until failure. Within LS-Dyna, the model time-step is dictated by a combination of element size and material properties but is generally significantly lower than that allowable in an implicit code. Therefore, a key issue to address in the development of the fatigue law is the relationship between time-step size and elapsed fatigue cycles. This must ensure that damage accumulates in sufficiently small increments to guarantee model stability, whilst avoiding excessively long model run-times.

For all the studies conducted in this chapter, fatigue is simulated by first applying a gradually increasing quasi-static load from zero to the maximum value in each fatigue cycle. This load is then held constant for a period long enough to allow any residual dynamic effects to stabilise, before the fatigue algorithm is activated. Once activated, the applied numerical load remains constant, but the fatigue law degrades the strength of interface elements based on the assumption of cyclic loading, allowing crack advance to occur (see Figure 5.7).

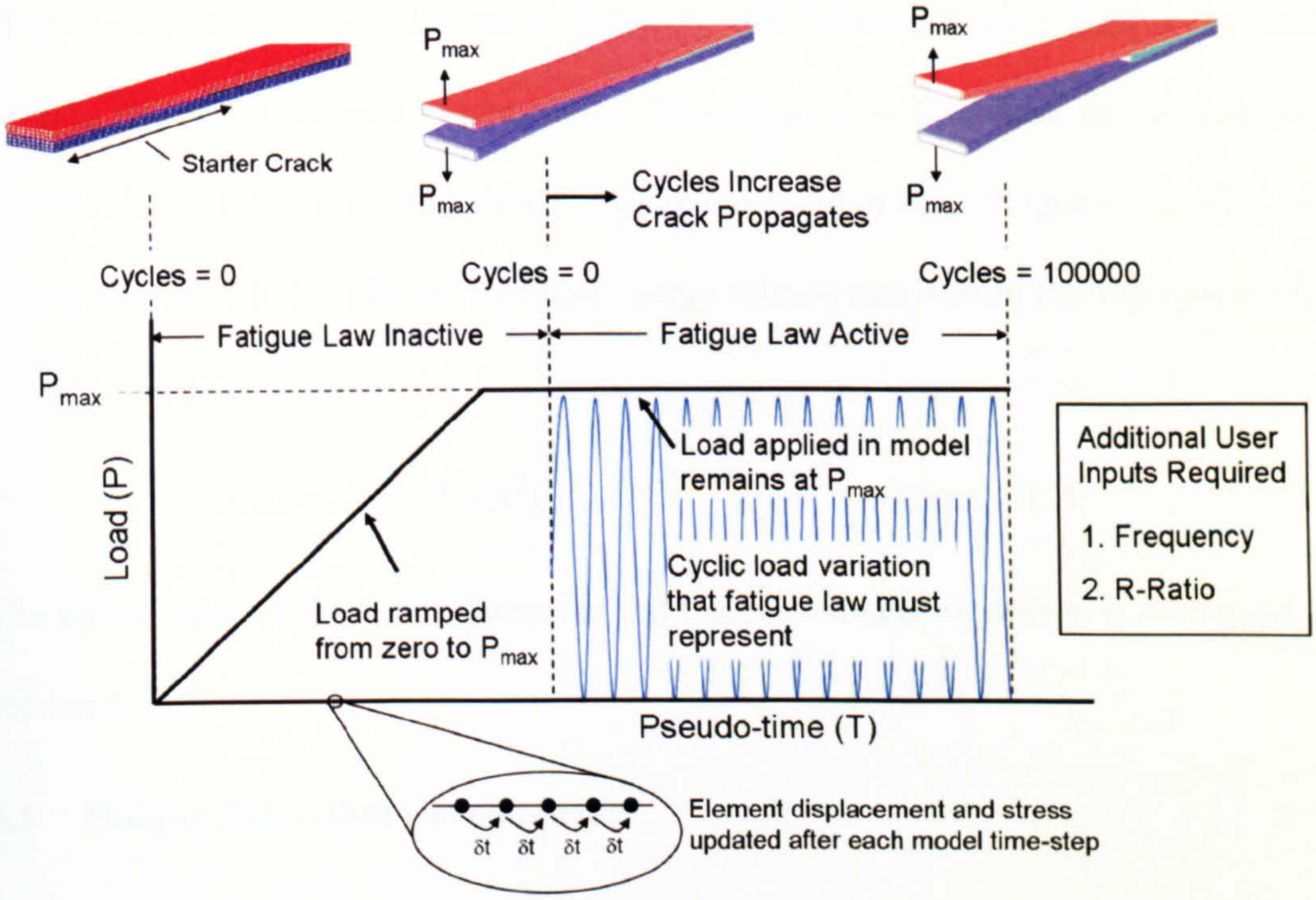

Figure 5.7: Simulation of cyclic loading within LS-Dyna

Since the applied numerical load remains constant, the user must supply the following model input parameters for cyclic loading to be accurately simulated:

i) Cycle frequency, $\partial N/\partial t$, expressed as cycles per second of LS-Dyna pseudo-time. This enables the crack propagation rate, $\partial a/\partial N$, expressed in terms of distance per cycle, to be converted to distance per unit of pseudo-time, $\partial a/\partial t$.

$$\frac{\partial a}{\partial t} = \frac{\partial a}{\partial N}\frac{\partial N}{\partial t} \qquad \text{(Eqn. 5.10)}$$

A value for $\partial N/\partial t$ must be selected which provides a good balance between model stability and reasonable model run-times. This can vary from values of approximately 1000 for load levels close to the critical fracture energy, G_C, to 1,000,000 for load levels close to the fatigue threshold, G_{th}. Details of how the crack propagation rate is related to damage growth across each individual interface element are provided in the following section.

ii) R-Ratio, defined as the ratio between the minimum and maximum load (P_{min}/P_{max}) within each fatigue cycle. Assuming tension-tension fatigue loading, this allows the maximum strain energy release rate in each fatigue cycle, G_{max}, to be converted to the change in strain energy release rate during each fatigue cycle, ΔG, using[45]:

$$\Delta G = G_{max}\,(1 - R^2) \qquad \text{(Eqn. 5.11)}$$

The significance of these parameters in the fatigue damage algorithm is discussed in section 5.5.

5.5 Fatigue Algorithm Development

The main difficulties in developing an accurate fatigue degradation algorithm linked directly to the Paris Law stem from development of the cohesive zone. In order to highlight these, a fatigue algorithm is presented which assumes that damage can be isolated to the element directly adjacent to the crack tip. In reality, with no crack path following algorithm, this is impossible to achieve because there is no way of detecting an interface element's position in relation to the crack tip from information available at the element level only. Hence, unwanted fatigue degradation occurs in adjacent interface elements within the cohesive zone before they in turn become the crack tip element. Numerical results are used to demonstrate this effect and to highlight its dependence on the number of elements within the cohesive zone, which is determined by both mesh density and cohesive zone length. An improved formulation is then presented, which takes into account fatigue damage accumulation in all interface elements within the cohesive zone.

5.5.1 Initial Fatigue Law Formulation

Provided that the mesh is sufficiently fine to extract an accurate value of strain energy release rate from the crack tip element, this can be converted to ΔG using the user-defined R-ratio in conjunction with equation (5.11). Assuming we also have appropriate Paris law constants, C and m, for the relevant mode-ratio (calculated using equations (5.6) and (5.7)), the required rate of crack propagation, $\partial a/\partial N$, can be calculated using the Paris law (equation (5.5)). If there is negligible change in strain energy release rate as the crack advances by the crack tip element's length, $L_{el,tip}$, the number of cycles required for the crack to advance by this length, N_F, is given by:

$$N_F = L_{el,tip} \Big/ \frac{\partial a}{\partial N} \qquad \text{(Eqn. 5.12)}$$

It should be noted that the element length specified is always the length in the direction of crack propagation. Presenting the damage formulation with respect to element length, as opposed to element area, preserves consistency with Paris Law $\partial a/\partial N$ data and avoids the need to account for the number of elements across the crack front. For the benchmark cases presented, this is trivial, as only one element exists across the width and the crack can only propagate along the length of each specimen. It will subsequently be shown that in the final version of the fatigue law (fatigue law 2), the only length present in the damage formulation is the fully developed cohesive zone length, $L_{CZ,f}$, in the direction of crack propagation.

Since the fatigue law is to be implemented in an explicit code, it is not possible to instantaneously fail the crack tip element and update the number of elapsed fatigue cycles by N_F. Instead, the element's strength must be incrementally degraded at a rate satisfying the number of cycles to failure. For this to be achieved,

a fatigue damage parameter, d_f, is used as a measure of crack advance across the interface element. As shown by Figure 5.8, this is added to the static damage parameter, d_s, giving a value for total damage accumulated, D_{tot}.

$$D_{tot} = d_s + d_f \qquad \text{(Eqn. 5.13)}$$

D_{tot} is used to calculate the interface element stress, σ_m, after each model time-step, with element failure occurring when the total damage (D_{tot}) reaches unity:

$$\sigma_m = \sigma_{m,max}(1 - D_{tot}) \qquad \text{(Eqn. 5.14)}$$

At time $t = t_0$, the point at which the fatigue law becomes active, no fatigue cycles have elapsed ($N = 0$) and the fatigue damage parameter is equal to zero, $d_f = d_{f,N=0} = 0$. If the strain energy release rate can be assumed to remain constant as the element fails, which implies that the static damage parameter also remains constant (i.e. there is no change in the interface element's relative displacement, as shown in Figure 5.8), the ratio of element crack length to total element length is given by:

$$\frac{L_D}{L_{el}} = \frac{d_f}{1 - d_s} \qquad \text{(Eqn. 5.15)}$$

As shown by Figure 5.8, this is consistent with having zero element crack length when $d_f = 0$ and the crack length being equal to the element length when $d_f = 1 - d_s$ (i.e. $D_{tot} = 1$) and the element fails.

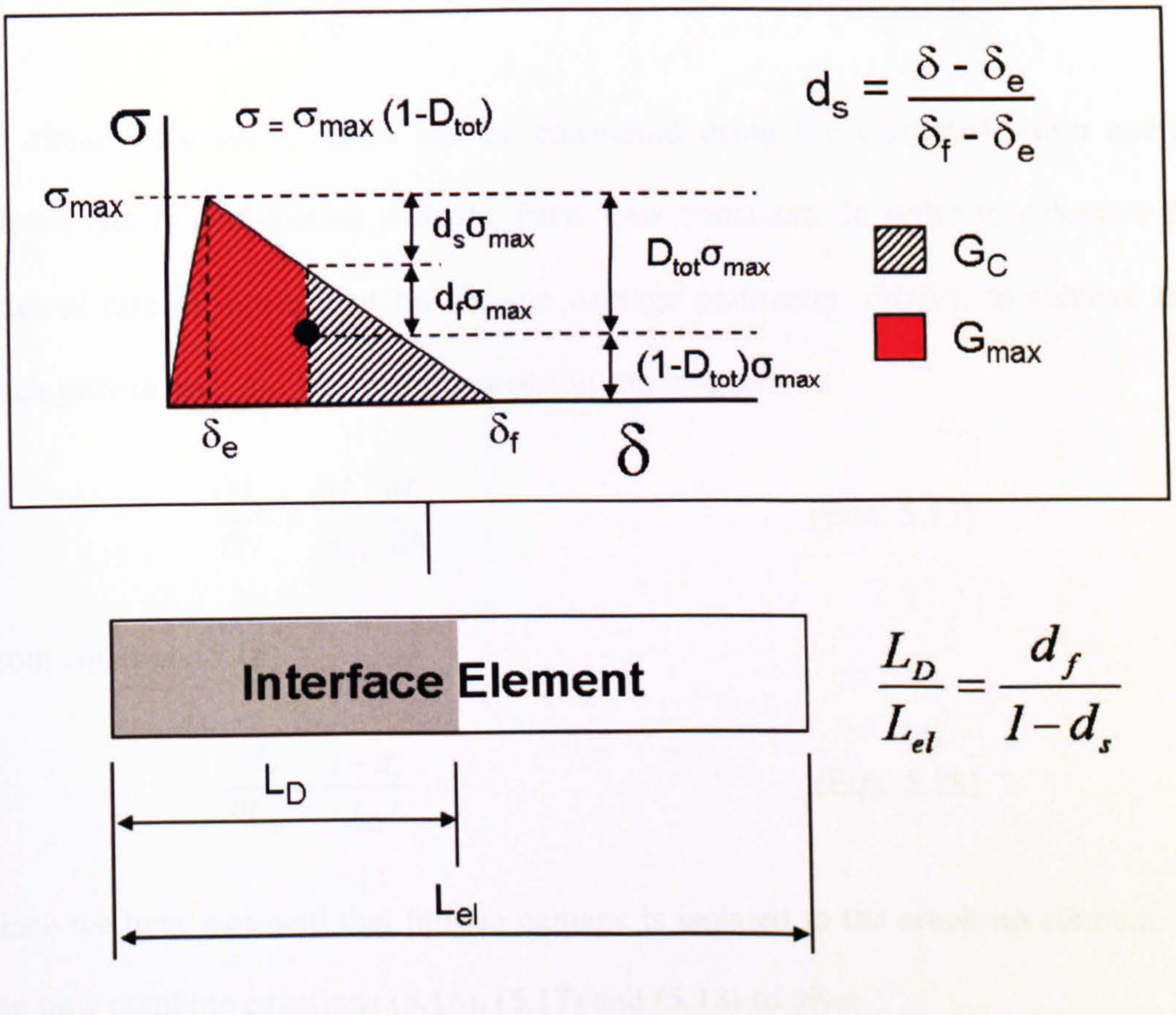

Figure 5.8: Interface element static and fatigue damage

Since the aim is to maintain a direct link with linear elastic fracture mechanics, the static damage parameter is considered to relate purely to the crack tip strain energy release rate and does not contribute to an increase in fatigue crack length. Also, although in reality there must be some increase in the static damage parameter (interface element relative displacement) as the element undergoes fatigue failure, this will be shown to be minor and hence, does not significantly affect the integrated strain energy release rate.

Based on the assumption that fatigue damage can be restricted to purely the crack tip element, the rate of damage length increase in the crack tip element is equal to the rate of crack advance:

$$\frac{\partial a}{\partial N} = \frac{\partial L_D}{\partial N} \qquad \text{(Eqn. 5.16)}$$

As already discussed, $\partial a/\partial N$ can be calculated using the extracted strain energy release rate in conjunction with the Paris Law constants. In order to calculate the required rate of increase of the fatigue damage parameter, $\partial d_f/\partial N$, to achieve this crack growth rate, the following expression can be used:

$$\frac{\partial d_f}{\partial N} = \frac{\partial d_f}{\partial L_D}\frac{\partial L_D}{\partial N} \qquad \text{(Eqn. 5.17)}$$

From equation (5.15),

$$\frac{\partial d_f}{\partial L_D} = \frac{1-d_s}{L_{el}} \qquad \text{(Eqn. 5.18)}$$

Since we have assumed that fatigue damage is isolated to the crack tip element, we can now combine equations (5.16), (5.17) and (5.18) to give:

$$\frac{\partial d_f}{\partial N} = \frac{1-d_s}{L_{el}}\frac{\partial a}{\partial N} \qquad \text{(Eqn. 5.19)}$$

where $\partial a/\partial N$ is calculated using the extracted strain energy release rate and mode-ratio in conjunction with the Paris law constants (see equations (5.5), (5.6) and (5.7)). For each model time-step, the fatigue damage parameter is updated using:

$$d_{f,new} = d_{f,old} + \delta N\frac{\partial d_f}{\partial N} = d_{f,old} + f\delta t\frac{\partial d_f}{\partial N} \qquad \text{(Eqn. 5.20)}$$

where f is the user-defined number of cycles per second of LS-Dyna pseudo-time,

$$f = \frac{\partial N}{\partial t} \qquad \text{(Eqn. 5.21)}$$

The accuracy of this fatigue algorithm relies on the following assumptions being satisfied:

i) An accurate value of strain energy release rate is gained by integrating the traction-displacement response of the crack tip interface element. This has been shown to be a reasonable assumption provided at least 10 elements are present within the cohesive zone.

ii) This value of strain energy release rate remains constant as the element undergoes fatigue failure (i.e. there is no significant variation in the interface element relative displacement).

iii) Fatigue damage is isolated to purely the crack tip element. Once this element fails, the algorithm becomes active on the new crack tip element, for which identical assumptions apply.

Figure 5.9 summarises this algorithm and the assumptions made, using the example of the mode I DCB specimen.

Example Parameters: $\Delta G/G_c = 0.35$, R = 0, $da/dN = 1 \times 10^{-6}$ mm/cycle
1s pseudo-time = 10,000 cycles, element length = 0.1mm

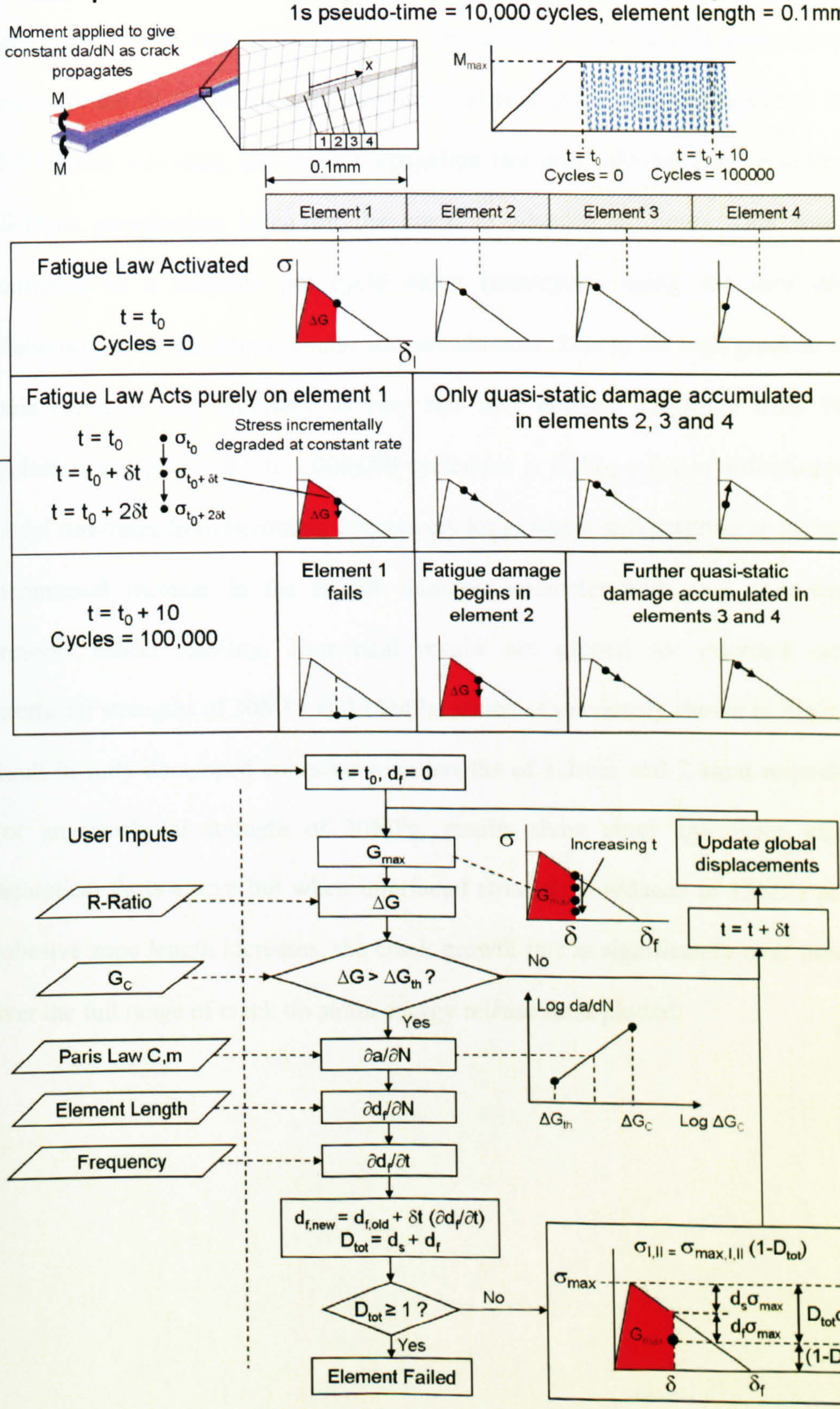

Figure 5.9: Summary of fatigue algorithm assuming isolation of damage to crack tip element

Figure 5.10 compares experimental crack propagation rate results and their Paris Law line of best fit (denoted as 'Theoretical Paris Curve') with numerical results for the DCB specimen. In the numerical analyses, a consistent element length of 0.125mm was used, and crack propagation rate was calculated by recording the LS-Dyna pseudo-time taken for the crack to advance by 5mm. This was then converted to a distance per cycle value (mm/cycle) using the user defined relationship between fatigue cycles and pseudo-time. Due to the high gradient of the Paris curve, it was necessary to vary this user defined frequency from 10,000 cycles/sec at $G_I/G_{IC} = 0.6$ to 1,000,000 cycles/sec at $G_I/G_{IC} = 0.2$ in order to prevent model run-times from becoming excessively long, whilst still ensuring an acceptable incremental increase in the fatigue damage parameter with each time-step, to preserve model stability. Numerical results are plotted for interface element interfacial strengths of 30MPa and 15MPa, which as previously shown in Figure 5.3, result in fully developed cohesive zone lengths of 1.2mm and 2.4mm respectively. For an interfacial strength of 30MPa, results show close agreement with the theoretical Paris Curve but when interfacial strength is reduced to 15MPa and the cohesive zone length increases, the crack growth rate is significantly over-predicted over the full range of crack tip strain energy release rates plotted.

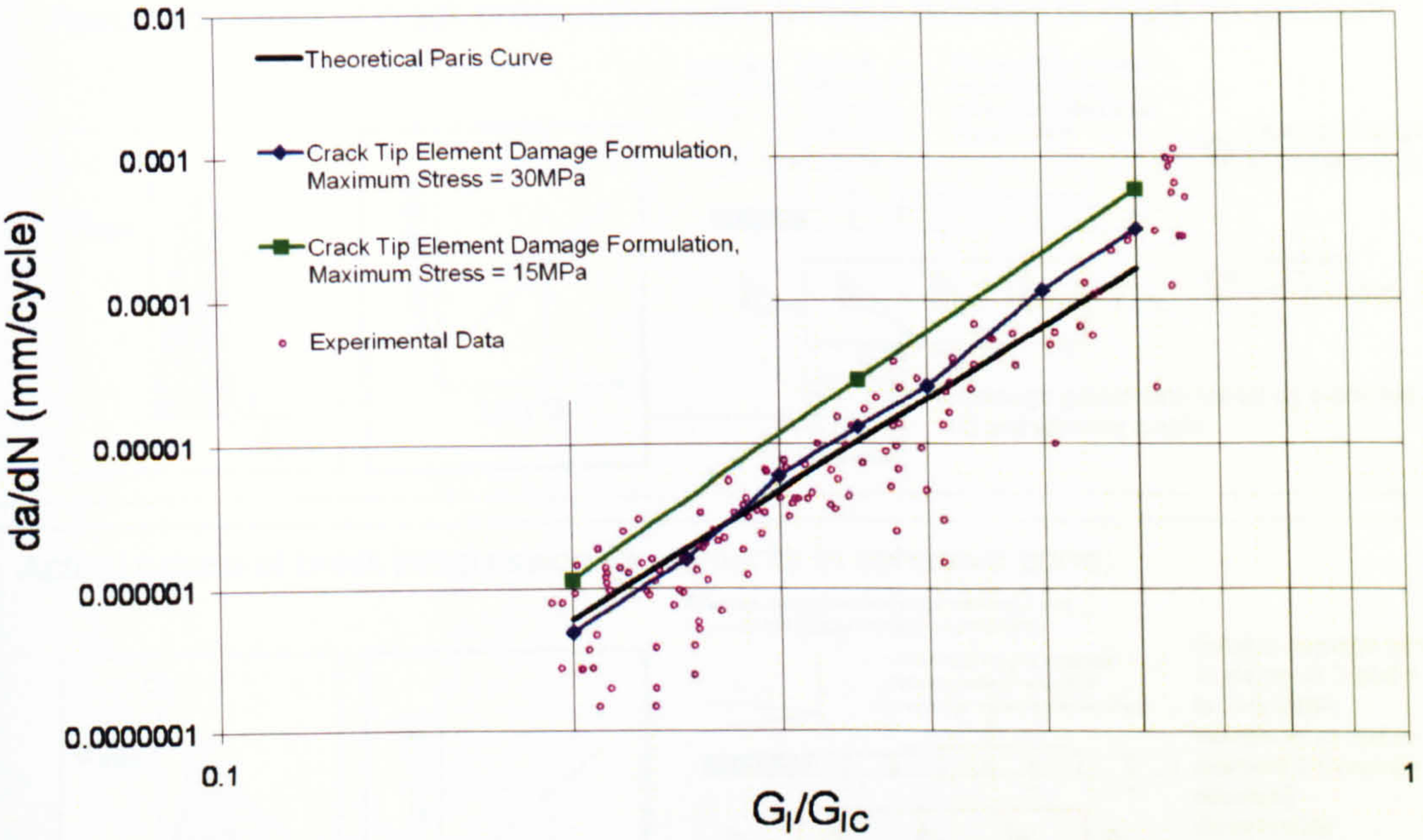

Figure 5.10: Paris Law Results for mode I DCB using initial fatigue law

As shown by Figure 5.11, these results can be explained by the increased number of interface elements within the cohesive zone when interfacial strength is decreased. With no crack path following algorithm, fatigue damage cannot be isolated to purely the crack tip element and unwanted fatigue damage can occur in interface elements within the cohesive zone that are not directly adjacent to the crack tip. Hence, if element length remains constant and the cohesive zone length increases, so too does the crack propagation rate. Exactly the same trend can be shown for cases where cohesive zone length remains constant but element length varies (i.e. it is the number of elements within the cohesive zone that matters, which is influenced by both mesh density and cohesive zone length).

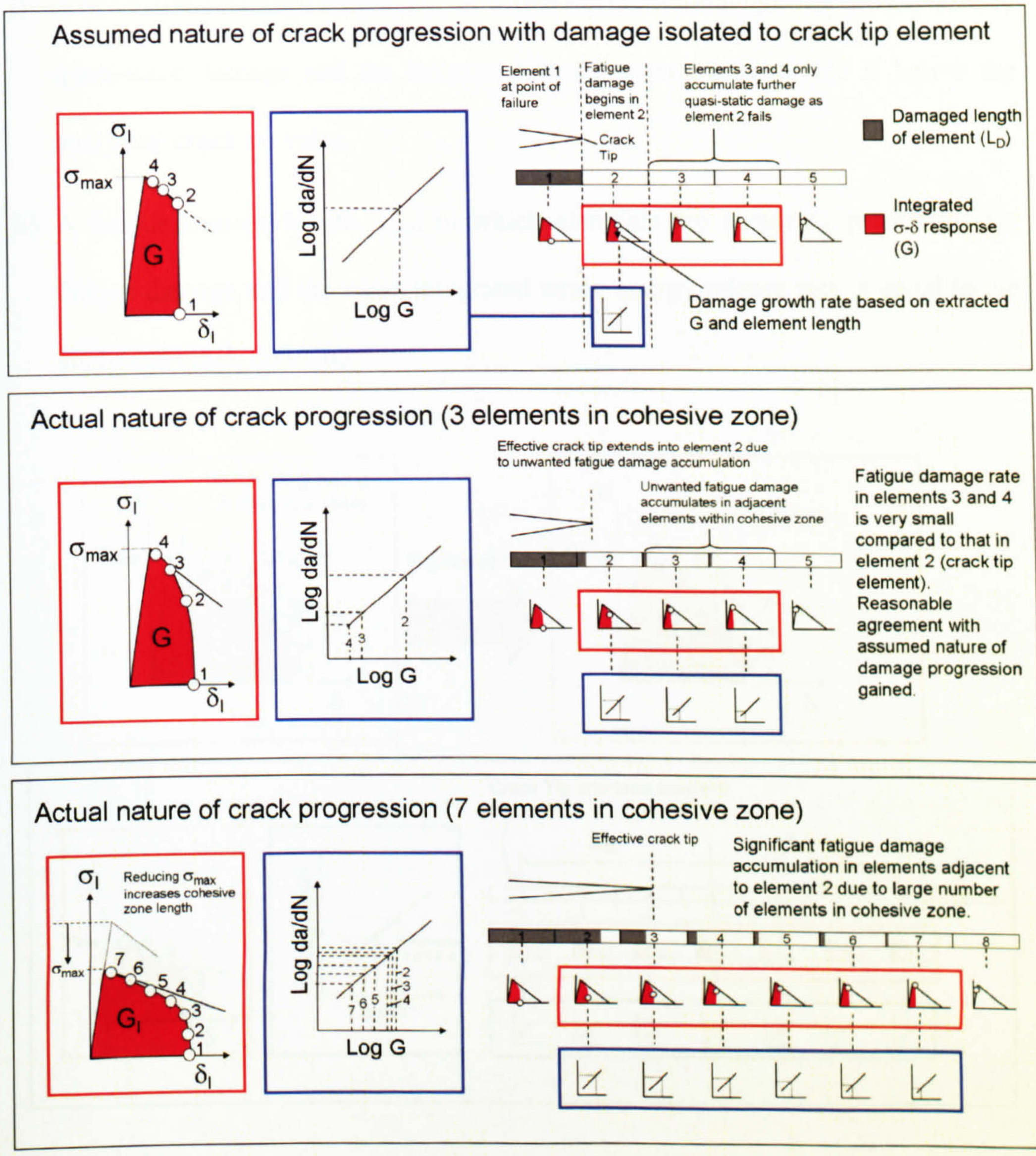

Figure 5.11: Sensitivity of initial fatigue law to number of elements within cohesive zone

5.5.2 Improved Fatigue Law Formulation

In order to correct for the sensitivity of the initial fatigue law to the number of elements within the cohesive zone, a modified damage algorithm has been developed. Noting the origin of the deficiencies of the first fatigue damage formulation, it can be seen that the cohesive zone can be split into two regions, as shown in Figure 5.12:

i) A quasi-static damage length, L_{qs}, in which elements are acquiring predominantly quasi-static damage and the integrated strain energy release rate is below the analytical crack tip value.

ii) A fatigue damage length, L_{fat}, in which elements are acquiring predominantly fatigue damage and the mean integrated strain energy release rate is equal to the analytical crack tip value.

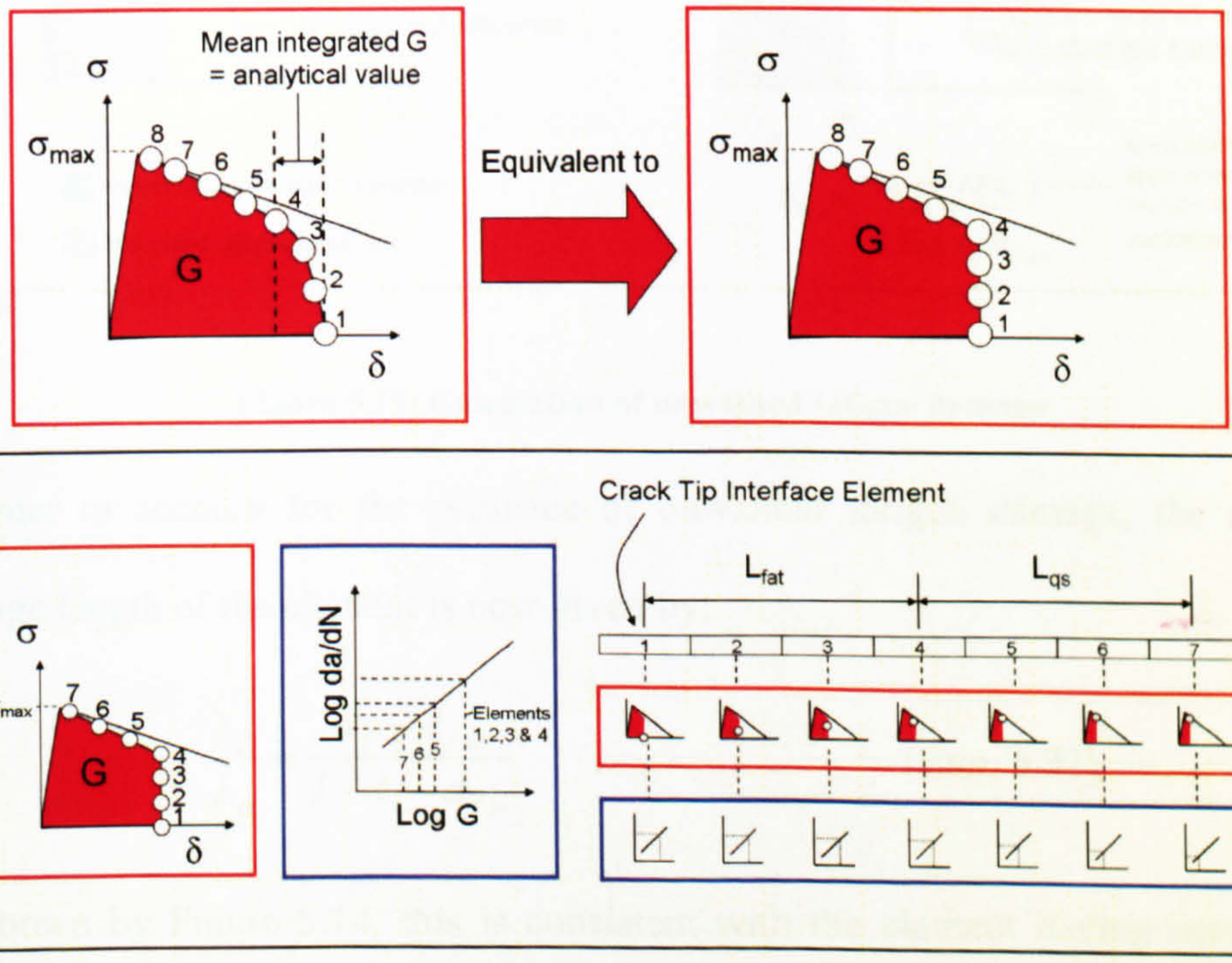

Figure 5.12: Equivalent model showing quasi-static and fatigue damage lengths

Since each interface element has no knowledge of its position within the cohesive zone, the accumulation of some fatigue damage in the quasi-static region cannot be prevented. Hence, it is necessary to account for this 'unwanted fatigue damage,' $d_{f,u}$, so that further fatigue damage can be applied at the correct rate when the element enters the fatigue damage zone. This is achieved by subtracting the integrated area under the actual traction-displacement response from the traction-displacement response assuming no fatigue damage, as shown in Figure 5.13. By

approximating the resultant area as a triangle, the magnitude of unwanted fatigue damage can be calculated.

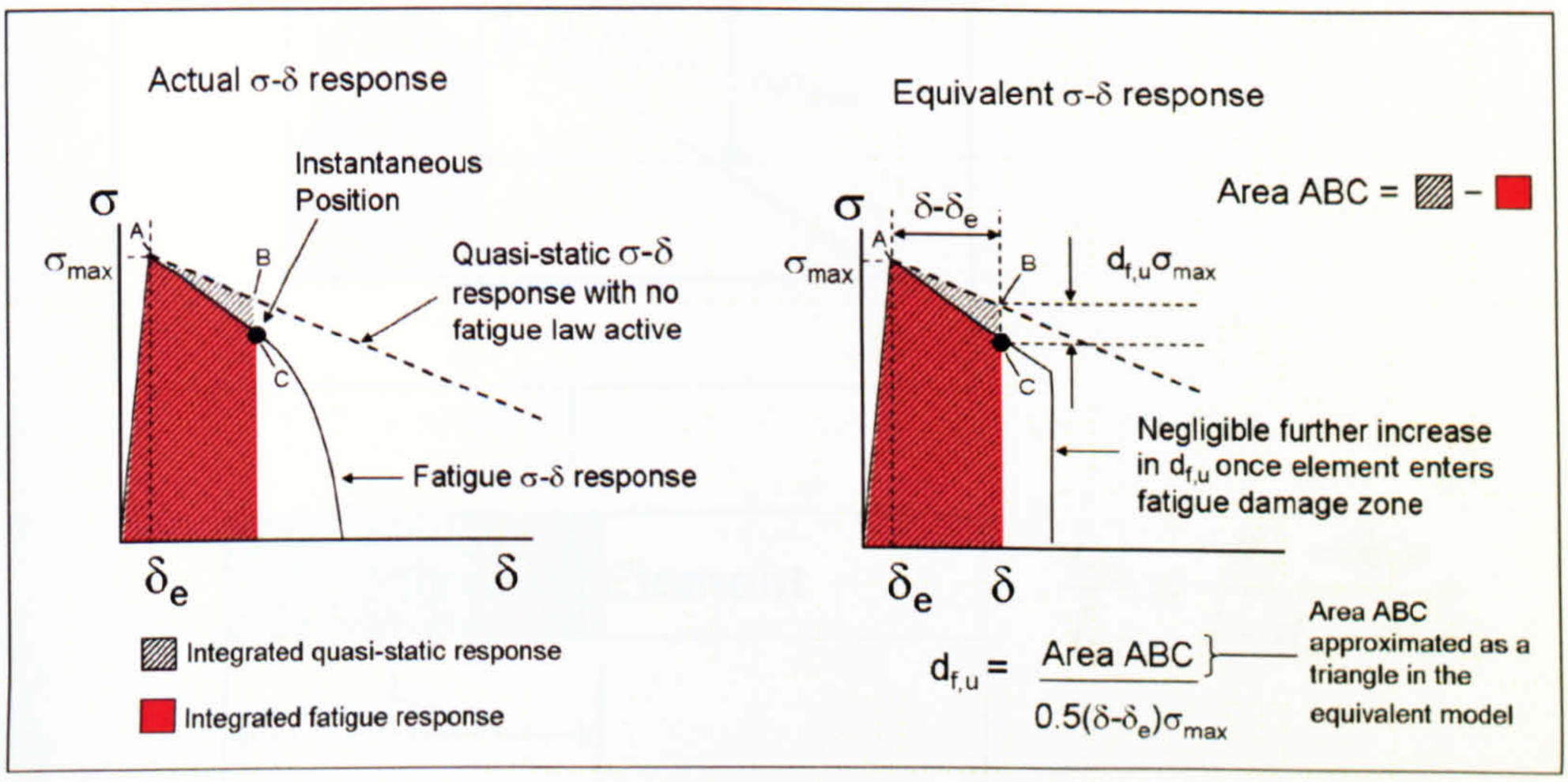

Figure 5.13: Calculation of unwanted fatigue damage

In order to account for the presence of unwanted fatigue damage, the assumed damage length of the element is now given by:

$$\frac{L_D}{L_{el}} = \frac{d_f - d_{f,u}}{1 - d_s - d_{f,u}} \qquad \text{(Eqn. 5.22)}$$

As shown by Figure 5.14, this is consistent with the element having zero fatigue damage length at the point of entry to the fatigue damage zone.

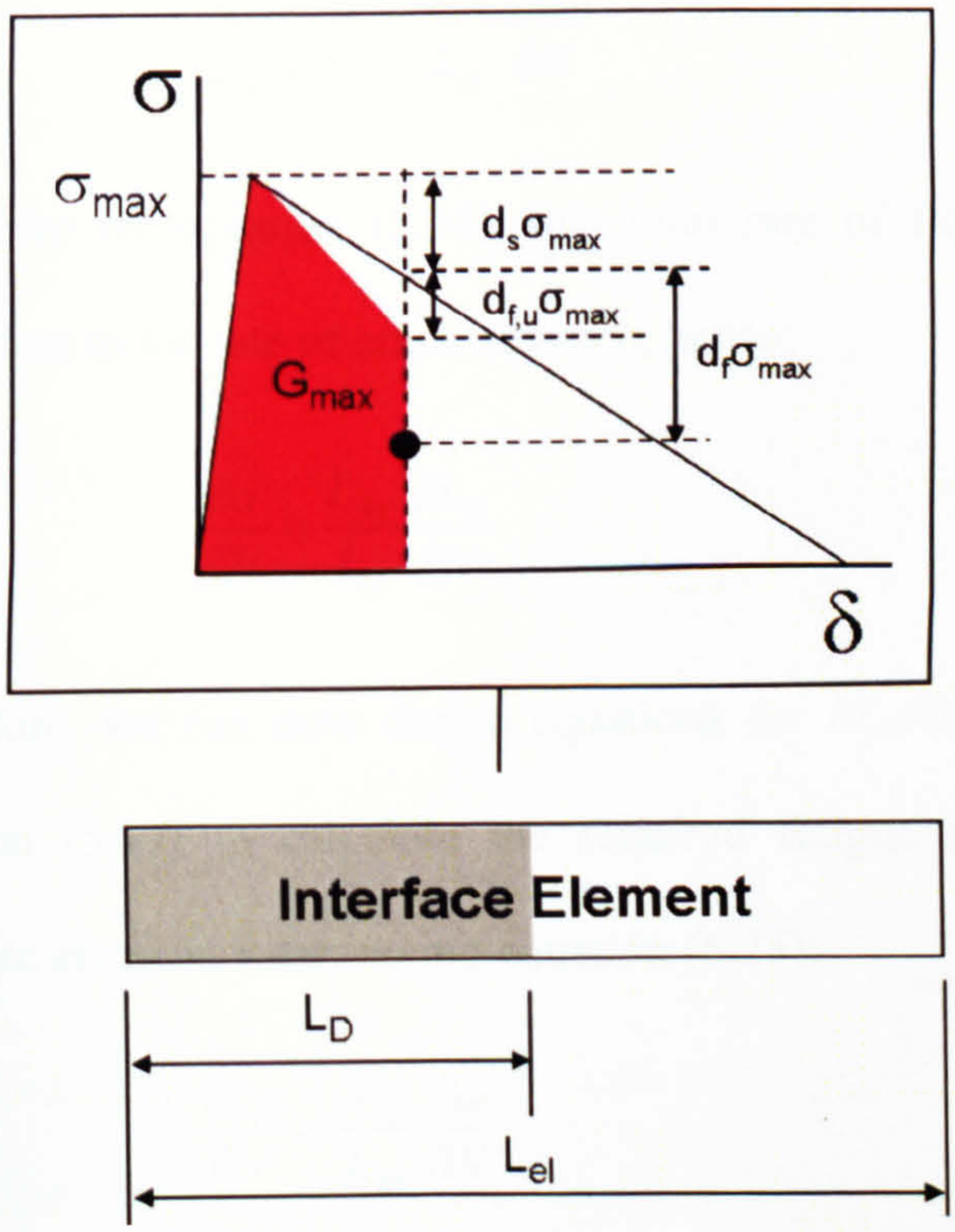

$$\frac{L_D}{L_{el}} = \frac{d_f - d_{f,u}}{1 - d_s - d_{f,u}}$$

Figure 5.14: Definition of damage length, accounting for unwanted fatigue damage

The total crack length is assumed to be equal to the sum of the damage lengths of all elements within the fatigue damage zone:

$$a = \sum_{e \in L_{fat}} L_D \qquad \text{(Eqn. 5.23)}$$

Therefore,

$$\frac{\partial a}{\partial N} = \sum_{e \in L_{fat}} \frac{\partial L_D}{\partial N} \qquad \text{(Eqn. 5.24)}$$

Since the rate of fatigue damage in each interface element, $\partial L_D/\partial N$, is calculated using the integrated strain energy release rate, assuming this is approximately equal for all elements within the fatigue damage length, the total rate of fatigue damage accumulation is given by:

$$\sum_{e \in L_{fat}} \frac{\partial L_D}{\partial N} = \frac{L_{fat}}{L_{el}} \frac{\partial L_D}{\partial N} \qquad \text{(Eqn. 5.25)}$$

As shown by equation (5.24), this total rate of fatigue damage accumulation is equivalent to the rate of crack advance, hence:

$$\frac{\partial a}{\partial N} = \frac{L_{fat}}{L_{el}} \frac{\partial L_D}{\partial N} \qquad \text{(Eqn. 5.26)}$$

As before, we can now derive equations for $\partial L_D/\partial N$ and $\partial d_f/\partial L_D$, and hence use equation (5.17) to calculate the required fatigue damage rate, $\partial d_f/\partial N$, in each interface element. Rearranging equation (5.25):

$$\frac{\partial L_D}{\partial N} = \frac{L_{el}}{L_{fat}} \frac{\partial a}{\partial N} \qquad \text{(Eqn. 5.27)}$$

Differentiating and rearranging equation (5.21),

$$\frac{\partial d_f}{\partial L_D} = \frac{1 - d_s - d_{f,u}}{L_{el}} \qquad \text{(Eqn. 5.28)}$$

Combining equations (5.26) and (5.27) with equation (5.17) gives:

$$\frac{\partial d_f}{\partial N} = \frac{1 - d_s - d_{f,u}}{L_{fat}} \frac{\partial a}{\partial N} \qquad \text{(Eqn. 5.29)}$$

Therefore, the rate of fatigue damage is not dependent on element length, but on the length of the fatigue damage zone in the direction of crack propagation. Another key feature of the formulation is that each interface element requires no knowledge of whether it is in the quasi-static or fatigue damage zone. The same algorithm applies in both, with the assumption that having entered the fatigue damage zone, any further increase in unwanted fatigue damage can be assumed negligible. This assumption is dependent on there being no significant further increase in the

interface element's relative displacement, which as will be shown in later examples, is generally a reasonable approximation.

With the fatigue law active, the length of the cohesive zone (comprising both the fatigue damage length and quasi-static damage length) can be estimated using the fully developed cohesive zone length under quasi-static loading, $L_{CZ,f}$, and the ratio between the integrated strain energy release rate, G_{max}, and the instantaneous critical fracture energy, G_C:

$$L_{CZ} = \frac{G_{max}}{G_C} L_{CZ,f} \qquad \text{(Eqn. 5.30)}$$

As will be demonstrated in later examples, it can generally be assumed that the quasi-static damage length and fatigue damage length each occupy half of this length, therefore:

$$L_{fat} = 0.5 \frac{G_{max}}{G_C} L_{CZ,f} \qquad \text{(Eqn. 5.31)}$$

Chapter 4 has demonstrated the difficulties associated with accurately calculating the fully developed numerical cohesive zone length, $L_{CZ,f}$, due to its dependence on a range of material and geometric properties. Although modifications to existing predictive formulae were presented for improved accuracy, further work remains to refine these and gain an accurate calculation of cohesive zone length for a general mixed mode load case. For this reason, the current version of the fatigue damage law requires the fully developed cohesive zone length as a user input, which is gained from a quasi-static analysis prior to fatigue law implementation. Future work will implement a calculation procedure for this parameter using material properties. It is important to note that for thin laminates, the structural depth will also

be required as a user input, due to its significant influence on cohesive zone length (refer to chapter 4, section 4.5).

Whilst the principle of creating a direct link between linear elastic fracture mechanics and damage mechanics (i.e. interface element fatigue damage) has previously been presented by Turon *et al.*[75,76], the damage formulation presented above is unique in two fundamental aspects:

i) Based on the detailed analysis of the cohesive zone presented in chapter 4, a precise method has been defined for the accurate extraction of strain energy release rate, which involves incremental integration of the interface element traction-displacement response as damage development occurs. This accounts for the variation in mode-ratio across the cohesive zone under mixed-mode load conditions. Turon *et al.*'s formulation calculates strain energy release rate using the interface element's instantaneous position on the traction-displacement response.

ii) With the fatigue law active, the cohesive zone is split into two distinct regions, a 'quasi-static damage length (L_{qs})' and a 'fatigue damage length (L_{fat}).' The interface element damage rate is calculated based on the extraction of strain energy release rate from the 'fatigue damage length,' which shows close agreement with the analytical fracture mechanics solution. The unavoidable accumulation of some unwanted fatigue damage across the 'quasi-static damage length' is monitored and corrected for. In Turon *et al.*'s formulation, the interface element damage rate is calculated based on the assumption that the analytical strain energy release rate is equal to the mean strain energy release rate extracted from all elements within the cohesive zone.

Figure 5.15 shows results for the mode I DCB specimen *using the improved* fatigue algorithm ('Fatigue Damage Zone Formulation'), again using a constant element length of 0.125mm and varying cohesive zone length by changing interfacial strength. Close correlation exists between the line of best fit through the experimental data (Theoretical Paris Curve) and numerical results for interfacial strengths of 30MPa and 15MPa, which give fully developed cohesive zone lengths of 1.2mm and 2.4mm respectively. This indicates that using the modified damage formulation, numerical results are no longer sensitive to the number of elements within the cohesive zone.

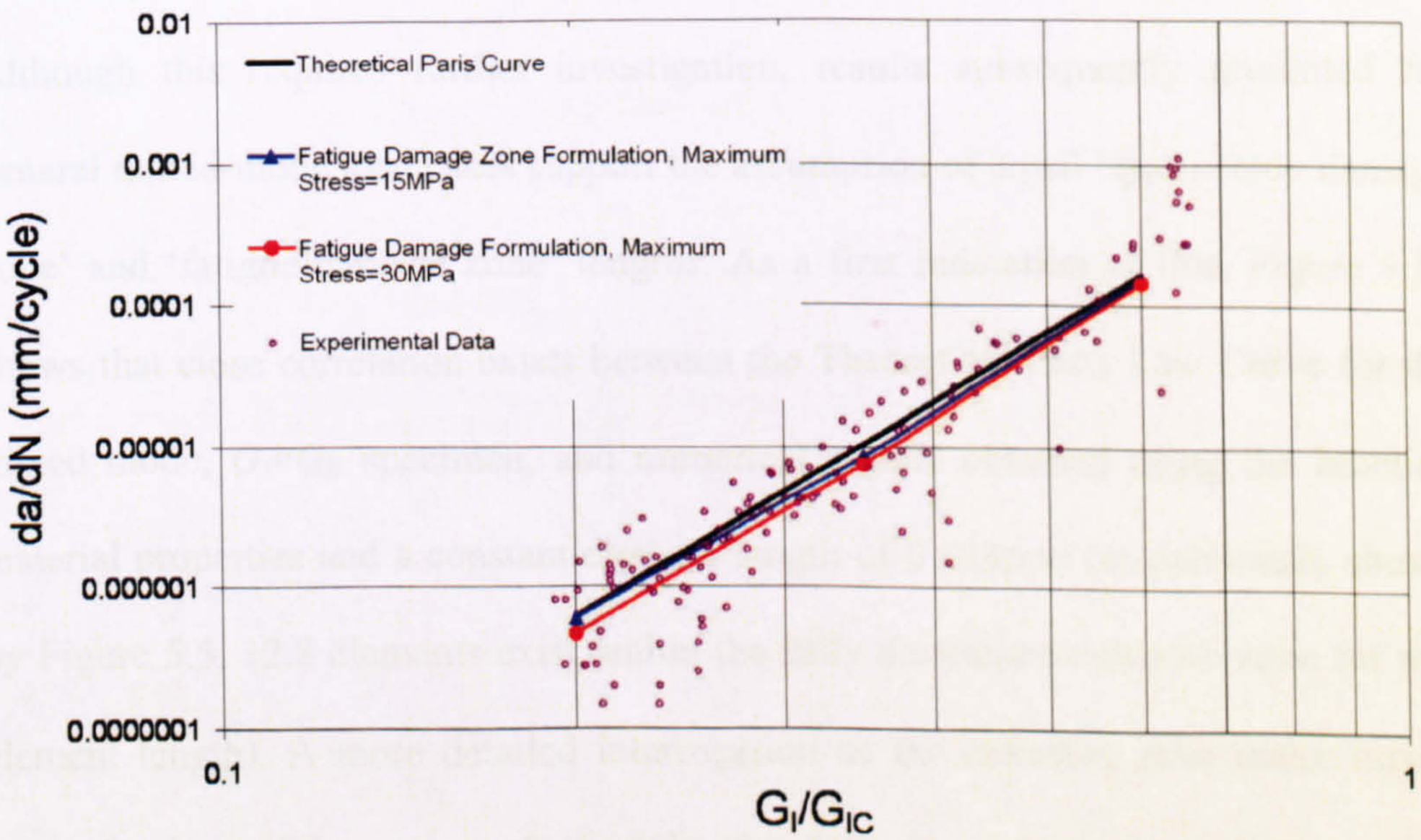

Figure 5.15: Mode I DCB Paris Law Results

The success of the 'Fatigue Damage Zone Formulation' in reducing the sensitivity of crack propagation rate to the number of elements within the cohesive zone is reinforced by Figure 5.16, which shows results for the mode II, 4 point ENF specimen. For this specimen, the number of elements within the cohesive zone is varied by changing element length and the interface element interfacial strength

remains constant at its baseline value of 60MPa. As previously shown in Figure 5.4, the element lengths of 0.125mm and 0.25mm used for these analyses result in 32.8 and 16.4 elements respectively within the fully developed cohesive zone length of 4.1mm, and there is no significant difference in the accuracy of strain energy release rate extraction. Although numerical crack growth rates for the two element lengths show close correlation, they are consistently lower than the Theoretical Paris Curve. Interrogation of the cohesive zone with the fatigue law active suggested that the 'quasi-static damage zone' forms a greater proportion of the cohesive zone length than the 'fatigue damage zone' for this particular case (i.e. an over-prediction of the 'fatigue damage zone' length results in an under-prediction of the crack growth rate). Although this requires further investigation, results subsequently presented for general mixed-mode load cases support the assumption of equal 'quasi-static damage zone' and 'fatigue damage zone' lengths. As a first indication of this, Figure 5.17 shows that close correlation exists between the Theoretical Paris Law Curve for the mixed mode, G_I=G_{II} specimen, and numerical results obtained using the baseline material properties and a constant element length of 0.125mm (as previously shown by Figure 5.5, 12.8 elements exist within the fully developed cohesive zone for this element length). A more detailed interrogation of the cohesive zone under mixed mode load conditions is performed in the following chapter on Fatigue Law Applications.

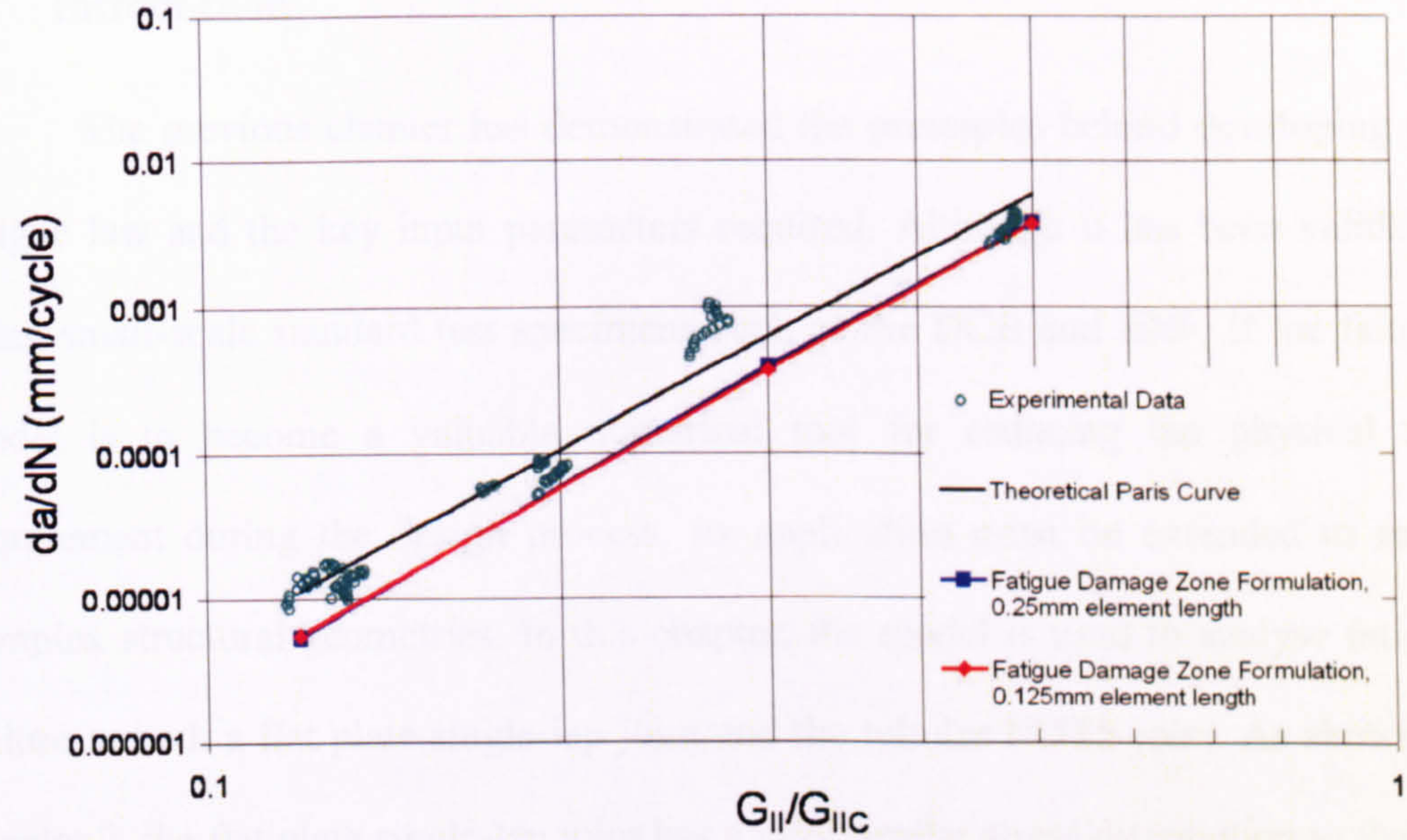

Figure 5.16: Mode II Paris Law Results

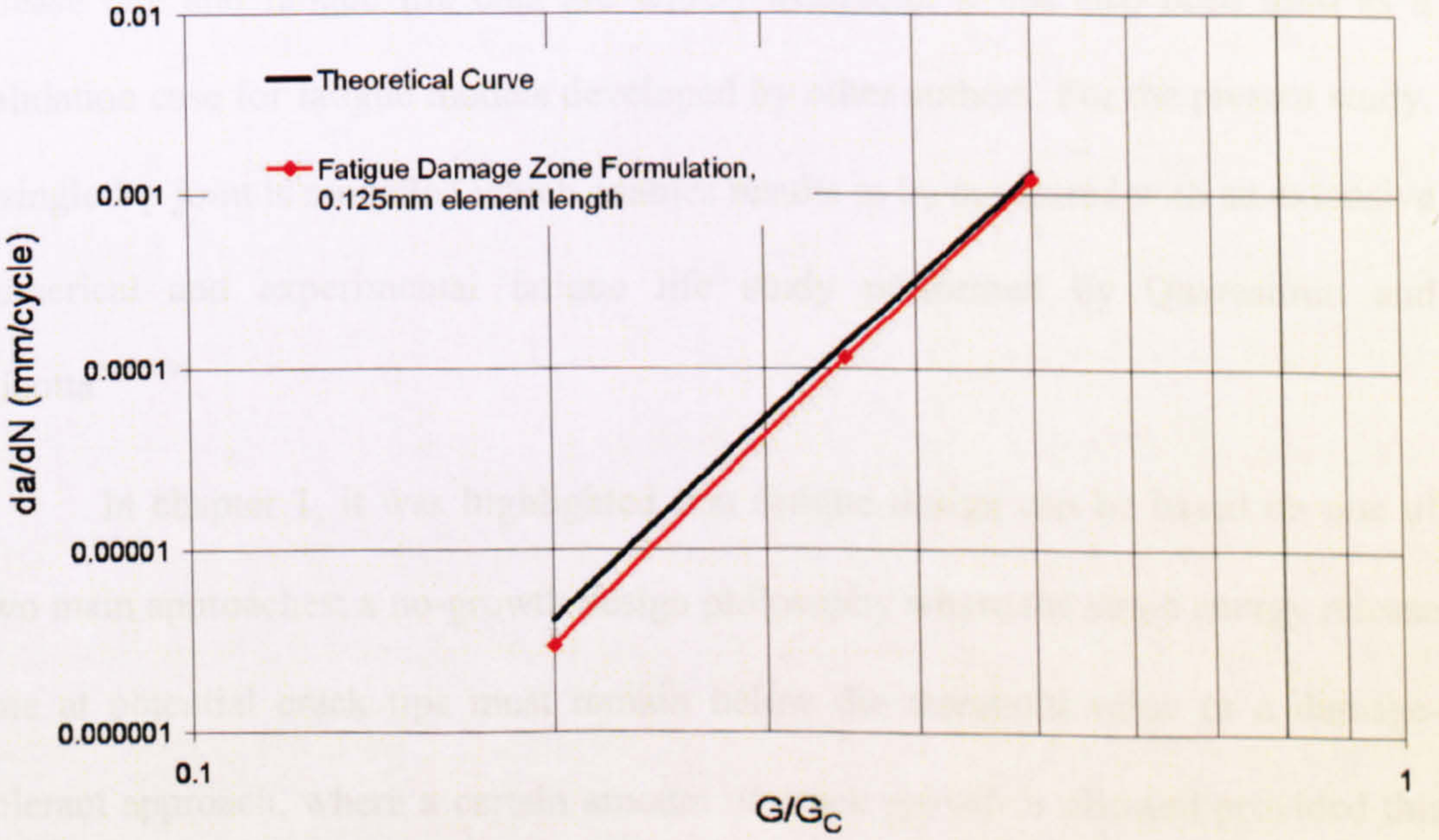

Figure 5.17: Mixed Mode Paris Law Results (GI = GII specimen)

6. Fatigue Law Applications

6.1 Introduction

The previous chapter has demonstrated the principles behind developing the fatigue law and the key input parameters required. Although it has been validated using small-scale standard test specimens such as the DCB and ENF, if the fatigue model is to become a valuable numerical tool for reducing the physical test requirement during the design process, its application must be extended to more complex structural geometries. In this chapter, the model is used to analyse fatigue failure in both a flat plate single-lap joint and the tubular NOTS joint. As shown in chapter 2, the flat plate single-lap joint has a very similar stress distribution to that of a tubular single-lap joint, but is a standard test configuration for which strain energy release rate and fatigue life data are widely available. It has also been used as a validation case for fatigue models developed by other authors. For the present study, a single lap joint is modelled which enables results to be compared with an extensive numerical and experimental fatigue life study performed by Quaresimin and Ricotta[51,90,91].

In chapter 1, it was highlighted that fatigue design can be based on one of two main approaches; a no-growth design philosophy where the strain energy release rate at potential crack tips must remain below the threshold value or a damage-tolerant approach, where a certain amount of crack growth is allowed provided this does not lead to catastrophic failure between inspection intervals. Both approaches rely on the ability to analyse the crack tip strain energy release rate, so that this can be used to determine whether the crack will grow and if so, at what rate. In chapters 5 and 6, the potential to achieve this aim by integrating the traction-displacement

response of the crack tip element has been demonstrated, but only for standard test specimens with large starter cracks. For the technique to be applicable as a useful design tool, it must be proven in realistic structures where initial starter cracks will typically be extremely small. For example, when analysing the fatigue life of composite components such as adhesive joints, the length and location of any initial cracks assumed in critical design cases is determined by manufacturing process control and the resolution of NDT techniques. As highlighted in chapter 2, for adhesive joints, initial cracks are generally assumed at the edge of the bond-line, where they have the most significant influence on the lifetime of the structure because their growth is promoted by the high shear and peel stresses that occur in this region. Whilst there are no specific design rules concerning the length of such cracks, typical inspection thresholds are in the range of 0.1 - 1mm, therefore starter cracks of this order of magnitude are investigated in the analyses presented here.

It is important to draw a clear distinction between crack initiation and crack propagation. Physically, there is no clear boundary between these two stages and the point at which a crack can be assumed to have initiated is generally determined by the resolution of applicable NDT techniques. Numerically, a clear distinction can be drawn when using interface elements incorporating a bi-linear traction-displacement response. A crack propagation fatigue law is considered to apply whenever an interface element lies on the softening region of the traction-displacement response, whereas a crack initiation law is considered to apply to the elastic region of the traction-displacement response. The need for an initiation law in the elastic regime may at first seem counter-intuitive as there must be non-linear deformation occurring for fatigue damage to initiate. However, this will often be on a microscopic scale around extremely small material defects, which cannot feasibly be modelled through

mesh refinement. All the work in this thesis concerns cases where there is an initial macroscopic crack or stress concentration, which requires only a numerical propagation law for fatigue life analysis. As discussed previously, this has been motivated by the difficulties in ensuring defect free manufacture in complex geometries such as the NOTS structure. However, in situations where carefully controlled manufacture can avoid initial defects and stress concentrations, the development of a crack initiation law is also required to accurately model total fatigue life. For example, this applies in adhesive joints where a tapered fillet geometry is used to avoid the severe peel and shear stress concentrations at the ends of the joint overlap. Work is being undertaken by colleagues at the University of Bristol to develop fatigue initiation laws applicable in such cases[92] and to integrate these with the propagation law developed within this thesis. Once fully validated, this will provide the ability to analyse total fatigue life, encompassing both crack initiation and crack propagation. Whilst total fatigue life models have already been presented by previous authors[50,51], these generally rely on separate numerical methods for analysing crack initiation and crack propagation, for example a stress intensity factor approach to analyse initiation and a VCCT approach for propagation. The development of a total fatigue life model for interface elements promises to offer a fully integrated analysis capability, which can be applied in a single coherent numerical simulation.

6.2 Single-Lap Joint

6.2.1 Model Geometry and Setup

The dimensions and material properties of the single-lap joint modelled are as shown in Figure 6.1 and Table 6.1. With respect to interfacial properties (quasi-

static), the only parameters *obtainable from* Quaresimin and Ricotta's previous fatigue life studies are an adhesive shear strength[90] and a mode I fracture toughness[51] (This is because, using VCCT, they used only the mode I fracture toughness, as opposed to any mixed-mode failure criteria, to signify final failure). Therefore, identical mode I/II interfacial strengths and mode I/II fracture toughness values have been assumed. As will be shown in section 6.2.2, strain energy release rate values extracted from interface elements using these material properties showed close agreement with those gained using the VCCT.

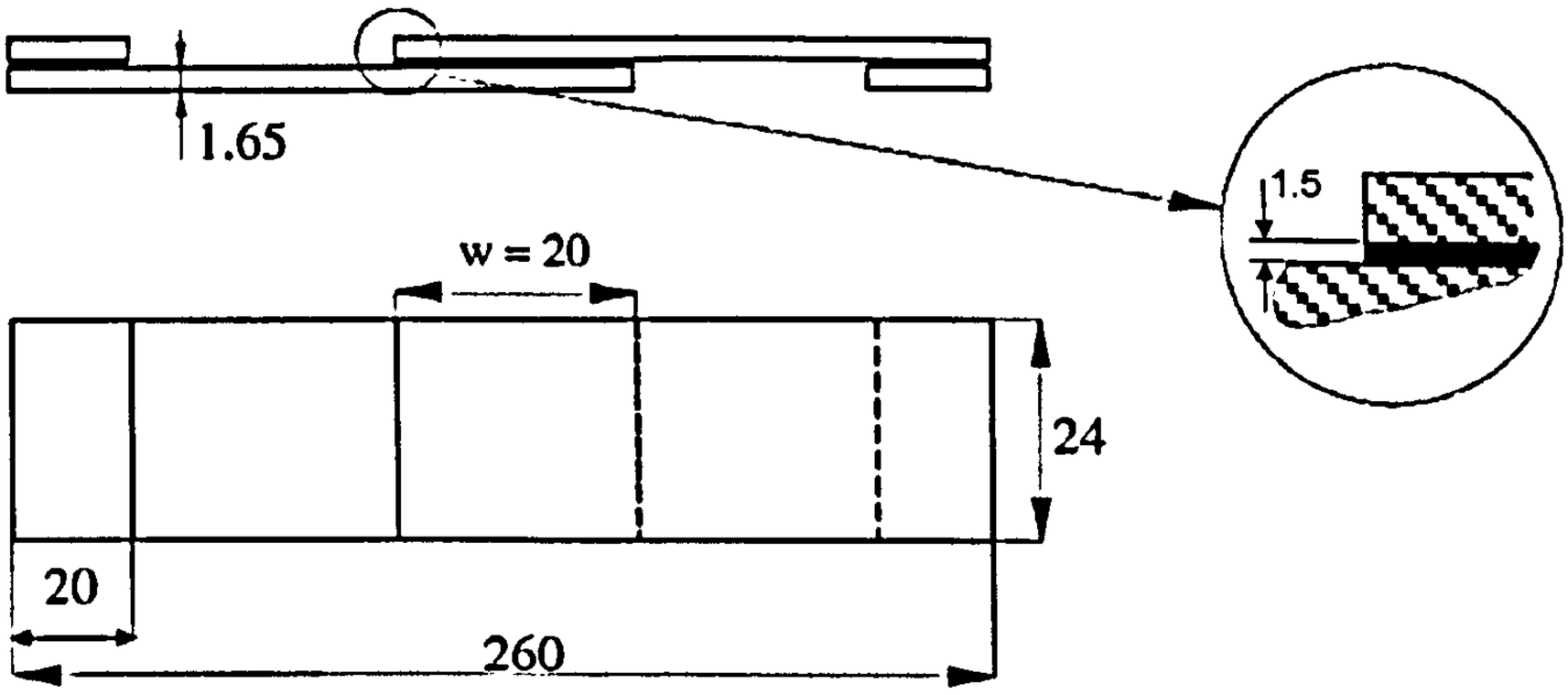

Figure 6.1: Single Lap Joint Dimensions[91]

Table 6.1: Adherend, Adhesive and Interfacial Properties used in the Numerical Analyses[51,90,91]

Adherend Properties (Orthotropic Elastic)					
E_{11} (MPa)	58050	ν_{12}	0.06	G_{12} (MPa)	3300
E_{22} (MPa)	58050	ν_{13}	0.27	G_{13} (MPa)	5000
E_{33} (MPa)	6000	ν_{23}	0.27	G_{23} (MPa)	5000
Adhesive Properties (Isotropic Elastic)					
E (MPa)	2870	G (MPa)	1050	ν	0.37
Interface Element Properties					
G_{IC} (N/mm)	0.9	$\sigma_{max,I}$ (MPa)	39.1	K_I (N/mm^3)	100,000
G_{IIC} (N/mm)	0.9	$\sigma_{max,II}$ (MPa)	39.1	K_{II} (N/mm^3)	100,000

Chapter 4 indicated that at least 10 interface elements should exist within the fully developed cohesive zone length, in order to extract an accurate value of strain energy release rate by integrating the crack tip element's traction-displacement response. Formulae for predicting cohesive zone lengths under pure mode I and mode II load conditions were also developed and it was shown that these must be modified in slender bodies to account for the influence of specimen depth. This resulted in 4 predictive formulae for cohesive zone length; mode I cohesive zone length in a non-slender body ($l_{ch,I}$), mode I cohesive zone length in a slender body ($l_{ch,slender,I}$), mode II cohesive zone length in a non-slender body ($l_{ch,II}$) and mode II cohesive zone length in a slender body ($l_{ch,slender,II}$). Due to the difficulty in defining a clear boundary between slender and non-slender bodies, it was recommended that the minimum value yielded by these formulae be used for designing an appropriate mesh. Table 6.2 shows the pure mode I/II cohesive zone lengths given by these formulae for the material properties of the single lap joint. A value for h of 1.65mm

was applied in the slender body equations and E'_I, E'_{II} and $E'_{II,slender}$ were calculated using the procedure detailed in appendix B. The shortest cohesive zone length was predicted to be 1.10mm for pure mode I loading in a slender body. In order to ensure a minimum of 10 interface elements within this length, an element length of 0.075mm was applied along the bonded region in the baseline model. Away from this region, the element length was gradually increased up to a maximum of 0.5mm to reduce model run-times. Details of the actual cohesive zone length seen in the analyses and the effects of reducing bond-line mesh density are discussed in the following section.

Table 6.2: Predicted mode I and mode II cohesive zone lengths for the single-lap joint model

Cohesive Zone Length Formula	
$l_{ch,I} = 0.5E'_I \frac{G_{IC}}{(\sigma_{I,max})^2}$	2.64mm (E'_I = 8976MPa)
$l_{ch,II} = 0.5E'_{II} \frac{G_{IIC}}{(\sigma_{II,max})^2}$	8.21mm (E'_{II} = 27,900MPa)
$l_{ch,slender,I} = 0.5\left(E'_I \frac{G_{IC}}{(\sigma_{I,max})^2}\right)^{\frac{1}{4}} h^{\frac{3}{4}}$	1.10mm (E'_I = 8976MPa)
$l_{ch,slender,II} = 0.5\sqrt{\left(E'_{II,slender} \frac{G_{IIC}}{(\sigma_{II,max})^2}\right) h}$	3.77mm ($E'_{II,slender}$ = 58,100MPa)

As shown in Figure 6.2, a half-model was used, with six elements through the depth of each laminate and three elements through the thickness of the adhesive. Solid interface elements, with an initial thickness of 0.015mm were inserted at the top and bottom interfaces between the laminate adherends and the adhesive. The thickness of the adhesive layer was reduced from 0.15mm to 0.12mm, to maintain a

constant total specimen depth. Initial symmetric bond-line cracks were modelled by deleting interface elements along the top and bottom interfaces. Nodes representing the specimen tabs were constrained in both X and Y directions at the left hand end of the specimen and only the Y direction at the right hand end, where load was applied.

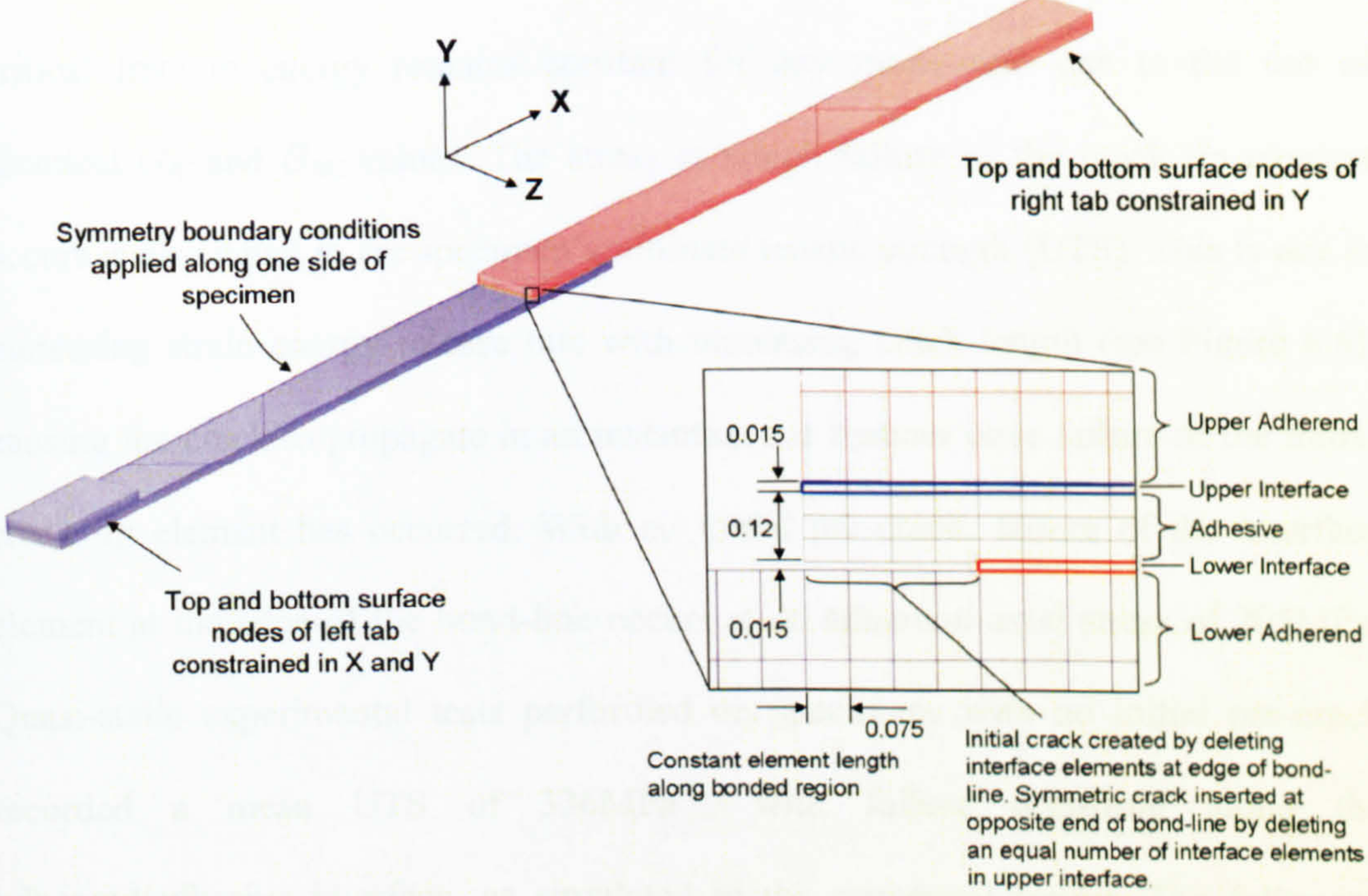

Figure 6.2: Single-lap Joint Model

6.2.2 Strain Energy Release Rate Analyses

Figure 6.3 shows the strain energy release rate extracted from the crack tip element under a linearly increasing applied load, for initial crack lengths of 0mm, 0.3mm and 5mm. The specimen's load-displacement relationship is also shown to highlight the non-linear nature of deformation due to the significant rotation of the bonded region. Since symmetric cracks were modelled, strain energy release rate results at each end of the bond-line showed negligible difference and only those for the left hand end are presented. Results are shown for the baseline element length of 0.075mm and a discussion of cohesive zone length and the effects of reduced mesh

density (i.e. the number of interface elements within the cohesive zone) is deferred until later in this section.

For each initial crack length, the strain energy release rate increases with applied load, until reaching the critical fracture energy of 0.9N/mm, at which point the crack tip element fails and the crack propagates. It should be noted that this critical fracture energy remains constant for any mode-ratio due to the use of identical G_{IC} and G_{IIC} values. The stress at which failure of the crack tip element occurs is also equal to the specimen's ultimate tensile strength (UTS). This is due to increasing strain energy release rate with increasing crack length (see Figure 6.6), causing the crack to propagate in an instantaneous manner once failure of the initial crack tip element has occurred. With no initial pre-crack, failure of the interface element at the edge of the bond-line occurs at an adherend axial stress of 205MPa. Quasi-static experimental tests performed on specimens with no initial pre-crack recorded a mean UTS of 336MPa[90], with failure occurring along the adherend/adhesive interface, as simulated in the numerical model. The following factors may be responsible for the 164% greater experimental UTS relative to the numerical UTS:

i) Small adhesive fillets were present at the ends of the experimental joint overlap, which would relieve the peel and shear stress concentrations. Although reference [90] states that square-edge joints were manufactured, even very small adhesive fillets at the end of the joint overlap may significantly reduce these stress concentrations. In the numerical model, the overlap was perfectly square, resulting in the maximum possible stress concentration.

ii) The adhesive was modelled as perfectly elastic, hence excluding potential stress relief due to plastic deformation.

iii) Uncertainty concerning the mode II fracture toughness value of the adhesive, G_{IIC} as detailed in section 6.2.1. For the interface elements at the left and right hand ends of the bond-line (the first two interface elements to fail), the instantaneous mode-ratio of the traction-displacement response decreased from approximately G_I/G_T=4/5 at damage initiation to G_I/G_T=2/3 at failure. As previously detailed in chapter 4, the mode-ratio will vary during damage development within a single element.) Despite this predominance of mode I loading, an increased G_{IIC} would raise the mixed-mode fracture toughness and hence failure load (refer to chapter 4, equation (4.2)).

Since the main aim of the numerical investigation was to investigate strain energy release rate extraction and to compare this with VCCT results, differences between the experimental and numerical failure loads were not studied further.

With symmetric cracks of 0.3mm inserted at both ends of the bond-line, there is a slight increase in the gradient of the strain energy release rate curve, causing a 2.4% reduction in UTS to 200MPa. With symmetric cracks of 5mm, there is a far more significant increase in the gradient of the strain energy release rate curve and UTS is reduced by 27% to 150MPa.

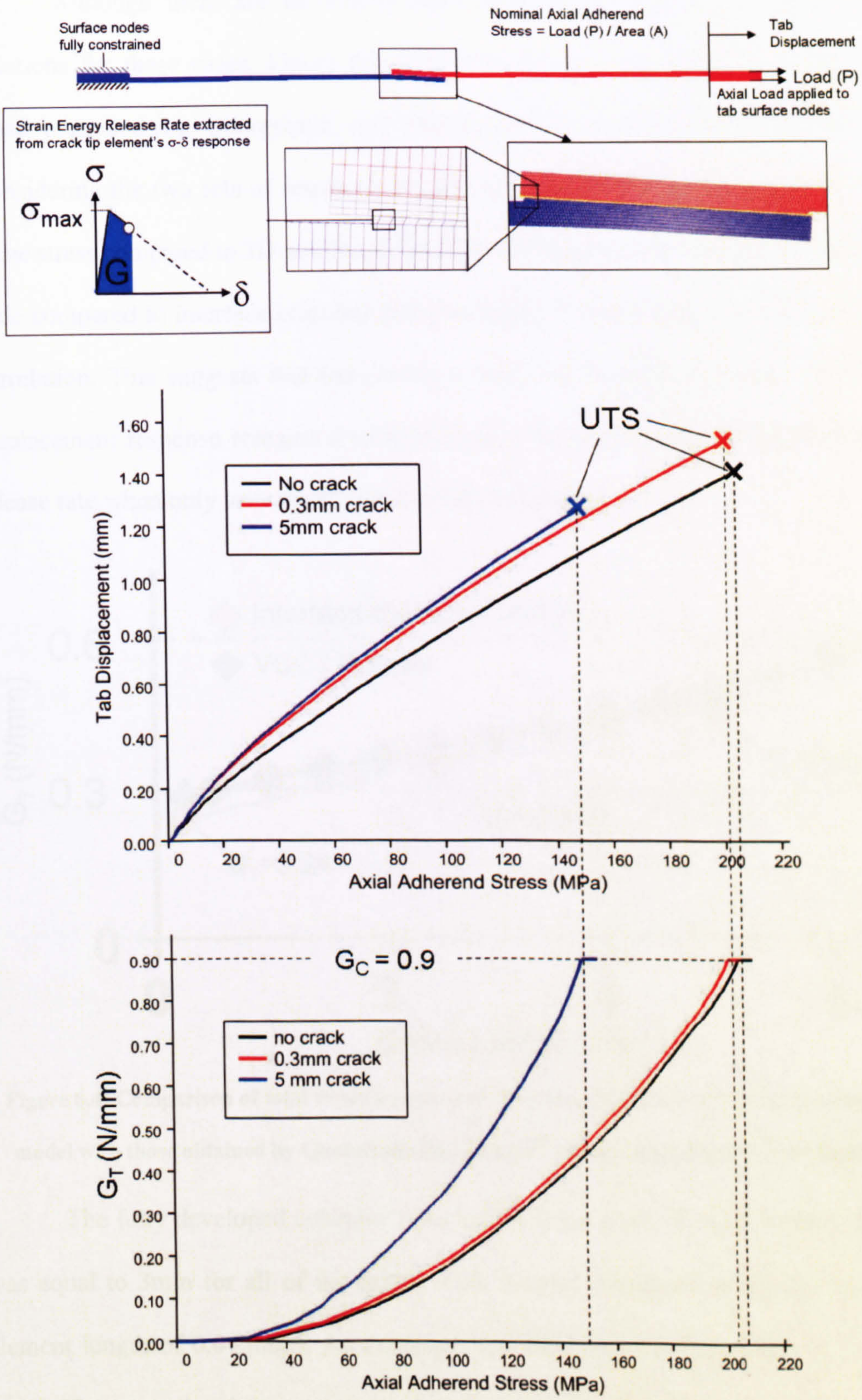

Figure 6.3: Global load-displacement and strain energy release rate results for various initial crack lengths in single-lap joint model

Although there are no closed form analytical strain energy release rate solutions for these cases, Figure 6.4 compares the interface element results with those presented by Quaresimin and Ricotta, which they gained using VCCT. Considering the two sets of results were obtained using different element types (2D plane stress compared to 3D solids) and analysis techniques (VCCT using an implicit code compared to interface elements using an explicit code), there is a high level of correlation. This suggests that integrating a crack tip interface element's traction-displacement response remains a valid technique for extracting total strain energy release rate when only very small initial cracks are present.

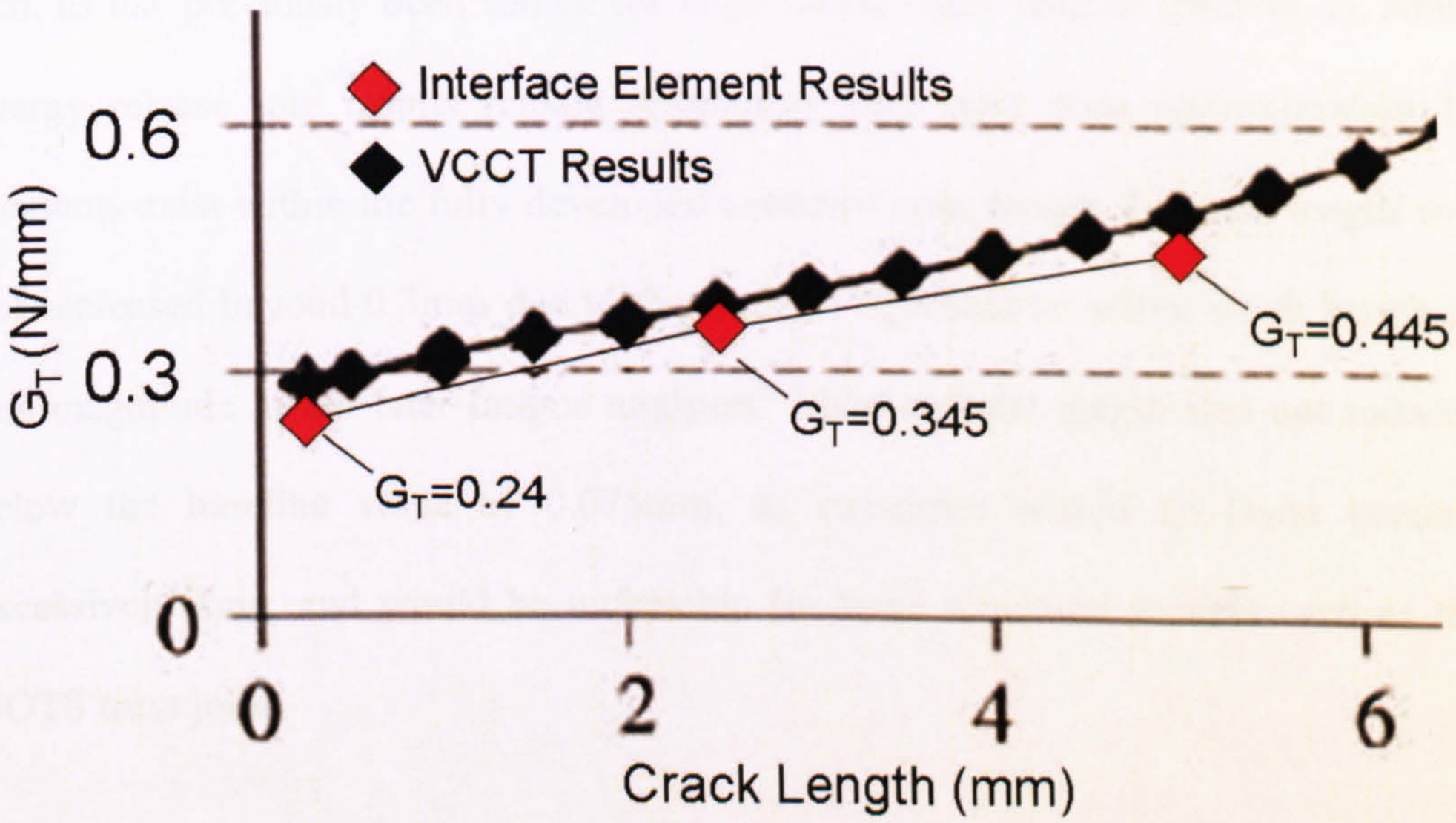

Figure 6.4: Comparison of total strain energy release rates extracted from interface element model with those obtained by Quaresimin and Ricotta[91] for an adherend stress of 110MPa

The fully developed cohesive zone length at the point of first element failure was equal to 3mm for all of the initial crack lengths (measured using the baseline element length of 0.075mm). As expected, this falls between the values of 1.1mm and 3.77mm predicted for pure mode I and pure mode II loading respectively in a slender body. However, further work is required to define formulae for accurately

defining cohesive zone lengths under general mixed-mode load conditions. Figure 6.5 shows the effects of element length (L_{el}) on the total strain energy release rate and the separate mode I/II components extracted from the crack tip element. Results are shown for a pre-crack of 5mm to enable a comparison with a mesh density study presented by Quaresimin and Ricotta[91] using VCCT (Figure 6.6). It should be noted that very similar trends were observed with starter cracks of 0mm and 0.3mm. As shown by Figure 6.5, very similar strain energy release rate results were obtained using element lengths of 0.075mm, 0.15mm and 0.3mm, which gave 40, 20 and 10 elements respectively within the fully developed cohesive zone length. This suggests that, as has previously been shown for large initial crack lengths (chapter 4), strain energy release rate results remain reasonably consistent once approximately 10 elements exist within the fully developed cohesive zone length. Element length was not increased beyond 0.3mm due to the need to represent an initial crack length of this magnitude in the later fatigue analyses. Also, element length was not reduced below the baseline value of 0.075mm, as run-times within LS-Dyna become excessively long, and would be unfeasible for large structural models such as the NOTS truss joint.

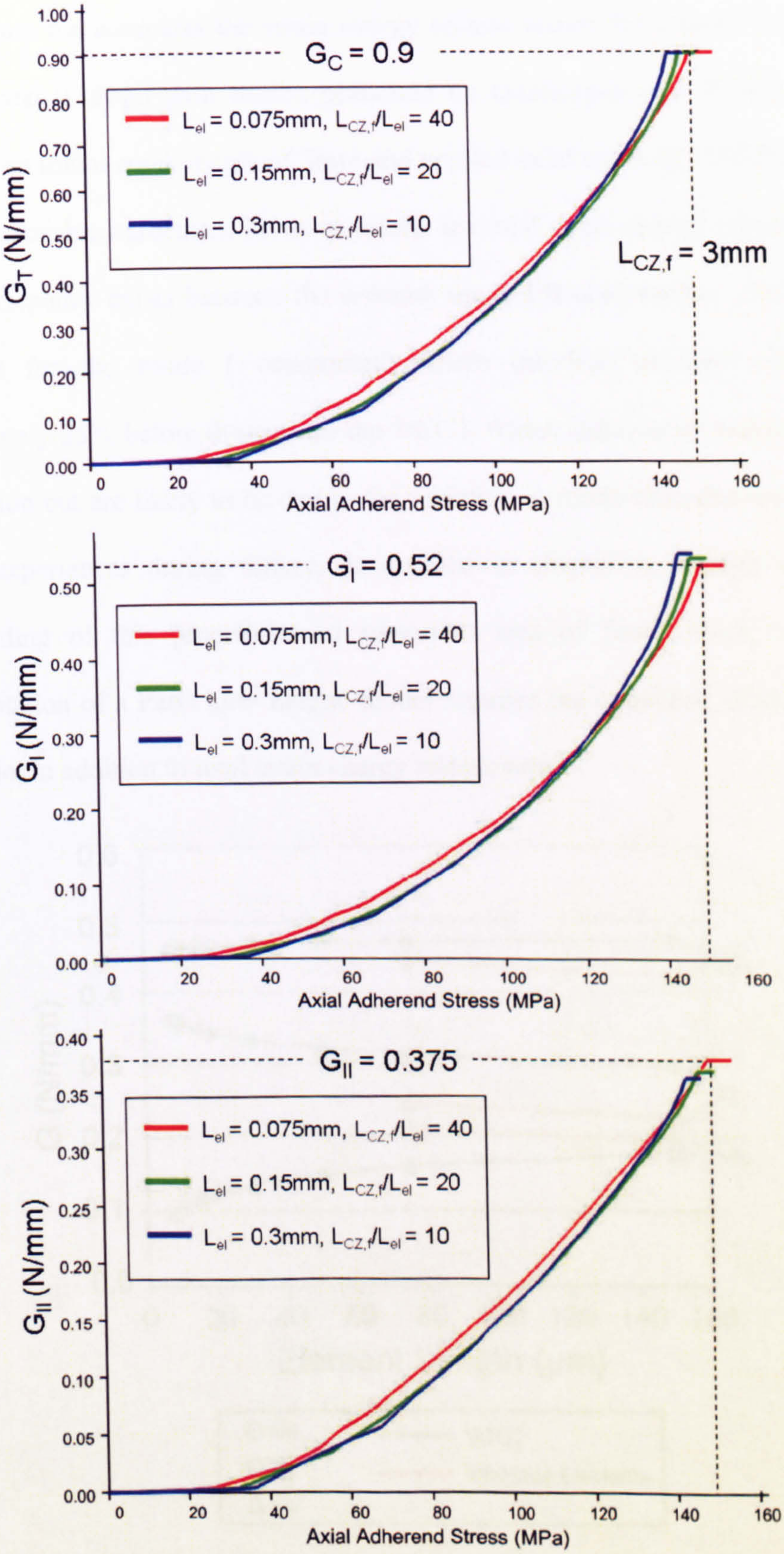

Figure 6.5: Strain Energy Release Rate extracted from crack tip interface element for various mesh densities with an initial pre-crack of 5mm.

Figure 6.6 compares the strain energy release results for element lengths of 0.075mm and 0.15mm with results presented by Quaresimin and Ricotta for the VCCT for an initial crack length of 5mm and applied axial stress of 110MPa. Whilst there is reasonable agreement between results for total strain energy release rate, a larger discrepancy exists between the separate mode I/II components. This is most significant for the mode I component, where interface element results are approximately 25% below those from the VCCT. These differences require further investigation but are likely to be due to the variation in mode-ratio that an interface element experiences during failure, as detailed in chapter 4. Gaining a deeper understanding of this process is an important area of future work, since the implementation of a Paris Law fatigue model requires the extraction of an accurate mode-ratio, in addition to total strain energy release rate.

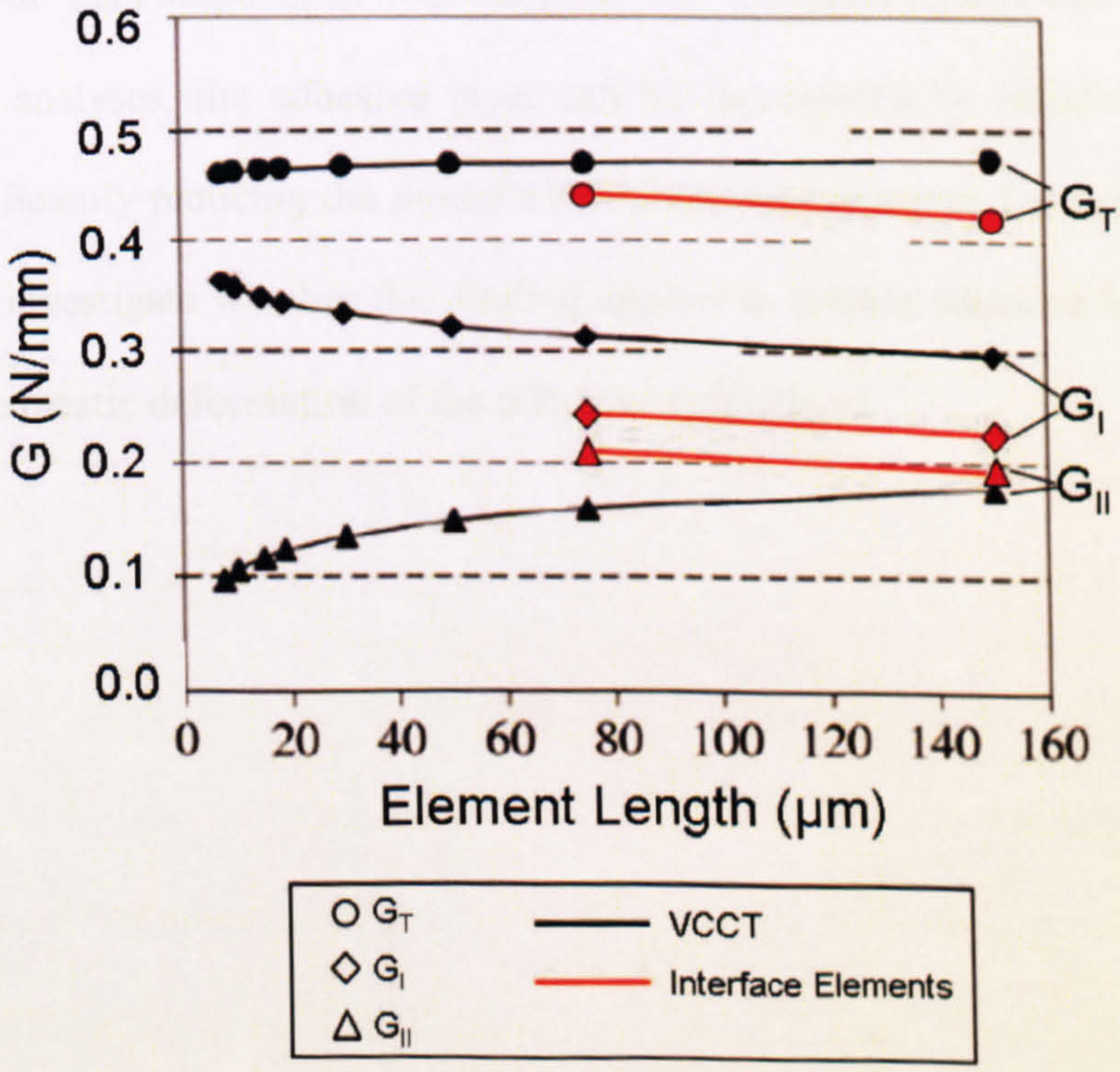

Figure 6.6: Comparison of interface element strain energy release rate results with VCCT results[91] for various element lengths (initial crack length = 5mm, axial stress = of 110MPa).

Modelling the adhesive layer, as detailed above, adds considerably to computational expense due to the need for elements of a very small thickness to represent this. Also, for adhesive joints produced using a co-bonding or co-curing process, the adhesive layer may be of negligible thickness and impractical to model. Therefore, in order to investigate the effects of the adhesive on strain energy release rate results, a second set of models were created with the adhesive layer represented by a single layer of 0.1mm thick interface elements. Although this resulted in a 0.05mm reduction in adhesive layer thickness, increasing interface element thickness to 0.15mm resulted in instabilities within the numerical analyses. Figure 6.7 shows strain energy release rate results extracted from models with and without the adhesive material included, for an initial crack length of 5mm. There is very close agreement between the two models, both for total strain energy release rate and the separate mode I/II components. This suggests that for strain energy release rate and fatigue life analyses, the adhesive layer can be represented by interface elements alone, significantly reducing the model's computational expense. Further research is required to investigate whether this finding applies to thicker adhesive layers and in cases where plastic deformation of the adhesive is included.

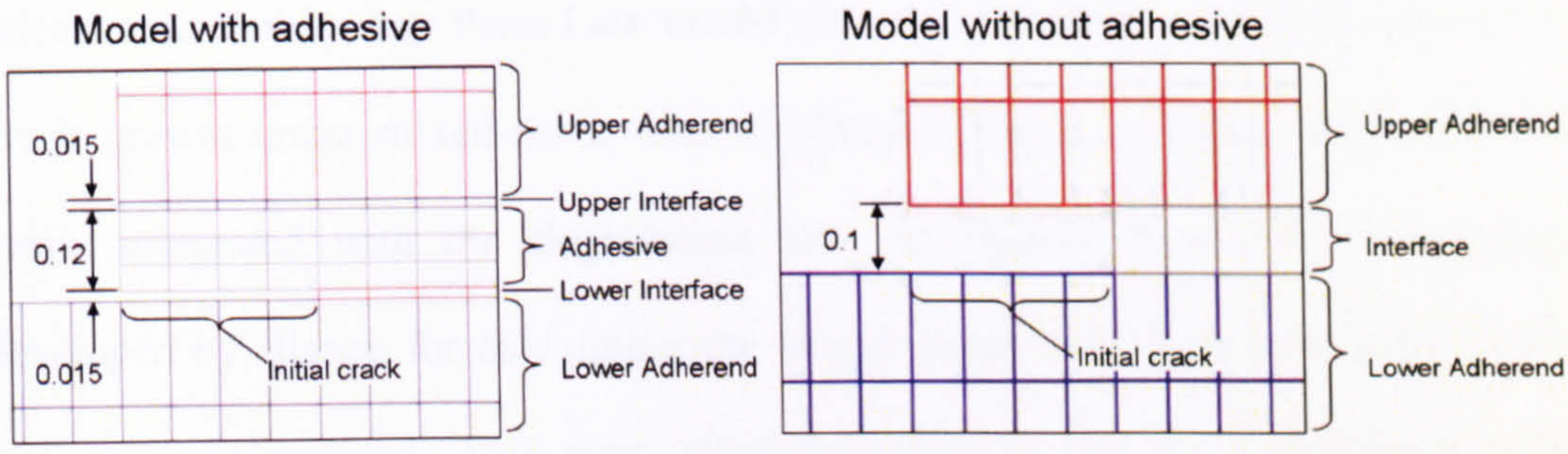

Figure 6.7: Strain Energy Release Results extracted from models with and without the adhesive material included, for an initial crack length of 5mm

6.2.3 Crack Propagation Analyses

A primary aim in developing the interface element fatigue degradation law has been to maintain a direct link with the Paris Law, due to its widespread use for predicting rates of delamination and bond-line failure in composite materials. This has been achieved by combining the technique developed for extracting strain energy release rate with a degradation law that accounts for the number of elements within the cohesive zone ahead of the numerical crack tip. The direct link with strain energy

release rate enables any Paris Law model (i.e. any model for predicting the rate of crack growth under mixed-mode load conditions) based on either G or ΔG to be easily integrated with the degradation law. In chapter 5, a Paris Law model developed by Blanco for calculating the mixed mode Paris Law constants, C_m and m_m, was implemented. This was selected because it had been developed using experimental data for the material (HTA/6376C) and test specimens modelled. However, as discussed in chapter 3, there are many alternative Paris Law models presented in the literature and the most appropriate model for a specific application is dependent on the material, structural geometry and whether any mixed mode test data exists. In order to remain consistent with Quaresimin and Ricotta's VCCT fatigue life analyses of the single lap joint, a Paris Law model is now implemented based on an equivalent strain energy release rate, G_{eqv}, where,

$$\frac{\partial a}{\partial N} = C\Delta G_{eqv}{}^{m} \qquad \text{(Eqn. 6.1)}$$

and G_{eqv} is calculated using,

$$G_{eqv} = G_I + \frac{G_{II}}{G_I + G_{II}} G_{II} \qquad \text{(Eqn. 6.2)}$$

Using this approach, constant values for the Paris Law constants, C and m are applied regardless of mode-ratio and the effects of mode-mixity on crack propagation rate are instead accounted for in the calculation of G_{eqv}. As shown in Figure 6.8, under pure mode I or mode II loading G_{eqv} is equal to G_I and G_{II} respectively. Under mixed-mode loading, G_{eqv} is less than the total strain energy release rate, reaching a minimum of $0.75G_T$ at a mode-ratio of 0.5.

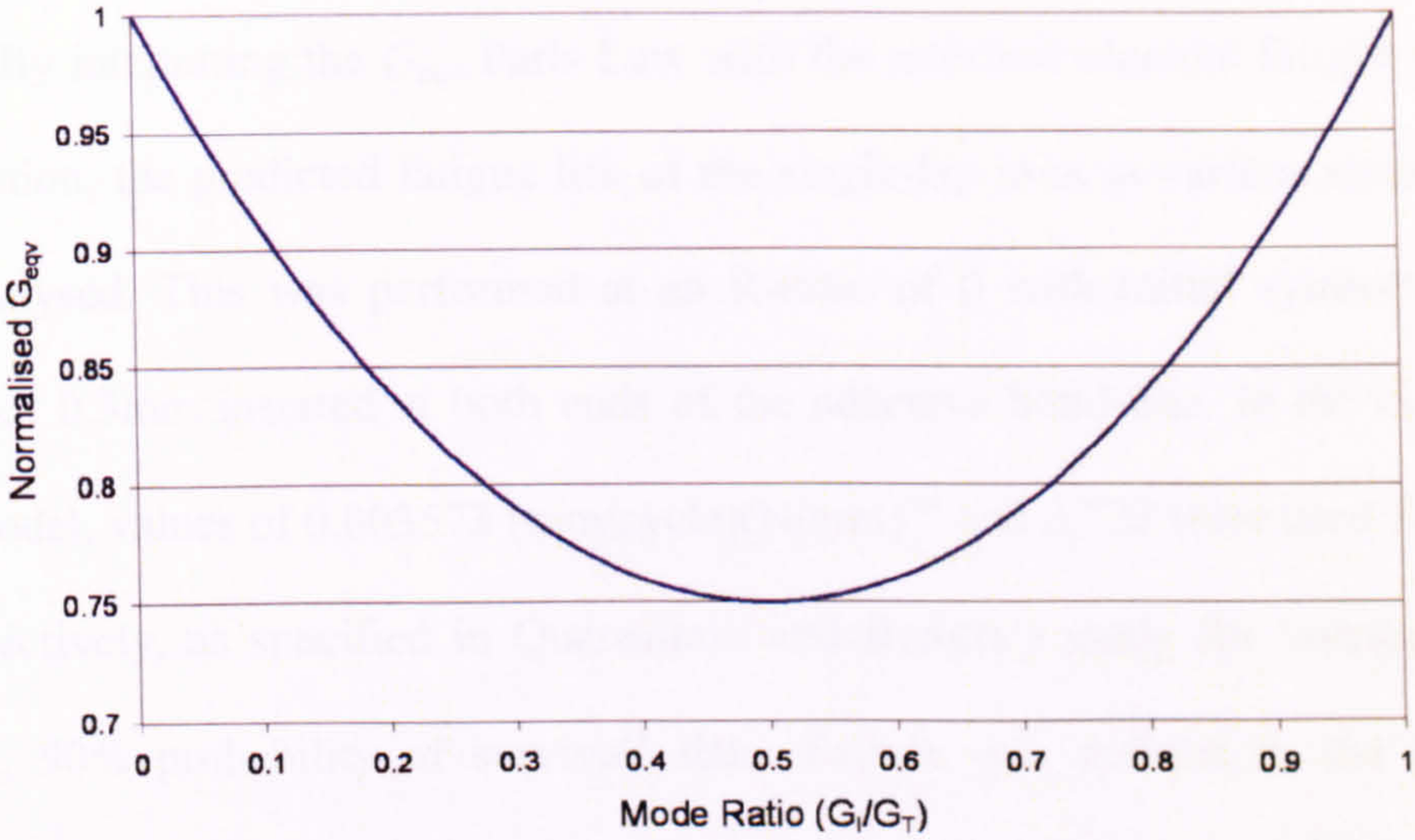

Figure 6.8: Variation of G_{eqv} with mode ratio

Figure 6.9 extends the previous comparison of strain energy results gained using interface elements with those obtained using the VCCT, by including results for G_{eqv}. The G_{eqv} values obtained from the two techniques show a similar level of correlation to those for G_T, agreeing to within approximately 10% for an element length of 0.075mm.

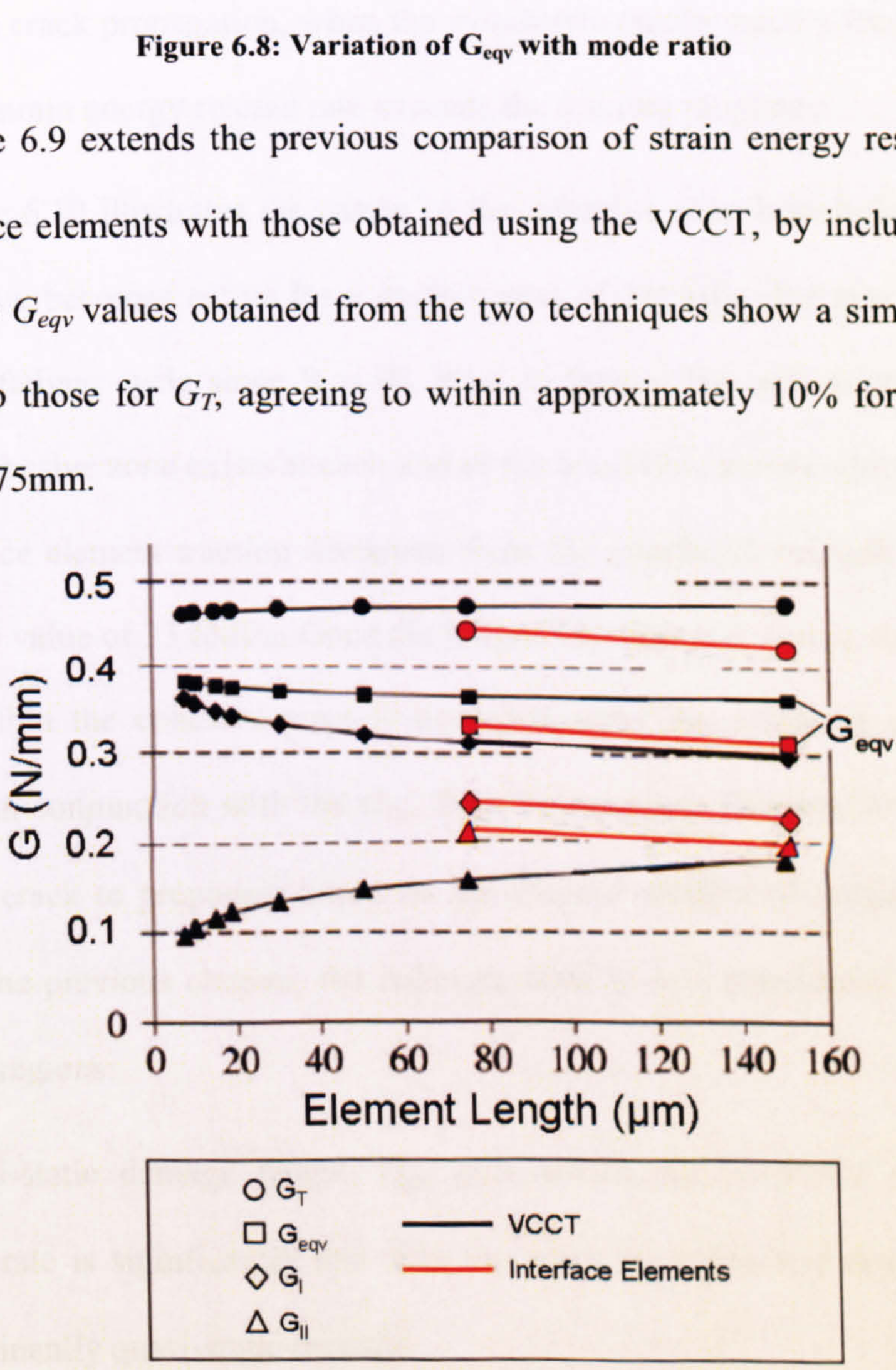

Figure 6.9: Comparison of G_{eqv} from interface element and VCCT models[91] for various element lengths (crack length = 5mm, axial stress = 110MPa).

By integrating the G_{eqv} Paris Law with the interface element fatigue damage formulation, the predicted fatigue life of the single-lap joint at various stress levels was analysed. This was performed at an R-ratio of 0 with initial symmetric pre-cracks of *0.3mm* inserted at both ends of the adhesive bond-line. In the G_{eqv} Paris Law model, values of 0.003573 (mm/cycle)(N/mm)$^{-m}$ and *2.723 were used for C and* m respectively, as specified in Quaresimin and Ricotta's study for 'average crack growth, 90% probability of survival' data. Failure was defined as the point of instantaneous crack propagation, when the symmetric cracks reach a length at which the crack tip strain energy release rate exceeds the fracture toughness.

Figure 6.10 illustrates the nature of the cohesive zone both before and after the fatigue law becomes active for a cyclic stress of 110MPa (the maximum stress within each fatigue cycle since R = 0). Prior to fatigue law activation, a partially developed cohesive zone exists at each end of the bond-line, across which the mixed-mode interface element traction decreases from the interfacial strength of 39.1MPa to a crack tip value of 33.6MPa. Once the fatigue law becomes active, the strength of elements within the cohesive zone is degraded using the crack tip strain energy release rate in conjunction with the G_{eqv} Paris Law model. This enables elements to fail and the crack to propagate based on the elapsed number of fatigue cycles. As detailed in the previous chapter, the cohesive zone is now considered to consist of two distinct regions:

i) A quasi-static damage length, L_{qs}, over which the integrated strain energy release rate is significantly less than the crack tip value and elements acquire predominantly quasi-static damage.

ii) A fatigue damage length, L_{fat}, over which the mean integrated strain energy release rate is equal to the crack tip strain energy release rate from a quasi-static analysis and elements acquire predominantly fatigue damage.

Interrogation of the cohesive zone stress distribution indicated that these two regions can be considered approximately equal in length, as was previously the case for the validation specimens with long initial pre-cracks analysed in chapter 5 (and is assumed within the fatigue degradation law for calculating interface element degradation rates). As shown in Figure 6.10, the mean integrated strain energy release rate, G_T, over the fatigue damage length, L_{fat}, was calculated as 0.27N/mm for a crack length of 0.9mm after 25,000 cycles. This gives close agreement with values obtained from both the VCCT and a crack tip interface element under a purely quasi-static analysis (see Figure 6.12). It is important to emphasise that the only parameter required by the fatigue algorithm to calculate the cohesive zone length under fatigue loading, and its component lengths, L_{qs} and L_{fat}, is the fully developed cohesive zone length, $L_{CZ,f}$, from a quasi-static analysis (refer to details of fatigue damage formulation in chapter 5). Due to the further work required to develop equations for accurately calculating $L_{CZ,f}$ under general mixed-mode load conditions, it is currently required as a user input. This requires a separate quasi-static failure analysis and results in a source of error if $L_{CZ,f}$ changes as a crack develops, due to mode-ratio or specimen depth variations. However, these variations are generally small for typical allowable crack growth lengths, as will be demonstrated in the following single-lap joint and NOTS truss joint analyses. Once improved predictive formulae for cohesive zone length are developed, these can be inserted within the fatigue algorithm, allowing $L_{CZ,f}$ to be continuously updated as a crack develops, using the instantaneous mode-ratio.

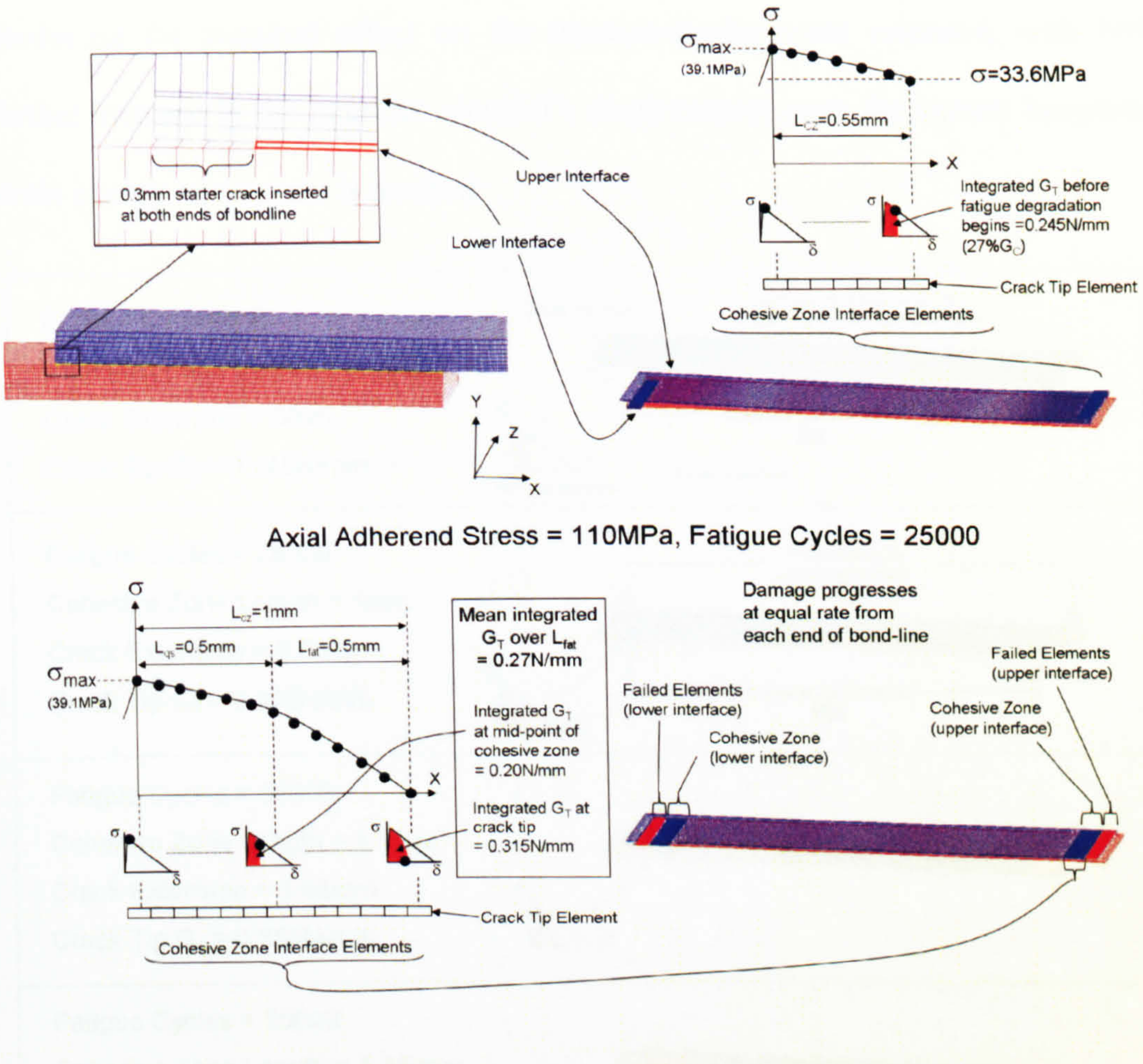

Figure 6.10: Cohesive zone development under fatigue loading

Figure 6.11 shows how damage progresses with elapsed fatigue cycles up to the point of failure. This indicates how the rate of crack propagation increases with crack extension due to the rising crack tip strain energy release rate. At zero cycles, before the fatigue law is activated, the strain energy release rate extracted from the crack tip interface element is equal to that obtained from a quasi-static analysis. All subsequent values of G_T listed, for increasing elapsed cycles, are those obtained from the crack tip element at the point of failure under fatigue degradation. As shown by Figure 6.12, these show close agreement with those obtained from the VCCT and interface element analyses for a quasi-static applied load of 110MPa on a model with

the same crack length. This validates that the fatigue damage formulation is producing the required effect on the traction-displacement response, with little further increase in the interface element's displacement once the correct integrated strain energy release rate is reached.

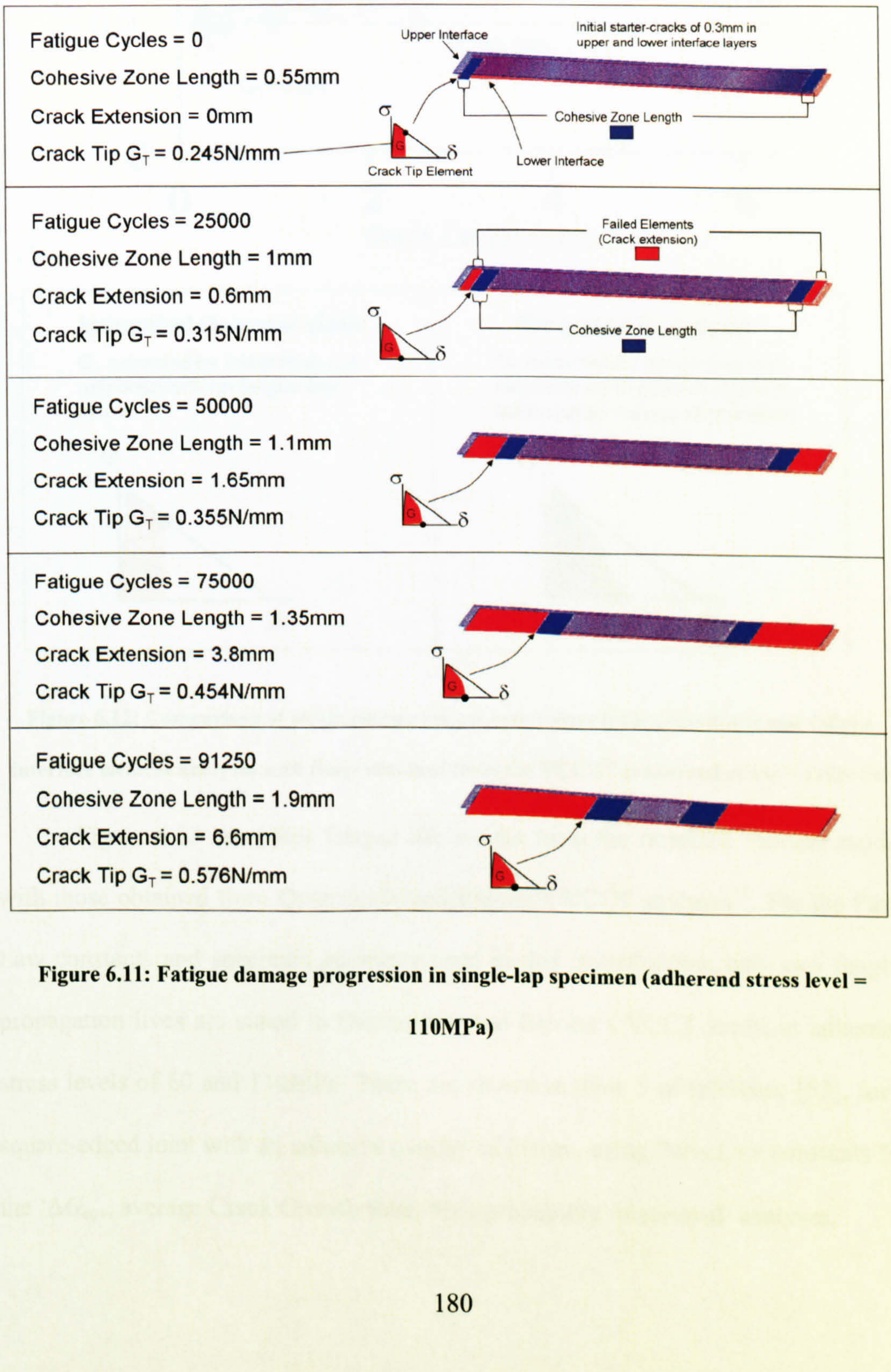

Figure 6.11: Fatigue damage progression in single-lap specimen (adherend stress level = 110MPa)

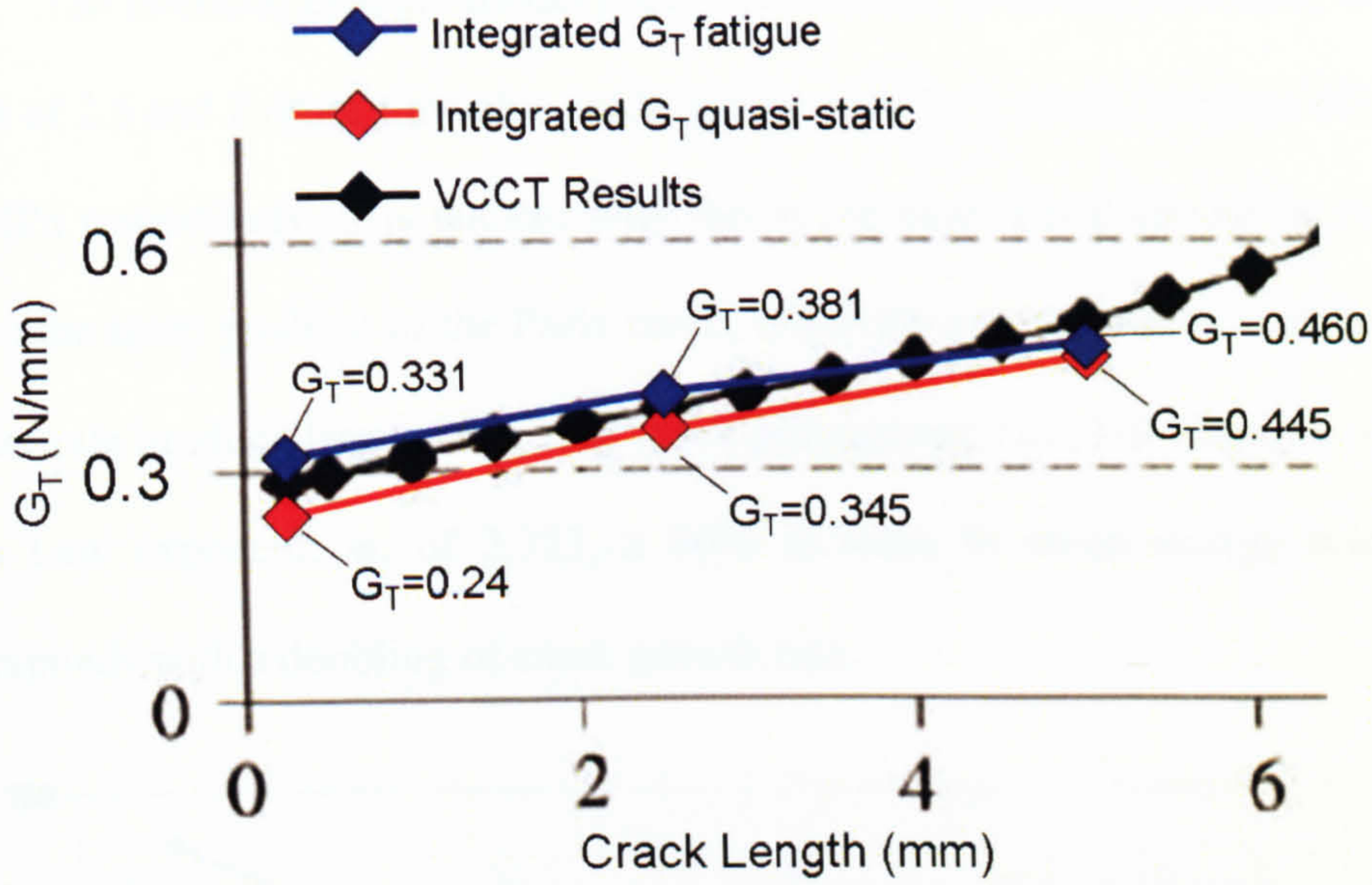

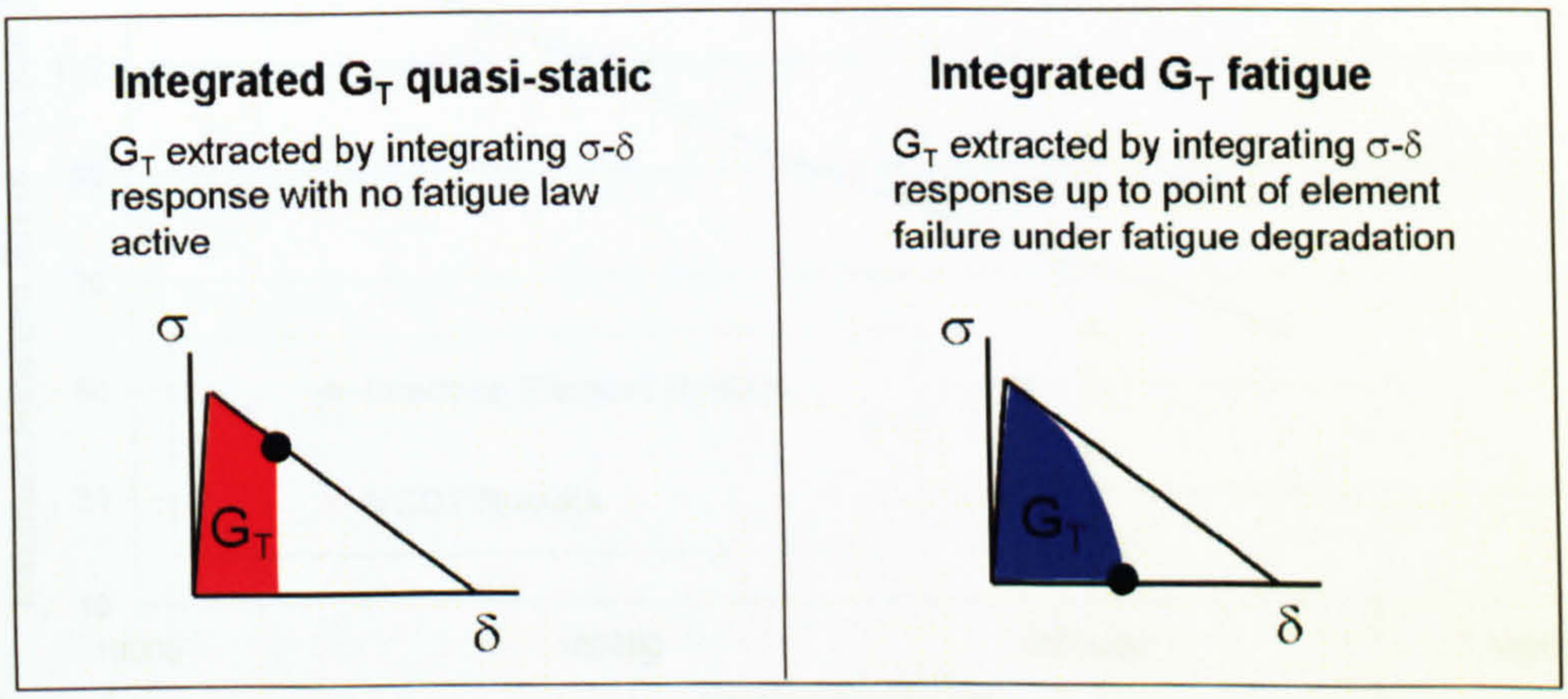

Figure 6.12: Comparison of strain energy release rate values from quasi-static and fatigue interface element analyses with those obtained from the VCCT[91] (adherend stress = 110MPa)

Figure 6.13 compares fatigue life results from the interface element model with those obtained from Quaresimin and Ricotta's VCCT analyses[51]. For the Paris Law constants and specimen geometry used in this investigation, only two fatigue propagation lives are stated in Quaresimin and Ricotta's VCCT study, at adherend stress levels of 60 and 110MPa. These are shown in table 5 of reference [51], for a square-edged joint with an adhesive overlap of 20mm, using Paris Law constants for the 'ΔG_{eqv}, average Crack Growth Rate, 50% probability of survival' analyses.

The interface element model predicts a number of cycles to failure, which is a factor of 2.5 and 2 times the value predicted by VCCT, at stress levels of 60MPa and 110MPa respectively. It is unclear why this is the case, but it should be noted that due to the steep gradient of the Paris curve, relatively small changes in strain energy release rate produce large changes in crack propagation rate. For example, using the Paris Law exponent, *m*, of 2.723, a 30% increase in strain energy release rate corresponds with a doubling of crack growth rate.

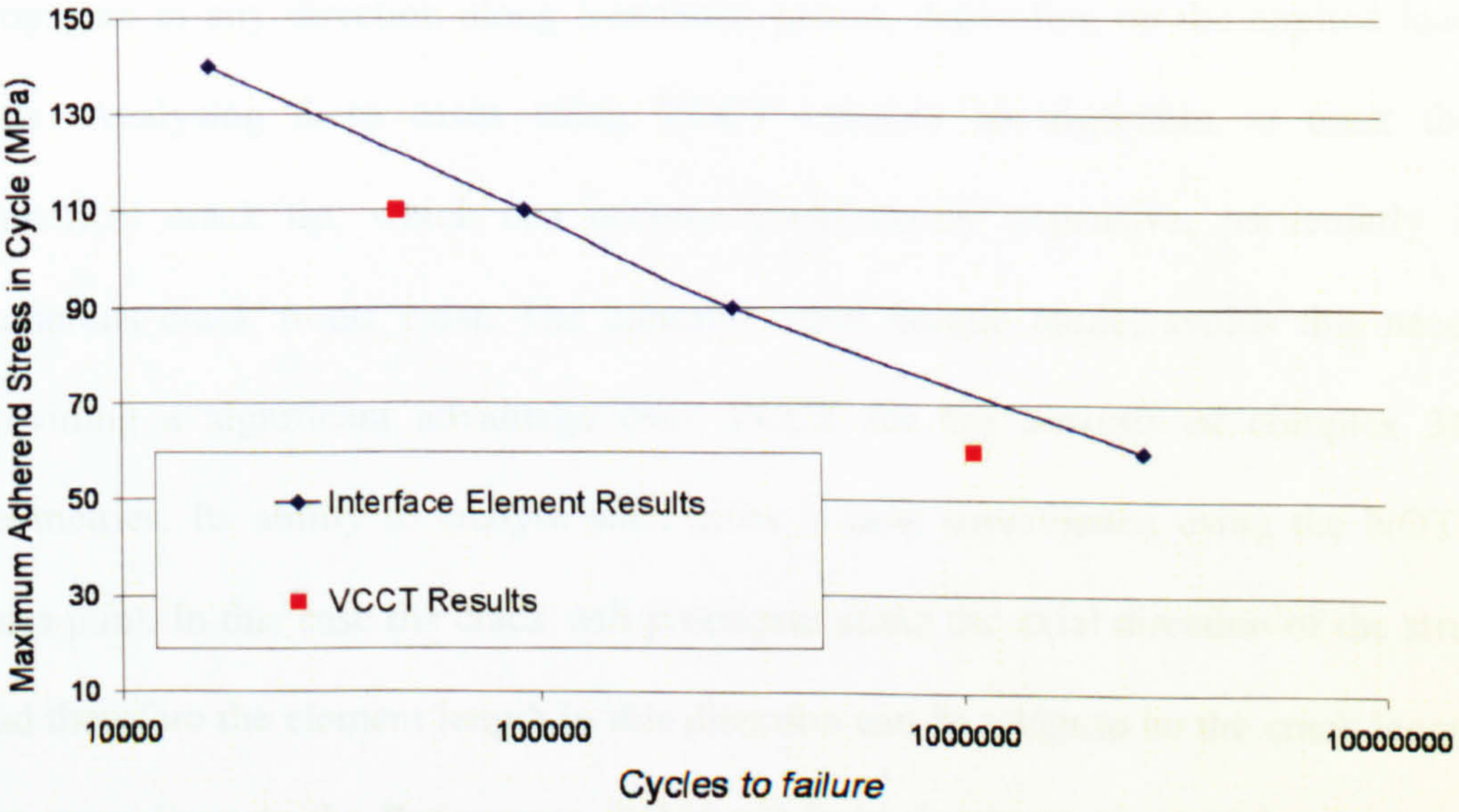

Figure 6.13: Fatigue crack propagation lifetimes predicted by interface element model and VCCT at various adherend stress levels

6.3 The NOTS Truss Joint

In the single-lap joint model previously discussed, a single element was used across the specimen width and consequently, the crack was constrained to propagate in one direction along the length of the bond-line. This enabled a direct comparison with Quaresimin and Ricotta's VCCT analyses[51,91], which were performed using 2D plane stress elements. A primary aim of developing the cohesive zone fatigue model has been to analyse cases of increased structural complexity, where cracks can propagate in any direction along interfacial planes, depending on the applied load state. Analysing these cases using VCCT requires an algorithm to track the numerical crack tip, which can become prohibitively expensive, particularly if numerous crack fronts exist. The cohesive zone fatigue model avoids this need, providing a significant advantage over VCCT for the analysis of complex 3D geometries. Its ability to analyse such cases is now investigated using the NOTS truss joint. In this case the crack will propagate along the axial direction of the strut and therefore the element length in this direction can be taken to be the crack length for comparison to the Paris curve. It has not been necessary to consider the more complex case of a crack front progressing in an arbitrary direction through a general mesh. This is left as further work for future studies.

6.3.1 Model Geometry and Setup

A truss joint model was created to represent the NOTS S2 test specimen detailed in chapter 2, the geometry of which is shown in Figure 6.14.

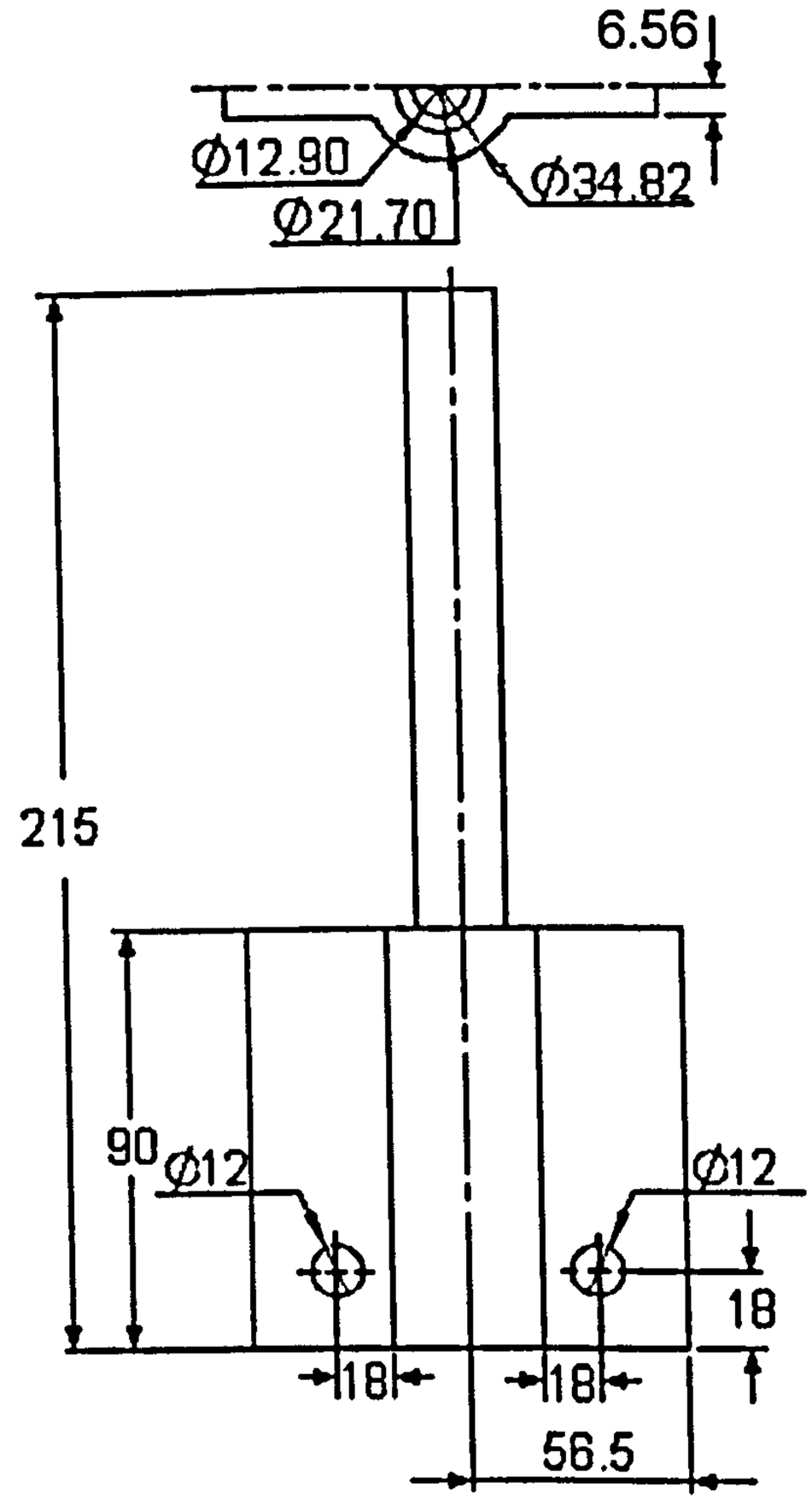

Figure 6.14: Truss Geometry

For pure axial loading, it was only necessary to model half the strut length and half of the cross-sectional area, as shown in Figure 6.15. To simulate the experimental S2 tests, a base plate and barrel nuts were included in the model as rigid bodies. These were constrained to move as a single entity, enabling load transfer from the base plate to the strut. Due to the tubular geometry, a cylindrical

co-ordinate system was applied to the strut, interface elements and cylindrical section of the nodal frame, as shown in Figure 6.15.

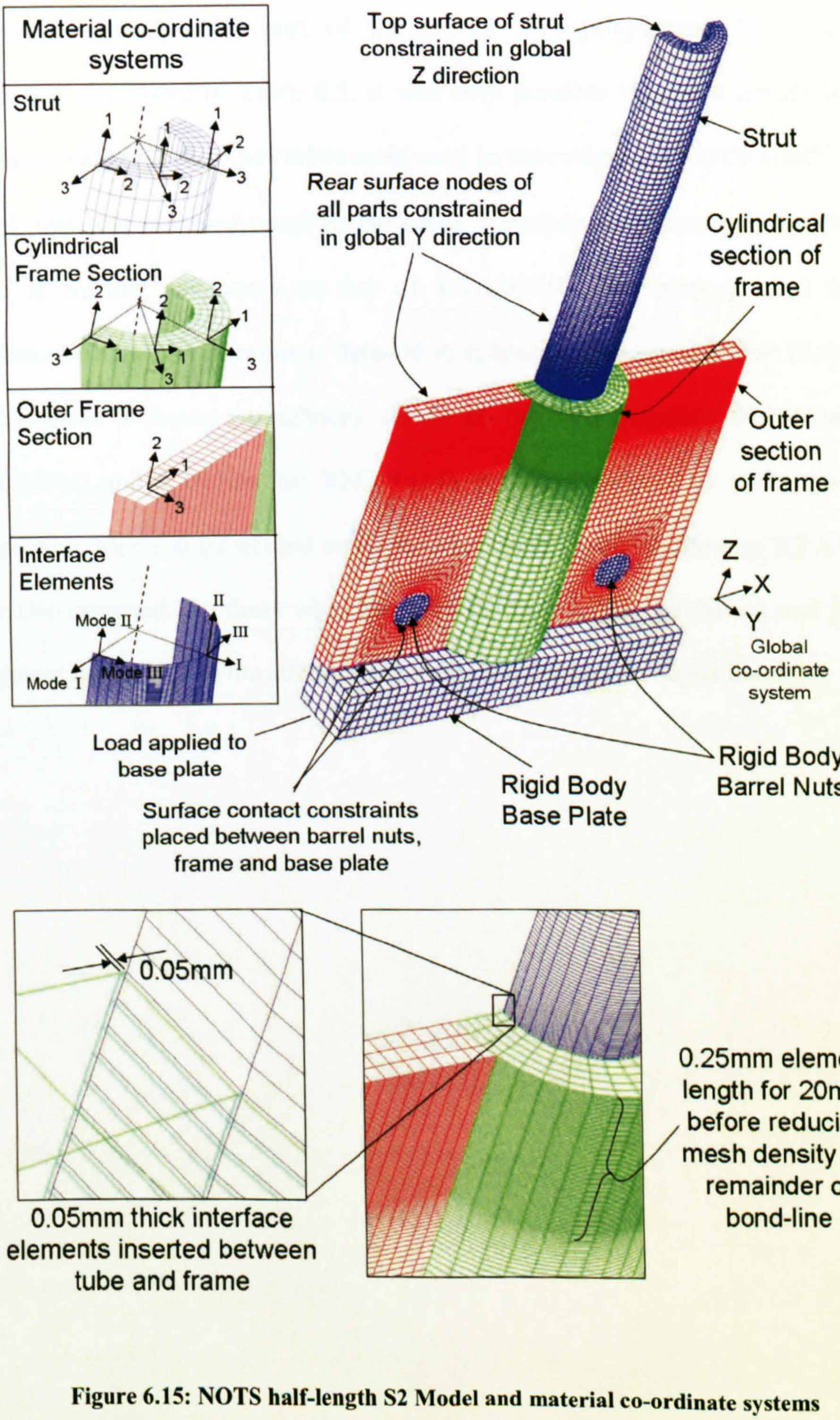

Figure 6.15: NOTS half-length S2 Model and material co-ordinate systems

Orthotropic elastic material properties were assigned to the strut and frame, as detailed in Table 6.3. These were gained from reference [30], a research thesis examining quasi-static design methods for composite truss structures at Oxford Brookes University, also part of the NOTS DTI programme. For interfacial properties, also listed in Table 6.3, it was only possible to gain a tensile fracture toughness value for the XMVR444 resin used in the co-bonded NOTS joint[93]. In the model, this was assumed equal to the mode I fracture toughness and an identical mode II fracture toughness to that of HTA/6376C, the prepreg used for the benchmark DCB/ENF specimens detailed in chapter 4 was applied. Due to the very similar mode I fracture toughness values of the two materials (0.26N/mm for HTA/6376C and 0.3N/mm for XMVR444), this was believed to be a reasonable assumption. Identical interfacial strengths and elastic moduli to those of HTA/6376C were also assumed, but these were less critical, since interfacial failure was fracture toughness driven due to the stress concentration at the square-edged overlap.

Table 6.3: Material Properties applied in S2 truss model

Orthotropic Elastic Properties of Strut and Nodal Frame					
	Nodal Frame	Strut			
E_{11} (MPa)	37600	88000			
E_{22} (MPa)	37600	30000			
E_{33} (MPa)	10000	30000			
ν_{12}	0.29	0.38			
ν_{13}	0.29	0.38			
ν_{23}	0.29	0.38			
G_{12} (MPa)	13100	6000			
G_{13} (MPa)	13100	6000			
G_{23} (MPa)	13100	6000			
Interface Element Properties					
G_{IC} (N/mm)	0.3	$\sigma_{max,I}$ (MPa)	30	K_I (N/mm^3)	100,000
G_{IIC} (N/mm)	1.0	$\sigma_{max,II}$ (MPa)	60	K_{II} (N/mm^3)	100,000

In order to allow an accurate analysis of bond-line failure, the mesh was refined in the region of the strut-node interface, with a minimum element length of 0.25mm extending along the first 20mm of the bonded region. This minimum element length was selected by applying the predictive formulae developed in chapter 4 for cohesive zone length, as previously performed for the single-lap joint model. Due to the different material properties and depths of the strut and nodal frame, it was necessary to apply the predictive formulae to each component. In the slender body equations, values for specimen depth, h, of 6.56mm (nodal frame thickness around strut) and 4.4mm (strut thickness) were applied for the frame and strut respectively. As shown by Table 6.4, the minimum predicted cohesive zone

length was 2.57mm, gained using the strut material properties in the slender body equation for pure mode I loading. This motivated the selection of a 0.25mm minimum element length, in order to ensure at least 10 elements within the cohesive zone for accurate strain energy release rate extraction. As will be shown in the following section, the fully developed cohesive zone under a purely quasi-static load was 4mm, for a mode ratio of G_I/G_T=0.73. This indicated that the predictive formulae were again successful in selecting an appropriate mesh density.

Table 6.4: Predicted cohesive zone lengths using the strut and nodal frame properties

Cohesive Zone Length Formula	Strut	Frame
$l_{ch,I} = 0.5E_I' \frac{G_{IC}}{(\sigma_{I,max})^2}$	4.11mm (E'_I = 24,685MPa)	2.60mm (E'_I = 15,615MPa)
$l_{ch,II} = 0.5E_{II}' \frac{G_{IIC}}{(\sigma_{II,max})^2}$	5.88mm (E'_{II} = 42,300MPa)	4.21mm (E'_{II} = 30,300MPa)
$l_{ch,slender,I} = 0.5\left(E_I' \frac{G_{IC}}{(\sigma_{I,max})^2}\right)^{\frac{1}{4}} h^{\frac{3}{4}}$	2.57mm (E'_I = 24,685MPa)	3.10mm (E'_I = 15,615MPa)
$l_{ch,slender,II} = 0.5\sqrt{\left(E_{II,slender}' \frac{G_{IIC}}{(\sigma_{II,max})^2}\right)h}$	5.32mm ($E'_{II,slender}$ = 92,600MPa)	4.19mm ($E'_{II,slender}$ = 38,500MPa)

6.3.2 Quasi-static Damage Progression and Strain Energy Release Rate Analyses

Figure 6.16 and Figure 6.17 show the nature of damage progression along the frame/strut interface under a linearly increasing tensile axial load applied to the base plate. As shown by Figure 6.16, a fully developed cohesive zone initially forms at the sides of the strut circumference closest to the barrel nuts, at an applied load of 35.1kN (60% final predicted failure load). As load increases further, the crack area increases and the cohesive zone develops as shown in Figure 6.17, with damage progressing inwards towards the centre of the strut circumference. This occurs in a stable manner until a fully developed cohesive zone exists around the entire strut circumference, at an applied load of 58.5kN. The crack then propagates in an unstable manner, resulting in instantaneous interfacial failure. The numerical UTS of 58.5kN exhibits close agreement with the mean experimental value of 61kN, indicating that appropriate interfacial properties have been applied.

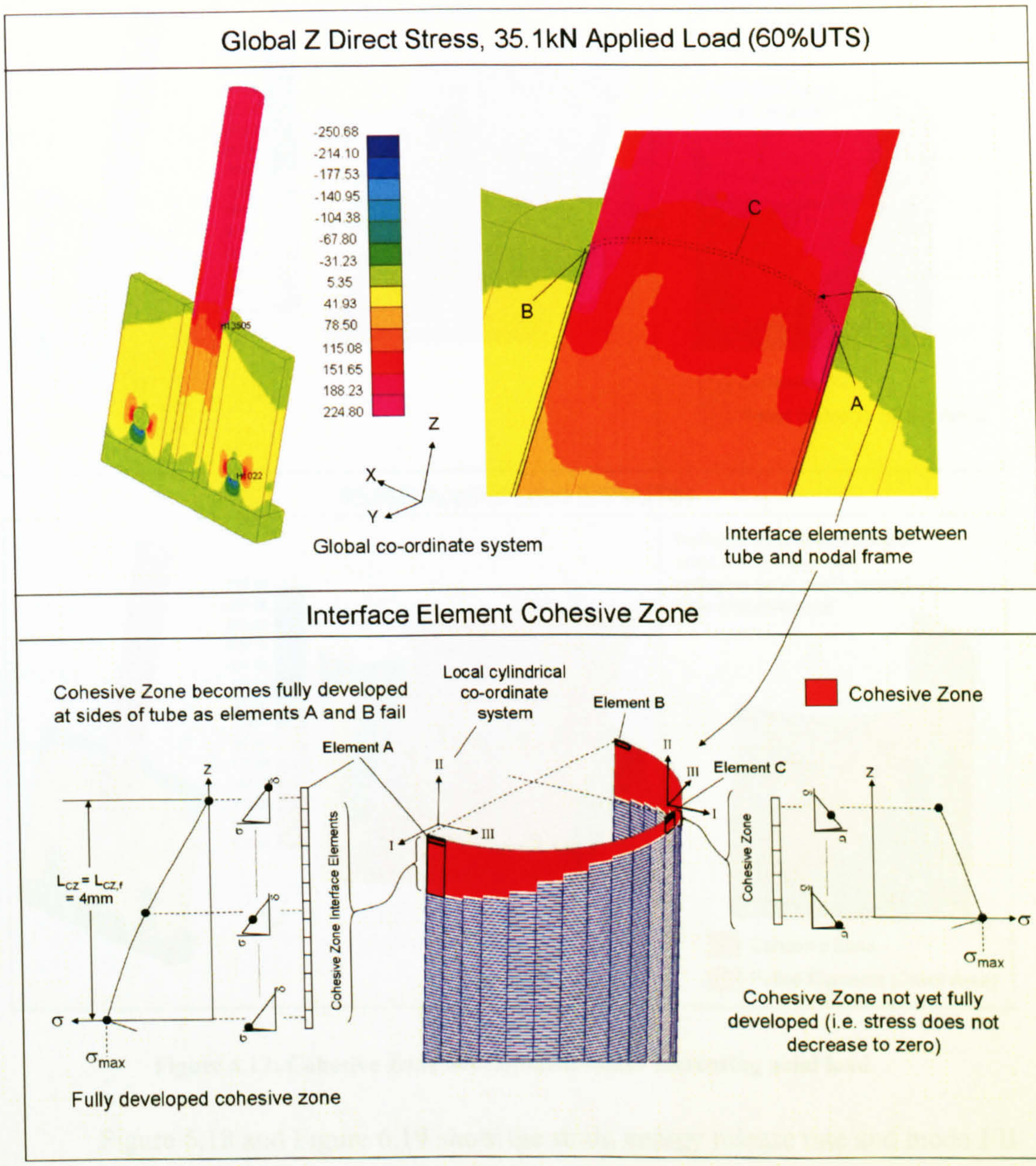

Figure 6.16: Global Z Direct Stress and Interface Element Cohesive Zone at 35.1kN applied load, the point of first interface element failure

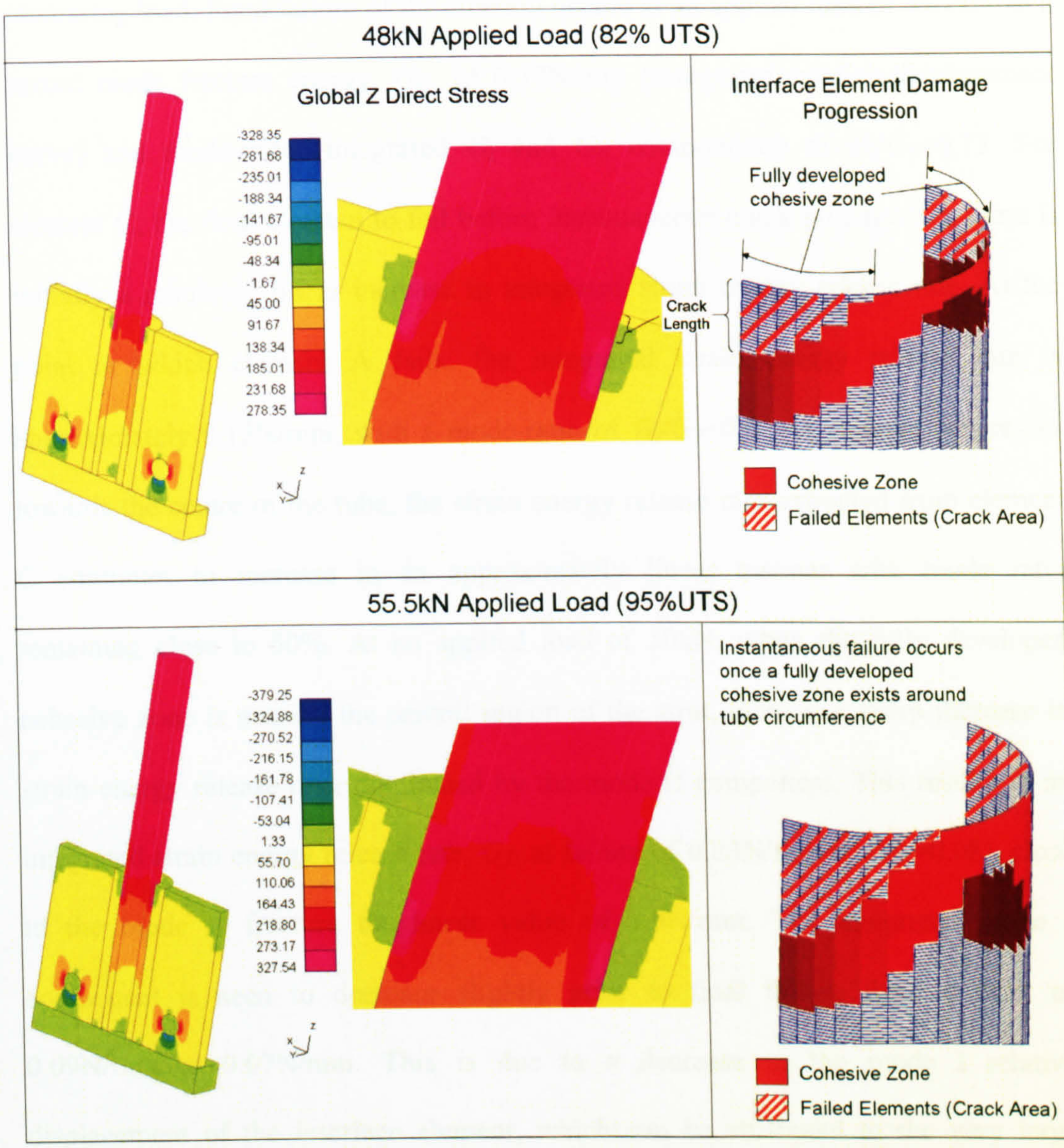

Figure 6.17: Cohesive Zone development under increasing axial load

Figure 6.18 and Figure 6.19 show the strain energy release rate and mode I/II components extracted from elements at the side (element A) and central region (element C) of the strut up to the point of final interfacial failure (refer to Figure 6.16 for exact element locations). Also shown is the global load-displacement relationship to indicate how the strain energy release rates correspond with applied load. For element A, the first element in the model to fail, producing a fully developed cohesive zone at the side of the strut, there is a sharply increasing integrated G_T with

increasing load. Final failure of the element occurs at an applied load of 35.1kN, at a mixed mode fracture energy, G_C, of 0.37N/mm (integrated traction-displacement curve) and mode-ratio (integrated G_I and G_{II} components) of G_I/G_T=0.73. For element C, the final element to fail before instantaneous crack propagation, there is initially a relatively linear increase in integrated strain energy release rate. At the point at which element A fails, the integrated strain energy release rate is approximately 0.12N/mm, with a mode-ratio of G_I/G_T=0.5. As damage progresses towards the centre of the tube, the strain energy release rate extracted from element C continues to increase in an approximately linear manner with mode ratio remaining close to 50%. At an applied load of 50kN, when the fully developed cohesive zone is nearing the central region of the strut, there is a sharp increase in strain energy release rate, dominated by the mode II component. This results in an integrated strain energy release rate, G_T, at failure of 0.83N/mm (G_I/G_T=0.08), close to the mode II fracture toughness value of 1.0N/mm. The integrated mode I component is seen to decrease slightly prior to final failure from a peak of 0.09N/mm to 0.07N/mm. This is due to a decrease in the mode I relative displacement of the interface element, which can be attributed to the very large change in its mode ratio prior to final failure.

This analysis was also performed with small initial starter cracks of 0.5mm and 1mm. These showed negligible differences in either the failure load or strain energy release rates extracted. Since the eventual aim is to integrate the fatigue degradation law with a crack initiation law, which can account for the effects of features such as adhesive fillets, only results with no initial starter crack are presented. This model setup, with no initial pre-crack inserted was also maintained for the subsequent fatigue analyses.

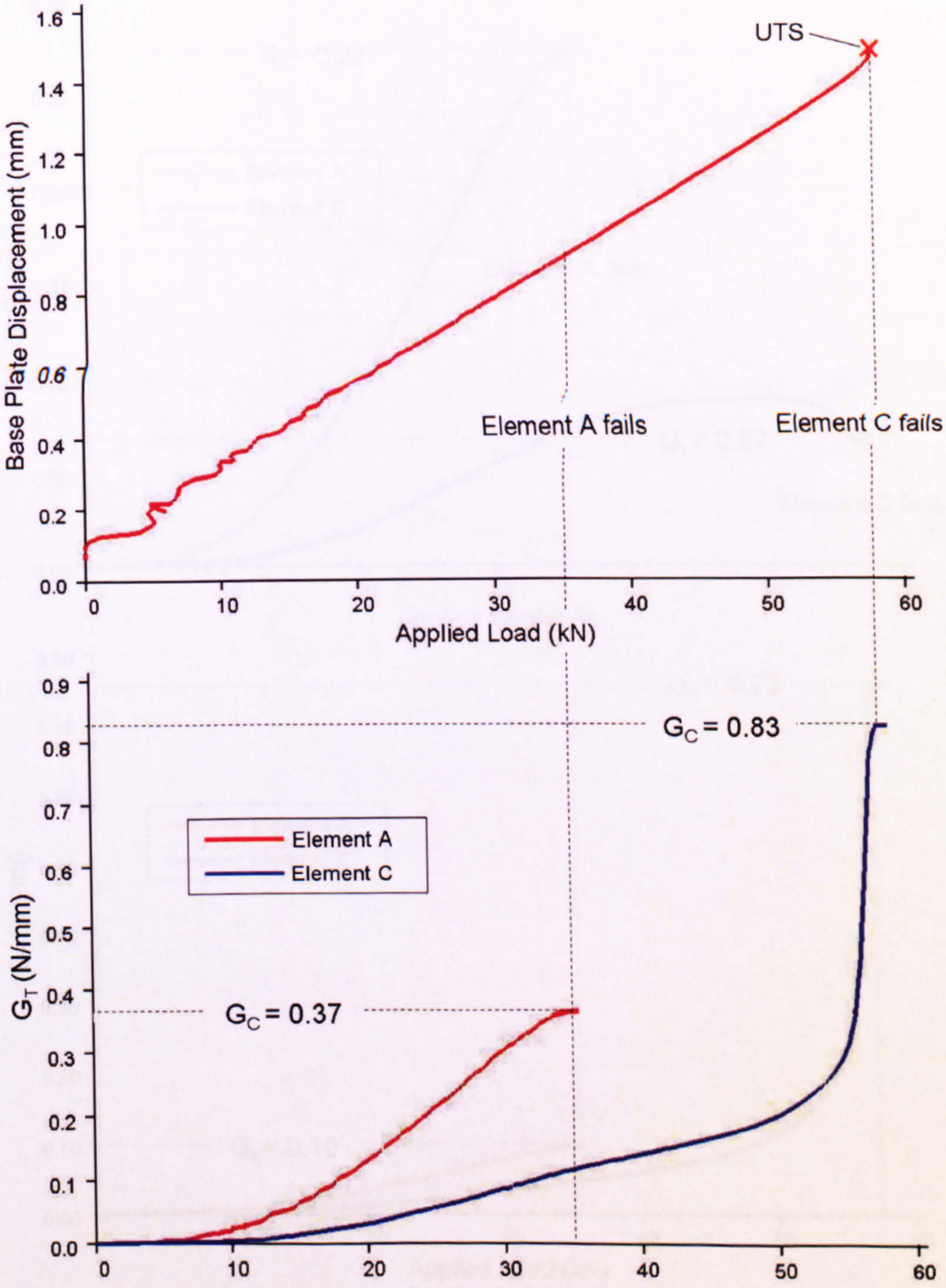

Figure 6.18: Strain Energy Release Rate extracted from sides and centre of strut in relation to global load-displacement relationship

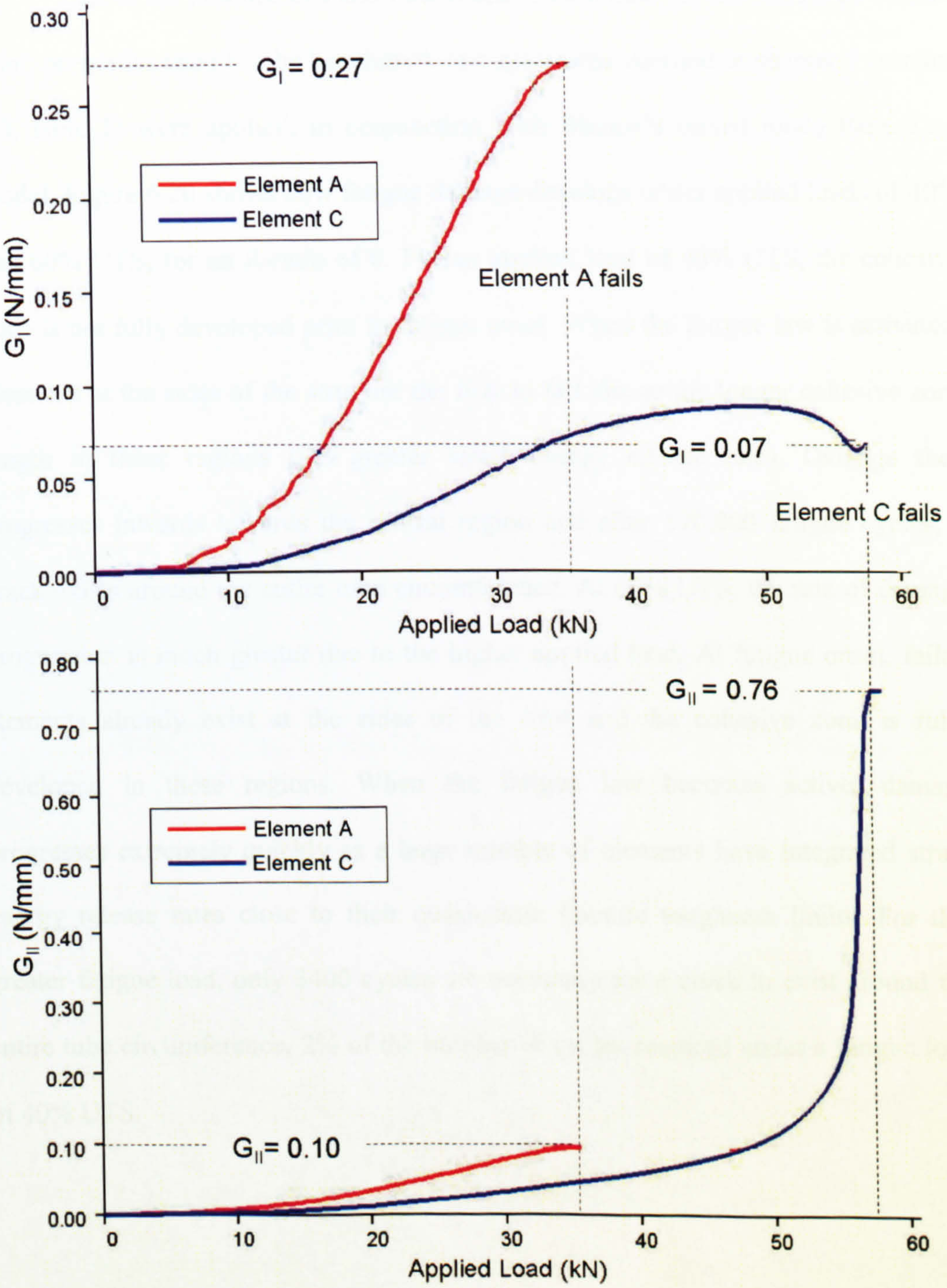

Figure 6.19: Strain Energy Release Rate components extracted from sides and centre of strut

6.3.3 Fatigue Analyses

Due to the absence of Paris Law crack growth data for the NOTS co-bonded joint, properties used for the benchmark test specimens detailed in chapter 5 (section 5.3, table 1) were applied, in conjunction with Blanco's mixed mode Paris Law model. Figure 6.20 shows how fatigue damage develops under applied loads of 40% and 60% UTS, for an R-ratio of 0. For an applied load of 40% UTS, the cohesive zone is not fully developed prior to fatigue onset. When the fatigue law is activated, elements at the sides of the strut are the first to fail due to the longer cohesive zone length in these regions (i.e. greater strain energy release rate). Damage then progresses inwards towards the central region and after 170,000 fatigue cycles, a crack exists around the entire tube circumference. At 60% UTS, the rate of damage progression is much greater due to the higher applied load. At fatigue onset, failed elements already exist at the sides of the strut and the cohesive zone is fully developed in these regions. When the fatigue law becomes active, damage progresses extremely quickly as a large number of elements have integrated strain energy release rates close to their quasi-static fracture toughness limits. For this greater fatigue load, only 3400 cycles are necessary for a crack to exist around the entire tube circumference, 2% of the number of cycles required under a fatigue load of 40% UTS.

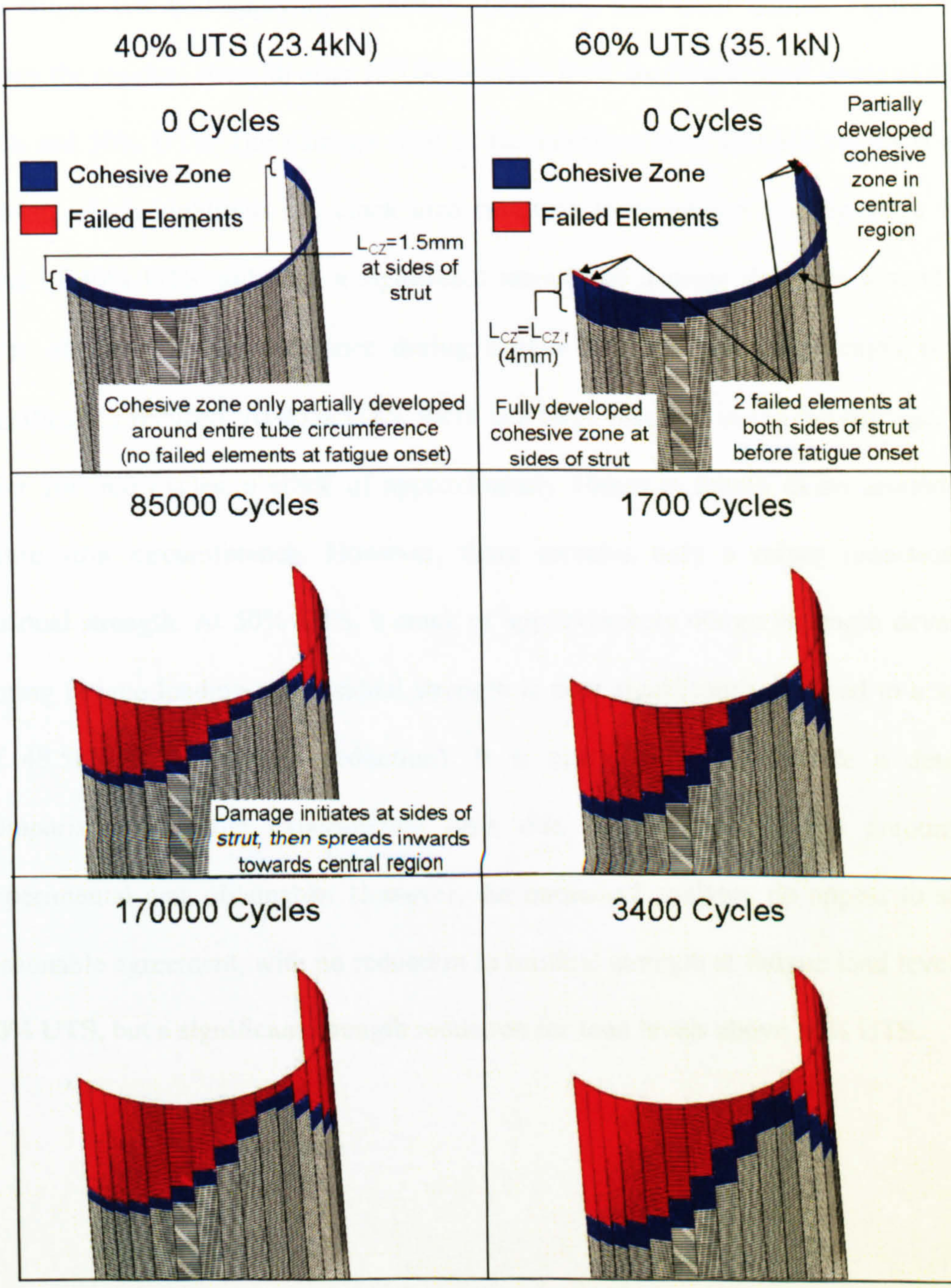

Figure 6.20: Interfacial Damage Progression under fatigue load levels of 40% and 60% UTS

The above analyses have demonstrated how the fatigue model can be used to simulate damage progression. This technique is now extended to include a residual strength check after a given number of elapsed fatigue cycles at a specified fatigue load. In order to remain consistent with the test procedure performed for the S2 experimental specimens, 100,000 fatigue cycles were applied, before de-activating

the fatigue law and applying a linearly increasing load until failure. Figure 6.21 shows the residual strength after 100,000 cycles, R=0, for fatigue load levels of 40%, 45% and 50% UTS. The damage state of the interface after 100,000 cycles is also shown, which highlights the crack area resulting from fatigue loading. At a load level of 40% UTS, although a significant amount of damage develops around the sides of the strut circumference during fatigue loading, residual strength is not significantly reduced. At 45% UTS, there is a large increase in fatigue damage, and after 100,000 cycles, a crack of approximately 10mm in length exists around the entire strut circumference. However, there remains only a minor reduction in residual strength. At 50% UTS, a crack of approximately 40mm in length develops during fatigue loading and residual strength is now significantly reduced to a value of 48.5kN (17% strength reduction). It is not possible to provide a detailed comparison with the experimental tests due to the very limited amount of experimental data obtainable. However, the numerical analyses do appear to show reasonable agreement, with no reduction in residual strength at fatigue load levels of 40% UTS, but a significant strength reduction for load levels above 50% UTS.

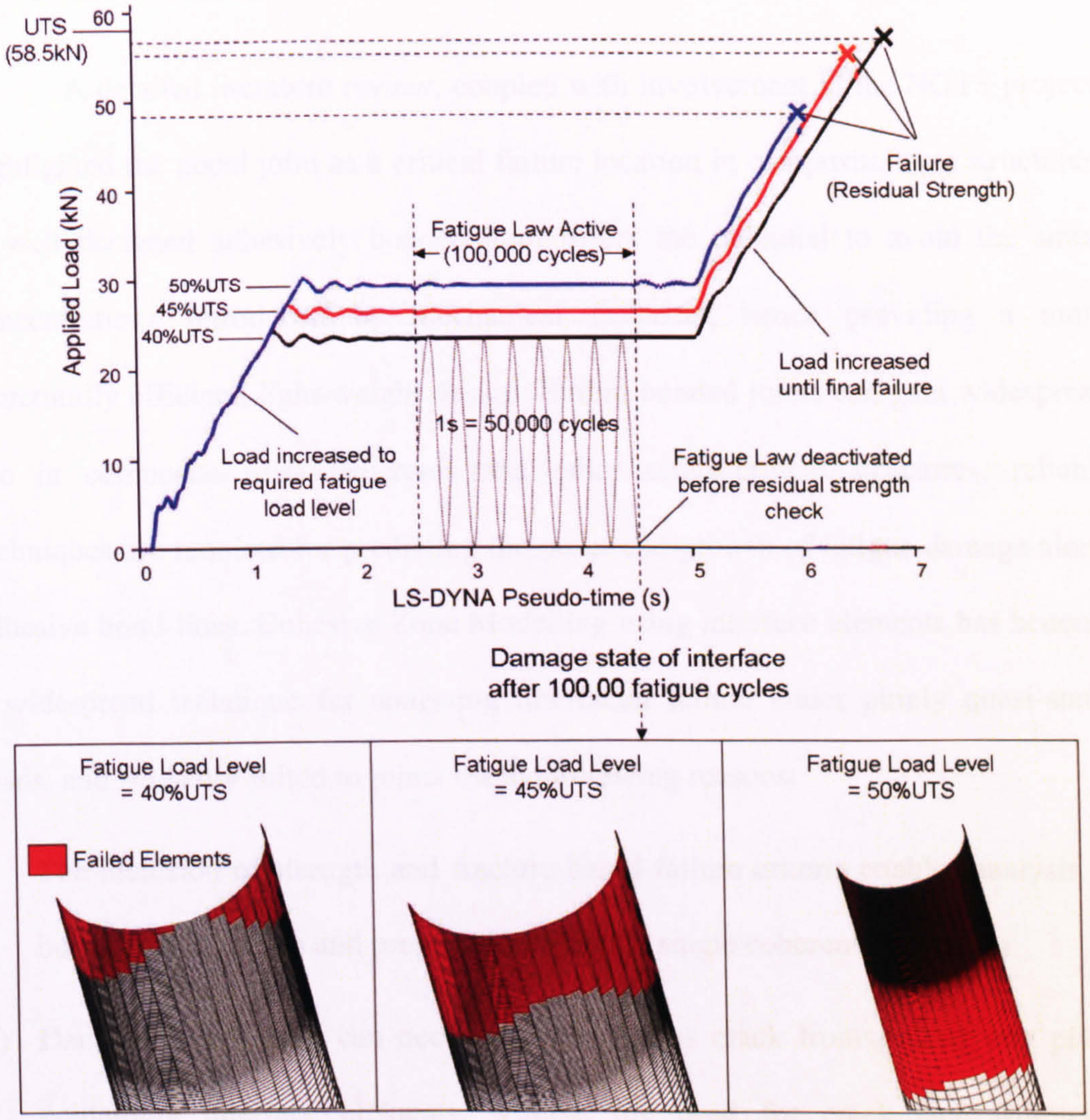

Figure 6.21: Residual Strength after 100,000 cycles at load levels of 40, 45 and 50% UTS

7. *Conclusions and Future Work*

A detailed literature review, coupled with involvement in the NOTS project, highlighted the nodal joint as a critical failure location in composite truss structures. A well designed adhesively bonded joint offers the potential to avoid the stress concentrations introduced by mechanical fasteners, hence providing a more structurally efficient, light-weight design. Before bonded joints can gain widespread use in composite truss structures and other safety-critical structures, reliable techniques are required for predicting the onset and growth of fatigue damage along adhesive bond-lines. Cohesive Zone Modelling using interface elements has become a widespread technique for analysing interfacial failure under purely quasi-static loads, and is ideally suited to joints for the following reasons:

i) The inclusion of strength and fracture based failure criteria enables analysis of both crack initiation and propagation within a single coherent simulation

ii) Damage propagation can occur from numerous crack fronts, along any plane containing interface elements, without the need for crack path following algorithms.

This research project has demonstrated how these advantages can be extended to fatigue analyses, through the development of an interface element fatigue crack propagation law. The law can be used to evaluate whether the crack tip strain energy release rate is sufficient for crack growth to occur and if so, to simulate the rate and direction of growth. The extraction of strain energy release rate from the cohesive zone enables a direct link with the Paris Law and experimental parameters obtained from standard fracture toughness specimens such as the DCB and ENF.

Whilst such an approach has been presented by previous authors, the novelty of the current work lies in the following areas:

i) A detailed analysis of the length and stress distribution of the cohesive zone, both under quasi-static loading and with the fatigue law active. This is essential for the accurate extraction of strain energy release rate and application of the required interface element failure rate under fatigue loading.

ii) Development of the law within the explicit FE code, LS-Dyna, which explicitly accounts for the strain energy release over the entire cohesive zone thus allowing a physical link to Paris type curves which are essentially rooted in linear elastic fracture mechanics.

iii) Application of the fatigue law to analyse interfacial crack propagation in a 3-D nodal truss joint, representative of a structural component for which large amounts of physical testing become prohibitively expensive. The ability to analyse the rate of damage progression and evaluate residual strength after a given number of fatigue cycles has been demonstrated.

Main achievements of the research presented and important areas of future work are now discussed in more detail.

7.1 The Numerical Cohesive Zone and Strain Energy Release Rate Extraction

Detailed analyses of numerical cohesive zone length and stress distribution have identified that crack tip strain energy release rate can be extracted by integrating the traction-displacement response of interface elements directly adjacent to the crack tip. As shown by Figure 7.1, for a bi-linear traction-displacement law, a minimum of 10 interface elements must exist within the fully developed cohesive zone length for a reasonably accurate value of strain energy release rate to be

extracted. This requires a significantly finer mesh than is necessary purely to perform a global load-displacement analysis, for which only 2-3 elements must exist within the fully developed cohesive zone length.

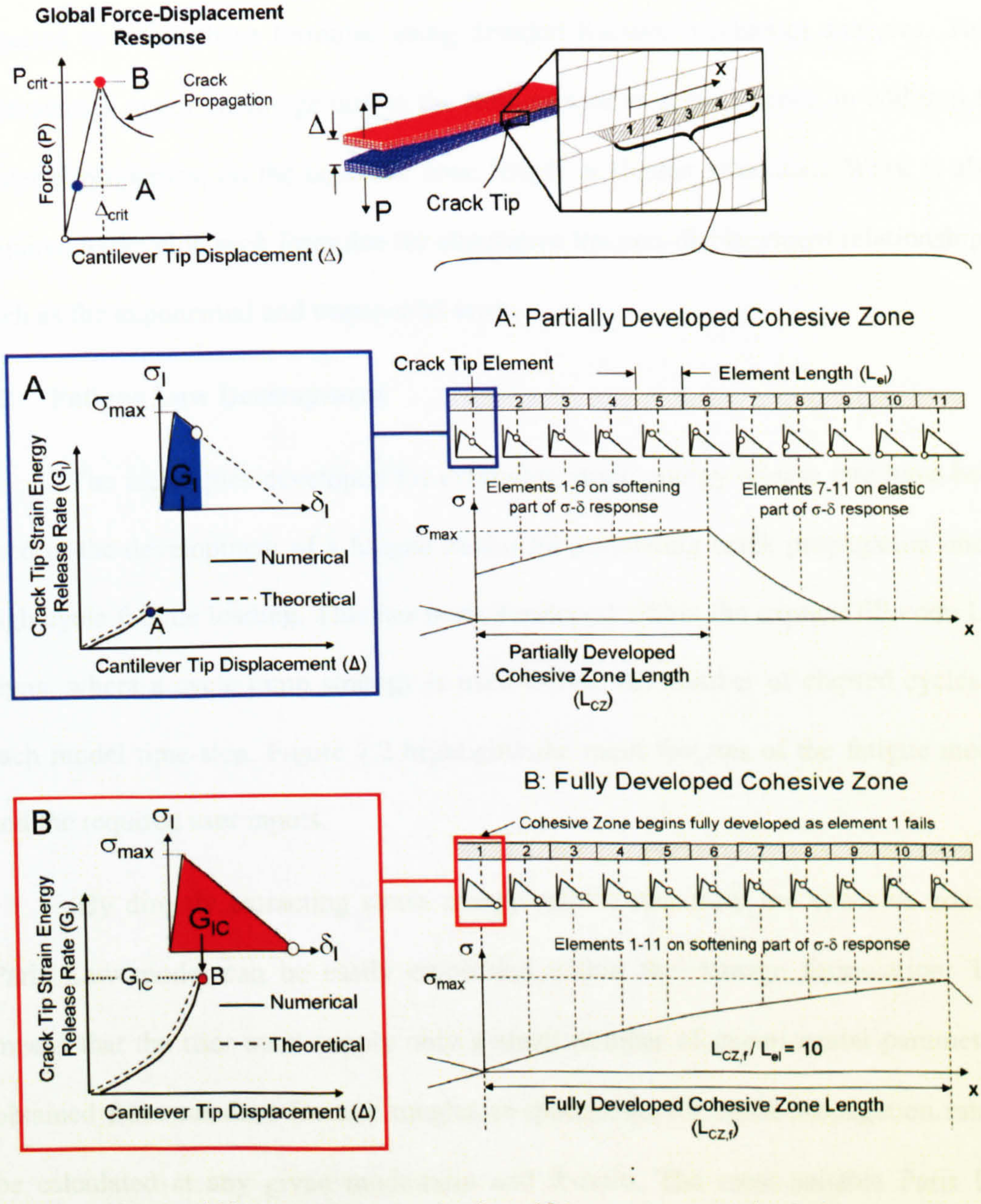

$L_{CZ,f} / L_{el}$ should be equal to or greater than 10 to ensure accurate strain energy release rate can be gained by integrating σ-δ response of crack tip interface element when cohesive zone is only partially developed

Figure 7.1: Strain energy release rate extraction from the cohesive zone

Existing formulae for predicting cohesive zone length and hence, design an appropriate finite element mesh, were found to give significant errors. Based on numerical analyses of standard fracture toughness specimens, modified versions of these formulae have been developed, providing improved accuracy. Further work is required to refine these formulae using detailed fracture mechanics analyses. This represents a major challenge due to the influence of structural depth, in addition to material properties, on the cohesive zone length in slender structures. Work is also required to develop such formulae for alternative traction-displacement relationships, such as the exponential and trapezoidal laws.

7.2 Fatigue Law Development

The techniques developed for extracting strain energy release rate have been used in the development of a fatigue model for simulating crack propagation under high cycle fatigue loading. This has been developed within the explicit FE code LS-Dyna, where a cycle jump strategy is used to link the number of elapsed cycles to each model time-step. Figure 7.2 highlights the main features of the fatigue model and the required user inputs.

By directly extracting strain energy release rate from the cohesive zone, a Paris Law model can be easily embedded within the damage formulation. This means that the user must supply only a small number of experimental parameters, obtained from standard fracture toughness specimens, for crack propagation rate to be calculated at any given mode-ratio and R-ratio. The most suitable Paris Law model is material dependent and the ability to insert this as a discrete component of the damage algorithm is of significant benefit in providing flexibility of application. Within this thesis, two distinct Paris Law models have been implemented within the

obtained from a quasi-static analysis to the same maximum load level. Elements in this region acquire predominantly fatigue damage.

These lengths are automatically calculated by the fatigue law using the user-defined fully developed cohesive zone length, combined with the strain energy release rate and quasi-static fracture toughness extracted from the model.

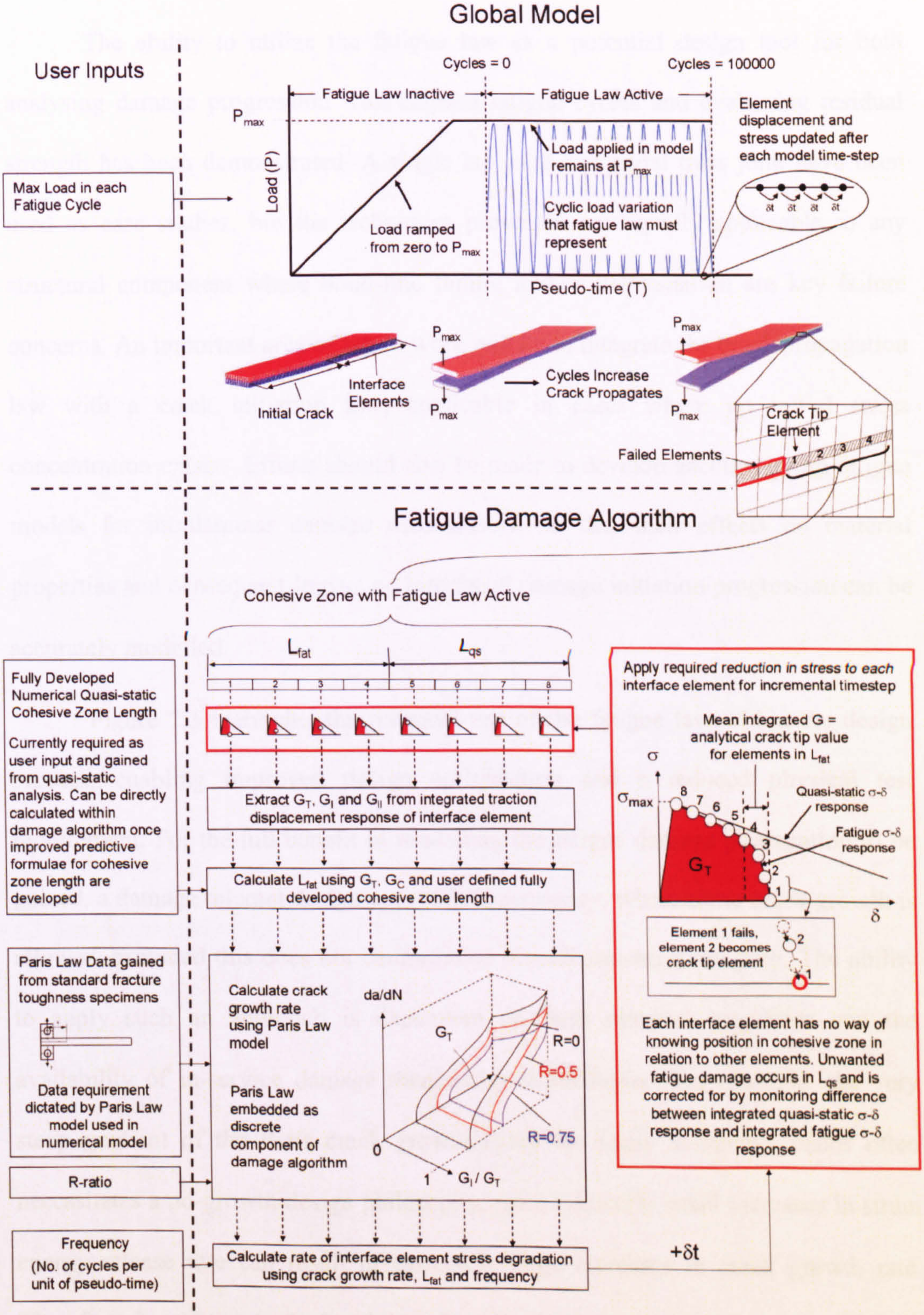

Figure 7.2: Main features of the interface element fatigue model and user inputs required

damage algorithm and used in conjunction with the strain energy release rate extracted from the cohesive zone in order to analyse crack propagation.

It has been shown that in order to avoid the need for a crack path following algorithm, the fully developed cohesive zone length under a quasi-static load must be known. Due to the further work required to develop improved predictive formulae for cohesive zone length, this parameter is currently supplied as a user input and must be gained from a quasi-static analysis prior to fatigue law application. Although the fully developed cohesive zone length can change as a crack propagates due to mode-ratio variations, only if these are very large will significant inaccuracies occur. Once improved predictive formulae for cohesive zone length are developed, these can be included within the fatigue damage algorithm, allowing the cohesive zone length used within the calculations to be continuously updated as a crack advances.

When the fatigue degradation law is active, the cohesive zone can be divided into two distinct regions:

i) A quasi-static damage length, L_{qs} over which the integrated strain energy release rate is significantly less than the crack tip value and elements acquire predominantly quasi-static damage. Due to the absence of a crack path following algorithm, interface elements have no way of knowing their position in relation to the crack tip and some unwanted fatigue damage within this region cannot be prevented. This unwanted damage is corrected for by monitoring the difference between the quasi-static traction-displacement response and the traction-displacement response with the fatigue law active.

ii) A fatigue damage length, L_{fat}, over which the mean integrated strain energy release rate is equal to the crack tip strain energy release rate that would be

7.3 Fatigue Law Applications

The ability to utilize the fatigue law as a potential design tool for both analysing damage progression with elapsed fatigue cycles and evaluating residual strength has been demonstrated. A single-lap joint and nodal truss joint have been used as case studies, but the techniques presented are equally applicable to any structural component where bond-line failure and/or delamination are key failure concerns. An important area of future work will be to integrate the crack propagation law with a crack initiation law, applicable in cases where no initial stress concentration exists. Efforts should also be made to develop accompanying fatigue models for intralaminar damage mechanisms, so that their effects on material properties and consequent impact on interfacial damage initiation/progression can be accurately modelled.

Figure 7.3 highlights the potential use of the fatigue law within the design process, enabling improved design optimisation and a reduced physical test requirement. For the full benefit of modelling the fatigue damage propagation to be gained, a damage tolerant design approach is necessary, where some crack growth is allowed, provided this does not compromise overall structural integrity. The ability to apply such an approach is dependent on both material properties and the availability of in-service damage monitoring technologies. For example, the very steep gradient of the Paris crack growth curve for many composite resins often necessitates a no-growth design philosophy, since relatively small increases in strain energy release rate can result in extremely large increases in crack growth rate. Therefore, in addition to further fatigue law development, research is also required to develop improved materials and damage monitoring technologies, so that a damage tolerant design approach can be more confidently applied.

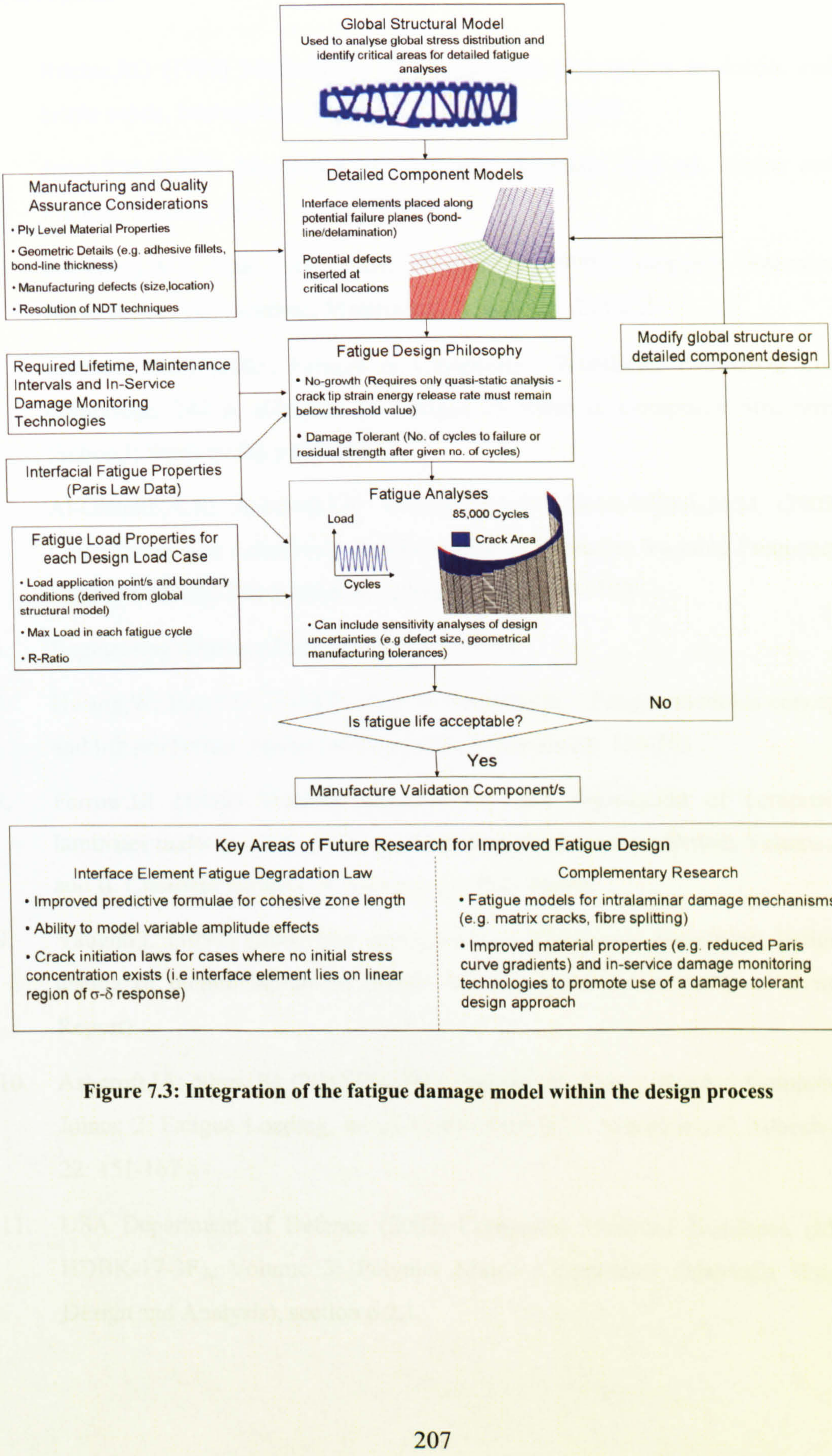

Figure 7.3: Integration of the fatigue damage model within the design process

References

1. Ritchie,RO (1999) Mechanisms of fatigue-crack propagation in ductile and brittle solids, International Journal of Fracture, 100: 55-83

2. Jones,RM (1999) Mechanics of composite materials. 2nd ed. Taylor and Francis, London, p333

3. De Goeij,WC; Van Tooren,MJL; Beukers,A (1999) Composite Adhesive Joints under cyclic loading, Materials & Design, 20: 213-221

4. Harris,B (Ed.) (2003) Fatigue in Composites. Woodhead Publishing Ltd, Cambridge. 742 p. (Chapter 23: Fatigue of Joints in Composite Structures (Schon,J; Starikov,R), p621-643)

5. Al-Ghamdi,A.H; Ashcroft,I.A; Crocombe,A.D; Abdel-Wahab,M.M (2003) Crack Growth in Adhesively Bonded Joints Subjected to Variable Frequency Fatigue Loading, The Journal of Adhesion, 79: 1161-1182

6. Engineering Sciences Data Unit (2004), 97018

7. Hwang,W; Han,KS (1986) Fatigue of Composites – Fatigue modulus concept and life prediction, Journal of Composite Materials 20: 154-165

8. Farrow,IR (1989) Damage accumulation and degradation of composite laminates under aircraft service loading: assessment and prediction. Volumes I and II. Cranfield Institute of Technology, PhD Thesis

9. Vaughn,L (1997) Innovative Approaches to Composite Structures: Fatigue testing of double lap-joints, Report No. 50 (Internal University of Bristol Report)

10. Ashcroft,IA; Shaw,SJ (2002) Mode I Fracture of Epoxy Bonded Composite Joints: 2. Fatigue Loading, International Journal of Adhesion and Adhesives, 22: 151-167

11. USA Department of Defence (2002) Composite Materials Handbook (ML-HDBK-17-3F), Volume 3: Polymer Matrix Composites (Materials Usage, Design and Analysis), section 6.2.1

12. Degrieck,J; Paepegem,WV (2001) Fatigue Damage Modelling of Fibre-reinforced Composite Materials: Review, Applied Mechanics Reviews, 54: 279-300

13. Curtis,PT (1998) Designing for fatigue and environmental effects in polymer composites, Structural Materials Centre, DERA, Farnborough, Document No. C536/012/98

14. Tserpes,KI; Papanikos,P; Labeas,G; Pantelakis,Sp (2004) Fatigue damage accumulation and residual strength assessment of CFRP laminates, Composite Structures, 63: 219-230

15. Gamstedt,EK; Andersen,S (2001) Fatigue Degradation and Failure of Rotating Composite Structures, Materials Research Department, Riso National Laboratory, Roskilde, Denmark, Document No. Riso-R-1261(EN)

16. Niu,MC. Composite airframe structures: practical design information and data. 2nd ed. Hong Kong: Conmilit, 1993. 664 p.

17. Adams,RD; Comyn,J; Wake,WC (1997): Structural Adhesive Joints in Engineering. 2nd ed. Chapman & Hall, London. 359 pages.

18. Yang,C; Huang,H; Guan,Z (2001) Stress Model of Composite Pipe Joints Under Bending, Journal of Composite Materials, 36: 1331-1348

19. USA Department of Defence (2002) Composite Materials Handbook (ML-HDBK-17-3F), Volume 3: Polymer Matrix Composites (Materials Usage, Design and Analysis), section 6.2.2.5

20. USA Department of Defence (2002) Composite Materials Handbook (ML-HDBK-17-3F), Volume 3: Polymer Matrix Composites (Materials Usage, Design and Analysis), section 6.2.2.3

21. Fitton,MD; Broughton,JG (2005) Variable Modulus Adhesives: An approach to optimised joint performance, International Journal of Adhesion and Adhesives, 25: 329-336

22. Potter,K; Guild,FJ; Harvey,HJ; Wisnom,MR; Adams,RD (2001) Understanding and control of adhesive crack propagation in bonded joints

between carbon fibre composite adherends: 1. Experimental, International Journal of Adhesion and Adhesives, 21: 435-443

23. Varvill,R; Bond,A (2004) Application of Carbon Fibre Truss Technology to the Fuselage Structure of the Skylon Spaceplane, Journal of the British Interplanetary Society, 57: 173-185

24. Potter,K (1998) Final Report of the IACS programme at Bristol University, Report No. 80 (Internal University of Bristol Report)

25. Clarke,AB; Davies,RGH; Potter,KD; Wisnom,MR, Adams,RD (1997) The Design and Manufacture of High Performance Unidirectional Composite Tubular Joints, Proceedings of ICCM-11, Gold Coast, Australia, 14th-18th July 1997, Volume VI: 84-94

26. www.netcomposites.com

27. Potter,KD; Towse,A; Wisnom,MR (1997) Design and Manufacturing Study for a Small, Complex Component required in Large Production Volumes, Proceedings of ICCM-11, Gold Coast, Australia, 14th-18th July 1997, Volume VI: 103-112

28. BSI (1995) Adhesives - Test methods for fatigue properties of structural adhesives in tensile shear, BS EN ISO 9664:1995

29. Broughton,B (2001): Measurement Good Practice Guide No.28: Durability Performance of Adhesive Joints (National Physics Laboratory)

30. Becerra,N (2006) Analysis and optimisation of composite truss structures for aircraft applications, Oxford Brookes University PhD thesis

31. Harper,P; Hallett,SR (2006) NOTS S2 Fatigue Test Report, Report No. DR6041

32. Suresh,S (1998) Fatigue of Materials, 2nd ed., Cambridge University Press, p11

33. ASTM D5528-01(2007)e1 Standard Test Method for Mode I Interlaminar Fracture Toughness of Unidirectional Fiber-Reinforced Polymer Matrix Composites.

34. ASTM D6115-97(2004) Standard Test Method for Mode I Fatigue Delamination Growth Onset of Unidirectional Fiber-Reinforced Polymer Matrix Composites

35. Stevanovic,D; Jar,PYB; Kalyanasundaram,S; Lowe,A (2000) On crack-initiation conditions for mode I and mode II delamination testing of composite materials, Composites Science and Technology, 60: 1879-1887

36. Tamuzs,V; Tarasovs,S; Vilks,U (2003) Delamination properties of translaminar-reinforced composites, Composites Science and Technology, 63: 1423-1431

37. Reeder,JR; Crews,JR; Demarco,K; Whitley,KS (2004) The use of doubler reinforcement in delamination toughness testing, Composites: Part A, 35:1337–1344

38. Kinloch,AJ; Wang,Y; Williams,JG; Yayla,P (1993) The Mixed-Mode Delamination of Fibre Composite Materials, Composites Science and Technology, 47: 225-237

39. Schuecker,C; Davidson,BD (2000) Evaluation of the accuracy of the four-point bend end-notched flexure test for mode II delamination toughness determination, Composites Science and Technology, 60: 2137-2146

40. ASTM D6671/D6671M-06 Standard Test Method for Mixed Mode I-Mode II Interlaminar Fracture Toughness of Unidirectional Fiber Reinforced Polymer Matrix Composites

41. Asp,EL; Sjogren,A; Greenhalgh,ES (2001) Delamination Growth and Thresholds in a Carbon/Epoxy Composite Under Fatigue Loading, Journal of Composites Technology & Research, 23: 55-68

42. Al-Ghamdi,AH; Ashcroft,IA; Crocombe,AD; Abdel-Wahab,MM (2003) Crack Growth in Adhesively Bonded Joints Subjected to Variable Frequency Fatigue Loading, The Journal of Adhesion, 79: 1161-1182

43. Juntti,M; Asp,LE; Olsson,R (1999) Assessment of Evaluation Methods for the Mixed-Mode Bending Test, Journal of Composites Technology & Research, 21: 37-48

44. Chen,H; Shivakumar,K; Abali,F (2006) A comparison of total fatigue life models for composite laminates, Fatigue and Fracture of Engineering Materials and Structures, 29: 31-39

45. Schon,J (1999) A model of fatigue delamination in composites, Composites Science and Technology, 60: 553-558

46. Blanco,N; Gamstedt,EK; Asp,LE; Costa,J (2004) Mixed-mode delamination growth in carbon-fibre composite laminates under cyclic loading, International Journal of Solids and Structures, 41: 4219-4235

47. Rybricki,EF; Kanninen,MF (1977) A finite element calculation of stress intensity factors by a modified crack closure integral, Engineering Fracture Mechanics, 9:931–938

48. Wang,J; Rider,AN; Heller,M, Kaye,R (2005) Theoretical and experimental research into optimal edge taper of bonded repair patches subject to fatigue loadings, International Journal of Adhesion and Adhesives, 25: 410-426

49. Abdel-Wahab,MM; Ashcroft,IA; Crocombe,AD; Smith,PA (2004) Finite element prediction of fatigue crack propagation lifetime in composite bonded *joints, Composites* Part A: Applied Science and Manufacturing, 35: 213-222

50. Hoyt,DM; Ward,SH; Minguet,PJ (2002) Strength and Fatigue Life Modelling of Bonded Joints in Composite Structure, Journal of Composites Technology and Research, 24: 190-210

51. Quaresimin,M; Ricotta,M (2006) Life prediction of bonded joints in composite materials, International Journal of Fatigue, 28 (n 10 SPEC. ISS.): 1166-1176

52. Deobald,LR; Mabson,GE; Dopker,B; Hoyt,DM; Baylor,J; Graesser,D (2007) Interlaminar Fatigue Elements for Crack Growth Based On Virtual Crack Closure Technique, 48th AIAA/ASME/ASCE/AHS/ASC Structures, Structural Dynamics, and Materials Conference, 23 - 26 April 2007, Honolulu, Hawaii

53. Deobald,LR; Mabson,GE; Dopker,B; Hoyt,DM; Baylor,J; Graesser,D (2007) Fracture Interface Elements for Static and Fatigue Analysis, ICCM - 16th International Conference on Composite Materials, 8th -13th July 2007, Kyoto, Japan

54. Sun CT; Jih CJ (1987) On strain energy release rates for interfacial cracks in bi-material media, Engineering Fracture Mechanics, 28:13–20

55. Crisfield,MA; Davies,GAO (1998) Progressive Delamination Using Interface Elements, Journal of Composite Materials, 32: 1246-1272

56. Petrossian,Z; Wisnom,MR (1998) Prediction of delamination initiation and growth from discontinuous plies using interface elements, Composites Part A: Applied Science and Manufacturing, 29A: 503-515

57. Chen,J; Crisfield,M; Kinloch,AJ; Busso,EP; Matthews,FL; Qiu,Y (1999) Predicting Progressive Delamination of Composite Material Specimens via Interface Elements, Mechanics of Composite Materials and Structures, 6: 301-317

58. Crisfield,MA; Alfano,G (2000) Finite element interface models for the delamination analysis of laminated composites: mechanical and computational issues, International journal for numerical methods in engineering, 50: 1701-1736

59. Camanho,PP; Davila,CG; De Moura,MF (2003) Numerical Simulation of Mixed-mode Progressive Delamination in Composite Materials, Journal of Composite Materials, 37: 1415-1424

60. Pinho,ST; Ianucci,L; Robinson,P (2006) Formulation and implementation of decohesion elements in an explicit finite element code, Composites Part A: Applied Science and Manufacturing, 37: 778-789

61. Jiang,WG; Hallett,SR; Green,BG; Wisnom,MR (2007) A concise interface constitutive law for analysis of delamination and splitting in composite materials and its application to scaled notched tensile specimens. International journal for numerical methods in engineering, 69: 1982-1995

62. Camanho,PP; Davila,CG; Pinho,ST (2003) Fracture Analysis of Composite Co-cured Structural Joints Using Decohesion Elements, Fatigue Fract Engng Mater Struct, 27: 745-757

63. Blackman,BRK; Hadavinia,H; Kinloch,AJ; Williams,JG (2003) The use of a cohesive zone model to study the fracture of fibre composites and adhesively-bonded joints, International Journal of Fracture, 119: 25-46

64. Li,S; Thouless,MD; Waas,AM; Schroeder,JA; Zavattieri,PD (2006) Mixed-mode cohesive-zone models for fracture of an adhesively bonded polymer-matrix composite, Engineering Fracture Mechanics, 73: 64-78

65. Goyal,VK; Johnson,ER; Goyal,VK (2008) Predictive strength-fracture model for composite bonded joints, Composite Structures, 82: 434-446

66. Cox,B; Yang,Q (2005) Cohesive Models for damage evolution in laminated composites, International Journal of Fracture, 133: 107-137

67. Shet,C; Chandra,N (2002) Analysis of Energy Balance When Using Cohesive Zone Models to Simulate Fracture Processes, Journal of Engineering Materials and Technology, 124: 440-450

68. Shet,C; Chandra,N (2004) Effect of the Shape of traction-displacement cohesive zone curves on the fracture response, Mechanics of Advanced Materials and Structures, 11: 249-275

69. Roe,KL; Siegmund,T (2001) An irreversible cohesive zone model for interface fatigue crack growth simulation, Engineering Fracture Mechanics, 70: 209-232

70. Yang,B; Mall,S; Ravi-Chandar,K (2001) A cohesive zone model for fatigue crack growth in quasibrittle materials, International Journal of Solids and Structures, 38: 3927-3944

71. Nguyen,O; Repetto,EA; Ortiz,M; Radovitzky,RA (2001) A cohesive model of fatigue crack growth, International Journal of Fracture, 110: 351-3

72. Robinson,P; Galvanetto,U; Tumino,D; Belluci,G (2005) Numerical simulation of fatigue-driven delamination using interface elements, International journal for numerical methods in engineering, 63: 1824-1848

73. Peerlings,RHJ; Brekelmans,WAM; DeBorst,R; Geers,MGD (2000) Gradient-enhanced damage modelling of high-cycle fatigue, International journal for numerical methods in engineering, 49: 1547-1569

74. Tumino,D; Cappello,F (2007) Simulation of Fatigue Delamination in Composites with Different Mode Mixtures, Journal of Composite Materials, 41; 2415-2441

75. Turon,A; Costa,J; Camanho,PP; Davila,CG (2007) Simulation of delamination in composites under high-cycle fatigue, Composites Part A: Applied Science and Manufacturing, 38: 2270-2282

76. Turon,A; Costa,J; Camanho,PP; Maimi,P (2007) Simulation of Delamination Onset and Propagation under Fatigue Loading using Cohesive Zone Models, ECCOMAS Thematic Conference on Mechanical Response of Composites, 12-14th September 2007, Porto, Portugal

77. Jacob,P; Goulding,L (2002) An Explicit Finite Element Primer, NAFEMS, Glasgow, 127 pages, ISBN 1 874376 45 X

78. Borg,R; Nilsson,L; Simonsson,K (2002) Modelling of delamination using a discretized cohesive zone and damage formulation, Composites Science and Technology, 62: 1299-1314

79. Li,X; Hallett,SR; Wisnom,MR (2008) Predicting the effect of through-thickness compressive stress on delamination using interface elements, Composites Part A: Applied Science and Manufacturing, 39: 218-230

80. Harper,P; Hallett,SR (2008); Cohesive zone length in numerical simulations of composite delamination, Engineering Fracture Mechanics 2008, 75:4774-4792

81. Borg,R; Nilsson,L; Simonsson,K (2004) Simulating DCB, ENF and MMB experiments using shell elements and a cohesive zone model, Composites Science and Technology, 64:269-278.

82. Hillerborg,A; Modeer,M, Petersson,PE (1976) Analysis of crack formation and growth in concrete by means of fracture mechanics and finite elements, Cement and Concrete Research, 6:773-782

83. Yang,QD; Cox,BN; Nalla,RK; Ritchie,RO (2006) Fracture length scales in human cortical bone: The necessity of nonlinear fracture models, Biomaterials, 27:2095-2113

84. Turon,A; Davila,CG; Camanho,PP; Costa,J (2007) An engineering solution for mesh size effects in the simulation of delamination using cohesive zone models, Engineering Fracture Mechanics, 74:1665-1682

85. Planas,J; Elices,M (1991) Nonlinear fracture of cohesive materials, International Journal of Fracture, 51:139-157

86. Smith,E (1999) The effect of the stress-relative displacement law on failure predictions using the cohesive zone model, International Journal of Fracture, 99:41-51

87. Williams,JG; Hadavinia,H (2002) Analytical solutions for cohesive zone models, Journal of the Mechanics and Physics of Solids, 50:809-825

88. Bao,G; Suo,Z (1992) Remarks on crack-bridging concepts, Applied Mechanics Reviews, 24:355-366

89. Massabo,R; Cox,BN (1999) Concepts for bridged mode II delamination cracks, Journal of the Mechanics and Physics of Solids, 47:1265-1300

90. M,Quaresimin; M,Ricotta (2006) Fatigue behaviour and damage evolution of single lap bonded joints in composite material, Composites Science and Technology, 66:176-187

91. M,Quaresimin; M,Ricotta (2006) Stress intensity factors and strain energy release rates in single lap bonded joints in composite materials, Composites Science and Technology, 66:647-656

92. M,May; S,R,Hallett (2008) Modelling mode I crack initiation in composites under fatigue loading using interface elements, ECCM-13, 13th European Conference on Composite Materials, June 2-5, 2008, Stockholm, Sweden

93. ACG (2003). XMVR444 Material Data Sheet

Appendix A: Corrected Beam Theory Equations

(a) Mode I DCB

Considering the DCB specimen as two single cantilever beams, of length equal to the crack length, a, simple beam theory can be applied to give:

$$\Delta_I = \frac{2Pa^3}{3E_{11}I} \qquad \text{(A.1)}$$

where,

Δ_I = Vertical separation of cantilever beam tips

P = Point load applied to the free end of each cantilever

E_{11} = Young's Modulus of each cantilever along its length

I = Second Moment of Area of each cantilever ($=Bh^3/12$, where B and h are the specimen width and half-depth respectively, as defined in Figure 4.2)

In order to correct the displacement for shear deformation and for local deformations that occur around the crack tip, a corrected beam theory method can be used, in which equation (A.1) becomes:

$$\Delta_I = \frac{2P(a+\chi h)^3}{3E_{11}I} \qquad \text{(A.2)}$$

where,

χ = Correction Parameter

h = cantilever depth

A value of χ can be determined both experimentally and analytically, but in this study, the analytical value presented by Reeder *et al.*[37] is used, where:

$$\chi = \sqrt{\frac{E_{11}}{11G_{13}}\left[3 - 2\left(\frac{\Gamma}{1+\Gamma}\right)^2\right]} \qquad \text{(A.3a)}$$

and

$$\Gamma = 1.18\frac{\sqrt{E_{11}E_{22}}}{G_{13}} \qquad \text{(A.3b)}$$

The mode I strain energy release is given by[37]:

$$G_I = \frac{P^2(a+\chi h)^2}{BE_{11}I} \qquad \text{(A.4)}$$

Under a linearly increasing tip displacement, the load (P) increases until the point where $G_I = G_{IC}$ and the crack begins to propagate. The subsequent load-displacement relationship for each increment of crack extension is found by combining equations (A.2) and (A.4) with G_I set equal to G_{IC}.

(b) Mode II 3ENF

The same principles apply for the 3 point ENF (see Figure 4.3(b)), in which the displacement and mode II strain energy release rate before initial crack propagation are given by[37]:

$$\Delta_{II} = \frac{3P(a+0.42\chi h)^3 + 2PL^3}{96E_{11}I} \qquad \text{(A.5)}$$

$$G_{II} = \frac{3(a+0.42\chi h)^2 P^2}{64BE_{11}I} \qquad \text{(A.6)}$$

The second moment of area, I, in equations (A.5) and (A.6) remains equal to that calculated for the DCB specimen, using half the specimen depth and the length, L, is as defined in Figure 4.3(b).

(c) Mixed-Mode FRMM

For the FRMM specimen (see Figure 4.3(c)), the upper cantilever tip displacement and separate mode I and mode II strain energy release rate components are given by[38]:

$$\Delta = \frac{PN'\left[7(a+0.42\chi h)^3 + (L+2\chi h)^3\right]}{2Bh^3E_{11}} \tag{A.7}$$

$$G_I = \frac{3FP^2(a+\chi h)^2}{B^2h^3E_{11}} \tag{A.8}$$

$$G_{II} = \frac{9FP^2(a+0.42\chi h)^2}{4B^2h^3E_{11}} \tag{A.9}$$

where F and N' are correction factors for large displacements and the length, L, is as defined in Figure 4.3(c). Due to the small displacement of approximately 3mm at the point of initial crack propagation, F and N' were assumed equal to unity for the FRMM specimen used in Chapter 4. Under a linearly increasing upper cantilever tip displacement, the analytical load, P, at which initial crack propagation occurs was calculated using the power law failure criterion given by Equation (4.2), with $\alpha = 1$.

Appendix B: Calculation of Elastic Modulus for Cohesive Zone Length Equations

The elastic constant E' that appears in equations (4.4) and (4.5) is dependent on the mode of loading, whether plane stress or plane strain conditions exist and whether the specimen can be considered as slender or infinite.

For a mode I crack in an infinite body under plane stress conditions[83]:

$$\frac{1}{E_I'} = \sqrt{\frac{b_{11}b_{33}}{2}}\sqrt{\left(\frac{b_{33}}{b_{11}}\right)^{1/2} + \frac{2b_{31}+b_{55}}{2b_{11}}} \tag{B.1}$$

where the b_{ij} are Voigt elastic constants defined by:

$$\varepsilon_i = \sum_{j=1}^{6} b_{ij}\sigma_j\,, \tag{B.2}$$

with $\varepsilon_1 \equiv \varepsilon_{11}, \ldots, \varepsilon_6 \equiv \varepsilon_{12}$; $\sigma_1 \equiv \sigma_{11}, \ldots, \sigma_6 \equiv \sigma_{12}$. For a specially orthotropic specimen (axes of orthotropy aligned with the axes of symmetry of the specimen), the Voigt elastic constants are related to the engineering elastic constants by:

$$b_{11} = 1/E_{11},\ b_{12} = -\nu_{12}/E_{11},\ b_{66} = 1/G_{12},$$

$$b_{22} = 1/E_{22},\ b_{23} = -\nu_{23}/E_{22},\ b_{55} = 1/G_{31}, \tag{B.3}$$

$$b_{33} = 1/E_{33},\ b_{31} = -\nu_{31}/E_{33},\ b_{44} = 1/G_{23},$$

where E_{ii} is the Young's modulus in the x_i direction, ν_{ij} is a Poisson's ratio and G_{ij} is an engineering shear modulus. For the alignment of the specimen in Figure 4.2, the engineering constants involved in E_I' are E_{11}, E_{33}, G_{31} and ν_{31}.

For a crack in an infinite body that is loaded in shear, the elastic constant becomes:

$$\frac{1}{E_{II}^{'}} = \sqrt{b_{11}/2}\sqrt{(b_{11}b_{33})^{1/2} + (b_{31} + b_{55}/2)} \qquad \text{(B.4)}$$

In a slender body, a different elastic constant appears. For example, in a thin plate or beam containing a mid-plane crack propagating in the x_1 direction and loaded in mode II, the elastic constant that appears in results for the cohesive zone length is the reduced Young's modulus:

$$E_{II,slender}^{'} = \frac{E_{11}}{1 - \nu_{13}\nu_{31}} \qquad \text{(B.5)}$$